

**PROCESS INTENSIFICATION ENABLING DIRECT COMPRESSION  
FOR PHARMACEUTICAL MANUFACTURING: FROM SPHERICAL  
AGGLOMERATION TO PRECISE CONTROL OF CO-  
AGGLOMERATION**

by

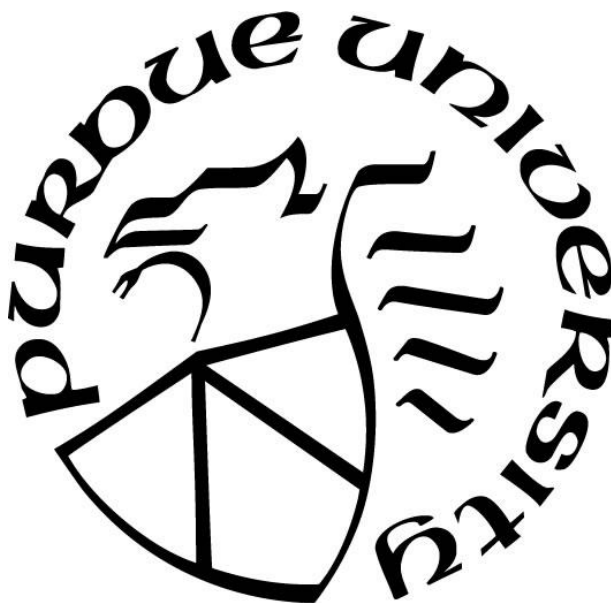
**Kanjakha Pal**

**A Dissertation**

*Submitted to the Faculty of Purdue University*

*In Partial Fulfillment of the Requirements for the degree of*

**Doctor of Philosophy**



Davidson School of Chemical Engineering

West Lafayette, Indiana

December 2019

**THE PURDUE UNIVERSITY GRADUATE SCHOOL  
STATEMENT OF COMMITTEE APPROVAL**

Dr. Zoltan K. Nagy, Chair

Davidson School of Chemical Engineering

Dr. Gintaras V. Reklaitis

Davidson School of Chemical Engineering

Dr. Doraiswami Ramkrishna

Davidson School of Chemical Engineering

Dr. Kingsly Ambrose

School of Agricultural and Biological Engineering

**Approved by:**

Dr. Sangtae Kim

Head of the Graduate Program

*I never lose, I either win or I learn*  
- *Nelson Mandela*

## **ACKNOWLEDGMENTS**

I thank Dr. Nagy for giving me the wonderful opportunity to work under his guidance – he kept the graduate experience constantly enriching and challenging for me, which helped a lot in my professional development. I also thank my thesis committee members Dr. Doraiswami Ramkrishna, Dr. Gintaras Rekalitis, Dr. Kingsly Ambrose for their valuable insights and suggestions throughout my graduate studies. Their expert insights were instrumental in my research endeavors and develop skillsets necessary for the purpose. I also thank my family for their constant encouragement throughout my undergraduate and graduate studies – it is safe to say I shall not be able to achieve even a fraction of what I have achieved today, without their support.

## TABLE OF CONTENTS

LIST OF TABLES .....	8
LIST OF FIGURES .....	9
ABSTRACT .....	15
1. INTRODUCTION .....	16
1.1 Motivation.....	16
1.2 Research Aims .....	16
1.3 Research Contributions.....	17
2. THEORY .....	20
2.1 Crystallization.....	20
2.1.1 Primary nucleation.....	20
2.1.2 Secondary nucleation and growth.....	21
2.2 Spherical agglomeration .....	21
2.3 Mathematical modeling using population balance equations .....	26
2.4 Process optimization .....	26
2.5 Model predictive control (MPC).....	27
2.5.1 Different types of model uncertainties .....	28
2.5.2 Model based control .....	29
2.6 Process analytical technology (PAT).....	30
3. ITERATIVE MODEL BASED EXPERIMENTAL DESIGN FOR SPHERICAL AGGLOMERATION PROCESS .....	35
3.1 Introduction.....	35
3.2 Theory.....	38
3.2.1 Mathematical modeling of SA.....	38
3.3 Materials and methods .....	53
3.4 Results and Discussions.....	53
3.4.1 Experiments for finding best model amongst suite of candidate models .....	53
3.5 Model discrimination .....	55
3.5.1 Model based design of experiments for refined parameter estimation.....	60
3.6 Conclusions.....	65

4. MODEL BASED OPTIMAL CONTROL OF SPHERICAL AGGLOMERATION UNDER PARAMETRIC UNCERTAINTIES .....	66
4.1 Introduction.....	66
4.2 Theory.....	68
4.2.1 Model predictive control (MPC) .....	68
4.3 Results and discussions.....	73
4.4 Conclusions.....	80
5. MECHANISTIC INSIGHTS INTO SPHERICAL CRYSTALLIZATION GUIDED BY PROCESS ANALYTICAL TECHNOLOGY : TOWARDS QUALITY BY DESIGN FOR PHARMACEUTICAL PROCESS INTENSIFICATION .....	82
5.1 Introduction.....	82
5.2 Experimental Section .....	84
5.2.1 Chemicals and analytical methods.....	84
5.2.2 Process Description .....	84
5.3 Results and Discussions.....	87
5.3.1 Effect of API Concentration .....	89
5.3.2 Effect of Emulsifier Concentration.....	93
5.3.3 Effect of stirring speed.....	97
5.3.4 Effect of Solvent to Antisolvent Ratio.....	99
5.3.5 Conceptual Model Formulation.....	103
5.4 Conclusions.....	104
6. MATHEMATICAL MODELING OF EMULSION SOLVENT DIFFUSION FOR SPHERICAL CRYSTALLIZATION: HOW TO DE-CONVOLUTE PRIMARY CRYSTAL SIZE DISTRIBUTION FROM AGGLOMERATE SIZE DISTRIBUTION? .....	106
6.1 Introduction.....	106
6.2 Theory.....	108
6.2.1 Process Description .....	108
6.2.2 Mathematical Modelling of Spherical Crystallization.....	113
6.2.3 Crystal agglomeration within droplets.....	123
6.3 Results and Discussions.....	126
6.4 Conclusions.....	132

7. MODEL-BASED OPTIMIZATION OF COOLING CRYSTALLIZATION OF ACTIVE PHARMACEUTICAL INGREDIENTS UNDERGOING THERMAL DEGRADATION .....	134
7.1 Introduction.....	134
7.2 Theory .....	137
7.3 Experimental Methods .....	141
7.3.1 Materials .....	141
7.4 Results and discussions.....	143
7.5 Optimization of batch cooling crystallization.....	144
7.5.1 Optimal Cooling for product crystal size maximization.....	144
7.6 Evolution of process variables .....	147
7.7 Multi-objective optimization .....	153
7.8 Conclusions.....	162
8. FUTURE DIRECTIONS .....	164
REFERENCES .....	165

## LIST OF TABLES

<b>Table 3-1.</b> Different agglomeration kernels used in this work where $x$ and $y$ are the volumes of the agglomerating particles .....	42
<b>Table 3-2.</b> Experimental design for model discrimination.....	54
<b>Table 3-3.</b> Parameter estimates of the agglomeration kernels obtained by minimizing the mean square error deviations between the experimental ASD and the model predicted ASD .....	55
<b>Table 3-4.</b> Mixing parameters associated with crystallizer.....	56
<b>Table 3-5.</b> Cross validation designed experiments for different agglomeration kernels. ....	58
<b>Table 3-6.</b> Bounds for experimental process variables. ....	61
<b>Table 3-7.</b> Parameter Estimates and Process Conditions .....	62
<b>Table 3-8.</b> MSE for each iteration of MBED showing the MSE decreases with increasing iterations. ....	64
<b>Table 4-1.</b> Estimated model parameters along with standard deviations.....	74
<b>Table 4-2.</b> Difference of MAS from set-point MAS for open loop optimizer, deterministic MPC with parametric uncertainty and MPC with surrogate model reconstruction. ....	79
<b>Table 5-1.</b> End-of-batch mean chord length increases with increase in API Concentration. ....	90
<b>Table 5-2.</b> Effect of emulsifier concentration on the end-of-batch mean chord length. ....	94
<b>Table 5-3.</b> Numerical Estimates for variables associated with mass flux of antisolvent and crystal growth .....	96
<b>Table 5-4.</b> End-of-batch Mean Chord Length decreases with increase in stirrer rpm .....	98
<b>Table 5-5.</b> End-of-batch mean chord length decreases with increase in sasr.....	101
<b>Table 5-6.</b> Timescales of diffusion and primary crystal growth at low and high sasrs.....	102
<b>Table 6-1.</b> Kinetic and process parameters associated with spherical crystallization.....	127
<b>Table 7-1.</b> Kinetic parameters of nucleation, growth and degradation processes.....	144
<b>Table 7-2.</b> Different Optimization studies with the optimization problem formulations and underlying mechanistic models.....	146
<b>Table 7-3.</b> Solubility of Salicylic Acid in ethanol and water at 25°C .....	150

## LIST OF FIGURES

<b>Figure 1-1.</b> Overall summary of research aims of this thesis.....	18
<b>Figure 1-2.</b> Major accomplishments of this thesis focusing on the gaps in prior understanding on each of the focus areas. The limitations associated with each topic necessitated the development of the successive topics.....	19
<b>Figure 2-1.</b> Phase diagram for generic cooling crystallization process.....	20
<b>Figure 2-2.</b> Rate processes and possible mechanisms during SA showing wetting and nucleation, distributive vs immersive modes of agglomeration, consolidation, breakage and granule attrition and granule growth.....	23
<b>Figure 2-3.</b> Different stages during SA as a function of increasing binder content (a) – (f).....	25
<b>Figure 2-4.</b> Nominal state evolution in the absence of uncertainties vs actual state evolution, in the presence of uncertainties.....	29
<b>Figure 2-5.</b> Shrinking horizon control model predictive control strategy.....	30
<b>Figure 2-6.</b> Schematic of Focused Beam Reflectance Measurement probe.....	31
<b>Figure 2-7.</b> ATR-UV/Vis spectroscope to measure solute concentration in solutions with solids present.....	32
<b>Figure 2-8.</b> Various stages of solute elution for reverse phase gradient elution chromatography.....	34
<b>Figure 3-1.</b> Finite volume grid for discretizing particle volumes. The actual particle volumes are represented by the grid points $v_i, v_{i+1}$ whereas the particle population in the $i$ -th C.V. are assumed to be concentrated at a representative volume $x_i$ for computational purposes.....	40
<b>Figure 3-2.</b> (a) Orthokinetic agglomeration of a large particle and a small particle due to fluid shear which is represented by Schomulowski's kernel, and (b) Perikinetic agglomeration of a large particle and a small particle due to random Brownian motion, which is represented by Brownian kernel.....	44
<b>Figure 3-3.</b> Agglomerate growth by layering of fine crystals in solution onto pre-formed agglomerates.....	45
<b>Figure 3-4.</b> (a) Continuous coalescence model where 100 large droplets all grow by coalescing with smaller sized droplets – Golovin kernel, and (b) Stochastic Growth Model where only a fraction (10%) of the larger sized droplets grow by coalescing with smaller sized droplets – reformulation of this mechanistic kernel gives the Thompson kernel.....	46
<b>Figure 3-5.</b> Overview of model discrimination followed by model-based design strategy used in this work. Model discrimination gives the best model that explains the initial experimental observations. Model based design uses information theory to design experiments which gives precise parameter estimates with minimal number of experiments.....	48

- Figure 3-6.** Algorithm for model based experimental design for precise estimation of model parameters. .... 51
- Figure 3-7.** (a) Experimental ASD of SA experiments (b) stereomicroscope images of agglomerates produced from Experiment 5. .... 54
- Figure 3-8.** ASD from Experiment 4 and model predictions with Golovin kernel. Model predicted ASD with optimized parameters ( $\beta_{02} = 7.87 \times 10^{-4}$ ) gives less mismatch to experimental ASD than ASD predicted with the parameter ( $\beta_{01} = 3 \times 10^{-2}$ ), used as initial guess. .... 57
- Figure 3-9.** ASD from Experiment 5 and model predictions with the optimal parameter estimates for Thompson and Golovin kernels. Model Predictions with Golovin kernel (MSE = 31.04%) has better agreement with the experimental ASD than the Thompson kernel (MSE = 58.17%). .... 59
- Figure 3-10.** Hypothetical mechanism of agglomeration where three difference agglomeration mechanisms (orthokinetic, gravitational, layering) all occur simultaneously. .... 60
- Figure 3-11.** ASD from experiments (a) E1, (b) E2, and (c) E3 and model simulations with parameter estimates of  $\beta_0$ . .... 63
- Figure 3-12.** Model predictions with optimal parameters from iteration 1 and iteration 3. .... 64
- Figure 4-1.** Conceptual experimental setup of online MPC with real-time imaging to find in-situ particle size. .... 69
- Figure 4-2.** Hypothetical uncertainty propagation and GPC reconstruction for a parameter space with 3 parameters and state space with 3 states. .... 71
- Figure 4-3.** Workflow for model predictive control of SA under parametric model uncertainties using low dimensional PCE based surrogate model reconstruction. .... 73
- Figure 4-4.** (a) Evolution of crystallizer during various stages in open loop optimization (b) Evolution of antisolvent flow rate indicating antisolvent addition in stage 3 (c) Evolution of solution flow rate indicating API solution addition in stage 1 (d) Evolution of binder flow rate indicating binder addition in stage 2 (e) Evolution of MAS indicating deviation of final MAS from set-point. .... 75
- Figure 4-5.** Model Prediction vs physical process for evolution in stage 3 of process after antisolvent addition. Model parametric uncertainties give rise to the plant-model mismatch. .... 76
- Figure 4-6.** (a) Evolution of crystallizer during various stages in MPC (b) Evolution of antisolvent flow rate indicating antisolvent addition in stage 3 (c) Evolution of solution flow rate indicating API solution addition in stage 1 (d) Evolution of binder flow rate indicating binder addition in stages 2 and 4 (e) Evolution of MAS indicating much less deviation of final MAS from set-point, compared to open-loop case. .... 77
- Figure 4-7.** (a) Evolution of crystallizer during various stages in RN MPC (b) Evolution of antisolvent flow rate indicating antisolvent addition in stage 3 (c) Evolution of solution flow rate indicating API solution addition in stages 1 and 2 (d) Evolution of binder flow rate indicating binder addition in stage 2 (e) Evolution of MAS indicating much less deviation of final MAS from set-point, compared to open-loop case. .... 79

**Figure 4-8.** Challenges with co-agglomerating APIs and excipients simultaneously, using binder. .... 81

**Figure 5-1.** Overview of process development for emulsion solvent diffusion (a) emulsifier is dissolved in antisolvent, which is stirred at constant rpm, (b) API solution is pumped into the antisolvent in the crystallizer. Since the solvent within the emulsion droplets and the antisolvent in the continuous phase are miscible, diffusion of antisolvent into the droplets takes place. (c) Since the API is insoluble in the antisolvent, it starts crystallizing out within the droplets. The API solution is stopped after 10 mins and the evolution of the process is tracked till the end-of-batch time (120 mins). (d) Diffusion of antisolvent into the emulsion droplets and solvent out of the emulsion droplets in stage (b) and (c). .... 86

**Figure 5-2.** Illustration of the two populations – droplet population and crystal population within the droplets. The droplet size distribution (DSD) can be measured using FBRM while the crystal size distribution (CSD) within the droplets cannot be measured directly, but its evolution can be inferred from the evolution of the droplet size distribution. .... 87

**Figure 5-3.** SEM image at (a) 1000X showing the presence of spherical co-agglomerates and (b) 4000X showing the presence of both ibuprofen (API) and talc (excipient) in the filtered co-agglomerates. (c) Optical micrographs of the final product co-agglomerates showing the presence of spherical particles. .... 88

**Figure 5-4.** End-of-batch chord length distribution (CLD) of ibuprofen-talc co-agglomerates at different initial API concentrations. The CLD becomes progressively right-skewed with increase in API concentration which indicates the formation of larger agglomerates. There are two peaks in the CLD – the peak at smaller chord length (~4  $\mu\text{m}$ ) arises due to air bubbles in the crystallizer, whereas the peak at larger chord lengths (~90-200  $\mu\text{m}$ ) occurs due to emulsion droplets, which ultimately form product agglomerates. .... 89

**Figure 5-5.** Evolution of FBRM counts for (a) 0.5 g/mL (b) 0.125 g/mL illustrating the difference in dynamical evolution of particle counts in FBRM, which shows the time lag in evolution of small and large particle counts for a lower API concentration. .... 90

**Figure 5-6.** Evolution of operating point in phase diagram shows higher supersaturation for higher API concentration, which gives higher nucleation and growth rates. .... 91

**Figure 5-7.** (a) Droplet expansion for lower API concentration, which shows crystal nucleation at  $t=2$  min followed by crystal growth at  $t = 8$  min. At  $t=10$  min, interfacial stress on droplets makes droplets expand which is recorded as increase of large particle counts in FBRM. At  $t=25$  min, the supersaturation is completely depleted, so the droplet stops expanding. (b) for higher API concentration, the rapid growth at 8 min leads to faster droplet expansion and since the supersaturation depletion is slower, the droplet keeps on expanding at  $t = 25$  min. .... 92

**Figure 5-8.** (a) End-of-batch chord length distribution becomes left skewed with increase of  $\phi_{emul}$  (b) FBRM counts at high emulsifier concentration  $\phi_{emul} = 1.25\%$  stabilize after 30 mins (c) FBRM counts at low emulsifier concentration  $\phi_{emul}=0.25\%$  keeps changing throughout the batch. .... 93

**Figure 5-9.** (a) At lower emulsifier concentration, droplets in solution that encounter each other coalesce to form a larger droplet (b) at higher emulsifier concentration, droplet coalescence is prevented due to steric repulsion between emulsifier molecules on adjacent droplets. .... 94

**Figure 5-10.** (a) End-of-batch CLD becomes left skewed with increase in rpm of stirrer, (b) evolution of FBRM counts at higher rpm (800) shows increase of smaller particle counts throughout the batch, which is indicative of droplet breakage in the crystallizer. .... 98

**Figure 5-11.** (a) End-of-batch Chord Length Distribution becomes left skewed with increase in sasr; (b) at lower sasr, small-particle(10-100  $\mu m$ ) FBRM counts increase monotonically throughout the batch; (c) at higher sasr, FBRM counts first increase but then decrease throughout the batch. .... 100

**Figure 5-12.** (a) Increase in sasr leads to an increase in the number of droplets in the crystallizer; (b) at a low sasr, the number number density of emulsifier molecules in solution is higher than nominal, while at high sasr, the number density of emulsifier molecules is lower than nominal. .... 102

**Figure 5-13.** (a) At higher sasr, the emulsifier concentration is lower than necessary; so the antisolvent diffusion is faster, which causes rapid crystallization and the droplets expand; (b) at lower sasr, the emulsifier concentration is higher than necessary; so the antisolvent diffusion is slower, which causes slower crystallization. .... 103

**Figure 6-1.** (a) An example process flow diagram of a traditional PM process for solid oral dosage pharmaceutical manufacturing, where the downstream manufacturing consists of seven unit operations, (b) Proposed process flow diagram of an intensified PM process, where the downstream drug manufacturing consist of only four unit operations. The unit operations milling, granulation and blending have been eliminated and the particle design for producing spherical agglomerates is carried out directly inside the crystallizer. .... 109

**Figure 6-2.** Process development for SC (a) API solution pumped into crystallizer creates droplet at the nozzle tip (b) Emulsifier attaches to detached droplet interface (c) Crystallization occurs within droplets due to supersaturation generation (d) Due to good miscibility, antisolvent from bulk solution diffuses into droplets while solvent inside droplets diffuses out. Since the API within the droplet is insoluble in the antisolvent, it crystallizes out. (e) Droplet breakage occurs due to collision with the stirrer, however droplet agglomeration is prevented due to emulsifier attached to droplet interface. .... 110

**Figure 6-3.** API tablet produced in the tablet press contains the spherical crystals, which forms the compact tablets due to the compression force exerted by the tablet press. The tablet ingested by the human is broken down in the digestive tract, however the actual bioavailability of the tablets depends on the primary crystal size distribution that forms the agglomerates. .... 111

**Figure 6-4.** (a) Interfacial mass transport model, where a heterogeneous droplet population is considered at the reactor inlet (b) Population balance model, where a homogeneous droplet population is considered at the reactor inlet. .... 113

**Figure 6-5.** Characteristic curves for solution of the population balance equations for droplet size distribution. When the droplet age  $\tau < t$  (time), the characteristic curve falls to  $\tau=0$  and the problem

reduces to solving the boundary value problem. However, then  $\tau > t$ , the characteristic curve falls to  $t=0$  and the problem reduces to solving the Initial Value Problem..... 121

**Figure 6-6.** DSD can be reconstructed from the FBRM measurements, while the CSD within the droplets need to be estimated from a mathematical model. The CSD depends on the droplet size and is very different (green and red curves) for different droplet sizes..... 125

**Figure 6-7.** Summary of important steps for solving multiscale PBEs..... 126

**Figure 6-8.** Particle size distribution for (a) smaller droplet of radius  $20 \mu m$ ; (b) larger droplet of radius  $240 \mu m$ . This illustrates that smaller droplets have higher nucleation rates of primary crystals, which produces smaller particles at the end of the batch. For larger droplets, the nucleation rates are lower and the crystallization process is growth dominated, which produces larger primary crystals at the end of the batch..... 128

**Figure 6-9.** Concentration evolution during the batch for two different droplet radii. For smaller droplet, the concentration rapidly decreases around 12.5 min due to high rates of primary nucleation..... 129

**Figure 6-10.** (a) For smaller droplets, rapid antisolvent diffusion into the droplet during 0-9 min creates high supersaturation which leads to high rate of primary nucleation at 12.5 min. However, the crystal growth rate is much lower which produces smaller Primary Crystals at the end of the process (b) For larger droplet, antisolvent diffusion is much slower which generates supersaturation more slowly. At 29 min, nucleation of primary crystals is triggered followed by crystal growth over the entire batch which produces larger end-of-batch primary crystals. .... 129

**Figure 6-11.** Operating curve in the phase diagram of API concentration-antisolvent concentration for two different droplet radii. For smaller radius droplet, nucleation happens at a higher supersaturation (point A), which generates smaller primary crystals. For larger droplets, nucleation happens at lower supersaturation (point B), which leads to lower nucleation rates but higher growth rates, which ultimately produces larger primary crystals. .... 130

**Figure 6-12.** Number density of primary crystals within droplet of size  $240 \mu m$  with and without agglomeration for (a)  $t = 29$  min; and (b)  $t = 120$  min; (c) Evolution of crystal agglomerates within the droplet. .... 132

**Figure 6-13.** Dilemma regarding initial process temperature for APIs undergoing thermal degradation..... 133

**Figure 7-1.** Schematic of experimental setup showing the jacketed crystallizer and Process Analytical Technology Tools..... 143

**Figure 7-2.** Simulated optimum cooling profiles for (O1) size maximization without degradation kinetics, (O2) size maximization with degradation kinetics and (O3) degraded product concentration minimization. .... 145

**Figure 7-3.** Evolution of mean crystal size for (O1) size maximization without degradation kinetics, (O2) size maximization with degradation kinetics and (O3) degraded product concentration minimization objective. The final Mean Crystal Size is higher for size maximization objective than degradation product concentration minimization objective. .... 146

**Figure 7-4.** Evolution of (a) API concentration (b) degradation product concentration. The API concentration reduces much faster with the concentration minimization objective. The final degradation product concentration is much higher with the concentration minimization objective.

..... 149

**Figure 7-5.** Nucleation rates for aspirin for (O1) size maximization without degradation kinetics, (O2) size maximization with degradation kinetics and (O3) degraded product concentration minimization. The supersaturation generated is much higher for concentration minimization objective. The growth rates are similar for both the objectives, but the nucleation rate is much higher for concentration minimization objective..... 151

**Figure 7-6.** Temperature profiles obtained from the multi-objective optimization using different weights between size maximization objective and degradation minimization objective. The cooling profile shows a monotonic shift in the shape of the profile as the weight given to the individual objective is changed..... 153

**Figure 7-7.** Experimental Concentration evolution of Aspirin (API) and salicylic acid (degraded product) for size maximization objective. The API concentration decreases due to crystallization and degradation while the degradation product concentration increases with time. .... 155

**Figure 7-8.** Experimental evolution of (a) number of chord counts for a certain size range per second (b) SWMCL in FBRM for objective of size maximization..... 155

**Figure 7-9.** PVM image of final product crystals when operated with the objective of size maximization..... 156

**Figure 7-10.** Concentration evolution of (a) aspirin, and (b) salicylic acid (degradation product) for optimization with objective as minimization of concentration of degraded product..... 157

**Figure 7-11.** Evolution of (a) counts/s in FBRM and (b) SWMCL for objective of minimization of concentration of degradation product. .... 158

**Figure 7-12.** PVM image of particles for objective of minimization of concentration of degradation product showing smaller crystals compared to size maximization..... 158

**Figure 7-13.** Concentration evolution of (a) aspirin (API) and (b) salicylic acid (degradation product) for two different adsorption kinetic constants. The API concentration does not change with change in adsorption kinetics because the growth rate of the API is assumed to be independent of the adsorption of impurities. The degradation product concentration changes on changing the adsorption kinetics since faster adsorption onto crystals leads to lower concentration of degradation product in the solution..... 159

**Figure 7-14.** Concentration of degradation product with optimal parameter estimate. The model simulations run with the optimal estimated parameter shows very good match to the experimental concentrations. The slight model mismatch happens because either (i) the degradation product (SA) first gets adsorbed onto the aspirin crystals but then desorption of the adsorbed also takes place, which was not considered in the kinetic model (ii) adsorption rate constant is actually temperature dependent which was not modeled in this work. .... 160

## ABSTRACT

Spherical agglomeration (SA) is a novel process intensification strategy for particulate manufacturing. In the context of pharmaceutical manufacturing, it has the potential to reduce the number of unit operations in downstream processing from seven to three, which significantly reduces the manufacturing cost. However, SA process development for a new API in the drug pipeline is still a challenging exercise, which has impeded its practical implementation. The major bottleneck lies in the lack of fundamental understanding of the mechanistic principles underlying agglomeration of primary crystals, which can enable rational process design. In addition, most SA processes reported in literature focus on only the API, which does not eliminate the blending and wet granulation unit operations. The major purposes of this thesis are to (i) develop a first principle mathematical framework which can identify the fundamental agglomeration mechanism (ii) develop a model based online optimization framework, which can control the process, even in the presence of model uncertainties (iii) develop a rational framework for co-agglomerating APIs and excipients, guided by process analytical technology tools. It is believed that the novel technology developed in this thesis will lay the groundwork for fast and robust process development of co-agglomerating APIs and excipients in the future, thereby enabling one-step direct compression. The large-scale development and deployment of this technology will significantly reduce the time to market and the manufacturing costs for new APIs, thereby ensuring higher accessibility of life-saving drugs.

# 1. INTRODUCTION

## 1.1 Motivation

However, in spite of the plethora of literature on SA starting from the 1980's, design of a SA process for a new API largely remains a trial-and-error exercise. The lack to fundamental understanding of SA has impeded the development of novel technologies to enable co-agglomeration of multiple APIs and/or excipients.

## 1.2 Research Aims

The aim of this thesis is to understand the fundamental mechanism of agglomeration during SA which will enable rationale design of a SA process for a new API. A combination of experimental and modeling approach has been adopted in this work to fulfill this aim.

A list of the major aims are summarized below:

1. To develop a mathematical framework that can distinguish plausible modes of agglomeration in the crystallizer based on knowledge of underlying physics.
2. To estimate parameters of the mathematical model by carrying out as less number of experiments as possible. This research thrust is focused to enable a paradigm shift in this field, where instead of exploring all corners of the design space via statistical DOE, the first principle mechanistic model is used to explore only those parts of the DS which provides maximum information about the mathematical model.
3. To develop a framework which enables online control of SA, using the first principle mathematical model, even under the presence of model parametric uncertainties. The goal of this framework is to obtain the customer specified Particle Size Distribution (PSD).
4. To develop and validate a novel particulate technology process which can co-agglomerate APIs and excipients with very different surface properties.
5. To mathematically model the co-agglomeration process, in order to understand the multiscale evolution of particles within the crystallizer and within individual droplets.
6. To develop a dynamic optimization technology which can minimize the amount of degradation inside the crystallizer and improve the process yield of SA.

### 1.3 Research Contributions

The overall aim of this thesis is to develop a deep fundamental understanding of SA to enable rapid design of this PI strategy for new API-excipient formulations, to enable direct compression. This aim has been achieved via a combined experimental and modeling study. A major emphasis in this work has been the *use of computational modeling to accelerate the development* of SA for new APIs, which is hitherto impossible following a completely experimental paradigm. Summarily the research contributions are

- a. Population balance models were used to mathematically model the SA process. A model discrimination study determined the fundamental mechanism to follow Golovin model, which indicated orthokinetic mechanism.
- b. The precise parameters of the agglomeration kernel were estimated by using MBED, which reduced the number of experiments necessary to 3. In contrast a traditional statistical DOE, needs at-least 64 experiments to even sparsely span the DS.
- c. A stochastic MPC controller was then designed which could generate the end-of-batch desired MPS, even under the presence of model parametric and process uncertainties. This was shown to be a major improvement over the open-loop control case, whose performance is shown to deteriorate under model parametric uncertainties.
- d. However, the previous SA technology, where the binder agglomerates particles, was then shown to be incapable to agglomerating APIs and excipients when their surface properties are widely different. A new Emulsion Solvent Diffusion Technology is then developed which can co-agglomerate APIs and excipients by confining them within micron sized droplets. In-situ Process Analytical Technology (PAT) tools were then used to understand the fundamental mechanisms underlying ESD.
- e. This novel ESD technology was then mathematically modeled using a multiscale Population Balance Modeling (PBM) framework. It was shown that the mathematical model can help elucidate the evolution of the crystal population within the droplets, as well as the global droplet population. This contribution also represents a paradigm shift in this area in using mathematical models to understand the fundamental mechanisms at play, which is hitherto impossible even using state-of-art PAT tools.
- f. A novel dynamical optimization framework was then developed which can maximize the mean crystal size and minimize the concentration of degradation product. This was shown

to significantly improve the process yield for an API undergoing thermal degradation while crystallizing out. Novel in-situ PAT tools were also developed to enable precise monitoring of the API and impurity concentrations during the process.

A summary of all the major research thrusts of this thesis is shown in the research tree in **Figure 1-1**. A brief summary of the gaps in prior understanding associated with each topic, and the subsequent advancements in this thesis is given in **Figure 1-2**. **Figure 1-2** also enumerates the limitations with each topic, which necessitated the development of the technologies associated with the subsequent topics.

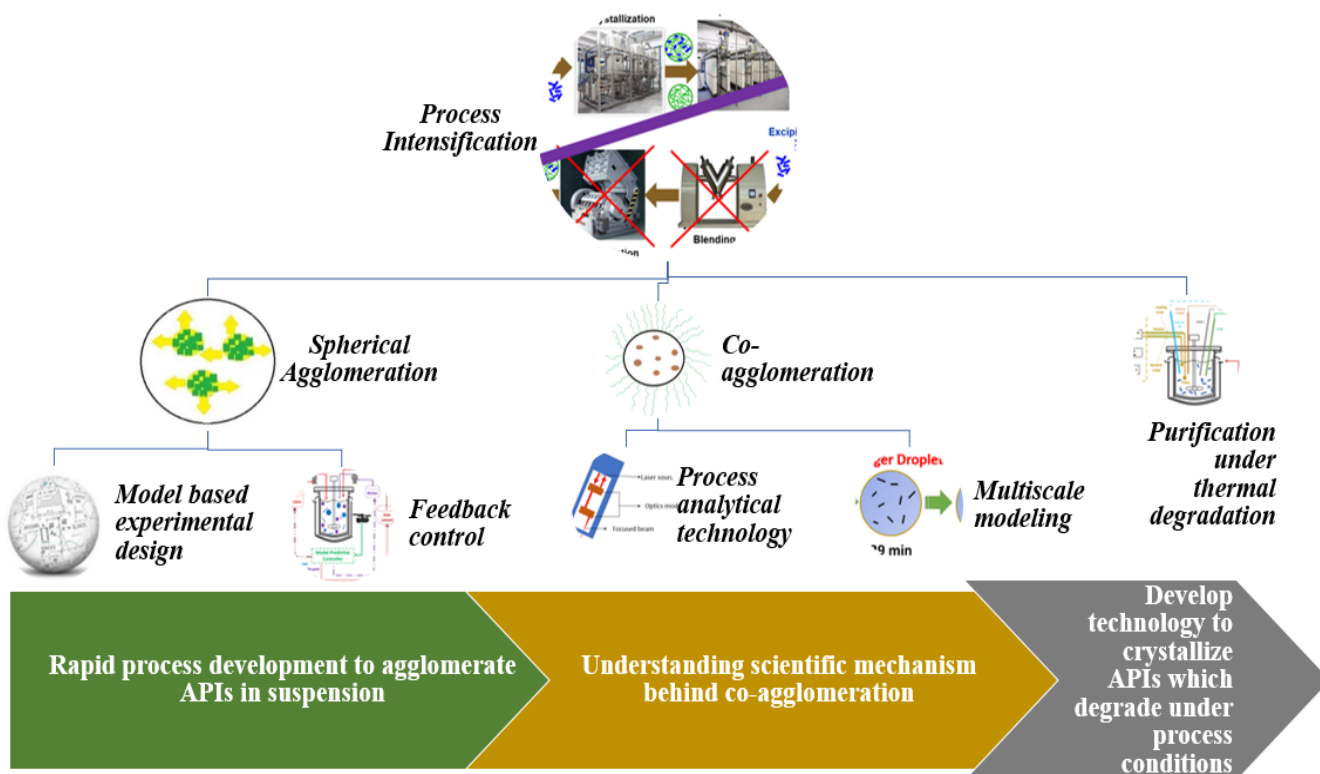


**Figure 1-1.** Overall summary of research aims of this thesis.

Topic	Gaps in prior understanding	Enabling solutions developed in this thesis
<b>Spherical Agglomeration of APIs</b>	<ul style="list-style-type: none"> <li>➤ Correct mechanism of agglomeration unknown!</li> <li>➤ Too many experiments needed to span design space</li> </ul>	<ul style="list-style-type: none"> <li>➤ Model based experimental design</li> <li>➤ Identify correct agglomeration mechanism</li> <li>➤ Number of experiments reduced from ~ 200 to 3</li> </ul>
<b>Limitations</b> Cannot co-agglomerate APIs and excipients with different surface wettabilities!	<ul style="list-style-type: none"> <li>➤ No quantification of parametric uncertainties</li> <li>➤ Open-loop optimization with nominal model parameters unable to reach set-point</li> </ul>	<ul style="list-style-type: none"> <li>➤ Closed loop feedback control steers system back to set-point</li> <li>➤ Stochastic model predictive control meets product specifications, even under parametric uncertainties</li> </ul>
<b>Co-agglomeration of APIs and excipients</b>	<ul style="list-style-type: none"> <li>➤ No use of in-situ PAT tools</li> <li>➤ No mechanistic process understanding</li> </ul>	<ul style="list-style-type: none"> <li>➤ FBRM used to gain fundamental mechanistic understanding</li> <li>➤ Relative time-scales of mass transfer and crystallization compared and contrasted</li> </ul>
<b>Limitations</b> API under investigation was degrading at higher temperatures	<ul style="list-style-type: none"> <li>➤ No multiscale modeling of co-agglomeration</li> <li>➤ No investigation into crystallization kinetics within droplets</li> </ul>	<ul style="list-style-type: none"> <li>➤ Multiscale modeling involving droplet population and internal crystal population</li> <li>➤ Elucidation of effect of crystallization kinetics based on droplet size</li> </ul>
<b>Crystallization with simultaneous API degradation</b>	<ul style="list-style-type: none"> <li>➤ API degradation during crystallization never taken into account</li> <li>➤ Alternate modes of crystallization viz. antisolvent crystallization chosen have reduced theoretical yield, and leads to formation of solvates</li> <li>➤ No use of in-situ PAT tools to monitor degradation</li> </ul>	<ul style="list-style-type: none"> <li>➤ Quantification of degradation kinetics and coupling with population balances</li> <li>➤ Model based optimization to minimize degradation and maximize crystal size</li> <li>➤ In-line UPLC used as novel PAT tool to monitor API and impurity concentration</li> </ul>

**Figure 1-2.** Major accomplishments of this thesis focusing on the gaps in prior understanding on each of the focus areas. The limitations associated with each topic necessitated the development of the successive topics.

## 2. THEORY

### 2.1 Crystallization

Crystallization is one of the most widely used unit operations in process separations [1]. Crystallization is a non-equilibrium kinetic process where the fundamental driving force is the supersaturation [2] in the crystallizer. Any solvent has an inherent capacity to hold a solute at a given temperature. The maximum amount of solute per unit mass of solvent is referred to as the solubility, which is a thermodynamic quantity [3]. The solubility generally increases [4] with temperature and solvent ratio, using which the solubility curve in the phase diagram can be constructed (**Figure 2-1**).

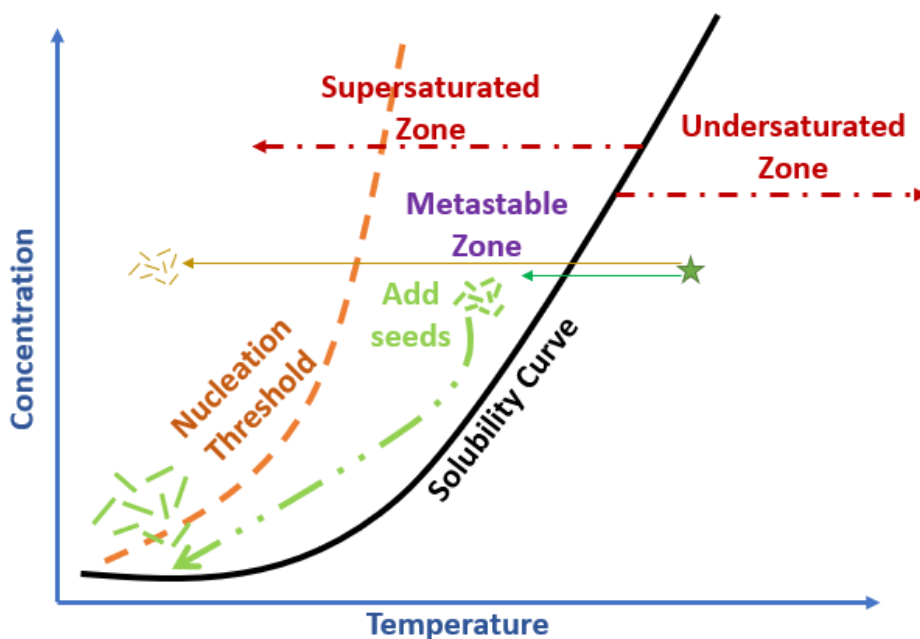


**Figure 2-1.** Phase diagram for generic cooling crystallization process.

#### 2.1.1 Primary nucleation

If a saturated solution is heated, it enters the undersaturated zone (**Figure 2-1**) where the solvent has a higher capacity for the solute. Conversely, if the saturated solution is cooled, it becomes supersaturated viz. the solvent theoretically has less capacity for solute at the specified temperature. However, when cooled, immediate phase separation does not occur. The temperature at which the solute nucleates out, on progressive cooling, is known as the cloud point ([5]). The temperature

difference between the cloud point and the saturation temperature, is known as the metastable zone width (MSZW) [6] which changes as a function of concentration. Primary nucleation [7] occurs beyond the primary nucleation threshold (PNT) viz. at temperature/sat below the critical value.

### **2.1.2 Secondary nucleation and growth**

Conversely, secondary nucleation (SN) and growth occur within the MSZ. Generally, for robust and control industrial crystallization processes, seed crystals are added within the MSZ. The solution is then de-supersaturated following a pre-defined cooling profile and/or antisolvent addition profile. Secondary Nucleation occurs due to multiple mechanisms viz. crystal-crystal collisions, crystal-impeller collisions, surface nucleation, etc. Crystal growth occurs via (i) diffusion of molecules across the boundary layer on the crystals to the crystal surface (ii) surface integration of molecular units onto the steps/kinks on the crystal surface.

## **2.2 Spherical agglomeration**

Spherical agglomeration (SA) is a novel Process Intensification (PI) technique for pharmaceutical manufacturing (PM). Traditional PM consists of the sequence of unit operations crystallization, filtration, drying, milling, granulation. Many Active Pharmaceutical Ingredients (APIs) form needle shaped crystals, which cause problems during filtration. These large-sized crystals also need to be milled down to smaller crystals to increase their bioavailability. However, the small sized crystals tend to segregate in the tablet press, so they need to be agglomerated in the granulation stage. Spherical Agglomeration solves these problems by producing fine particles in the crystallizer and then agglomerating them in-situ in the crystallizer. The small size of the primary crystals ensures enough bioavailability whereas the spherical shape of the agglomerates decreases the time required for filtration and drying. These spherical agglomerates can then be sent directly to the tablet press bypassing the milling and granulation unit operations.

There have been numerous reports in literature on improvements in micrometric properties of agglomerates, compared to the primary crystals. Zhang et al. [8] showed that particulate properties of cefotaxime sodium viz. flowability, compactability, bulk density improved drastically on agglomerating the PCs. There have been similar reports in literature concerning improvements in micrometric properties, for other APIs as well viz. bucollamine [9], salicylic acid [10]. Maghsoodi et al.[11] showed carbamazepine agglomerates showed higher tensile strength

compared to PCs. They suggested that agglomerates deform much more upon compression, leading to inter-particle bond formation between the PCs, therefore giving higher tensile strength. Spherical agglomerates are also highly desirable as vehicles for drug delivery[12] since spheres have the highest surface area-to-volume ratio among all shapes. However, development of a SA for a new API remains a challenging exercise primarily due to two major reasons (i) solvent selection [13] for a new API is a challenging problem. The solvent-antisolvent combination has to be carried out to enable maximum process yield during the crystallization stage. In addition, the binder needs to be chosen such that it is insoluble in the solvent-antisolvent mixture (ii) choice of the optimal process parameters[11][14] largely remains a trial and error exercise. This work primarily concerns with tackling the second problem by using a combination of mathematical modeling and directed experimentation.

SA involves two stages (i) reverse antisolvent crystallization to form small size primary crystals (PCs) (ii) agglomeration by binder addition, which agglomerates the crystals. The fundamental rate processes at play during the agglomeration stage are very similar to the ones during wet granulation, as shown in **Figure 2-2**. The initial stage of granule nucleation via wetting of the PCs by the binder follows two modes (i) when droplets are smaller than the crystals, the droplets coat the crystal surfaces and form agglomerate nuclei, which is known as the distribution mechanism (ii) when the droplets are larger than the crystals, an immersive mode of agglomeration occurs where the crystals first coat the droplet surface. The rate of coating depends on the surface wettability of the droplets on the crystals. This is followed by penetration of the crystals onto the droplets, which forms the granule nuclei. This is followed by a progressive compaction and consolidation of the agglomerated nuclei, which results in a reduction in the size of the agglomerates and porosity. Breakage and attrition of the agglomerates can also occur within the crystallizer, depending on the process conditions. Breakage occurs due to imposed shear forces on the agglomerates resulting from agglomerate-particle collisions or agglomerate-stirrer collisions. The hydrodynamic conditions within the crystallizer viz. the average shear rate, tip speed, which depend on the stirrer rpm, affect the breakage and attrition kinetics. There are alternate modes of granule growth described in literature viz. layering of particles onto the agglomerates. It is to be noted that the attrition fragments can also layer onto the agglomerates, thereby contributing to the agglomerate growth.

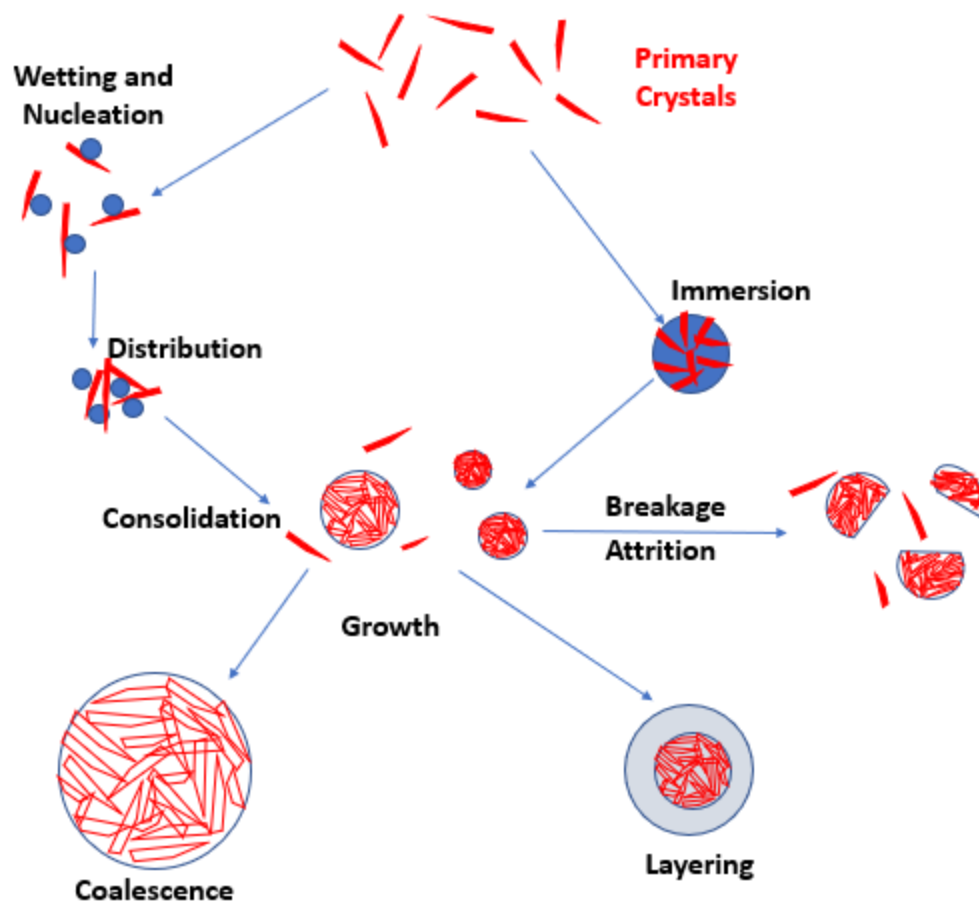


**Figure 2-2.** Rate processes and possible mechanisms during SA showing wetting and nucleation, distributive vs immersive modes of agglomeration, consolidation, breakage and granule attrition and granule growth.

There are a multitude of process and material parameters that affect SA, including (i) solvent-antisolvent-binder combination (ii) temperature (iii) agitation rate (iv) binder to solids ratio. The effect of each of these process parameters on the SA process is next discussed in detail.

### 2.2.1 Choice of solvent-antisolvent-binder

The choice of the solvent-antisolvent pair decides the fate of the crystallization process. Since the first phase is reverse antisolvent crystallization, the choice of the antisolvent is crucial to ensure (i) process yield [15] (ii) phase purity[16]. Moreover, for some antisolvents the initial supersaturation generated can be so high that oiling out of crystals occurs, which can lead to (i) loss of process yield due to crystals sticking on the crystallizer walls (ii) problems during scale-up since droplet breakage is hard to effectively control during scale-up.

The binder also needs to be chosen such that it is insoluble in the solvent-antisolvent mixture so that it forms discrete binder droplets. Typically, ternary phase diagrams of the solvent-antisolvent-binder are constructed to identify the critical operating space. For example, ternary phase diagrams have been used to design SA processes for ketoprofen [17], benzoic acid [18] and etodolac [19].

### 2.2.2 Temperature

Temperature has opposing effects on the outcome of SA process:

- (a) It affects the relative solubility of the various solvent species viz. solvent-antisolvent-binder. Thus, it changes the relative mole fractions of the different components under process conditions.
- (b) It affects the nucleation and growth kinetics of the crystals, which is typically modeled using an Arrhenius rate law viz. Wu et al [20].
- (c) The instantaneous rate of agglomeration depends on the local supersaturation [21] for many APIs, especially when hydrodynamics in the reactor is the critical factor behind agglomeration. Since temperature affects the local supersaturation, it has an indirect effect on the agglomeration kinetics.

Kawashima et al.[22] showed that agglomerate size first decreased with an increase of temperature, followed by an increase. This apparent contradictory effect was attributed to the opposing effects of the various factors outlined above. Thati et al.[23] also showed that the process yield of SA decreased on increasing the temperature, along with a slight increase of the agglomerate size.

#### *Agitation rate*

The agitation rate of the stirrer affects the outcome of the SA by virtue of its effect on the reactor hydrodynamics [24]. Agitator rpm has two opposing effects on the agglomerate size. Initially, with increasing agglomeration, the rate of agglomeration increases, which increases the agglomerate size [18]. However, with further increase in the agitator rpm, breakage and attrition of the agglomerate occurs, which decreases the agglomerate size [25]. However, the agitator rpm needs to be high enough to ensure well-mixedness in the reactor, otherwise there may be particulate settling in the reactor.

Agitator rpm affects solution mixing at all scales viz. micromixing, mesomixing and macromixing. Increasing the agitator rpm improves the bulk scale macromixing in the reactor by decreasing the circulation time. Increasing the agitator rpm also decreases the micromixing time scale [26] by increasing the turbulent kinetic energy dissipation rate. For reverse antisolvent crystallization, which is the first step of SA, increasing the rpm also improves the mesomixing [27] viz. the interaction between the inlet fluid stream and the bulk solution. If mesomixing is not proper, there may be a local zone of high supersaturation at the mouth of the dip tube, which can drastically change the nucleation kinetics in the reactor and subsequently the PSD. Thus, the agitator rpm is carefully chosen to (i) ensure well-mixedness (ii) ensure no breakage or attrition (iii) generate optimal micromixing to cause particulate collisions with sufficient velocity to form agglomerates.

### 2.2.3 Effect of binder to solids ratio

One of the critical process parameters during agglomeration is the binder to solids ratio (BSR) [28]. The relative proportion of the binder compared to the solids decides the rate of agglomeration. **Figure 2-3** shows the progressive change in the degree of agglomeration upon increasing the BSR. If the BSR is too low, no agglomeration occurs [29] viz. **Figure 2-3 a**. However, if the BSR is too high, a paste like slurry forms viz. **Figure 2-3 f**. The BSR during all stages of the process need to be within the critical BSR range indicated in Figure 2-3**c-d**.

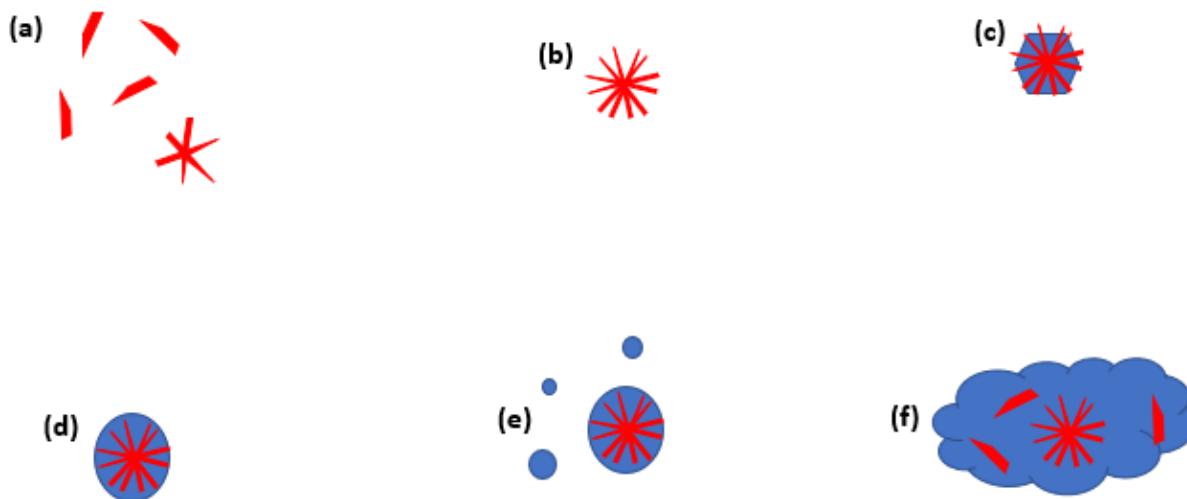


**Figure 2-3.** Different stages during SA as a function of increasing binder content (a) – (f).

However, determining the optimal process conditions and the material properties for SA remains a Herculean task, which makes mathematical modeling imperative for process development.

### **2.3 Mathematical modeling using population balance equations**

Population balance equations (PBE) [30] have been widely used to model particulate processes. PBEs effectively capture the fundamental mechanisms at play during crystallization viz. nucleation [31], growth [32], breakage [33] and agglomeration [34]. PBEs provide a quantitative estimate [35] of the evolution of the number density of the particulate population within the crystallizer. PBEs had its genesis in the classical work of Hulbert and Katz [36], who formulated the equations from a statistical mechanics perspective. Randolph et al. [37] discussed in detail the use of PBEs to model crystallization process. However, PBEs have also found use in modeling population evolution in other diverse fields of engineering and science viz. biomedical engineering [38], electrochemistry [39], catalysis [40], geography [41] and agricultural engineering [42].

### **2.4 Process optimization**

Mathematical models have been widely used for in-silico process optimization [43]. Traditionally process optimization has been carried out using statistical design of experiments (DOE) [44]. However, depending on the number of factors, the number of experiments necessary to get to the process optimum can be prohibitive. To add to the complexity, identifying the critical factors necessary to define the DS is challenging because of compounding effect amongst the different process parameters. Dynamical process optimization [45] solves a lot of these challenges by identifying the critical factors in-silico as a solution of a user-defined non-linear programming (NLP) problem [46], while at the same time minimizing the experimental burden. Generally, chemical processes are modeled as a system of differential algebraic equations (DAEs) [47] where the differential equations quantify the dynamical evolution of the system and the algebraic equations describe the underlying constitutive relationships. There are two major approaches to solving dynamical optimization problems involving DAEs viz. the variational approach [48] and NLP. The variational approach solves the first order necessary conditions for optimality [49], which are derived using Pontryagin's maximum principle. However, using the variational approach becomes tough especially if there are multiple active inequality constraints[50].

Moreover, the solution requires initial guess values [51] of all the state variables, which requires sufficient engineering expertise. This makes the variational approach restrictive for solving most engineering problems, including optimization of SA which involves multiple state equations and active inequality process constraints.

Dynamic optimization using NLP methods can be broadly classified into two approaches which use (i) sequential methods (ii) simultaneous methods. Sequential approach [52] discretizes only the control variable, while the simultaneous approach [53] discretizes both the control and the state variables. For a given set of initial conditions (IC) on the control (and state for simultaneous approach) variables, the DAEs can be integrated to obtain the objective function (OF) [54]. Depending on the user-specifications, the OF can incorporate values of the control (and state) variables during all the discretization time steps or only at the final time point. A NLP solver [55] is then used to find the optimal control (and state) variables which minimize the OF. In terms of robustness, simultaneous approaches score higher [56] since they can identify unstable solution modes, thereby purging infeasible guess values. However, since all the state and control variables are discretized, simultaneous approach typically gives rise to large scale NLP problems, which typically make them infeasible [57] for most practical engineering problems. In this thesis, sequential approaches have been primarily used due to their simplicity and since the optimization problem structures did not necessitate the use of computationally intensive simultaneous approaches.

## **2.5 Model predictive control (MPC)**

However, the optimal process conditions, obtained from offline process optimization, do not always produce the best results when implemented on an actual plant. This discrepancy stems primarily due to two reasons (i) any mathematical model contains uncertain model parameters. However, when process optimization is carried out, these uncertainties are typically neglected and the process is optimized considering the nominal values of the model parameters (ii) there are disturbances inherent in any plant operation, which are typically not modeled. These inherent uncertainties lead to non-optimal solutions when the open-loop calculated optimal profile is implemented industrially.

### 2.5.1 Different types of model uncertainties

These uncertainties stem from (i) model parametric uncertainties [58] (ii) measurement uncertainties [59] (iii) structural uncertainties [60]. A generalized state space model is shown in equation (1), where  $\mathbf{x}$  is the state vector,  $\mathbf{u}$  is the vector of control moves and  $\boldsymbol{\theta}$  is the parameter vector.

$$\frac{d\mathbf{x}(t)}{dt} = f(\mathbf{x}(t), \mathbf{u}(t), \boldsymbol{\theta}), \mathbf{x}(t_0) = \mathbf{x}_0 \quad (1)$$

Model parametric uncertainties [61] essentially arise because all parameters are estimated from offline experimental data, and there are uncertainties associated with all lab-scale experiments. Typically, the uncertainties can be quantified using a multidimensional normal distribution viz. equation, where  $\boldsymbol{\theta}_0$  is the nominal values of the model parameters and  $\Sigma$  is the variance-covariance matrix. It can be seen from equations that the final state vector for a system evolving with the nominal model parameters viz.  $\mathbf{x}_1(t_f)$  (equation (3)) and actual model parameters (sampled from (2)) viz.  $\mathbf{x}(t_f)$ , from equation (1), are generally different.

$$\boldsymbol{\theta} \sim N(\boldsymbol{\theta}_0, \Sigma) \quad (2)$$

$$\frac{d\mathbf{x}_1(t)}{dt} = f(\mathbf{x}_1(t), \mathbf{u}(t), \boldsymbol{\theta}_0), \mathbf{x}(t_0) = \mathbf{x}_0 \quad (3)$$

Measurement uncertainties arise due to sensor noise [62] and/or sensor drift [63]. Typically the state vector  $\mathbf{x}$  is not directly measured, but is estimated from measured vector  $\mathbf{z}$  viz. equation (4), which contains measurement uncertainties  $\mathbf{W}$ .

$$\mathbf{z} = \mathbf{H}\mathbf{x} + \mathbf{w} \quad (4)$$

Structural uncertainties [64] arise due to fundamental differences in model formulation viz. failing to capture certain aspects of the underlying physics in the process model. Mathematically, the process is modeled according to equation (1), while the real underlying process evolves according to equation (5), where  $f_1 \neq f$ .

$$\frac{d\mathbf{x}(t)}{dt} = f_1(\mathbf{x}(t), \mathbf{u}(t), \boldsymbol{\theta}), \mathbf{x}(t_0) = \mathbf{x}_0 \quad (5)$$

### 2.5.2 Model based control

Given the fact that the process model has inherent uncertainties, the open loop optimal control profile does not give the best process performance. This is illustrated in **Figure 2-4**, where the actual state evolution is much different from the open loop model predictions. This necessitates the use of feedback control [65], which can correct for any deviations from the nominal state evolution, by adjusting the process conditions online in real time.



**Figure 2-4.** Nominal state evolution in the absence of uncertainties vs actual state evolution, in the presence of uncertainties.

There are many feedback control strategies viz. PID control [66], internal model control (IMC) [67], etc. Model predictive control (MPC) [68] is a special class of advanced feedback control strategies, which solves a mathematical optimization problem online to calculate the optimal control moves in real-time. However, only the first of the calculated control moves is implemented and the optimization problem is solved repeatedly online at each sampled time instant. MPC for batch reactors [69] have been typically solved using a shrinking horizon strategy, where the model predictions are carried out till the end of the batch and is illustrated in **Figure 2-5**.

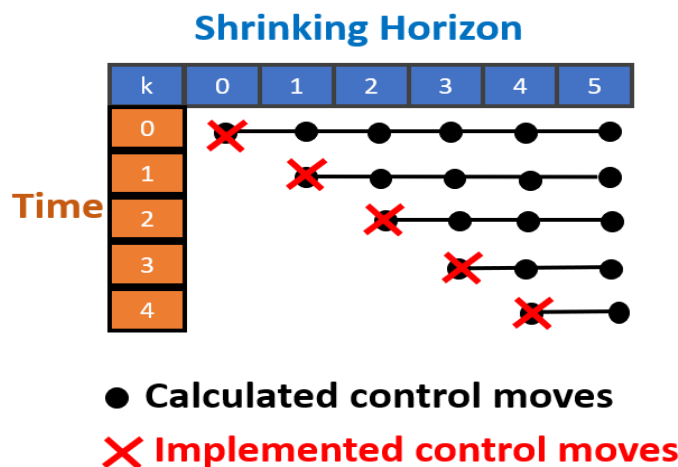


**Figure 2-5.** Shrinking horizon control model predictive control strategy

MPC has its genesis in Bellman's theory of dynamic programming [70]. The earliest reported works on MPC were from researchers at Shell Oil Company, which they formulated as dynamical matrix control (DMC) problem [71]. However, solving constrained multivariable optimization problems still remained a challenging endeavor [68], which necessitated the reformulation of the DMC problem as a quadratic programming problem [72] with explicit constraints. However, most real-world problems involve inherently nonlinear problems [73]. Traditionally MPC on non-linear systems involved linearizing the nonlinear model around the operating point [66], followed by implementing DMC on the linearized model. However, higher quality specifications [74] and increasing productivity constraints [75], stricter environmental regulations [76] necessitate process systems to operate over a wide range of process conditions. Linearized process models fail to accurately capture the system dynamics [77] when operating at process conditions far from the operating point. This has necessitated the use of nonlinear process models to describe the system dynamics, which has necessitated the development of nonlinear MPC.

## 2.6 Process analytical technology (PAT)

PAT tools are inline process sensors which provide information about the real-time evolution of critical quality attributes (CQAs) of the product. In the context of crystallization, PAT tools can provide in-situ measurements of the product quality viz. particle size distribution and solute concentration. The process analytics data recorded by PAT tools also serve as the in-situ

measurements for the implementation of online MPC. The various PAT tools used for crystallization/spherical agglomeration are now described below.

### 2.6.1 Focused beam reflectance measurement (FBRM)

FBRM probe is used for in-situ measurements of the chord length distributions of particles in solution. FBRM probe has an inbuilt rotating scanning laser inside the probe, which traces a circular path at a constant velocity. This produces a highly focused light beam near the probe window, which gets reflected to the probe when a particle comes in the path of the beam (**Figure 2-6**). The tangential velocity of the laser is known apriori which, multiplied by the time the beam was reflected, gives the length of the chord intercepted by the beam. The length measured by the FBRM software is, in fact, a chord length and not the particle diameter, with the exception of spherical particles. This is because the probability of the laser beam passing through the center of non-spherical particles is very low. An assumption in these calculations is that the velocity of the rotating laser is much higher than the particle velocity, which holds good for most practical applications.

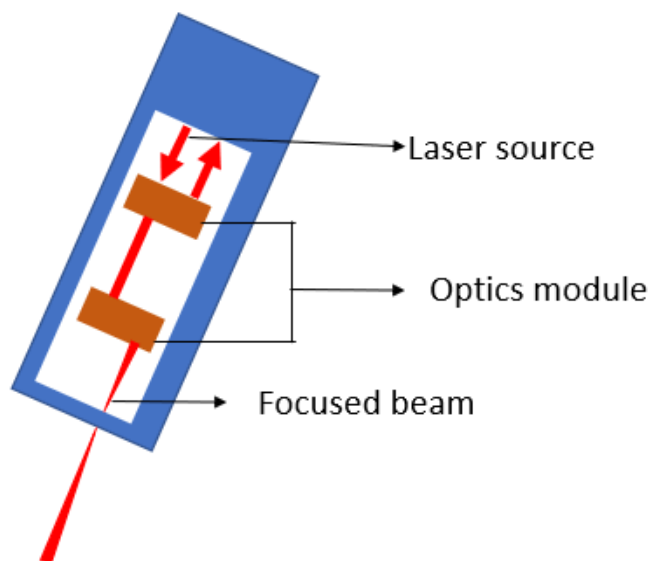


**Figure 2-6.** Schematic of Focused Beam Reflectance Measurement probe.

### 2.6.2 ATR-UV/Vis

UV spectroscopy measures the photon absorption in the visible and ultraviolet spectra which span 400-800 nm and 200-400 nm respectively. The absorbance recorded by the UV/Vis

spectrophotometer is correlated to the solute concentration according to the Beer Lambert Law, where  $\epsilon$  is the molar extinction coefficient,  $c$  is the solute concentration and  $l$  is the path length. The absorbance of solutions of known concentrations can be recorded using the UV-Vis spectrophotometer, from which a calibration curve can be constructed. This can then be further used to find the concentration of an unknown API solution.

$$A = \epsilon Cl \quad (6)$$

However, the UV-Vis spectrophotometer does not yield accurate measurements when there are solids present in the solution, which has necessitated the development of attenuated spectrophotometers (**Figure 2-7**). The ATR-UV/Vis probe sends a light signal which travels normal to the probe surface and excites the solute. Attenuated total reflection (ATR) works on the principle that when light travels from a material with high refractive index (RI) to a material with low RI, the intensity of the reflected wave is severely attenuated. This allows detection of the signal intensity of the reflected wave using traditional UV detectors, without any prior sample preparation. Thus, problems associated with offline sampling viz. chances of recrystallization during filtration, do not pose a problem in these methods. Additionally, slurries with high solids concentration can also be accurately measured using this technique.

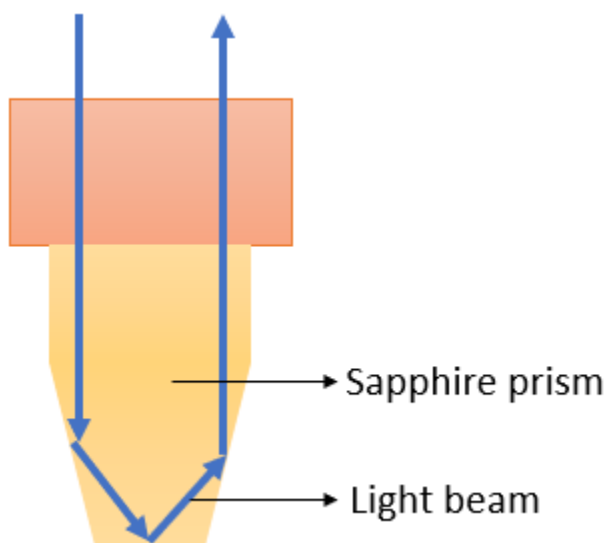


**Figure 2-7.** ATR-UV/Vis spectroscope to measure solute concentration in solutions with solids present.

### 2.6.3 Ultrapformance liquid chromatography (UPLC)

However, UV/Vis spectroscopy has severe limitations when there are multiple components in solution. In this thesis, Chapter 7 studies simultaneous crystallization and degradation of an API ,where there were two distinct components in solution viz. the API and the degradation product. However, the UV-Vis spectra of both the components were very similar which made post-processing using traditional techniques nearly impossible. Liquid Chromatography (LC) provides a potential solution since it can separate the various components temporally depending on the sorption-desorption equilibrium. The fundamental principle of LC is shown in **Figure 2-8**. The LC column is loaded with the stationary phase on a silica support. In reverse phase chromatography, the LC column has preferential absorbability for the non-polar analyte. For gradient elution chromatography, a gradient of velocity/solvent composition is imposed on the mobile phase. Initially the mobile phase is primarily composed of the polar analyte and due to lower velocity, preferential adsorption of the non-polar analyte on the stationary phase occurs. At later stages, the mobile phase is composed of mostly the organic phase which leads to desorption of the non-polar analyte. The higher solvent velocity of the mobile phase towards the later stages also contributes to the faster desorption. The UV detector detects the various components viz. polar and non-polar analytes as a function of time, which leads to temporal resolution of the different components. UPLC is a special class of LC instruments, which can operate at very high column pressures (upto 14,000 psi). This leads to superior resolution capabilities for UPLC compared to conventional high performance liquid chromatography (HPLC), which can operate at maximum 6000 psi.

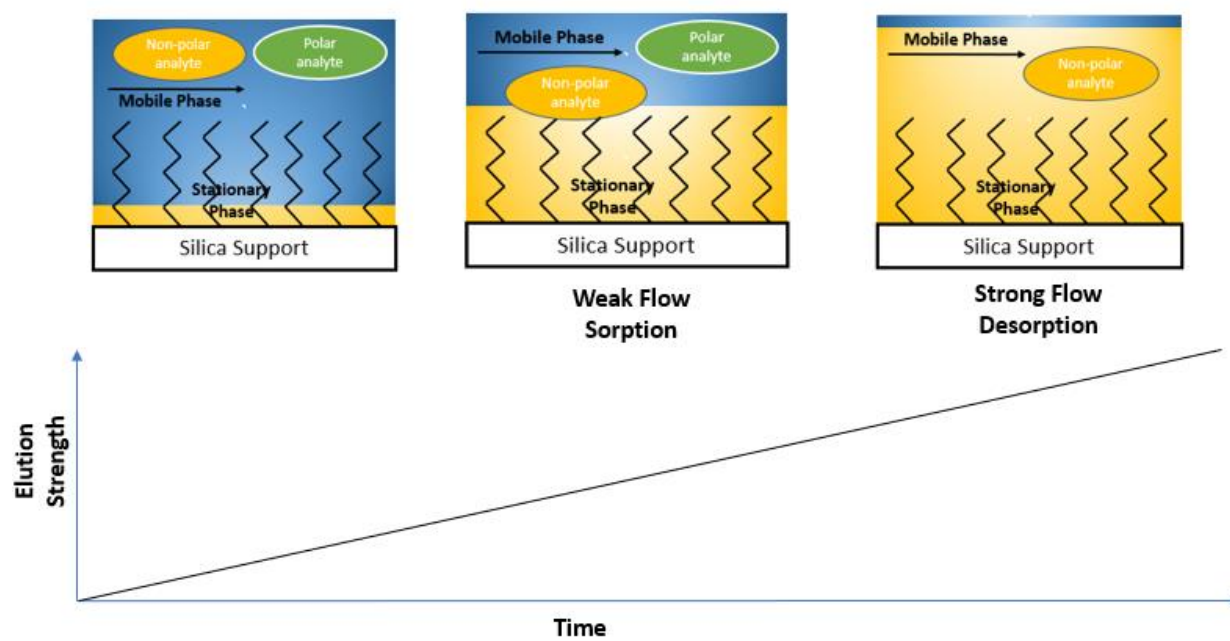


**Figure 2-8.** Various stages of solute elution for reverse phase gradient elution chromatography.

### 3. ITERATIVE MODEL BASED EXPERIMENTAL DESIGN FOR SPHERICAL AGGLOMERATION PROCESS

Reproduced with permission from Kanjakha Pal<sup>+</sup>, Botond Szilagyi<sup>+</sup>, Christopher L. Burcham<sup>\*</sup>, Daniel J. Jarmer<sup>\*</sup>, Zoltan K. Nagy<sup>+</sup>. Submitted to *the Journal of Crystal Growth and Design*, in review.

<sup>+</sup>School of Chemical Engineering, Purdue University, West Lafayette, IN 47907, US

<sup>\*</sup>*Eli Lilly and Company, Lilly Technology Center, Indianapolis, IN, US*

#### 3.1 Introduction

Crystallization is a widely used separation and purification process [1], which is used to separate the compound of interest from a solvent or a mixture of solvents [78]. As a unit operation, it is widely used in a multitude of industries including chemical [79], food processing [80], petrochemical and microelectronics [81]. Crystallization functions as an impurity rejection and particle design unit operation, and plays a vital role in the pharmaceutical industry [82]. Although crystallization might give particles of desired purity, designing a crystallization process followed by scale up requires considerable investment of time and resources [83]. In the pharmaceutical industry, various downstream processes [84] are necessary following crystallization, such as filtration [85], milling [86], blending [87] and granulation [88] to produce particles of desired attributes, including size [89], and morphology [90]. However, this sequence of unit operations often have conflicting design objectives in terms of particulate properties. For example, efficient filtration necessitates the mean particle size from the crystallizer to be as large as possible [91]. However large sized crystals often do not satisfy bioavailability requirements or content uniformity (e.g. they do not dissolve fast enough in the body), hence they need to be milled [92]. However very fine particles cause problems during tableting due to segregation or poor flowability [93] within the tablet press, hence they need to be granulated to form compact spherical particles.

Spherical agglomeration (SA) offers a solution to the aforementioned problems by agglomerating crystals directly within the crystallizer [14]. The idea behind SA is to produce fine crystals (primary crystals, PC) by crystallization [23] and then agglomerate them *in-situ* by adding a bridging liquid. The small size of the PCs meet the bioavailability requirements while the large size and shape of the spherical agglomerates reduces the filtration time, and increases flowability and processability, in general for non-cohesive powders. The filtered agglomerates can then be

directly sent to the tablet press, bypassing the milling and granulation stages. However, selecting the process parameters for obtaining spherical agglomerates with desired product properties (flowability, friability) is challenging. Subero-Coureyor et al. [10] showed that numerous process parameters, including the wetting period and the mode of binder injection affects the final agglomerate size. Thati et al. [14] demonstrated that binder to solid ratio (BSR), batch time, rotational speed of the stirrer and the temperature influence the size and product quality of the agglomerates. Mathematical models can give insights into process dynamics and guide judicious selection of process conditions for obtaining agglomerates with desired particulate attributes.

Petela et al. [94] was one of the first to model the agglomeration of fine particles. They carried out a force balance on the fine particles undergoing agglomeration and developed predictive models for the end-of-batch mean agglomerate size. David et al. [95] modeled the agglomeration process using a combined agglomeration kernel, which took into account three agglomeration mechanisms - brownian, laminar and turbulent modes of agglomeration. Blandin et al. [9] used population balance equations (PBE) to describe agglomeration in suspension using a novel agglomeration kernel which involved both the agglomeration frequency and the agglomeration efficiency in its formulation. However, all these descriptors of SA modeled the entire particulate population within the reactor as a single population while there are two distinct populations during SA – the PCs and the agglomerates. Peña et al. [96] was one of the first to consider both these populations in their PBM formulation. However, the model parameters describing their agglomeration kernel were taken from literature and not estimated from experimental data. Moreover, the agglomeration kernel was chosen rather arbitrarily from literature rather than using a systematic selection criterion directly based on experimental data.

In most of the published literature on agglomeration, the agglomeration kernels are chosen based on intuition about the physical mechanism behind the agglomeration process. However, it is quite conceivable that the agglomeration process is so complex that selecting the right agglomeration kernel from intuition about the process physics is not plausible. This is particularly true for SA process where there are multiple mechanisms of agglomerate formation followed by growth of agglomerates that can occur. Data based model identification (MI) is a strategy to discriminate amongst various models and identify the model that best fits the experimental observations. Reilly et al. [97] explained various statistical methods of model discrimination for identification of the correct model for chemical kinetics. Hsiang et al. [98] used a personalistic

Bayesian methodology to discriminate amongst different mechanistic models, which did not need model linearization or assumed any specific form of the error distribution. Vatcheva et al.[99] developed a procedure to discriminate among several semi-quantitative models that explained the growth of phytoplankton in a bioreactor. They formulated a statistical criterion to design additional experiments when the existing experimental data was not sufficient for model discrimination. Hsu et al. [100] developed a Bayesian framework to build kinetic models of catalytic reactions where the prior knowledge of the experimenter could be incorporated in the model discrimination framework. One of the key features of their approach was the use of distribution of model parameters rather than point estimates, which avoided regression from model data and allowed incorporation into a Bayesian model discrimination framework.

Once an appropriate mathematical model has been identified, the model parameters need to be estimated accurately for *in-silico* predictions of process outcomes. Traditionally, experimental design for model parameter estimation have been carried out using a statistical design of experiments (DOE) [101] including full factorial design, and fractional factorial design, among others. However, increased number of experiments are typically necessary to get precise estimates of model parameters using traditional DOE methodologies. Model based experimental design (MBED) is a framework to use an imprecise mathematical model to guide the design of future experiments which, in turn, improves the model fidelity. The rationale behind MBED is to use information theoretic tools [102] on the mathematical model to design experiments such that the information content obtained from successive experiment is maximized. Gadkar et al. [103] developed an iterative approach to identify models in biological networks. They found that optimal experimental design was crucial to obtain information-rich experimental data, which maximized the accuracy of the estimated model parameters. Rojas et al. [104] adopted a min-max approach to robust optimal experimental design for energy systems with bounded power inputs. They found that optimal experimental design substantially improved the worst-case performance of the system model over the nominal experimental design. Galvanin et al. [105] proposed a novel online model based redesign of experiments (OMBRE) for estimating model parameters in dynamical systems. Their method utilized the experimental information as soon as it was generated and used it online to redesign the experiments in real time. This online redesign of experiments substantially reduced the time to obtain precise estimates of model parameters over a sequential MBED strategy. MBED has also been used to estimate kinetic parameters in crystallization literature. Chung et al. [106]

used D-optimal experimental design criterion to minimize the number of experiments necessary to obtain precise parameter estimates of nucleation and growth kinetics for crystallization.

Although there are numerous publications on model identification and optimal experimental design for precise parameter estimates in biological networks, catalysis, crystallization, a similar data-based model identification strategy is lacking in the particulate agglomeration literature. The focus of this work is to first identify the correct mechanism for SA by discriminating among various agglomeration kernels each of which gives a different interpretation of the fundamental agglomeration mechanism. Once the correct agglomeration mechanism has been identified, an Iterative Model Based Experimental Design (IMED) approach is then developed where information theoretic tools are used to minimize the number of experiments to obtain precise estimates of parameters of the agglomeration kernel.

## 3.2 Theory

### 3.2.1 Mathematical modeling of SA

In a batch SA process [14], the anti-solvent is initially stirred in a crystallizer. The active pharmaceutical ingredient (API), dissolved in a solvent, is then added to the crystallizer. Since the API is insoluble in the anti-solvent, as soon as the solution droplets contact the antisolvent, a high degree of local supersaturation is created. This leads to rapid, primary nucleation of API crystals followed by crystal growth. After crystallization is complete, the bridging liquid is added into the crystallizer. The bridging liquid is chosen so that it is insoluble in the solvent-antisolvent mixture and wets the surface of the API particles. The discrete binder droplets then bring the crystals together and form granule nuclei, which after a period of particulate layering, forms compact spherical agglomerates.

The crystals and agglomerates in the solution are rarely monodisperse and there is typically a size distribution associated with the particulate population(s). Population Balance Equations (PBE) are widely used to characterize the evolution of the particulate population in solution. The size distribution of the crystals and agglomerates in solution are characterized by their number densities  $n_c(v,t)$  and  $n_a(v,t)$  respectively. Since the process is a semi-batch process, the volume in the solution changes throughout the batch. To take this dilution effect into account, a modified number density  $\tilde{n}(v,t)$  is used where  $V(t)$  is the volume of the solution in the vessel.

$$\tilde{n}(v, t) = n(v, t)V(t) \quad (7)$$

$$\frac{\partial \tilde{n}_c(v, t)}{\partial t} = -\frac{\partial}{\partial v} (G(v)\tilde{n}_c(v, t)) + B\delta(0, v)V(t) - \tilde{n}_c(v, t) \int_0^{\infty} \beta(v, \lambda)\tilde{n}(\lambda, t) d\lambda \quad (8)$$

$$\frac{\partial \tilde{n}_a(v, t)}{\partial t} = \frac{1}{2} \int_0^v \beta(v-v', v')\tilde{n}(v-v', t)\tilde{n}(v', t) dv' - \tilde{n}_a(v, t) \int_0^{\infty} \beta(v, \lambda)\tilde{n}(\lambda, t) d\lambda \quad (9)$$

$$\tilde{n}(v, t) = \tilde{n}_c(v, t) + \tilde{n}_a(v, t) \quad (10)$$

Equation (8) represents the PB for the crystals in solution where the nucleation, growth and agglomeration of the crystals have been considered. Equation (9) represents the PBE for the agglomerates in the solution where birth and death of agglomerates occur only due to agglomeration. The rate of agglomeration is quantified by an agglomeration kernel  $\beta(v, v')$ , which represents the rate of agglomeration of particles characterized by volumes  $v$  and  $v'$ . It is to be noted that agglomeration can happen between both crystals and/or agglomerates, which need to be reflected in the integral terms for agglomeration. Thus a total population of particles  $\tilde{n}(v, t)$  is redefined in equation (10), which is a combination of the crystal and agglomerate population. The driving force for crystallization is the instantaneous supersaturation in the solution given by equation (11), where  $C_s$  is the API concentration.

$$S = \frac{C_s}{C_{sat}} \quad (11)$$

$C_{sat}$  is the saturation concentration of the API, which is a function of the instantaneous solvent to antisolvent ratio ( $x_{sasr}$ ) in the vessel, given by equation (12).

$$c_{sat} (gm / gm) = 0.5526 - 1.2327(1 - x_{sasr}) + 0.2724(1 - x_{sasr})^2 + 0.912(1 - x_{sasr})^3 - 0.4985(1 - x_{sasr})^4 \quad (12)$$

The nucleation and growth rates of the crystals are given by equations (13)-(14). In equation (13), both primary and secondary nucleation have been taken into account, where  $M$  is the total mass of crystals in the solution. All model parameters were taken from reference [107].

$$B = k_b (S-1)^b (1+0.5M) \quad (13)$$

$$G = k_g (S-1)^g \quad (14)$$

The PBEs are coupled with the mass balance equations (15)-(17).

$$\frac{dm_{liq}}{dt} = F_s \quad (15)$$

$$\frac{dc_s}{dt} = \left( \frac{c_{s,in}F_s - 3\rho_c k_v G \mu_2}{m_{liq}} \right) \quad (16)$$

$$\frac{dx_{sasr}}{dt} = \frac{F_s}{m_{liq,0}} \quad (17)$$

Equation (15) is the mass balance for total slurry in the crystallizer where  $m_{liq}$  is the mass of the solution and  $F_s$  is the mass flow rate of solution into the crystallizer. Equation (16) represents the mass balance for the solute (API) in the crystallizer where  $c_{s,in}$  is the inlet API concentration.  $\rho_c$  is the density of the API crystals,  $k_v$  is the shape factor of the crystals. Here  $\mu_2$  is the second moment of the crystal population which appears due to the consumption of solution supersaturation from crystal growth. Equation (17) represents the dynamics of solvent to anti-solvent ratio in the agglomeration vessel, where  $m_{liq,0}$  is the initial mass of antisolvent in the vessel .

### 3.2.2 Finite Volume Solution of PBEs

Equations (8)-(9) are discretized over a computational finite volume grid and solved by using high resolution schemes for the growth terms following Qamar et al. [108] and fixed pivot techniques for the agglomeration terms following Kumar et al. [109]

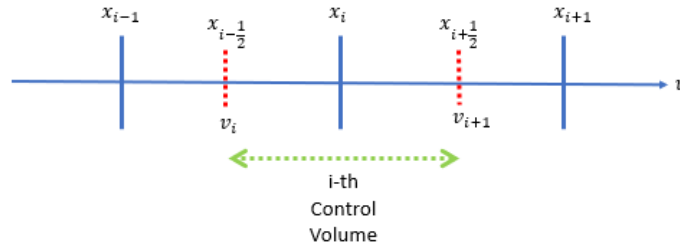


**Figure 3-1.** Finite volume grid for discretizing particle volumes. The actual particle volumes are represented by the grid points  $v_i, v_{i+1}$  whereas the particle population in the  $i$ -th C.V. are assumed to be concentrated at a representative volume  $x_i$  for computational purposes.

**Figure 3-1** shows a representative grid for the particulate volume in the context of the fixed pivot technique. The internal variable  $v$  of the PBEs is divided into  $\xi$  control volumes where the  $i^{\text{th}}$  control volume is assumed to lie between the particle volumes  $v_i$  and  $v_{i+1}$ . The particulate population in the  $i^{\text{th}}$  C.V. is represented by a representative volume  $x_i$  where the grid is chosen such that  $v_i = (x_{i-1} + x_i)/2$  [109]. To maintain consistency with the nomenclature followed in Qamar et al. [108] for the high resolution method for the growth terms, the faces of the  $i^{\text{th}}$  C.V. are also marked as  $x_i^+$  and  $x_i^-$ . The total number of particles contained in the  $i^{\text{th}}$  C.V. is given by (18).

$$N_i = \int_{v_i}^{v_{i+1}} n(v,t)dv \quad (18)$$

Finite volume discretization of equations (8) - (9) then gives equations (19) - (20).

$$\frac{d\tilde{N}_{c,i}}{dt} = -(G\tilde{N}_{c,x_i^+} - G\tilde{N}_{c,x_i^-}) + B(t)V(t) - \tilde{N}_{c,i} \sum_{k=1}^{\xi} \beta_{i,k} \tilde{N}_k \quad (19)$$

$$\frac{d\tilde{N}_{a,i}}{dt} = \sum_{x_{i-1} \leq (x_j + x_k) \leq x_{i+1}}^{k \leq j} \left(1 - \frac{1}{2} \delta_{j,k}\right) \eta \beta_{j,k} \tilde{N}_j \tilde{N}_k - \tilde{N}_{a,i} \sum_{k=1}^{\xi} \beta_{i,k} \tilde{N}_k \quad (20)$$

where  $\beta_{i,k} = \beta(x_j, x_k)$  represents the rate of agglomeration of particles of volumes  $x_j$  and  $x_k$ .

Here  $\eta$  is a parameter that is important for preserving number and mass during agglomeration [109].

$$\eta = \begin{cases} \frac{x_{i+1} - v}{x_{i+1} - x_i}, & x_i \leq v \leq x_{i+1} \\ \frac{v - x_{i-1}}{x_i - x_{i-1}}, & x_{i-1} \leq v \leq x_i \end{cases} \quad (21)$$

The discretized ODEs (19)-(20) at each of the  $\xi$  grid points are solved along with the ODEs for mass balance (15) - (17) to get the evolution of the primary crystal size distribution (CSD) and the agglomerate size distribution (ASD).

For ease of comparison, all the model predictions and experimental measurements were normalized according to equations (22)-(23). Here  $\tilde{f}_{model}$  and  $\tilde{f}_{exp}$  are the normalized number of particles from the model and experiments respectively. It is to be noted that the number of grid

points for the model predictions and the experiments are different ( $\xi$  and  $\psi$  respectively). However, for parameter estimation purposes, the model predictions  $\tilde{f}_{model}$  are re-computed at the experimental grid-points.

$$\tilde{f}_{model,i} = \frac{\tilde{N}_{a,i}}{\sum_{i=1}^{\xi} \tilde{N}_{a,i}} \quad (22)$$

$$\tilde{f}_{exp,i} = \frac{\tilde{N}_{exp,i}}{\sum_{i=1}^{\psi} \tilde{N}_{exp,i}} \quad (23)$$

### 3.2.3 Different agglomeration kernels and initial parameter estimation

**Table 3-1.** Different agglomeration kernels used in this work where  $x$  and  $y$  are the volumes of the agglomerating particles

Kernel	Expression	Parameter Vector
<i>Schomolowski kernel</i> [110]	$Q = \beta_0(x^{1/3} + y^{1/3})^3$	$\beta_0$
<i>Brownian kernel</i> [42]	$Q = \beta_0 \frac{(x^{1/3} + y^{1/3})}{(xy)^{1/3}}$	$\beta_0$
<i>Zauner Jones Kernel</i> [111]	$Q = a_{rot}(b_{rot} + c_{rot}\epsilon^{0.5} - d_{rot}\epsilon)S^e$	$[a_{rot} \ b_{rot} \ c_{rot} \ d_{rot} \ e]$
<i>Thompson kernel</i> [110]	$Q = \beta_0 \frac{(x - y)^2}{(x + y)}$	$\beta_0$
<i>Golovin kernel</i> [41]	$Q = \beta_0(x + y)$	$\beta_0$
<i>Sastry kernel</i> [112]	$Q = \beta_0 \frac{(x^{2/3} + y^{2/3})}{\left(\frac{1}{x} + \frac{1}{y}\right)}$	$\beta_0$

**Table 3-1** shows the different agglomeration kernels considered in this study where  $x$  and  $y$  are the volumes of the particles undergoing agglomeration. Each of the agglomeration kernels considered in this study refer to different modes of agglomeration, which are now described briefly.

*Smoluchowski and Brownian Kernels*

In Smoluchowski's theory of agglomeration [110], two different modes of agglomeration were defined – perikinetic and orthokinetic. There is a fundamental mechanistic difference between the two agglomeration mechanisms – perikinetic agglomeration occurs due to random Brownian motion of the particles while orthokinetic agglomeration refers to the agglomeration of two particles due to imposed velocity gradients from the fluid motion.

However, the Schmolowski agglomeration kernel referred to in this work represents only the rate of orthokinetic agglomeration of two particles. For a laminar flow field, the agglomeration kernel constant  $\beta_0$  depends on the fluid shear rate. For a turbulent flow field, the agglomeration constant depends on the rate of turbulent energy dissipation in the agglomerator. Thus, the Smoluchowski orthokinetic agglomeration kernel is fundamentally dependent on the fluid mechanics conditions, which is lumped into a constant parameter  $\beta_0$ . This represents a subtlety in the use this kernel – all the experiments for the parameter estimation and the subsequent model-based design experiments need to be carried out under experimental conditions that conserve the fluid mechanical conditions in the agglomerator viz. same stirring speed of the stirring, etc. **Figure 3-2** provides a schematic representation of these two mechanisms.

The Brownian kernel [110] represents perikinetic mode of agglomeration in Smoluchowski's theory, which occurs due to random fluctuations of the particles in solution due to Brownian motion and is unaffected by any fluid mechanical conditions. Brownian diffusivity of particles is dependent on the solution temperature: at higher temperature, the diffusivity of particles is higher leading to higher rates of agglomeration. However, the PCs in this work are generated exclusively via antisolvent crystallization, so cooling crystallization is not necessary. Hence, the effect of process temperature on the agglomeration kernel is not explicitly considered in this work.

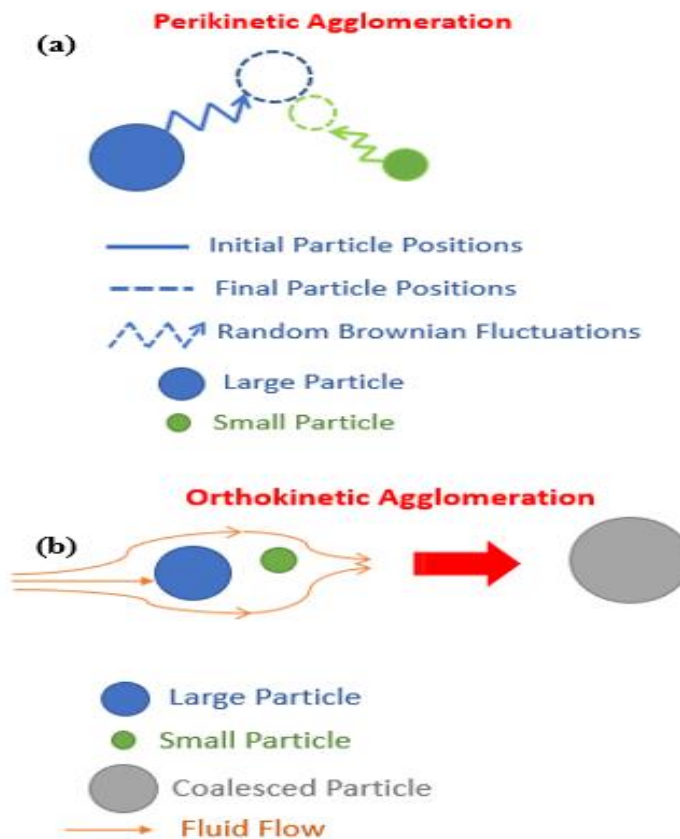


**Figure 3-2.** (a) Orthokinetic agglomeration of a large particle and a small particle due to fluid shear which is represented by Schomulowski's kernel, and (b) Perikinetic agglomeration of a large particle and a small particle due to random Brownian motion, which is represented by Brownian kernel

#### *Zauner-Jones Kernel*

The Zauner-Jones Kernel [111] considers two fundamental mechanisms of agglomeration – (i) agglomeration of two particles via orthokinetic agglomeration and (ii) growth of agglomerates *via* layering of particles from solution onto pre-formed agglomerates (**Figure 3-3**). Since the orthokinetic mode of agglomeration depends on the fluid mechanical conditions, the mean rate of dissipation of turbulent kinetic energy ( $\varepsilon$ ) is explicitly considered in this kernel. Growth of agglomerates due to particle layering is dependent on the local supersaturation ( $S$ ). However, since the crystallizer is assumed to be well mixed, the supersaturation  $S$  is a measure of the average supersaturation in the entire solution while the spatial inhomogeneities in the local agglomeration is discounted in this work.

### Layering of particles onto agglomerates

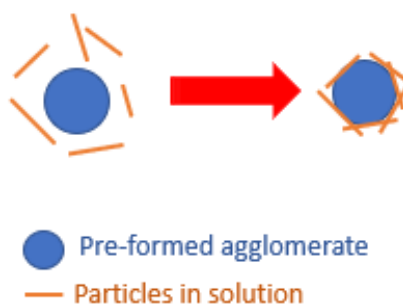


**Figure 3-3.** Agglomerate growth by layering of fine crystals in solution onto pre-formed agglomerates

#### *Thompson and Golovin Kernels*

Berry et al. [113] modeled the agglomeration of cloud droplets using two different models – the continuous model and the stochastic model. The continuous model assumed that smaller water droplets formed a continuous phase around the larger discrete cloud droplets (**Figure 3-4a**), which essentially led to droplet coalescence growing following a deterministic rate law. In fact the continuous mode of droplet growth with a summation kernel (Golovin kernel) was solved earlier by Golovin et al. [114] analytically.

However, the stochastic model assumed that not all the large droplets collect smaller droplets (**Figure 3-4b**) – in fact, a fraction of the large droplets collect smaller droplets which was modeled as a Poisson process. It was found that although the stochastic model gave similar growth rates to the continuous model, the predictions of the actual droplet distributions was significantly better for the stochastic model. However, one limitation of the stochastic model formulation was the high computational cost associated with solving the underlying stochastic differential equations. Thompson et al. [115] proposed a new kernel to reduce the computational costs of solving Berry's agglomeration kernel, while preserving its mechanistic aspects. At the same time, Thompson's reformulated kernel made deterministic solution of the PBEs possible which was considerably simpler than solving the stochastic differential equations.

It is to be noted that the Thompson kernel is just a reformulation of the Golovin summation kernel but in a stochastic mode of agglomeration. Thus, comparison between the model predictions between the Golovin (**Figure 3-4a**) and Thompson (**Figure 3-4b**) kernels essentially

provides evidence on whether the deterministic or stochastic mode of agglomeration is predominant in the agglomeration vessel.

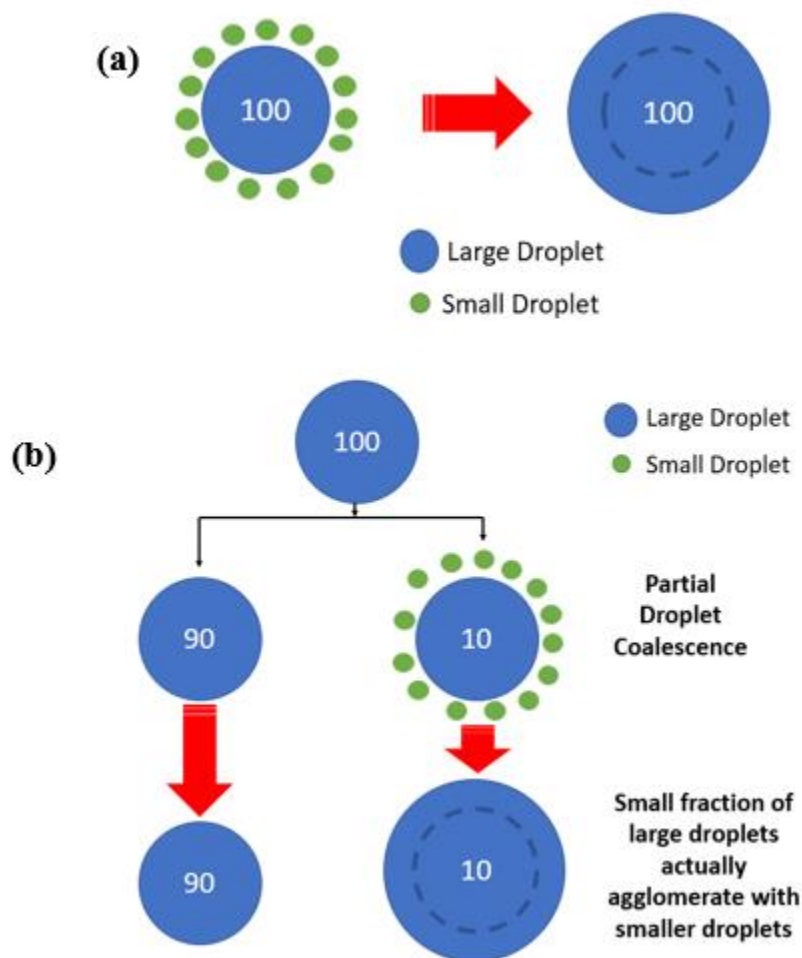


**Figure 3-4.** (a) Continuous coalescence model where 100 large droplets all grow by coalescing with smaller sized droplets – Golovin kernel, and (b) Stochastic Growth Model where only a fraction (10%) of the larger sized droplets grow by coalescing with smaller sized droplets – reformulation of this mechanistic kernel gives the Thompson kernel.

#### *Sastry Kernel*

Sastry et al. [40] proposed an empirical agglomeration kernel based on their observations of granule nucleation followed by granule growth in a batch agglomerator. They formulated two rules which formed the basis of their agglomeration kernel.

- (a) The driving force for coalescence of particles is provided by the surface area of the agglomerating particles viz. particles with larger surface areas have a higher probability to agglomerate.
- (b) The resistance to coalescence is provided by the particulate volumes viz. particles with larger volumes have less tendency to undergo deformation which is necessary for particulate agglomeration.

Since their agglomeration kernel is largely empirical, there is no mechanistic interpretation about the fundamental mechanism of agglomeration.

### 3.2.4 Modification of agglomeration kernels

It was pointed out by Pena et al. [96] that spherical agglomerates were only formed under a limited range of BSR's. During the process of binder addition, the agglomeration kernel will change throughout the process and this will be critically dependent on the volume of binder in the suspension, which is not considered in all the kernels mentioned previously in **Table 3-1**. Here the dependence of the agglomeration kernel on the cumulative binder volume in the system is taken into account using a linear relationship (24).

$$Q_{ac} = \left\{ \begin{array}{l} Q \frac{vol_{binder,t}}{vol_{binder,ref}} ; 0 < t < t_{binder} \\ Q ; t > t_{binder} \end{array} \right\} \quad (24)$$

where  $vol_{binder,t}$  is the volume of binder in the agglomerator at time  $t$  and  $vol_{binder,ref}$  is the total volume of binder at time  $t = t_{binder}$ .

### Model Discrimination and Precise Parameter Estimation

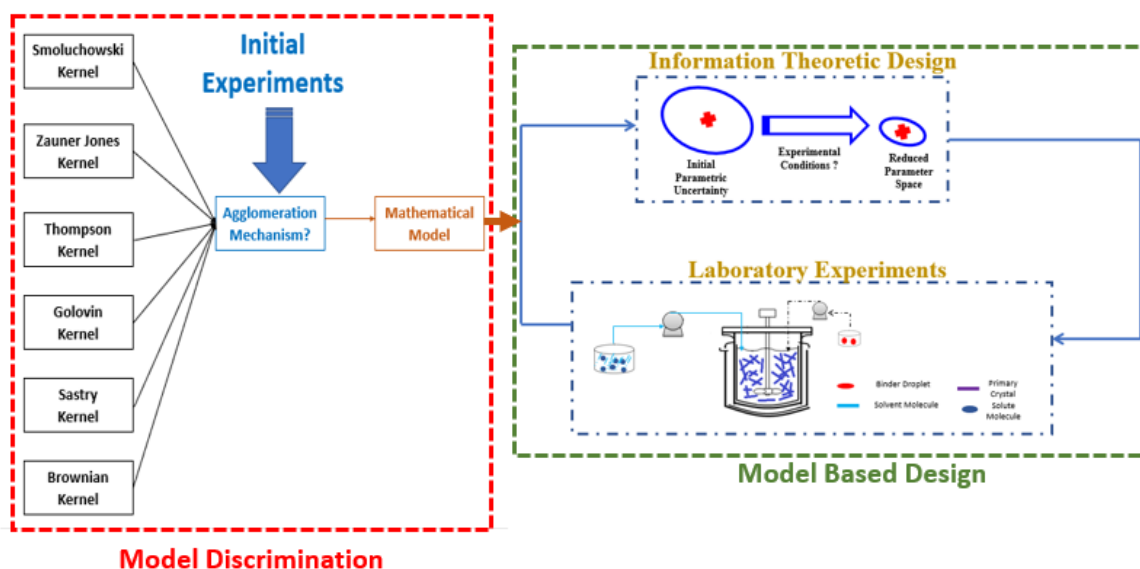


**Figure 3-5.** Overview of model discrimination followed by model-based design strategy used in this work. Model discrimination gives the best model that explains the initial experimental observations. Model based design uses information theory to design experiments which gives precise parameter estimates with minimal number of experiments.

Once a database of different agglomeration mechanisms was developed, initial experiments were carried out to discriminate among the different agglomeration kernels. The model parameters of this best agglomeration kernel were then precisely estimated using a model-based design approach where experiments were sequentially designed to minimize the uncertainties associated with the parameter estimates at each iteration.

#### 3.2.5 Model Discrimination

Although different agglomeration kernels were proposed in Table 3-1 which correspond to different agglomeration mechanisms, there needs to be a statistical criterion to differentiate between the different agglomeration kernels. If the number of model parameters is increased, the model is expected to fit the experimental data better. But if the model complexity is too high, model overfitting occurs viz. the model gets finely tuned to the noise in the experimental data. The Akaike information criterion is a statistical criterion to differentiate between different models (25) where  $k$  is the number of model parameters and  $L$  is the maximum likelihood estimate which is an indication of the goodness of fit between the model predictions and the experimental observations.

$$AIC = 2k - \ln(L) \quad (25)$$

To quantify the maximum likelihood estimate for the different models ( $L$ ), the K-fold leave-one-out cross-validation procedure is applied over all the experiments and for all the kernels in **Table 3-1**. If  $N_{exp}$  is the total number of experiments, one experiment is left out during the model training process. The model parameter is estimated by minimizing the deviation between the experimental ASD and the model predicted ASD using (26) where  $\theta_k$  is the parameter estimate by leaving out the  $k^{\text{th}}$  experiment during the model training process. This parameter estimate is then used on the left-out experiment to calculate the error on the test experiment ( $\phi_k$ ). The average error over the K-fold cross validation is then calculated using (28) which works as a proxy for the maximum likelihood function estimate ( $L$ ) for the model.

$$\theta_k = \min_{\theta} \sum_{\substack{i=1 \\ i \neq k}}^{N_{exp}} \phi_k \quad (26)$$

$$\phi_k = \sum_{j=1}^{\Psi} \left( \tilde{f}_{exp,i,j}(v_j, t_{final}; \theta_k) - \tilde{f}_{model,i,j}(v_j, t_{final}; \theta_k) \right)^2 \quad (27)$$

$$\phi = \frac{1}{N_{exp}} \sum_{k=1}^{N_{exp}} \phi_k \quad (28)$$

It can be observed from Table 3-1 that except the Zauner-Jones kernel, all other agglomeration kernels have just one model parameter ( $\beta_0$ ). Thus, for model discrimination, the AIC criterion is not calculated but a more pragmatic approach is adopted here:

- (i) Model parameters of each of the agglomeration kernels in Table 3-1 are estimated using K-fold cross-validation.
- (ii) The average error between the model predictions and the experimental observations is then calculated from the errors at each iteration of cross-validation.
- (iii) If the Zauner-Jones kernel has the best model fit from step (ii), there is a chance that the superior goodness of fit was due to a greater number of model parameters (4). The AIC criterion then needs to be calculated for all the kernels in **Table 3-1**. However, if the Zauner-Jones kernel does not give the best model fit from step (ii), computing the

AIC criterion will not give additional information since Zauner-Jones kernel has higher model complexity. This comparison is explained schematically in (29).

$$\begin{aligned}
AIC_{ZJ} &= 2k_{ZJ} - L_{ZJ} \\
AIC_{others} &= 2k_{others} - L_{others} \\
k_{ZJ} &> k_{others} \\
\text{Case a :} \\
\text{If } f_{ZJ} &< f_{others} \\
\Rightarrow -L_{ZJ} &< -L_{others} \\
\mapsto AIC_{ZJ} &< AIC_{ZJ} \\
\text{Case b :} \\
\text{If } f_{ZJ} &> f_{others} \\
\Rightarrow -L_{ZJ} &> -L_{others} \\
\Rightarrow AIC_{ZJ} &< AIC_{ZJ}
\end{aligned} \tag{29}$$

### 3.2.6 Precise Parameter Estimation

The experiments used during the initial parameter estimation were designed using intuition about the process physics and heuristic understanding of the experimental operating space for SA. But these experiments were not optimally designed for precise estimation of the model parameters, so the fidelity of the model parameters estimated at this stage may not be high . The rationale behind optimal experimental design is to use an information theoretic measure to design new experiments which minimizes the parametric uncertainties.

Mathematically, the parametric uncertainties are quantified by the volume of the confidence hyper-ellipsoid of the parameter covariance matrix which scales as  $|V_\theta|^{-1}$ . Here  $V_\theta$  is the marginal posterior density covariance of the parameters and S is the parameter sensitivity matrix which indicates the sensitivity of the model output (ASD) is to changes in the parameter vector  $\theta$ , at the final time  $t_{final}$  .

$$V_\theta = \sum_{j=1}^{\psi} S_j V S_j^T \tag{30}$$

$$S_j = \frac{\partial \tilde{f}_{model,j}(\varphi, \theta, t_{final})}{\partial \theta} \Big|_{\theta=\theta^*} \tag{31}$$

The D-optimality criterion [106], which minimizes the volume of the confidence hyper-ellipsoid, is used in this work to design the optimal experimental conditions by solving the optimization problem (32)

$$\begin{aligned} \Phi_{opt} = \min_{\Phi} |V_{\theta}|^{-1} \\ \text{s.t.} \left\{ \begin{array}{l} Conc_{min} \leq Conc \leq Conc_{max} \\ SASR_{min} \leq SASR \leq SASR_{max} \\ BSR_{min} \leq BSR \leq BSR_{max} \\ F_{sol,min} \leq F_{sol} \leq F_{sol,max} \end{array} \right. \end{aligned} \quad (32)$$

The experimental design space  $\Phi$  consists of (a) concentration of API in inlet solution (Conc), (b) solvent to anti-solvent ratio (SASR), (c) binder to solid ratio (BSR), and (d) Volumetric flow rate of inlet solution ( $F_{sol}$ ). The bounds on the experimental conditions are introduced as constraints in the optimization problem (32).

The overall procedure for precise parameter estimation is illustrated in **Figure 3-6**.

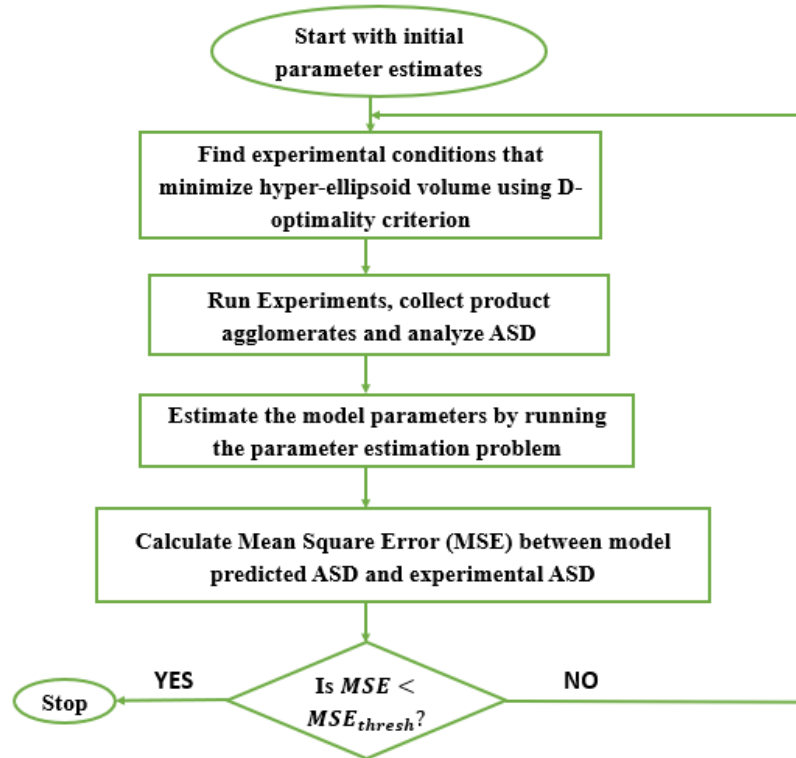


**Figure 3-6.** Algorithm for model based experimental design for precise estimation of model parameters.

### 3.2.7 Effect of Mixing

There are two fundamental rate processes in the crystallizer, which are dependent on the mixing modalities viz. antisolvent crystallization and agglomeration. The flow conditions within the crystallizer viz. laminar vs turbulent flow regimes depends on the Reynolds number (equation (33) ).

$$N_{Re} = \frac{ND^2\rho}{\mu} \quad (33)$$

The time constant for macromixing ( $\tau_M$ ) is related to the circulation time ( $\tau_C$ ) in the crystallizer according to equation (34). The circulation time is calculated according to relation (35), which depends on the impeller dimensions relative to the crystallizer diameter, type of impeller, etc.

$$\tau_M \approx 4\tau_C \quad (34)$$

$$N\tau_C = \kappa \quad (35)$$

The time scale for micro-mixing ( $\tau_E$ ) is given by equation (36), where  $\varepsilon$  is the average energy dissipation rate per unit mass calculated from equation (37).  $P$  is the power input into the impeller which can be calculated from equation (38), and  $N_p$  is the power number for the impeller .

$$\tau_E = 17.3 \left( \frac{\nu}{\varepsilon} \right)^{\frac{1}{2}} \quad (36)$$

$$\varepsilon = \frac{P}{\rho V} \quad (37)$$

$$N_p = \frac{P}{\rho N^2 D^5} \quad (38)$$

### 3.3 Materials and methods

Benzoic acid (>99.5 % purity, BASF Corporation) was used as model API. Absolute ethanol (99.5% w/w) from Fisher Scientific was used as the solvent. Deionized water, produced in-house, was used as the anti-solvent. Toluene (> 99.5%, Fisher Scientific) was used as the binding agent. A 500 mL jacketed crystallizer equipped with a 0.05m three-blade retreat curve impeller was used for all experiments. The solution temperature was maintained at 20°C for all experiments. The anti-solvent is initially stirred at constant speed (400 rpm) in the crystallizer. The API is then dissolved in the solvent in a beaker and the API solution is pumped into the agglomerator at a constant flow rate (2mL/min). Peristaltic pumps from Cole-Palmer and platinum-cured silicone tubing from MasterFlex (L/S, Inner diameter = 1.6 mm) were used for solution addition. The tubing was dipped into the bulk solution and the API solution was charged near the impeller to ensure rapid mixing. After 1 hour, the binder is added at constant flow rate (4 mL/min) and the rotational speed of the stirrer is increased to 600 rpm. After 2 hours, the solution is taken out of the crystallizer and filtered using a vacuum filter equipped with a Butchner funnel. The filtered agglomerates are then washed with a solvent mixture (5% w/w ethanol-water mixture), followed by drying in an air-oven at 40 °C for 1 day. The moisture content in the agglomerates was analyzed using a halogen moisture analyzer (Mettler H53, Mettler Toledo), which consistently showed that the residual solvent content was less than 0.1% in all the product agglomerates. Photomicrographs of these samples are then taken using a Nikon SMZ stereo microscope. The captured images are further analyzed using ImageJ software from which the ASD is reconstructed.

The system of Differential Algebraic Equations (15)-(21) are solved using ode15s function of **MATLAB R2016a**. The optimization problems(26), (32) were solved using the genetic algorithm function *ga* of the global optimization toolbox of **MATLAB R2016a**.

### 3.4 Results and Discussions

#### 3.4.1 Experiments for finding best model amongst suite of candidate models

The experimental design space consists of the solute concentration (Conc), solvent to anti-solvent ratio (SASR), binder to solids ratio (BSR), and flow rate of solution ( $F_{sol}$ ). Since the most important factors were Conc and SASR [116], the experimental design space (**Table 3-2**) for initial parameter

estimation was constructed with only these two process variables while the other process variables were kept constant at  $BSR = 1.0$  and  $F_{sol} = 2\text{mL/min}$ .

**Table 3-2.** Experimental design for model discrimination

Experiment Number	Conc (g/mL)	SASR
1	0.15	0.175
2	0.15	0.35
3	0.25	0.175
4	0.25	0.35
5	0.25	0.5
6	0.375	0.175

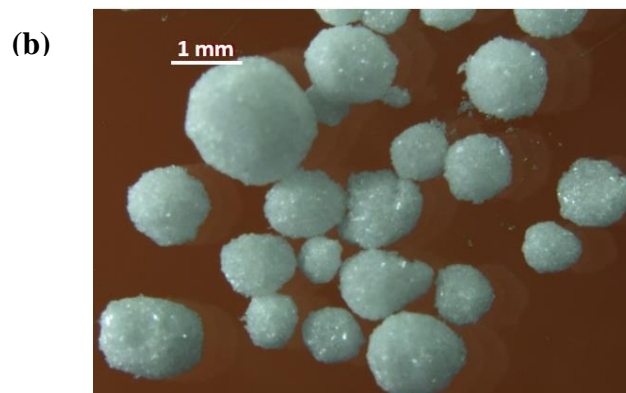
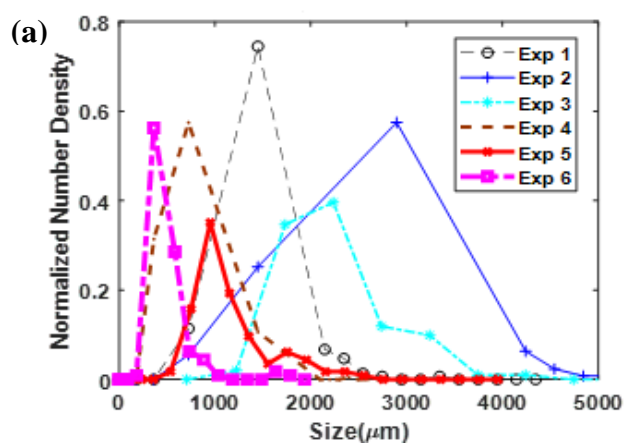


**Figure 3-7.** (a) Experimental ASD of SA experiments (b) stereomicroscope images of agglomerates produced from Experiment 5.

**Figure 3-7a** show the ASD of the experiments from **Table 3-2** and **Figure 3-7b** shows a typical stereomicrograph of the agglomerates. The experimental conditions were chosen such that the expected final product ASD is significantly different for different experiments, which is necessary for the initial parameter estimation. The detailed explanation of how changes in Conc and SASR change the ASD is beyond the scope of this work and interested readers are referred to the relevant literature [14][23].

### 3.5 Model discrimination

#### *Initial Parameter Estimation*

**Table 3-3.** Parameter estimates of the agglomeration kernels obtained by minimizing the mean square error deviations between the experimental ASD and the model predicted ASD

Kernel	Parameter	Parameter Value
<i>Zauner Jones</i>	a	$5 \times 10^{-16}$
	b	1.734
	c	1.781
	d	2.84
	e	4.896
<i>Thompson</i>	$\beta_0$	0.091
<i>Schomolowski</i>	$\beta_0$	$2.23 \times 10^{-5}$
<i>Sastry</i>	$\beta_0$	$1.54 \times 10^{-6}$
<i>Golovin</i>	$\beta_0$	$7.87 \times 10^{-4}$
<i>Brownian</i>	$\beta_0$	$1.495 \times 10^{-16}$

**Table 3-3** shows the parameter estimates of each of the agglomeration kernels given in Table 3-1 by solving the optimization problem (26). It is to be noted that the change in volume of the solution (30 mL) is not significant (7.5%) compared to the initial volume of antisolvent (400 mL), so the hydrodynamic effect can be assumed to be constant throughout the experiment.

The critical variables associated with the mixing kinetics in the crystallizer are given in **Table 3-4**. Since the Reynolds number is higher than the critical Reynolds Number

(4000), the flow conditions in the crystallizer can be assumed to be turbulent. Since  $\tau_M \gg \tau_C$ , the crystallizer can be considered to be well mixed. The Kolmogorov microscale ( $\eta$ ) within the crystallizer is calculated to be  $1671 \mu m$ , which lies in the range of the agglomerate sizes (**Figure 3-8**). It is known that the relative importance of some of the effects viz. orthokinetic, perikinetic may change depending on the size of the crystals/agglomerates relative to  $\eta$ . However, since  $\eta$  lies in the range of the particle sizes, a full-fledged model discrimination is necessary to elucidate the most probable agglomeration mechanism.

**Table 3-4.** Mixing parameters associated with crystallizer

Variable	Value
$\frac{D}{T}$	$\frac{1}{3}$
$N_{Re}$	$1.75 \cdot 10^4$
$\tau_M$	8 s
$\tau_C$	2s
$N\tau_C$	5.3
$\tau_E$	0.0543 s
$\eta$	$1671 \mu m$

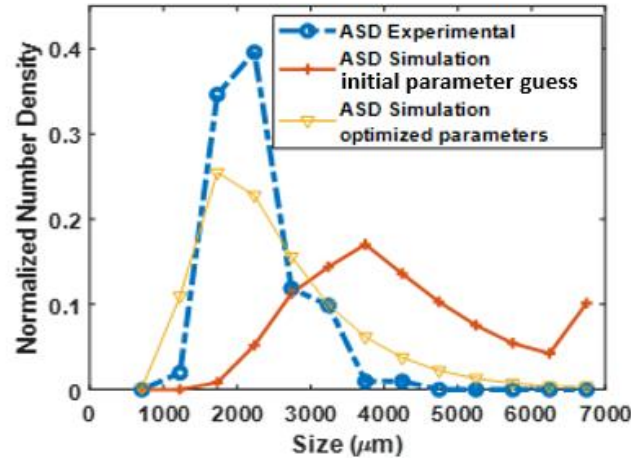


**Figure 3-8.** ASD from Experiment 4 and model predictions with Golovin kernel. Model predicted ASD with optimized parameters ( $\beta_{02} = 7.87 \times 10^{-4}$ ) gives less mismatch to experimental ASD than ASD predicted with the parameter ( $\beta_{01} = 3 \times 10^{-2}$ ), used as initial guess.

**Figure 3-8** shows the experimental ASD for Experiment 4 and the model predicted ASD using the Golovin kernel. To illustrate that the optimal parameter gave better prediction comparison with the experimental ASD, the model predictions were run with the initially guessed kernel constant,  $\beta_{01}=3 \times 10^{-2}$  in addition to the optimal estimated kernel constant  $\beta_{02}=7.87 \times 10^{-4}$ . This is clearly shown in Figure 3-8. This is further supported by the Mean Square Errors (MSE) between the experimental ASD and the model predictions where the model simulations with non-optimal parameter estimates has much higher MSE (30.83%) than the models with optimized parameter estimate (5.03%).

#### *Cross-Validation Computer Experiments*

**Table 3-5** shows the average MSE for different agglomeration kernels. The Golovin kernel and the Smoluchowski kernels give the best fit to the experimental data while the Thompson kernel gives the worst average error.

The deterministic Golovin kernel performs better than the stochastic Thompson kernel which is further exemplified in **Figure 3-9**, for experiment 5. The MSE between the experimental ASD and the model predicted ASD is also much more for the Thompson kernel (58.17%) than the Golovin kernel (31.04%). This can be due to two major reasons (i) the stochastic mode of agglomerate growth as mentioned in Berry et al. [113] does not actually take place in SA, which

is quite plausible, and (ii) the numerical assumptions made in Thompson et al. for reformulation of the stochastic Golovin agglomeration kernel does not apply here. Based on just these experimental observations and model predictions, it is not plausible to point to the precise reason behind this discrepancy. But for all pragmatic purposes of model predictions, the Thompson kernel can be excluded from the list of possible kernels to consider. The Sastry kernel also gives a high MSE (62.13%) and hence can be discarded from future model predictions.

**Table 3-5.** Cross validation designed experiments for different agglomeration kernels.

<b>KERNEL</b>	<b>KERNEL FORM</b>	<b>AVERAGE MSE (%)</b>
<b>SMOLUCHOWSKI</b>	$Q = \beta_0(x^{1/3} + y^{1/3})^3$	<b>38.65</b>
<b>BROWNIAN</b>	$Q = \beta_0 \frac{(x^{1/3} + y^{1/3})}{(xy)^{1/3}}$	<b>61.1</b>
<b>ZAUNER-JONES</b>	$Q = a_{rot}(b_{rot} + c_{rot}\epsilon^{0.5} - d_{rot}\epsilon)S^e$	<b>43.86</b>
<b>GOLOVIN</b>	$Q = \beta_0(x + y)$	<b>36.27</b>
<b>THOMPSON</b>	$Q = \beta_0 \frac{(x - y)^2}{(x + y)}$	<b>70.48</b>
<b>SASTRY</b>	$Q = \beta_0 \frac{(x^{2/3} + y^{2/3})}{(\frac{1}{x} + \frac{1}{y})}$	<b>62.13</b>

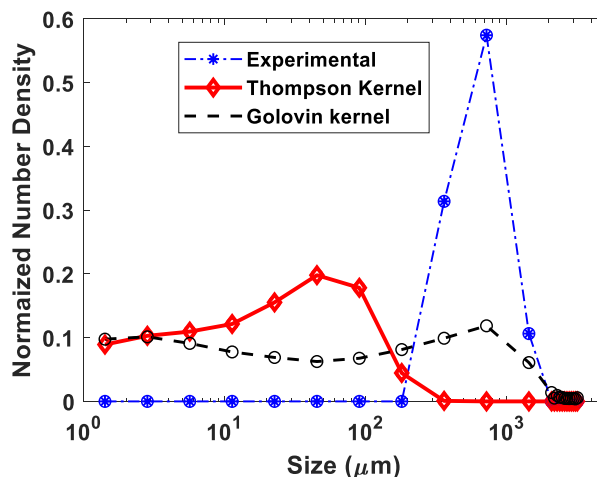


**Figure 3-9.** ASD from Experiment 5 and model predictions with the optimal parameter estimates for Thompson and Golovin kernels. Model Predictions with Golovin kernel (MSE = 31.04%) has better agreement with the experimental ASD than the Thompson kernel (MSE = 58.17%).

The kernels with the best predictive power are the Golovin (36.2%), Smoluchowski (38.6%) and the Zauner-Jones (43.8%) kernels. Since the Zauner-Jones kernel does not give a lower MSE than all other kernels, the AIC criterion is not calculated. However, the differences between the MSE are too small to draw mechanistic conclusions about the actual agglomeration mechanism in the process. It is quite plausible that the mechanism by which the particles agglomerate is a combination of the fundamental agglomeration mechanisms underlying the three kernels. For example, an agglomerate might be formed by a combination of orthokinetic agglomeration, layering of particles and gravitational settling (**Figure 3-10**) which would need the formulation of new mechanistic agglomeration kernels. In this work, a more pragmatic approach to model discrimination is adopted, i.e. the Golovin kernel is chosen as the best kernel for model predictions and is further used for refined parameter estimation. However, if the goal is to pinpoint the actual mechanism of agglomeration, a second step of model-based design for model discrimination is necessary after this step.

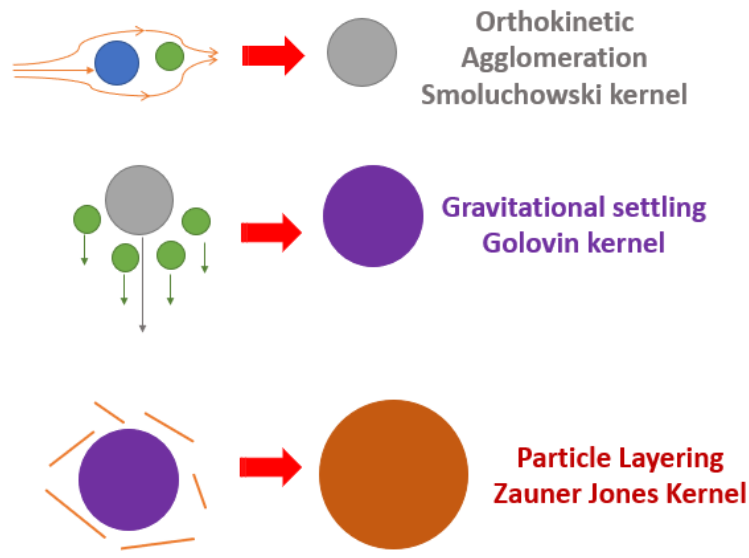


**Figure 3-10.** Hypothetical mechanism of agglomeration where three different agglomeration mechanisms (orthokinetic, gravitational, layering) all occur simultaneously.

It is to be noted that the MSE for experiment 5 only is much lower than the average errors given in **Table 3-5**. The reason is that in **Table 3-5**, the errors are averaged over all the six cross-validation experiments; in some experiments the MSE is much higher, which increases the average error. This points to the fact that there can be substantial improvements made to the parameter estimate  $\beta_0$  of the Golovin kernel, which necessitates parameter re-estimation experiments.

### 3.5.1 Model based design of experiments for refined parameter estimation

The initial parameter estimate of  $\beta_0 = 7.87 \times 10^{-4}$  (**Table 3-6**) is chosen for model refinement. The lower and upper bounds of the process variables are given in **Table 3-6** which were chosen based on prior experience from conducting experiments.

**Table 3-6.** Bounds for experimental process variables.

<b>Process Condition</b>	<b>Lower Bound</b>	<b>Upper bound</b>
Concentration of solute (gm/gm)	0.15	0.3
Solvent to Antisolvent Ratio (SASR)	0.09	0.18
Binder to Solid Ratio (BSR)	0.85	1.2
Volumetric flow rate of solution (mL/min)	1	10

At each stage of the iterative parameter estimation process, the optimization problem (32) is solved to generate the new experimental conditions. The new experiments are now run with these experimental conditions and the product agglomerates are collected and analyzed to determine the new ASD. A parameter re-estimation problem is run again to find the new estimates of model parameters. This process is run sequentially until convergence (**Figure 3-6**). **Table 3-7** shows the prior estimates of  $\beta_0$ , the new experimental conditions and the posterior estimates of  $\beta_0$  after parameter re-estimation. The parameter estimation process converged within three iterations.

**Table 3-7.** Parameter Estimates and Process Conditions

<b>Iteration Number</b>	<b>Prior estimate of <math>\beta_0</math></b>	<b>Process Variable</b>	<b>Experiment Number</b>	<b>Process Condition</b>	<b>New Estimate of <math>\beta_0</math></b>
1	$7.87 \times 10^{-4}$	Conc (g/mL)	E1	0.29	$2.621 \times 10^{-3}$
		SASR		0.09	
		BSR		1.0	
		$V_{sol}$ (mL/min)		4.42	
2	$2.621 \times 10^{-3}$	Conc (g/mL)	E2	0.287	$5.637 \times 10^{-3}$
		SASR		0.09	
		BSR		1.1	
		$V_{sol}$ (mL/min)		9.87	
3	$5.637 \times 10^{-3}$	Conc (g/mL)	E3	0.251	$5.637 \times 10^{-3}$
		SASR		0.135	
		BSR		1.0	
		$V_{sol}$ (mL/min)		1.99	

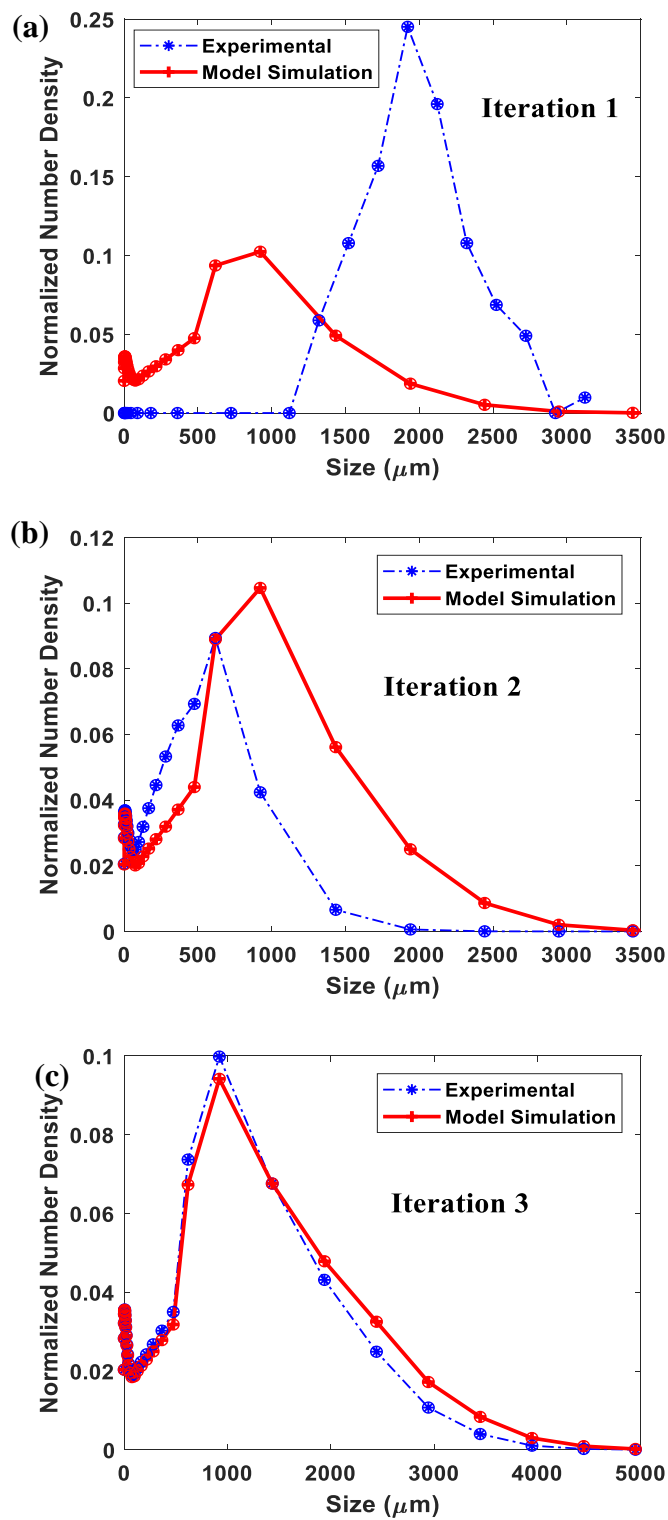


**Figure 3-11.** ASD from experiments (a) E1, (b) E2, and (c) E3 and model simulations with parameter estimates of  $\beta_0$ .

**Figure 3-10** shows the ASD obtained from model predictions with parameter estimates of  $\beta_0$  and the experimental ASD at each iteration of the MBED experiments. It is clear from **Figure 3-10** and **Table 3-8** that the deviation between the experimental ASD and the model predicted ASD decreases with increasing number of iterations. **Figure 3-11** shows the ASD estimated with the model parameters in iteration 3 is much closer to the experimental ASD than the ASD estimated from iteration 1. This also proves that the model predicted ASD indeed becomes closer to the experimental ASD with increasing number of iterations of MBED. The number of experiments necessary to obtain refined estimates of model parameters is substantially reduced compared to traditional statistical DOE. If each of the four factors had four levels, a fractional factorial design would need at least  $4^{4-1} = 64$  experiments. The number of experiments in MBED is substantially reduced (only three), which proves the utility of the proposed MBED framework to find precise estimates of model parameters for SA.

**Table 3-8.** MSE for each iteration of MBED showing the MSE decreases with increasing iterations.

Experiment	MSE (%)
E1	60.2
E2	13.6
E3	2.1

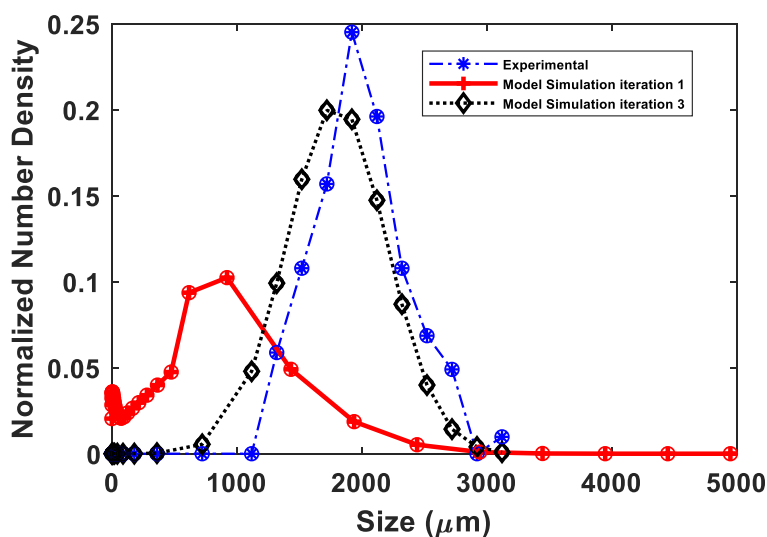


**Figure 3-12.** Model predictions with optimal parameters from iteration 1 and iteration 3.

### 3.6 Conclusions

In this work a two-tiered strategy for model discrimination followed by parameter estimation was introduced. The initial goal of this work was to discriminate among various mechanistic kernels for spherical agglomeration. From the initial cross-validation experiments, some kernels could be immediately rejected due to the high mean square error. But it was found that precise discrimination between Golovin, Smoluchowski, Zauner-Jones kernels was not possible from available experimental data. It was hypothesized the actual agglomeration mechanism may be a combination of orthokinetic, gravitational agglomeration along with layering of particles from solution. A more pragmatic approach towards model selection was then adopted where the Golovin kernel, which gave the least MSE, was selected as the best agglomeration kernel with the full understanding that developing a precise mechanistic description for spherical agglomeration needs further investigation. The model parameters of the Golovin kernel was then re-estimated using a MBED framework. The D-optimality criterion was used to find the experimental conditions, which minimized the uncertainties of the estimated model parameters. It was found that the MBED framework converged within three experimental iterations and the estimated model parameters fit the experimental data very well. This two-tiered model-discrimination and refined parameter estimation framework can work as a generic framework for a variety of model development problems in particle technology. An additional step will be further introduced in the future where the mathematical model is used in a model based experimental design framework to discriminate among the various mechanistic kernels before using this framework for parameter re-estimation.

## 4. MODEL BASED OPTIMAL CONTROL OF SPHERICAL AGGLOMERATION UNDER PARAMETRIC UNCERTAINTIES

Reproduced with permission from Kanjakha Pal<sup>+</sup>, Francesco Rossi<sup>+</sup>, Gintaras V. Reklaitis<sup>+</sup>, Zoltan K. Nagy<sup>+</sup> Submitted to *Journal of Process Control*, in review.

<sup>+</sup>School of Chemical Engineering, Purdue University, West Lafayette, IN 47907, US

### 4.1 Introduction

Spherical agglomeration (SA) is a novel process intensification (PI) method [117] for pharmaceutical manufacturing (PM), which reduces the number of unit operations in downstream manufacturing. Traditional PM consists of several unit operations, namely, crystallization, milling, filtration, drying and granulation, followed by blending and tablet pressing [118]. The rationale behind SA is to add a binder into the crystallizer to agglomerate the crystals in-situ [10]. The primary advantage of this approach is that spherical particles offer much better filtration performance [119] than needle or plate shaped crystals, which are usually encountered in PM. The flowability of the spherical agglomerates is also much higher [120], which reduces the cost of transportation in bulk solids handling between different unit operations. Thus, SA allows for control of the manufacturability of the product agglomerates, while simultaneously allowing for handling smaller sized primary crystals without the penalty associated with processing very fine powders.

Although SA has the aforementioned advantages, the highly coupled and nonlinear phenomena, on which it relies, inherently reduce the robustness [121] of the intensified unit operation. Mathematical models of processes can provide predictions [122] of the process output under process uncertainties. Blandin et al. [9] modeled the SA process using a phenomenological model. They formulated the agglomeration kernel as a product of two factors, which describe the probability of two particles colliding and their sticking efficiency after collision. Madec et al. [123] formulated a new multi-dimensional kernel, which gave insight into the effects of size and binding agent composition on the mechanism of agglomeration. They found their agglomeration kernels were able to explain the qualitative trends in the evolution of the particle size distribution. However, the previous works considered the entire particulate population within the crystallizer as a single population, which is physically unrealistic. Pena et al. [96] modeled the particulate population as

two separate populations of crystals and agglomerates and formulated population balance equations for each population. They also solved a model-based optimization problem to get the desired end-of-batch manufacturability and bioavailability of the agglomerates. However, their work considered the mathematical model to be perfect, with model parameters taken from literature data. Moreover, the optimization problem was solved only in open loop viz. no feedback from the process was considered in their work.

Advanced control strategies [124] using mechanistic mathematical models, can be applied to steer the batch to the desired end-of-batch state, even in the presence of process uncertainties. However, control of batch processes [125] is challenging endeavor due to the inherent dynamic nature of batch systems. Model predictive control (MPC) [126] has been widely used for batch process control, which ensures that the process attains the target end-of-batch product attributes, including process yield and product quality. However, MPC exhibits limitations in control performance, especially when there are uncertainties inherent in the process models [127]. Parametric uncertainty [128] is one of the most well-known and widely studied class of uncertainties, which arise in process models. Uncertainty in model parameters often arise due to unavoidable errors in the experimental measurements, which are used to compute the model parameters. Uncertainties may also arise from the lack of experimental measurements, which makes it impossible to accurately estimate all the model parameters. Robust control strategies [68] allow mitigation of these issues by computing robust control actions, which allow precise set-point tracking and enforce all the key operational constraints, even in the presence of uncertainty on the model parameters. Such model parametric uncertainties also arise naturally during the formulation of SA models because the mechanistic models of nucleation, growth and agglomeration contain kinetic parameters which are estimated from lab-scale experiments. This makes traditional deterministic MPC unsuitable for batch process control of SA. However, robust NMPC [129] takes such parametric uncertainties into account while calculating the optimal control moves and hence is more suitable for batch process control under uncertainty.

In this work, the uncertainties in the model parameters associated with the SA model is first estimated from experimental measurements. An open-loop optimization of the SA process is solved with the nominal values of model parameters, to obtain the target MAS in the crystallizer. A closed loop deterministic MPC problem is then solved, and its solution is compared to the open loop optimization problem. Model parameters are then sampled from this multidimensional

distribution, which are then propagated through the nonlinear process model to obtain the uncertain model outputs. A low dimensional model is then reconstructed from these model outputs using Polynomial Chaos (PC) Theory[18] [19][132][133], which is used as a surrogate model for MPC. A robust nonlinear model predictive control (RN MPC) problem is then solved using this surrogate model reconstruction, and its performance is then compared to the open loop optimizer and deterministic MPC.

## 4.2 Theory

### 4.2.1 Model predictive control (MPC)

Closed loop predictive control involves taking experimental measurements of PSD, followed by solving an online optimization problem, to predict the future control moves for the crystallizer. The control moves for the SA process include (a) API solution flow rate, (b) antisolvent flow rate, and (c) binder flow rate (**Figure 4-1**). There have been many techniques reported in literature to find the evolution of particle size in the crystallizer using process analytical technology (PAT) [134] tools, including focused beam reflectance measurement (FBRM) [135], bulk video imaging (BVI) [136], and other in-situ and inline imaging systems[137], [138] . However, accurate reconstruction of the PSD using online measurements from PAT tools remains a challenging task to date [139]. In this work, it is assumed that online measurements of the ASD is available from PAT measurements viz. **Figure 4-1**.

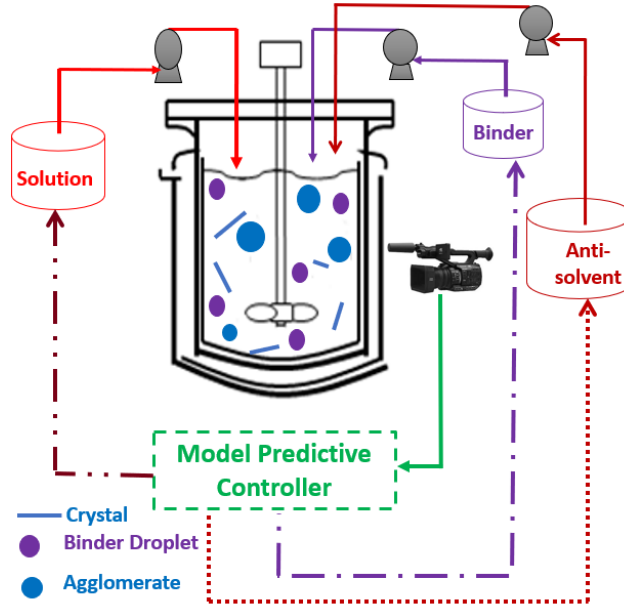


**Figure 4-1.** Conceptual experimental setup of online MPC with real-time imaging to find in-situ particle size.

#### *Optimization problem formulation*

The MPC problem is formulated as a Mayer control problem in equation (39)

$$\mathbf{u}_{opt}(t_1), \dots, \mathbf{u}_{opt}(t_f) = \min_{\mathbf{u}(t_1), \dots, \mathbf{u}(t_f)} J(\mathbf{x}(t_f)) = \left| \frac{\bar{x}_{sp} - \bar{x}(t_f)}{\bar{x}_{sp}} \right|$$

$$s.t. \left\{ \begin{array}{l} \frac{d\mathbf{x}(t)}{dt} = f(\mathbf{x}(t), \mathbf{u}(t)) \\ F_{S,\min} \leq F_S(t_i) \leq F_{S,\max} \\ F_{AS,\min} \leq F_{AS}(t_i) \leq F_{AS,\max} \\ F_{bin,\min} \leq F_{bin}(t_i) \leq F_{bin,\max} \\ \bar{x}(t_f) = \frac{\sum_{i=1}^{2M-1} x_i N_{a,i}(t_f)}{\sum_{i=1}^{2M-1} N_{a,i}(t_f)} \end{array} \right. \quad (39)$$

$$\forall i = 1, \dots, N_T$$

Here, the final mean particle size predicted from the model is calculated from the end-of-batch particle size distribution at the final time using equation (40).

$$\bar{x}(t_f) = \frac{\sum_{i=1}^{2M-1} x_i N_{a,i}(t_f)}{\sum_{i=1}^{2M-1} N_{a,i}(t_f)} \quad (40)$$

The MPC problem (39) is a multivariable control problem viz. there are 3 manipulated variables for the MPC problem which are given by (41).

$$\mathbf{u}(t) = [F_s(t), F_{AS}(t), F_{bin}(t)] \quad (41)$$

The optimization problem (39), solved online after taking the measurements at each sampled instant, gives the optimal control moves. However, only the first optimal control move is implemented, and the process is repeated iteratively until the end of the batch process. The batch MPC represents a shrinking horizon control problem, where the control horizon is shrunk iteratively viz. the number of predicted control moves is reduced as the batch progresses. The measurements included the full ASD obtained from in-situ imaging. The sampling time was 11.11 mins, which was chosen to balance controller performance vs computational effort for the solution of the online optimization problem. The sampling time was constant for all calculations of the online optimization problem (39). The measurement error was a random number bounded within 10% of the current value of the state measurement. Full-state feedback was not considered in this work since the measured ASD forms only a part of the full state. Extended Kalman Filter (EKF) [140] was used as the state estimator for all the computations.

### *MPC under parametric uncertainties*

For the parametric uncertainty formulation, the uncertain model parameter vector is given by equation (42) where all the parameters are uncorrelated and assumed to follow Gaussian distributions.

$$\Theta = [k_g, g, k_b, b, \beta_0] \quad (42)$$

The process model with parametric uncertainties is now given by equation (43).

$$\frac{d\mathbf{x}(t)}{dt} = f(\mathbf{x}(t), u(t), \Theta), \quad \mathbf{x}(t_0) = \mathbf{x}_0 \quad (43)$$

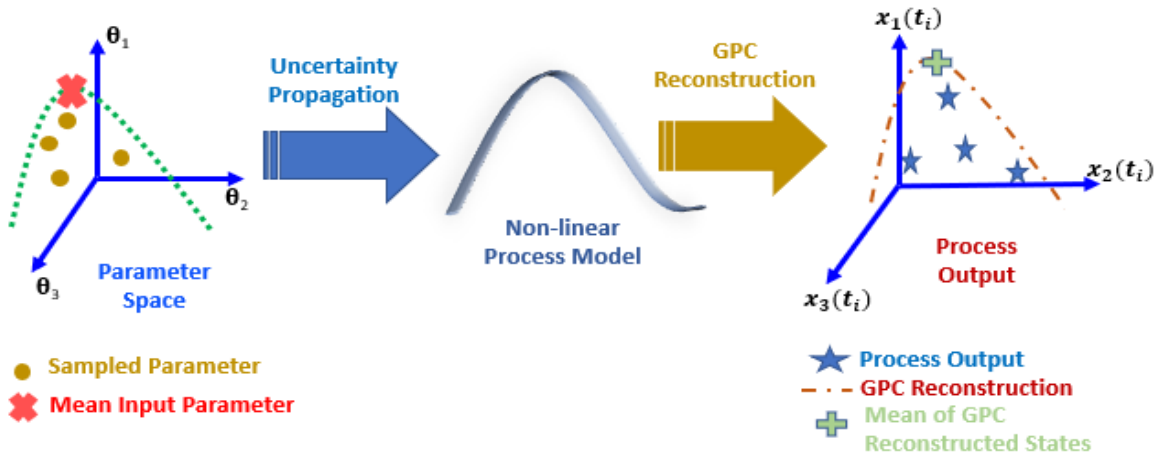


**Figure 4-2.** Hypothetical uncertainty propagation and GPC reconstruction for a parameter space with 3 parameters and state space with 3 states.

The uncertain parameter space of the model parameters  $\Theta$  is sampled as shown in **Figure 4-2**. The resulting scenarios are then propagated through the non-linear process model and the process outputs at prediction time  $t_1, \dots, t_N$  are computed viz.  $\mathbf{x}(t_1), \dots, \mathbf{x}(t_N)$ . Since the parameter vector  $\Theta$  is a stochastic variable, the estimated states  $\mathbf{x}(t)$  are also stochastic variables. Generalized Polynomial Chaos (GPC) theory is now used to reconstruct the output state  $\mathbf{x}(t)$  as a function of the model parameters  $\Theta$  according to equation (44), where  $\Gamma_{\alpha_k}(\Theta)$  is a multivariate polynomial in the model parameter  $\Theta$ . In addition,  $\Gamma_{\alpha_k}(\Theta)$  is a multiplication of univariate polynomials  $\Gamma_{\alpha_{i,k}}(\theta_i)$  in  $\theta_i$  of degree  $\alpha_{i,k}$ , according to equation (45).

$$\mathbf{x}(t) = \sum_{k=0}^{\infty} a_k(t) \Gamma_{\alpha_k}(\Theta) \quad (44)$$

$$\Gamma_{\alpha_k}(\Theta) = \prod_{i=1}^5 \Gamma_{\alpha_{k,i}}(\theta_i) \quad (45)$$

Here, since the model parameters are assumed to be gaussian random variables, the Hermite polynomials are chosen for the univariate polynomials  $\Gamma_{\alpha_{i,k}}$ , according to the Wiener Askey scheme for Polynomial Chaos [141].

To use the  $L_2$  convergent expansion for  $\mathbf{x}(t)$ , its expansion is truncated depending on the order of

the Polynomial Chaos expansion (p) according to  $\sum_{i=1}^5 \alpha_{i,k} \leq p$ . In addition, the total number of

terms in the PC expansion is given by  $N_{PC} = \frac{(5+p)!}{5! p!}$ , and the approximated PC expansion is given

by equation (46).

$$\mathbf{x}(t) = \sum_{k=0}^{N_{PC}-1} \mathbf{a}_k(t) \Gamma_{\alpha_k}(\boldsymbol{\theta}) = \mathbf{A}(t)^T \boldsymbol{\Xi}(\boldsymbol{\theta}) \quad (46)$$

Here  $\boldsymbol{\Xi}(\boldsymbol{\theta}) = [\Gamma_{\alpha_0}, \dots, \Gamma_{\alpha_{N_{PC}-1}}]$  is the vector of multivariate polynomials and

$\mathbf{A}(t) = [\mathbf{a}_0(t), \dots, \mathbf{a}_{N_{PC}-1}(t)]^T$  is the vector of coefficients. The coefficients of the PCE expansion are

calculated using probabilistic collocation method (PCM) [142], where the collocation points are

selected to be the roots of a one-degree-higher orthogonal Hermite polynomial than the PCE order.

After the PCE coefficients are estimated, the mean final state can be calculated from

$E(\mathbf{x}(t)) = \mathbf{a}_0(t)$ , where  $\mathbf{a}_0(t)$  is the first term in the PCE.

The optimization problem, iteratively solved within the MPC, is now reformulated as Equation

(47). Here  $N_{a,i}(t_f) = a_{o,i}(t_f)$ , and is calculated from the first term in the PCE.

$$\mathbf{u}_{opt}(t_1), \dots, \mathbf{u}_{opt}(t_f) = \min_{\mathbf{u}(t_1), \dots, \mathbf{u}(t_f)} J(\mathbf{x}(t_f)) = \left| \frac{\bar{x}_{sp} - \bar{x}_{sim}(t_f)}{\bar{x}_{sp}} \right|$$

$$s.t. \left\{ \begin{array}{l} \frac{d\mathbf{x}(t)}{dt} = f(\mathbf{x}(t), u(t), \boldsymbol{\Theta}), \mathbf{x}(t_0) = \mathbf{x}_0 \\ \mathbf{x}(t) = \sum_{k=0}^{N_{PC}-1} \mathbf{a}_k(t) \Gamma_{\alpha_k}(\boldsymbol{\theta}) \\ E\{N_{a,i}(t_f)\} = a_{o,i}(t_f) \\ \bar{x}_{sim}(t_f) = \frac{\sum_{i=1}^{2M-1} x_i E\{N_{a,i}(t_f)\}}{\sum_{i=1}^{2M-1} E\{N_{a,i}(t_f)\}} \end{array} \right. \quad (47)$$

Here, an approximation has been introduced because  $\bar{x}_{sim}$  is not the expected value of the end-of-batch MAS but approximates the MAS over all the simulations. The approximation is

necessary because the expectation of a random variable is a linear operator, thus does not scale over the division operator viz. (48).

$$E\{\bar{x}(t_f)\} \neq \frac{\sum_{i=1}^{2M-1} x_i E\{N_{a,i}(t_f)\}}{\sum_{i=1}^{2M-1} E\{N_{a,i}(t_f)\}} \quad (48)$$

An overview of development and implementation of the robust MPC, based on the low dimensional surrogate model is given in **Figure 4-3**.

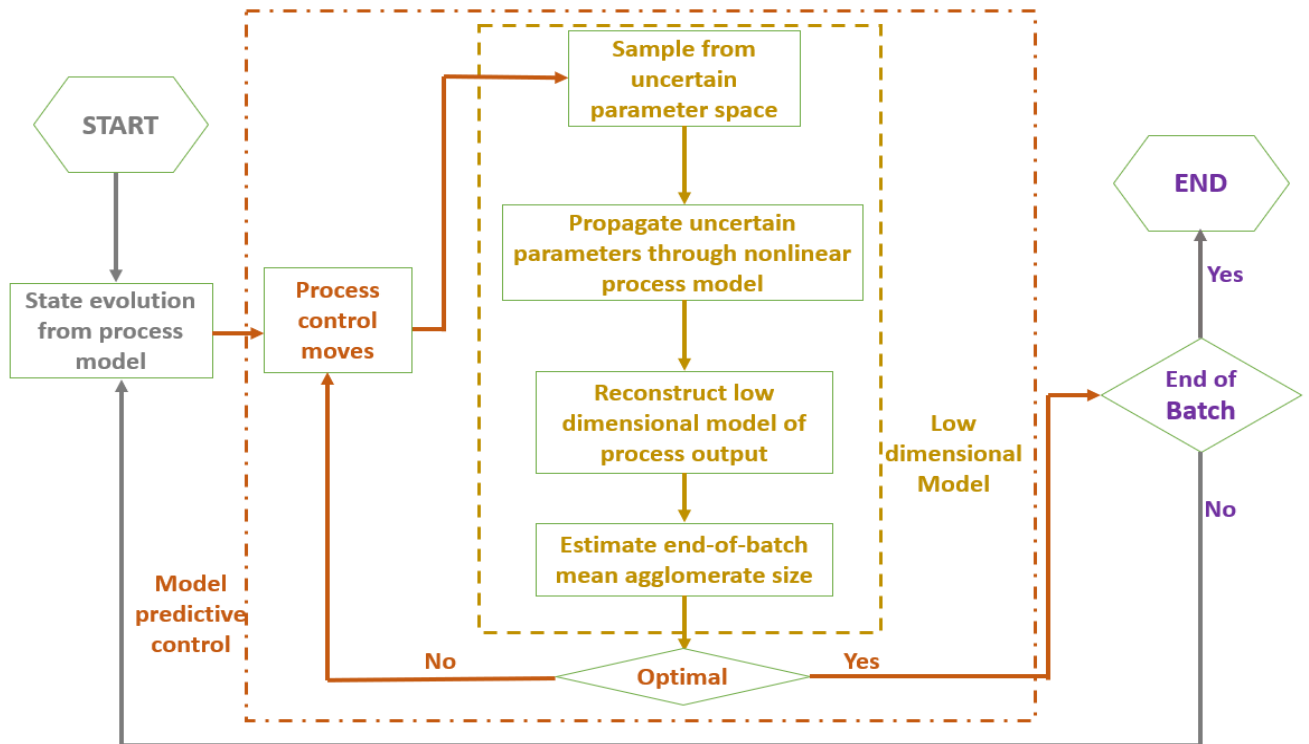


**Figure 4-3.** Workflow for model predictive control of SA under parametric model uncertainties using low dimensional PCE based surrogate model reconstruction.

### 4.3 Results and discussions

The system of differential algebraic equations (DAEs) was solved using *ode15s* of Matlab R2017b, run on an i7-2600 CPU (3.40 GHz). The optimization problem (47) was solved using the gradient-based solver *fmincon* of Matlab. The open loop optimization problem was solved using the genetic algorithm optimizer *ga* of Matlab. However, for solving the closed loop model-based optimization and stochastic optimization problems, *ga* was too slow. The optimal control profile calculated

using *ga* was used as an initial control profile for solving a local optimization problem, using the function *fmincon* of Matlab. The model parameter vector  $\Theta$  is estimated by carrying out batch experiments under different process conditions and minimizing the deviation between the time-course measurements of experimental data and model predictions. The experimental data used for parameter estimation included (i) particle size distribution from Malvern Mastersizer 3000 and (ii) API concentration from ultraperformance liquid chromatography (UPLC, Waters Corporation). The uncertainty in the model parameters was estimated by Markov Chain Monte Carlo (MCMC) sampling, using MatlabStan, the Matlab interface to the Stan Modeling Language[143]. For brevity the full experimental results are not shown here, but only the estimated model parameters along with their standard deviations are shown in **Table 4-1**. Here the model parameters follow a multidimensional normal distribution with diagonal variance-covariance matrix viz. the model parameters are uncorrelated. This later assumption simplified the solution of the RN MPC problem. For calculating the model prediction errors, 500 MCMC simulations were run with sampled model parameters for all the cases viz. open loop, MPC, RN MPC.

**Table 4-1.** Estimated model parameters along with standard deviations

Parameter	Mean	Standard Deviation
$k_b$ (#/cm <sup>3</sup> -min)	720	60
$k_g$ (cm/min)	4.49 X 10 <sup>-4</sup>	0.18 X 10 <sup>-4</sup>
$g$	1.0025	0.01
$b$	1.1860	0.11
$\beta_0$	0.0001	0.0002

### 4.3.1 Open loop optimization

The open loop optimization problem was solved considering the nominal values of model parameters, while the actual process evolved with uncertainties in model parameters. **Figure 4-4a-c** show evolution of antisolvent, API solution and binder flow rates and **Figure 4-4e-h** shows a schematic of the process evolution. During stage 1, API solution is added to the antisolvent (**Figure 4-4a**) which induces API crystallization (**Figure 4-4e**). During stage 2, addition of API solution is

stopped and binder is added to induce agglomeration (**Figure 4-4f**), which increases the MAS (**Figure 4-4d**). However, the MAS overshoots the set-point MAS (**Figure 4-4d**) in stage 3a (**Figure 4-4g**) due to rapid granule growth. Hence, antisolvent is again added in stage 3a (**Figure 4-4c**) to induce further API crystallization. The rationale behind the further addition of antisolvent in stage 3 was to form smaller crystals, which upon agglomeration, would have given rise to smaller agglomerates. However, due to plant-model mismatch (**Figure 4-5**), the rate of API nucleation is much higher than the model predictions, which reduces the MAS drastically below the set-point MAS. It can be seen from **Figure 4-4d**, that the uncertainty associated with the MAS predictions are huge, since the open-loop optimizer is not aware of the plant-model mismatch.

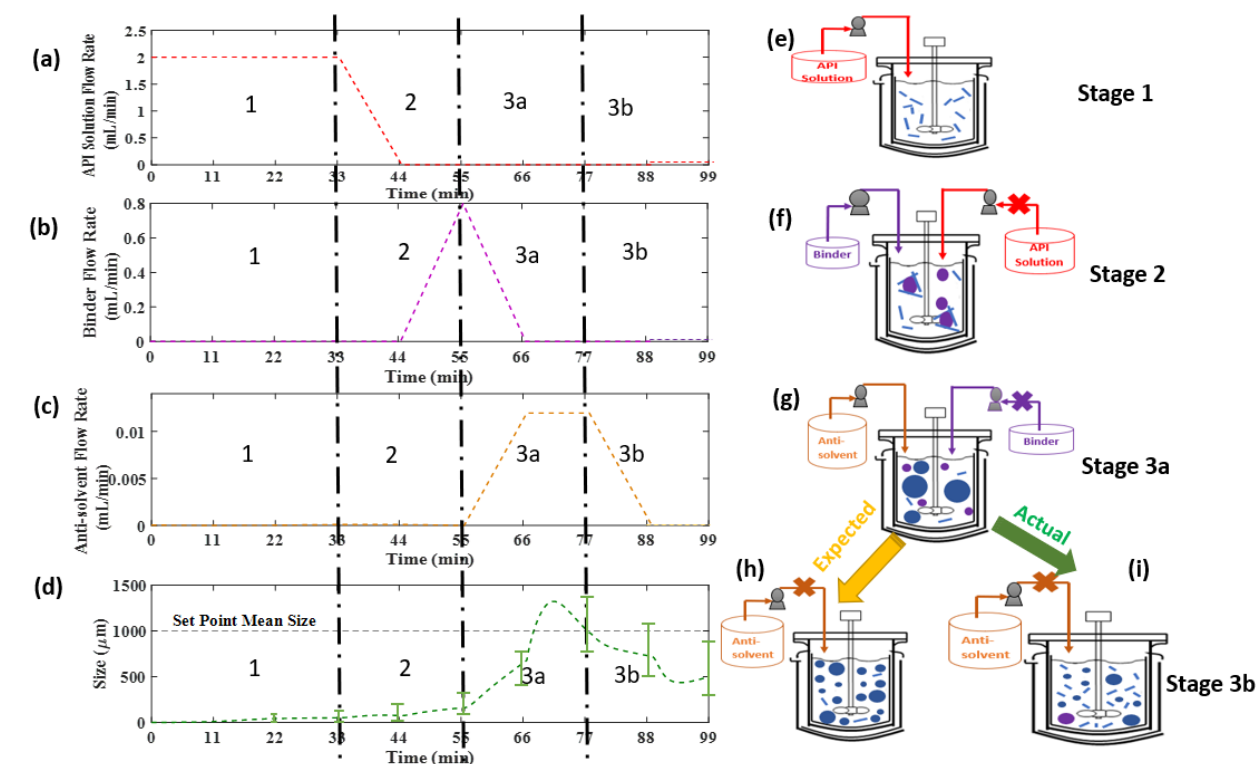


**Figure 4-4.** (a) Evolution of API solution flow rate, (b) binder flow rate, (c) anti-solvent flow rate, and (d) particle size during the different stages of optimization. (e) In stage 1, API solution is added to antisolvent to form the primary crystals. (f) In stage 2, addition of API solution is stopped and binder is added to induce agglomeration. (g) In stage 3a, binder addition is stopped and antisolvent addition is started to induce further formation of primary crystals by desupersaturation (h) In expected scenario stage 3b, smaller agglomerates were expected. (i) However in reality in stage 3b, due to excessive primary nucleation, there was not enough binder to agglomerate the primary crystals.

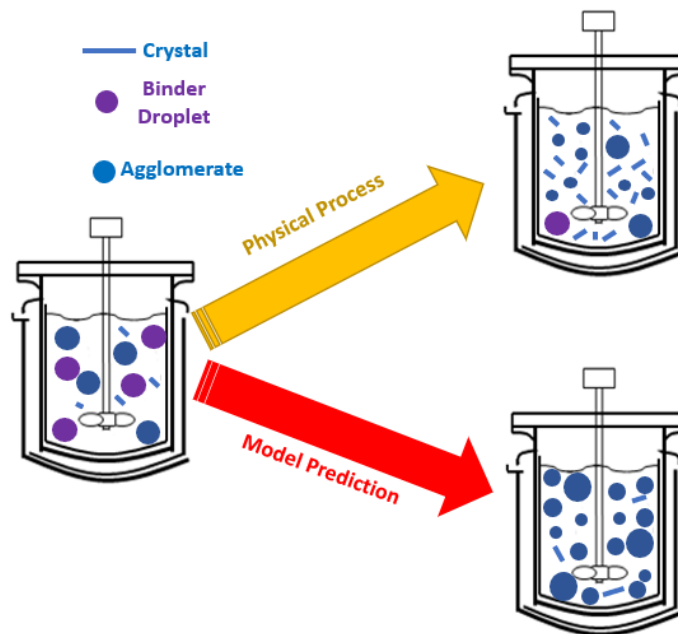


**Figure 4-5.** Model Prediction vs physical process for evolution in stage 3 of process after antisolvent addition. Model parametric uncertainties give rise to the plant-model mismatch.

#### 4.3.2 Deterministic MPC

**Figure 4-6a-c** show the evolution of the process variables and **Figure 4-6d** shows the evolution of the mean agglomerate size. Comparing **Figure 4-6a-c** and **Figure 4-4 a-c**, it can be seen that the major differences in flow rate profiles occur during stages 3a-b. The antisolvent addition is stopped during stage 3b, since the controller anticipated the MAS would end up below the threshold MAS, due to rapid API nucleation during stage 3b. Thus, although the controller is not aware of the plant-model mismatch, it takes proactive actions to mitigate the effects viz. addition of more binder in stage 3b (**Figure 4-6b**). This induces further agglomeration of the fine crystals generated in stage 3b, which increases the MAS (**Figure 4-6d**) after the slight dip. This illustrates the efficiency of feedback control to steer the system close to the target end-of-batch MAS, even in the presence of parametric uncertainties. A schematic of the evolution of the system in the various stages is shown in **Figure 4-6e-h**. However, even after introduction of feedback control, the end-of-batch MAS ( $1150 \mu\text{m}$ ) is still higher than set-point MAS ( $1000 \mu\text{m}$ ), which necessitates the use of RN MPC to improve controller performance. It can be seen from **Figure 4-6d** that the uncertainty associated with the MAS predictions are much less compared to **Figure 4-4d**, even

under the presence of plant-model mismatch. This points to the efficacy of feedback control to bring the system to the desired end-of-batch set-point and simultaneously reduced the uncertainty.

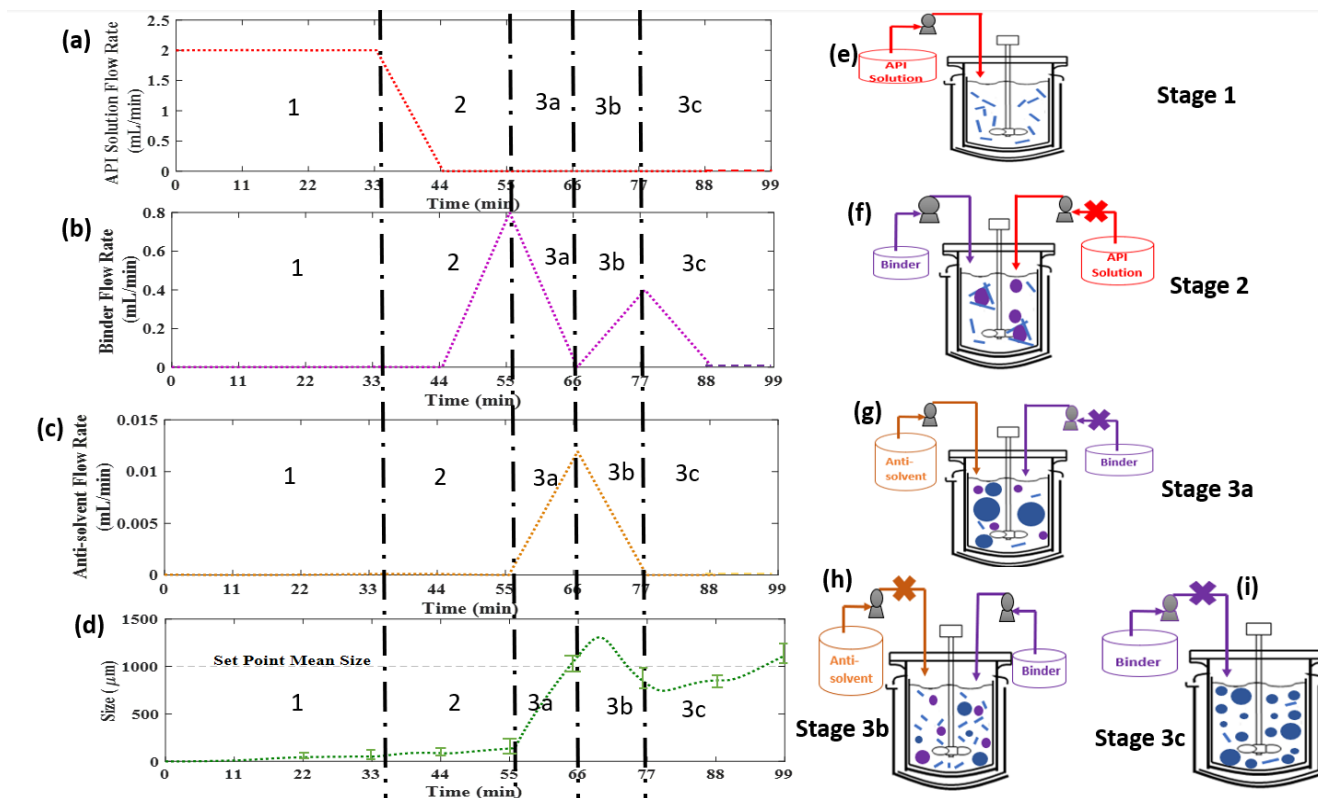


**Figure 4-6.** (a) Evolution of API solution flow rate, (b) binder flow rate, (c) anti-solvent flow rate, and (d) particle size during the different stages of optimization. (e) In stage 1, API solution is added to antisolvent to form the primary crystals. (f) In stage 2, addition of API solution is stopped and binder is added to induce agglomeration. (g) In stage 3a, binder addition is stopped and antisolvent addition is started to induce further formation of primary crystals by desupersaturation (h) In stage 3b, the optimizer predicts excessive nucleation and hence stops antisolvent addition and induces further agglomeration via binder addition (i) In stage 3c, binder addition is stopped and the process MPS reaches very close to the set-point MPS.

### 4.3.3 Robust nonlinear model predictive control (RNMPC)

**Figure 4-7a-c** shows the evolution of the process variables and **Figure 4-7e-h** show a schematic of the process evolution on implementing RNMPC. Comparison of **Figure 4-6b** and **Figure 4-7b** shows that the binder is added much earlier in the process during RNMPC. This is due to the inherent nature of the controller formulation viz. the controller anticipates the uncertainties in the process output due to model parametric uncertainties. Thus, it takes the riskier control moves viz. binder addition earlier in the process to hedge against the inherent process risk. **Figure 4-7d** shows

that the MAS increases beyond the set-point again around 70 mins. However, after antisolvent addition in stage 3 (**Figure 4-7c**), the end-of-batch MAS ( $995 \mu\text{m}$ ) is very close to the target MAS. Addition of further antisolvent in stage 3a depletes the residual supersaturation and generates fine PCs. The residual binder from stage 2 now agglomerates the in-situ generated crystals in stage 3a, to produce agglomerates of desired size.

**Table 4-2** shows the difference from the end-of-batch MAS and set-point MAS for the three cases, averaged over 500 model simulations. The difference is the highest for open-loop optimization which diminishes upon implementation of MPC. However, the difference (15%) is still higher than the user-specified threshold (5%). Implementation of RN MPC reduces the difference to 2% and drastically improves controller performance. It is to be noted that the solution time of the open-loop optimization problem is the highest, since a global optimizer was used for this case. But for solutions of MPC and RN MPC problems, a local optimizer was used, which provided faster solutions. However, the solution time for one-run of the RN MPC (13.6 mins) is higher than the sampling time (11 mins), which makes its practical implementation infeasible. In the future, faster methods for RN MPC implementation need to be developed to enable real-time process implementation. It can also be seen from **Figure 4-7d** that the uncertainty associated with SMPC is much less, compared to **Figure 4-4d** and **Figure 4-6d**. This is because when the online controller carries out stochastic simulations, it finds the optimal control moves which reduce the uncertainty associated with the model output, along with reducing the end-of-batch deviation between the expected value of the deviation between the model predictions and the set-point. It is to be noted that in **Figure 4-7d**, the MPS decreases rapidly around 66 mins due to rapid nucleation from the antisolvent addition. However, the residual binder from Stage 1 agglomerates these fine crystals, which again increases the MAS in stage 3b.

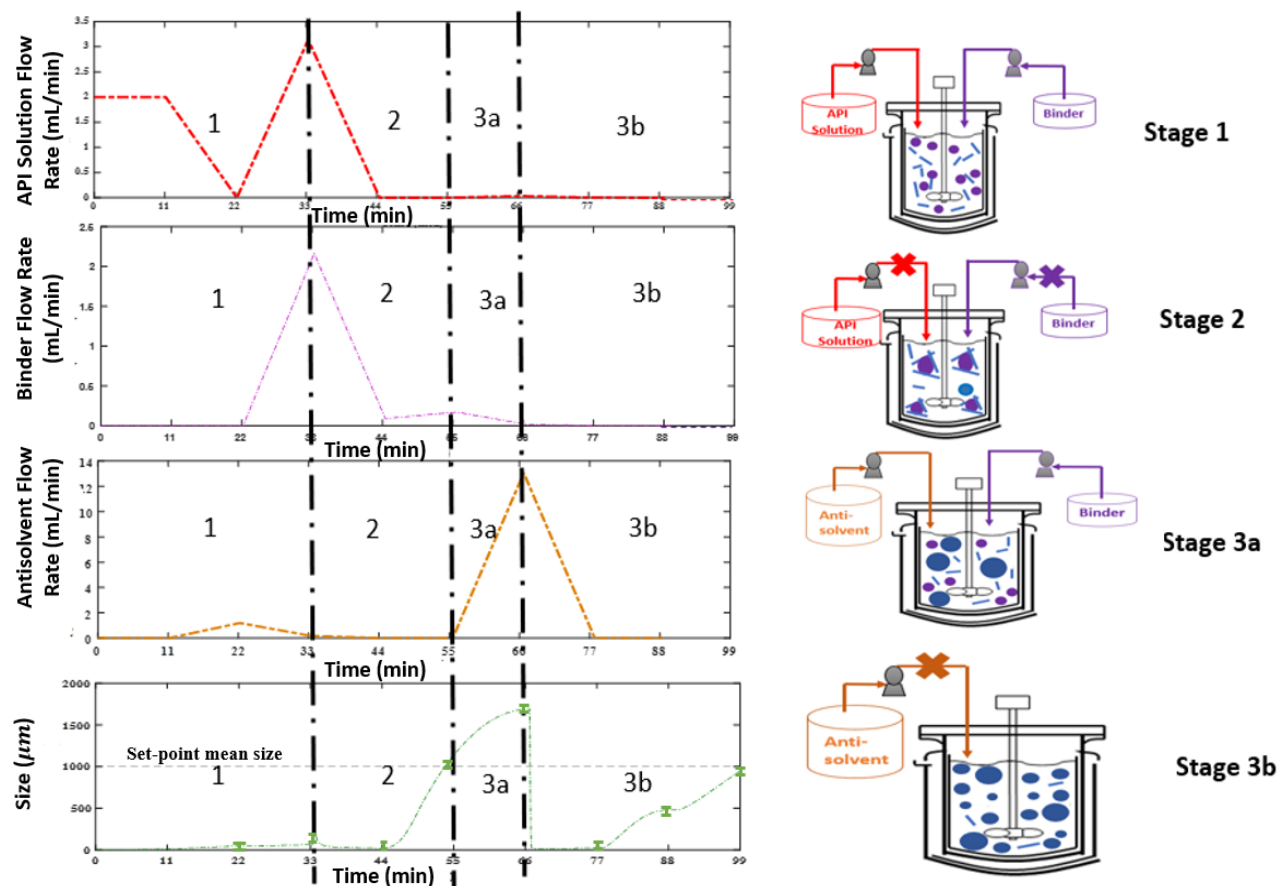


**Figure 4-7.** (a) Evolution of API solution flow rate, (b) binder flow rate, (c) anti-solvent flow rate, and (d) particle size during the different stages of optimization. (e) In stage 1, API solution and binder are added to antisolvent to form the primary crystals and agglomerate them (f) In stage 2, API solution and binder addition are stopped. (g) In stage 3a, antisolvent addition is started to induce further formation of primary crystals via de-supersaturation (h) In stage 3b, antisolvent addition is stopped and the system reaches the desired end-of-batch mean particle size.

**Table 4-2.** Difference of MAS from set-point MAS for open loop optimizer, deterministic MPC with parametric uncertainty and MPC with surrogate model reconstruction.

Controller Type	End-of-batch MAS	Deviation	Solution Time (mins)
Open Loop Optimizer	515 $\mu\text{m}$	48%	200.8
Deterministic MPC	1153 $\mu\text{m}$	16%	7.1
Robust NMPC	995 $\mu\text{m}$	2%	13.6

#### 4.4 Conclusions

In conclusion, a comparative study over different kinds of controller designs viz. open loop vs closed loop, was carried out on a SA process. The target of the controller was to design the control moves viz. flow rates of API solution, antisolvent and binder, to obtain the set-point end-of-batch MAS specified by the customer. The process model was constructed, and the uncertainties in the model parameters were quantified from lab scale experimental data. The open loop optimization problem, run with nominal values of the model parameters, was found to be insufficient to reach the target end-of-batch MAS. MPC, which incorporates feedback control via solution of an online optimization problem, was found to be give much better controller performance. Since MPC updates the model predictions in real-time based on in-situ measurements, it was able to predict the large deviations in the end-of-batch product quality and adjust for the controller actions accordingly. However, the deviation in the MPC objective was still higher than the user-specified threshold (5%), which necessitated the use of RN MPC based on surrogate model reconstruction using PCE. The controller performance from the RN MPC improved drastically, as quantified by the very low deviation (2%) from the user-specified threshold. However, the solution of the RN MPC takes much longer since multiple optimization problems are solved, based on sampling of the uncertain parameter space. In the future, faster techniques for RN MPC implementation need to be developed to enable real-time implementation. Alternatively, process modifications can be carried out to change the process dynamics, to enable real-time implementation of RN MPC in its current formulation. One limitation of the proposed RN MPC formulation is that the model parameters were assumed to be uncorrelated, which simplified the solution of the RN MPC problem. However, depending on the API, this assumption may not always hold good. In the future, novel PC expansions viz. arbitrary polynomial chaos[144] need to be developed, which can generate low dimensional surrogate models for correlated model parameters.

However, one of the major problems with traditional SA technology is that it is very difficult to co-agglomerate APIs and excipients using a binder. The difficulty stems from the differences in surface wettabilities of the APIs and excipients (**Figure 4-8**). If there are PCs of API and excipients in solution, the only situation when the binder will wet both the APIs and excipients, with equal vigor, is if the contact angle of the binder is the same for both. However, for most practical situations, the contact angles are different, due to which the binder preferentially binds the APIs and not the excipients. At the end of the experiment, this produces a slurry of API agglomerates

and primary particles of excipients, which defeats the primary purpose of co-agglomeration. This necessitated the development and deployment of a novel Spherical Crystallization technology to enable rapid co-agglomeration, as discussed in the following chapters.

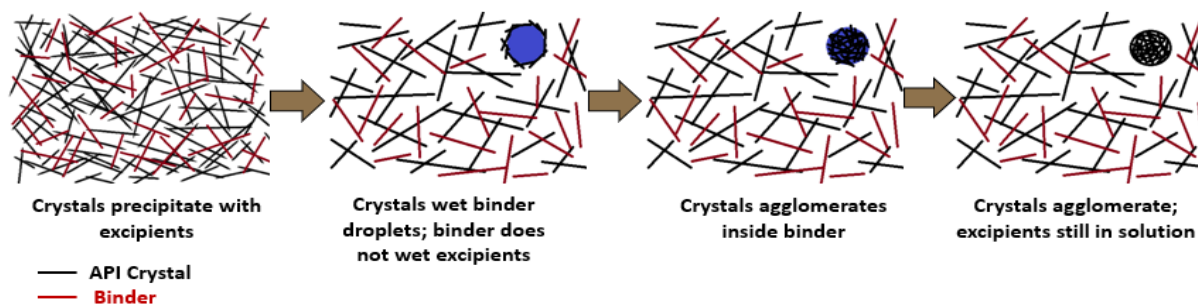


**Figure 4-8.** Challenges with co-agglomerating APIs and excipients simultaneously, using binder.

## 5. MECHANISTIC INSIGHTS INTO SPHERICAL CRYSTALLIZATION GUIDED BY PROCESS ANALYTICAL TECHNOLOGY : TOWARDS QUALITY BY DESIGN FOR PHARMACEUTICAL PROCESS INTENSIFICATION

Reproduced with permission from Kanjakha Pal<sup>+</sup>, Christopher L. Burcham<sup>\*</sup>, Daniel J. Jarmer<sup>\*</sup>, Ramon Peña<sup>+</sup>, Zoltan K. Nagy<sup>+</sup>. Submitted to *Crystal Growth and Design*, in review.

<sup>+</sup>*Davidson School of Chemical Engineering, Purdue University, West Lafayette.*

<sup>\*</sup>*Eli Lilly and Company, Lilly Technology Center, Indianapolis.*

### 5.1 Introduction

Spherical Crystallization (SC) [145] [117] is a bulk property enhancing crystallization technique that can be carried out through emulsion solvent diffusion (ESD) [146] or spherical agglomeration (SA) [147]. ESD is a particle design technique [148] that requires the stabilization of an emulsion, carrying the active pharmaceutical ingredient (API) solution, followed by crystallization within the emulsion via solvent diffusion. SA [14] agglomerates crystals in suspension by the addition of a bridging liquid (binder), which is immiscible with the solvent mixture and preferentially wets the crystals [10]. SC enables process intensification (PI) [116] in Pharmaceutical Manufacturing (PM) by reducing the number of downstream unit operations such as milling [149][150], and granulation [88].

The key breakthrough in these particle technologies will be the ability to formulate the drug product (DP) directly in suspension [151]. Excipients are added to the active ingredient to increase the downstream manufacturability [152] and bioavailability [153][134] of the tableted DP. Incorporating excipients within the API agglomerates [154] using SA has been very challenging due to the complex nature of surface interactions with the binder. ESD enables co-agglomeration of APIs and excipients directly within the crystallizer, which can potentially lead to direct compression formulations [155]. Pawar et al. [156] was the first to experimentally prove the concept of co-agglomerating an API with an excipient using SC. Genikal et al. [157] described the formulation of co-agglomerates of Naproxen with Polyvinyl Pyrrolidone and Polyethylene Glycol. Raval et al. [158] elucidated the role of excipients in the crystallization of albendazole and found the presence of excipients to be critical to obtain co-agglomerates with desired powder properties. Garala et al. [159] used Quality-by-Design (QbD) approaches to develop co-

agglomerates of racecadotril and loperamide hydrochloride. They demonstrated that multivariate statistical methods including factorial Design of Experiments (DOE), and Response Surface Modeling (RSM) could be used to characterize the sources of variability in the co-agglomeration process. Co-agglomeration of two active ingredients have also been demonstrated using ESD. Viswanathan et al. [160] agglomerated Mefanamic Acid and Nabumetone to produce spherical particles with improved micrometric properties.

In recent years, the USFDA has been encouraging pharmaceutical companies to shift from the traditional Quality-by-Testing (QbT) framework to a Quality-by-Design (QbD) framework [118][161]. QbD emphasizes a systematic approach to process development [162] based on thorough scientific understanding of the manufacturing processes. However, fundamental mechanistic understanding of the ESD process is still lacking from literature. Process analytical technology (PAT) tools [163] are one of the key enablers of QbD. PAT enables process understanding [164] and can enhance prior process knowledge during process development. PAT tools [54] including focused beam reflectance measurement (FBRM) [165], spectroscopic tools, such as UV-Vis [166], Raman [167], and IR [168] have been the mainstay of pharmaceutical process understanding, especially crystallization. Howard et al. [169] carried out a PAT based investigation of polymorphic transformation during antisolvent crystallization of sodium benzoate from IPA/water. Simone et al. [166] used a composite sensor array of spectroscopic tools including NIR and ATR-UV/Vis along with FBRM and particle vision and measurement (PVM) [170] [171] to design an intelligent decision support system for pharmaceutical crystallization. However, literature studies on the use of PAT tools for process understanding of ESD have been relatively scarce.

The focus of this work is to understand the fundamental mechanism of crystallization of API particles inside the emulsion droplets. This is critical to controlling the primary particle size distribution of API inside the co-agglomerates, which influences the bioavailability of the agglomerates. However, due to the fundamental multiscale nature of the process., the evolution of the particulate population within the droplets cannot be observed experimentally. On the other hand, the evolution of the droplet population can be experimentally observed by using in-situ PAT tools viz. FBRM. The dynamics of crystallization within the droplets also depend on the critical process parameters (CPPs) viz. API solution concentration, solvent to antisolvent ratio, emulsifier concentration, which is ultimately reflected in the statistics of droplet population recorded via the

FBRM. This work develops the first-of-its-kind inferential deductive approach (IDA) where statistics from time evolution of FBRM counts has been used to infer the relative time scales of nucleation and growth within the droplets. This work thus proposes a new multiscale framework where in-situ macroscale process data from PAT tools can be used to understand the fundamental mechanisms at the microscale, which will open new vistas for product and process design.

## 5.2 Experimental Section

### 5.2.1 Chemicals and analytical methods

#### *Materials*

Ibuprofen (>99 % purity, BASF Corporation) was used as model API. Polyvinyl Alcohol (4% Aqueous Solution, Ward's Science) was used as an emulsifier. Acetone (99.5 % purity, Fischer Chemicals) was used as solvent. Talc (99.3 % purity, Fischer Chemicals) was used as an excipient. Deionized water was used as the antisolvent.

#### *Sample characterization*

Optical micrographs of the spherical agglomerates were taken using an optical microscope (Nikon SMZ 1500 stereomicroscope) at 0.75X resolution. The samples were also characterized by using a Scanning Electron Microscope (FEI Quanta 3D FEG Dual Beam SEM). A G-400 FBRM probe from Mettler-Toledo with IC FBRM 4.3 software (Mettler-Toledo) was used to monitor the Droplet Size Distribution within the crystallizer.

### 5.2.2 Process Description

An overview of the process development is shown in **Figure 5-1**. All experiments were carried out in batch mode. A 1L jacketed crystallization vessel was filled with the antisolvent, water and the water-soluble stabilizer (PVA) was dissolved in it. The system was stirred at the desired agitation rate (400-800 rpm). The API was dissolved in acetone (solvent) in a feed vessel. Talc (excipient) was dispersed in the API solution under constant agitation and the dispersion was pumped into the antisolvent at a controlled rate of 2 mL/min as shown in **Figure 5-1a**.

As soon as the API solution droplets meet the antisolvent, the emulsifier attaches to the droplets (**Figure 5-1b**). This is necessary to prevent droplet coalescence, which would cause random particulate agglomeration, thereby preventing the formation of spherical co-agglomerates with controlled size distribution. Since the solvent within the emulsion droplets and the antisolvent in

the continuous phase are miscible, diffusion of antisolvent into the emulsion droplets starts immediately (**Figure 5-1c**). Since the API is insoluble in the antisolvent, it starts crystallizing within the droplets. The excipients are trapped within the emulsion droplets, which ultimately leads to the formation of API-excipient co-agglomerates. The pumping of API solution is stopped after 10 min (**Figure 5-1d**) and the evolution of the process is tracked until the end-of-batch time (2 h). At the end of the batch, the suspension is filtered under vacuum and then air dried in an oven at 35°C for one day. The dried agglomerates are then characterized for further analysis.

**Figure 5-2a** shows a schematic of the droplet population within the crystallizer along with the FBRM. The FBRM only measures the chord length distribution of the droplet population, from which the droplet size distribution (**Figure 5-2b**) can be calculated [172]. However, the crystal population within the droplet viz. the primary particles are not measured by the FBRM directly. In this work, the dynamics of the droplet size distribution is used to get an inferential understanding on the evolution of the primary particle population within the droplets (**Figure 5-2b**). It is to be noted that the agglomerates influence the manufacturability of the drug substance, such as flowability whereas the primary particles influence the bioavailability (**Figure 5-2a**).

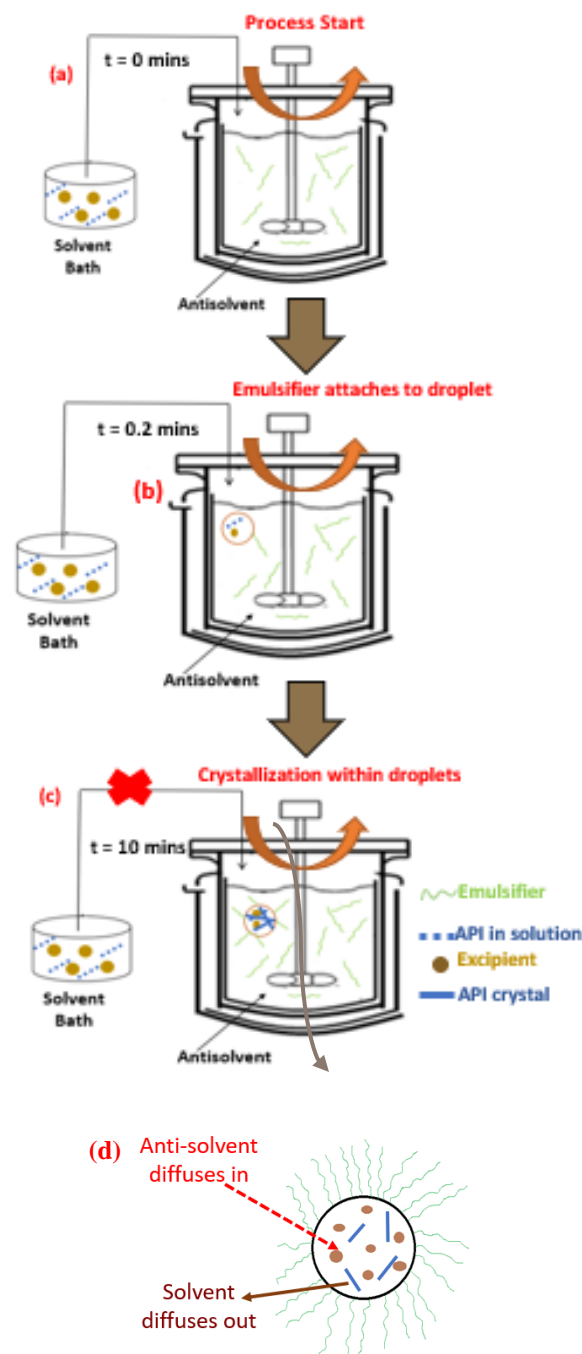


**Figure 5-1.** Overview of process development for emulsion solvent diffusion (a) emulsifier is dissolved in anti-solvent, which is stirred at constant rpm, (b) API solution is pumped into the anti-solvent in the crystallizer. Since the solvent within the emulsion droplets and the anti-solvent in the continuous phase are miscible, diffusion of anti-solvent into the droplets takes place. (c) Since the API is insoluble in the anti-solvent, it starts crystallizing out within the droplets. The API solution is stopped after 10 mins and the evolution of the process is tracked till the end-of-batch time (120 mins). (d) Diffusion of anti-solvent into the emulsion droplets and solvent out of the emulsion droplets in stage (b) and (c).

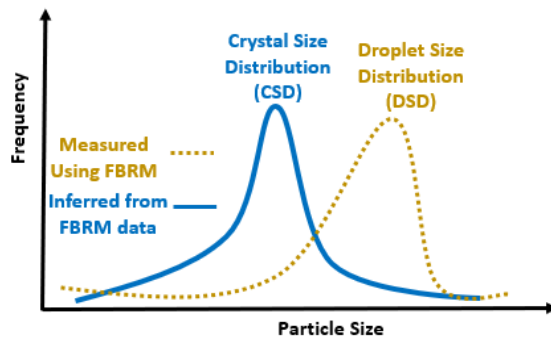


**Figure 5-2.** Illustration of the two populations – droplet population and crystal population within the droplets. The droplet size distribution (DSD) can be measured using FBRM while the crystal size distribution (CSD) within the droplets cannot be measured directly, but its evolution can be inferred from the evolution of the droplet size distribution.

### 5.3 Results and Discussions

The initial experiments were run with API concentration of 0.5 g/mL,  $\phi_{emul} = 0.25\%$ ,  $sasr = 0.025$  and at 800 rpm. **Figure 5-3a-b** shows SEM images of the dried co-agglomerates. **Figure 5-3a** shows the spherical morphology of a singular product agglomerate. **Figure 5-3c** shows optical micrographs of the co-agglomerated product, which clearly shows the presence of spherical agglomerates. It is clear from **Figure 5-3b** that primary particulates of different morphologies are present in the final drug product. This is indicative of the presence of the API and the excipient inside the co-agglomerates where the well-defined primary particles are the Ibuprofen crystals and the particles of irregular morphology are the excipient particles. This provides evidence that the ESD process designed in **Figure 5-1** can produce well-dispersed primary particles of APIs and excipients within the spherical drug product. However, the mere presence of API and talc in the product co-agglomerates does not provide any mechanistic process understanding. To gain a better process understanding, the effect of process perturbations on the dynamical evolution of FBRM counts is next investigated.

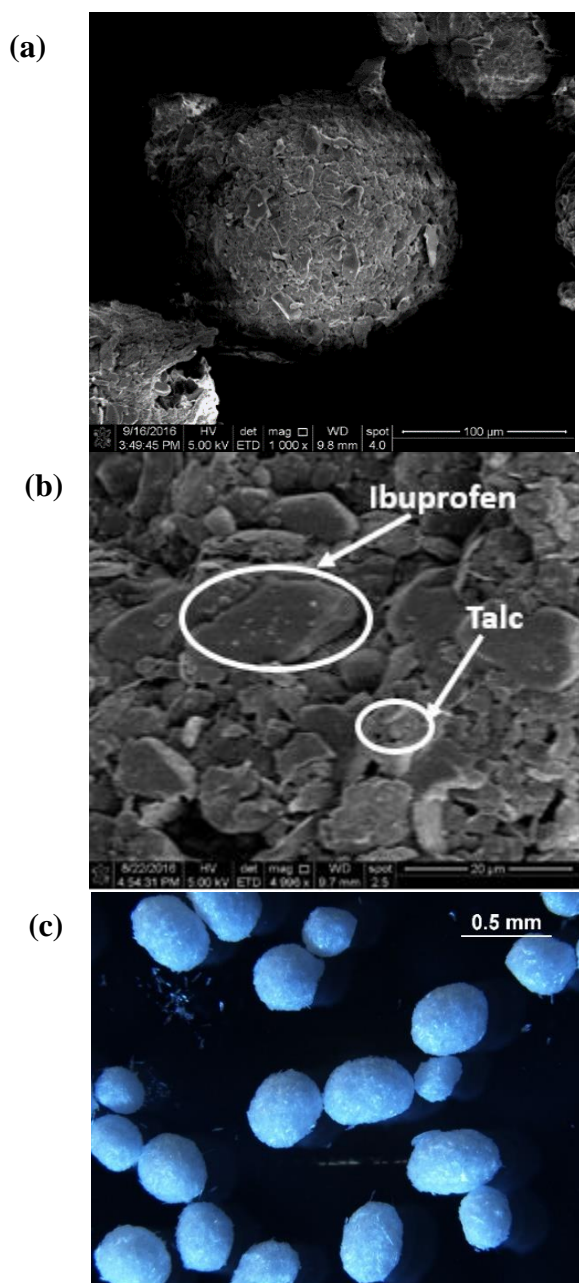
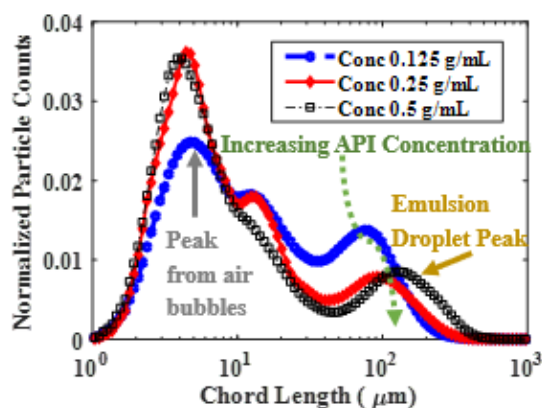


**Figure 5-3.** SEM image at (a) 1000X showing the presence of spherical co-agglomerates and (b) 4000X showing the presence of both ibuprofen (API) and talc (excipient) in the filtered co-agglomerates. (c) Optical micrographs of the final product co-agglomerates showing the presence of spherical particles.

### 5.3.1 Effect of API Concentration

**Figure 5-4** shows the effect of concentration of initial API solution on the end-of-batch chord length distribution (CLD) in the crystallizer. There are two populations within the crystallizer – the air bubbles and the emulsion droplets, which ultimately form the spherical agglomerates. A blank experiment was carried out where only the solvent (without any API) was pumped into the antisolvent. To distinguish between the FBRM peaks coming from the particles in the crystallizer and from the free emulsion droplets, a blank experiment was also carried out with just the emulsion droplets in the system (not shown). From these initial experiments, it was seen that the emulsion droplet peaks correspond to the peak at lower chord lengths ( $\sim 3 \mu\text{m}$  and  $15 \mu\text{m}$ ). These peaks at lower chord lengths were discarded from the subsequent analysis since only the peaks in CLD due to the particles were of interest.

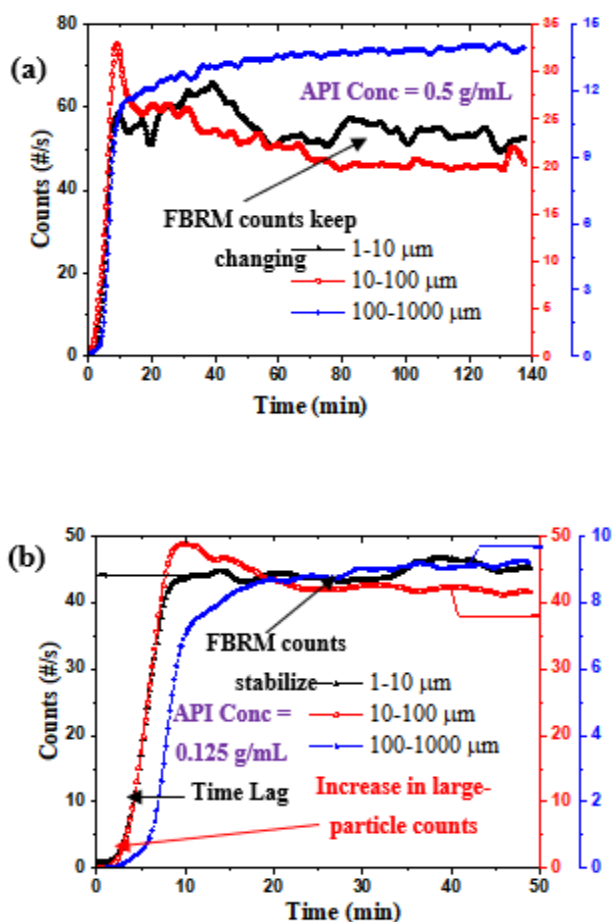
**Figure 5-4** also shows that with increase of API concentration, the end-of-batch CLD shifts to the right increasing the final mean chord length (**Table 5-1**). **Figure 5-5a-b** **Figure 5-7a-b** show the difference in the evolution of FBRM counts for two different API concentrations of 0.5 g/mL and 0.125 g/mL. In **Figure 5-5ba** time lag between the FBRM counts evolution of smaller ( $10\text{--}100 \mu\text{m}$ ) and larger ( $100\text{--}1000 \mu\text{m}$ ) particles is observed, which is not present in **Figure 5-5a**. The FBRM counts in **Figure 5-5a** also keep changing throughout the entire duration of the batch whereas the FBRM counts in **Figure 5-5b** stabilize after  $\sim 25$  mins.



**Figure 5-4.** End-of-batch chord length distribution (CLD) of ibuprofen-talc co-agglomerates at different initial API concentrations. The CLD becomes progressively right-skewed with increase in API concentration which indicates the formation of larger agglomerates. There are two peaks in the CLD – the peak at smaller chord length ( $\sim 4 \mu\text{m}$ ) arises due to air bubbles in the crystallizer, whereas the peak at larger chord lengths ( $\sim 90\text{--}200 \mu\text{m}$ ) occurs due to emulsion droplets, which ultimately form product agglomerates.

**Table 5-1.** End-of-batch mean chord length increases with increase in API Concentration.

API Concentration (g /mL)	Mean Chord Length ( $\mu\text{m}$ )
0.125	83
0.25	92
0.5	147

**Figure 5-5.** Evolution of FBRM counts for (a) 0.5 g/mL (b) 0.125 g/mL illustrating the difference in dynamical evolution of particle counts in FBRM, which shows the time lag in evolution of small and large particle counts for a lower API concentration.

A mechanistic hypothesis is proposed for the above observations in **Figure 5-7a-b**. For lower API concentration ( $C_1 = 0.125$  g/mL), the supersaturation generated is lower ( $S_1$ ) as illustrated in **Figure 5-6**. Thus, at  $t = 2$  min, the rate of nucleation within the droplet is low followed

by low growth rates at  $t = 8$  min (**Figure 5-7a**). At  $t = 10$  min, the crystals within the droplet grow to a large enough size to exert stress on the droplet interface, which then starts to expand (**Figure 5-7a**). This expansion of the droplet interface manifests as an increase in droplet size, which is then recorded as an increase in large particle counts in FBRM (**Figure 5-7b**). At  $t = 25$  min, the supersaturation within the droplets is completely depleted, so the crystals within the droplets stop growing which leads to no expansion of the droplet interface (**Figure 5-7a**). This, in turn, manifests as stabilization of particle counts in FBRM (**Figure 5-7b**).

However, at higher API concentration ( $C_2 = 0.5$  g/mL), the supersaturation generated is higher ( $S_2$ , **Figure 5-6**). This gives rise to higher nucleation rates at  $t = 2$  min (**Figure 5-7b**) followed by rapid crystal growth at  $t = 8$  min, which puts high interfacial stress on the droplets. This yields a faster rate of droplet expansion, which leads to no time lag between the small and large particle counts in **Figure 5-7a**. The supersaturation within the emulsion droplets is now depleted at a slower pace, which leads to crystal growth and droplet expansion throughout the entire period of the batch. This manifests in continuous increase of droplet counts in the FBRM throughout the batch (**Figure 5-7a**).

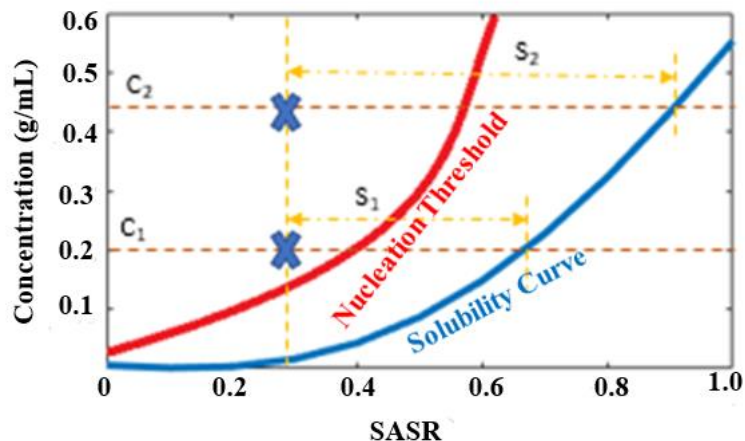


**Figure 5-6.** Evolution of operating point in phase diagram shows higher supersaturation for higher API concentration, which gives higher nucleation and growth rates.

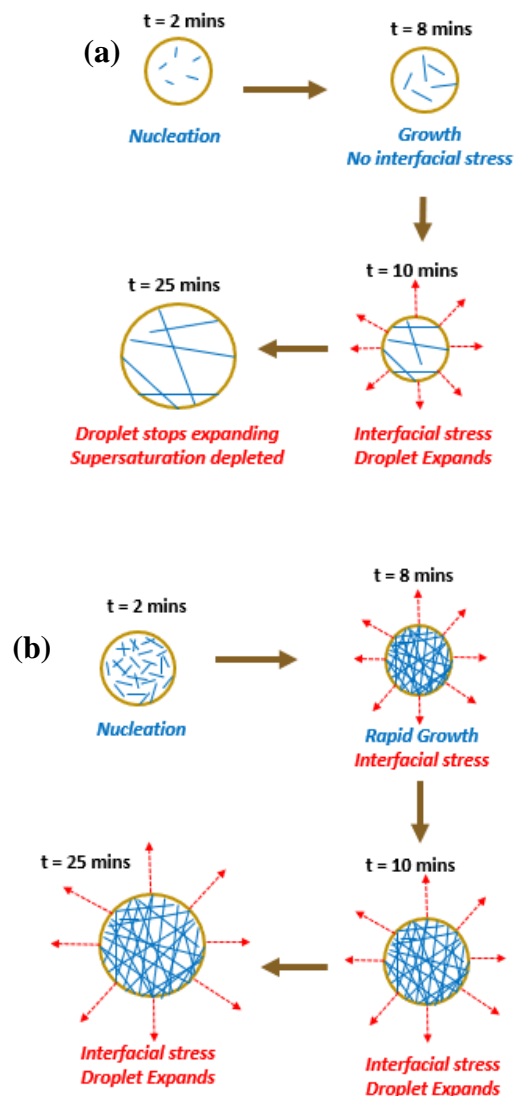


**Figure 5-7.** (a) Droplet expansion for lower API concentration, which shows crystal nucleation at  $t=2$  min followed by crystal growth at  $t=8$  min. At  $t=10$  min, interfacial stress on droplets makes droplets expand which is recorded as increase of large particle counts in FBRM. At  $t=25$  min, the supersaturation is completely depleted, so the droplet stops expanding. (b) for higher API concentration, the rapid growth at 8 min leads to faster droplet expansion and since the supersaturation depletion is slower, the droplet keeps on expanding at  $t=25$  min.

### 5.3.2 Effect of Emulsifier Concentration

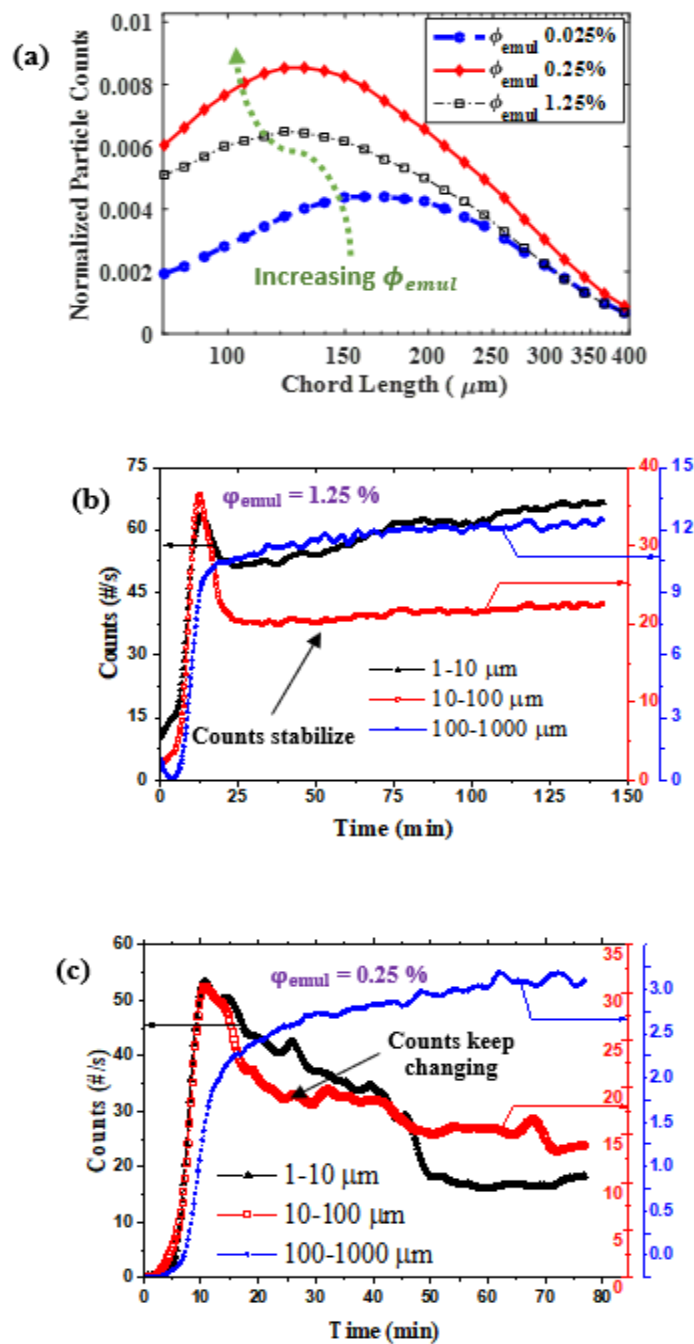


**Figure 5-8.** (a) End-of-batch chord length distribution becomes left skewed with increase of  $\phi_{emul}$  (b) FBRM counts at high emulsifier concentration  $\phi_{emul} = 1.25\%$  stabilize after 30 mins (c) FBRM counts at low emulsifier concentration  $\phi_{emul} = 0.25\%$  keeps changing throughout the batch

Experiments were conducted at 3 different emulsifier concentrations. **Figure 5-8a** shows that as the emulsifier concentration is increased, smaller sized particles are obtained. **Figure 5-8b-c** shows an interesting dynamical observations – for higher emulsifier concentration, the counts stabilize while for lower emulsifier concentration, the FBRM counts keep changing throughout the process.

**Table 5-2.** Effect of emulsifier concentration on the end-of-batch mean chord length.

Emulsifier Concentration (%)	Mean Chord Length ( $\mu m$ )
0.025	195
0.25	144
1.25	143

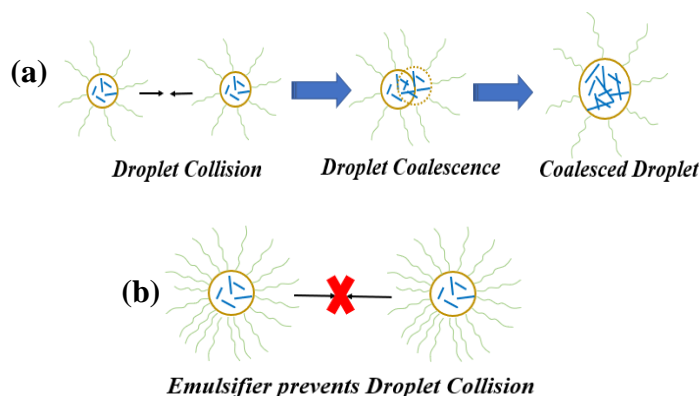


**Figure 5-9.** (a) At lower emulsifier concentration, droplets in solution that encounter each other coalesce to form a larger droplet (b) at higher emulsifier concentration, droplet coalescence is prevented due to steric repulsion between emulsifier molecules on adjacent droplets.

There are two hypothesis that can explain this observation

(H1) The crystallization dynamics inside the droplets is different for  $\varphi_{\text{emul}} = 0.25\%$  ,  $1.25\%$  similar to **Figure 5-7a-b**. This gives rise to differences in the growth rates of the droplets, which ultimately leads to different dynamics in the evolution of FBRM counts.

(H2) Coalescence of droplets happens at low emulsifier concentration because the steric repulsion is not enough to prevent coalescence (**Figure 5-9a**). However, at higher emulsifier concentration, steric repulsion prevents droplet coalescence (**Figure 5-9b**).

To quantitatively investigate the veracity of H1, the mass flux equation is taken into consideration following the Epstein-Plesset equation. A representative droplet of size  $150 \mu m$  has

been considered in this study. The API concentration inside the droplet has been assumed to be at its initial concentration of 0.5 gm/gm with a saturation concentration of 0.25 gm/gm. The radius of gyration of the polymer chain has been calculated according to the relation (49) [173], where  $N_{pva}$  is the number of repeat units. The length of a polymer step has been calculated from equation (50), and the expanded coil radius of the polymer chains has been calculated according to equation (51). It has been assumed the polymers attach as a monolayer layer on the droplets, with the length of the polymer chain attached to the interface being equal to the expanded coil radius.

$$R_g = N_{pva}^{0.65} \quad (49)$$

$$l_{pva} = \left( \frac{6R_g^2}{N_{pva}} \right)^{0.5} \quad (50)$$

$$R_{exp} = N_{pva}^{0.6} l \quad (51)$$

The rate of diffusion of the antisolvent into the droplet is determined by the proportion of the surface area on the droplets, which is free of emulsifier. The total number of droplets and the total number of polymer chains in solution are calculated according to equations (52)-(53). Here  $V_{sol}$  is the total volume of API solution and  $V_{drop}$  is the volume of the droplet.  $V_{tot}$  is the total solution volume in the reactor,  $f_{emul}$  is the volumetric fraction of the emulsifier,  $\rho_{poly}$  is the density of the polymer solution and  $MW_{poly}$  is the molecular weight of the polymer.

$$N_{drop} = \frac{V_{sol}}{V_{drop}} \quad (52)$$

$$N_{poly} = \frac{V_{tot} f_{emul} \rho_{poly}}{MW_{poly}} \quad (53)$$

The total expanded coil radius of all polymer molecules is calculated from equation the total perimeter of all the droplets is calculated from equation (55). The fraction of surface area of droplets occupied by the emulsifiers is calculated according to equation (56).

$$R_{exp,tot} = R_{exp} N_{poly} \quad (54)$$

$$P_{tot} = 2\pi R N_{drop} \quad (55)$$

$$f_{occ} = \frac{R_{exp,tot}}{P_{tot}} \quad (56)$$

The mass flux is calculated according to the Epstein-Plesset equation [174], where the mass flux has been calculated at 40 min. The time-scale of diffusion of antisolvent into the droplets is calculated according to equation (58), and the time-scale for growth of primary crystals (PC) is calculated according to equation (59). Here  $L_C$  is a representative length of PCs and  $G$  is the growth rate calculated according to equation (60).

$$\frac{dm}{dt} = 4\pi R^2 f_{occ} D(c - c_s) \left( \frac{1}{R} + \frac{1}{\sqrt{\pi D t}} \right) \quad (57)$$

$$t_{MT} = \frac{V_{drop} \rho_{AS}}{\frac{dm}{dt}} \quad (58)$$

$$t_G = \frac{L_C}{G} \quad (59)$$

$$G = k_{G0} \exp\left(\frac{T}{k_{G1}}\right) \left(\frac{c}{c_s}\right) \quad (60)$$

**Table 5-3.** Numerical Estimates for variables associated with mass flux of antisolvent and crystal growth

Variable	Numerical Estimate
$D$	$2.2 * 10^{-5} \frac{cm^2}{s}$
$L_C$	40 $\mu m$
$MW_{pva}$	100,000
$t_{MT}$ ( $f_{emul} = 0.25\%$ )	2.68 s
$t_{MT}$ ( $f_{emul} = 1.25\%$ )	2.76 s
$t_G$	3.1 s

**Table 5-3** shows that  $t_{MT}$  is comparable to  $t_G$ , and changing the emulsifier conc from 0.25% to 1.25% does not cause any substantial difference to  $t_{MT}$ . This disproves hypothesis H1 and the only other plausible hypothesis i.e. H2 is selected.

### 5.3.3 Effect of stirring speed

**Figure 5-10a** shows that with increase in rpm of the stirrer, the end-of-batch mean chord length decreases which is substantiated in **Table 5-4**. The average shear rate is related to the impeller rpm according to equation (61), where  $K_s$  is a proportionality constant.  $K_s$  is calculated from equation (62), where  $N_q$  is the impeller pumping number.  $N_q$  is obtained from **Table 5-4** in reference [175] and depends on the Reynolds number, which is obtained from equation (63). For the range of  $Re$  in Table 4 in reference [175],  $N_q=0.35$  and hence  $K_s=2.45$ . This implies the average shear rate scales directly with  $N$ , which is also illustrated in **Table 5-4**. The tip speed of the stirrer is calculated from equation (64).

$$\langle \dot{\gamma} \rangle = K_s N \quad (61)$$

$$K_s = 7N_q \quad (62)$$

$$Re = \frac{ND_s^2}{\nu} \quad (63)$$

$$U_{tip} = \pi D_s N \quad (64)$$

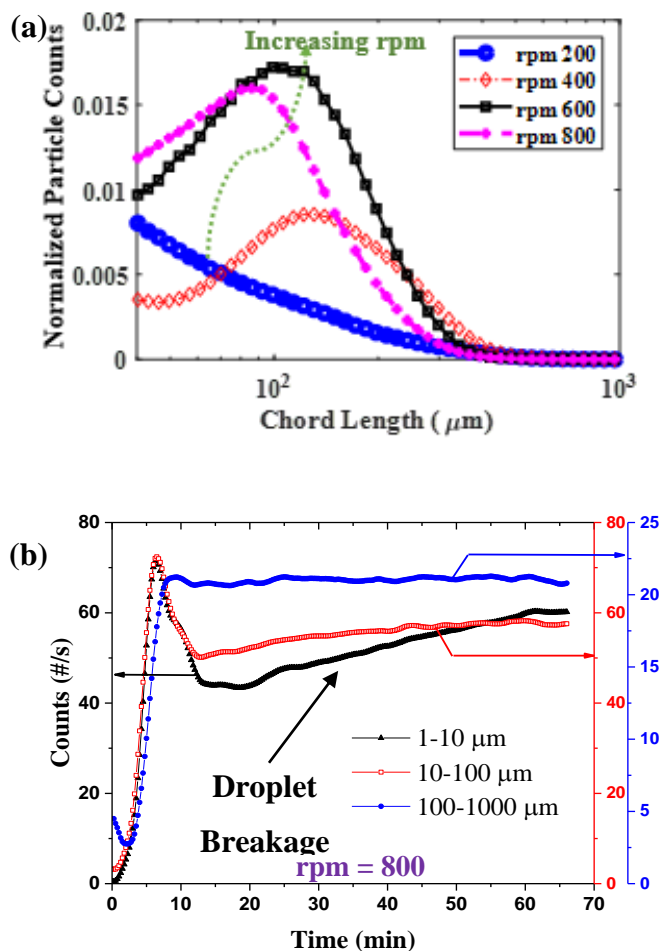


**Figure 5-10.** (a) End-of-batch CLD becomes left skewed with increase in rpm of stirrer, (b) evolution of FBRM counts at higher rpm (800) shows increase of smaller particle counts throughout the batch, which is indicative of droplet breakage in the crystallizer.

**Table 5-4.** End-of-batch Mean Chord Length decreases with increase in stirrer rpm

Stirrer rpm	$U_{tip}$ (cm/s)	Re	$\langle \dot{\gamma} \rangle$ (1/s)	Mean Chord Length ( $\mu\text{m}$ )
400	104.72	1123.6	16.33	142
600	157.08	1658.4	24.5	123
800	209.43	2247.2	32.67	98

Hall et al.[176] showed that the Sauter mean diameter ( $d_{32}$ ) is inversely correlated with the rotor tip speed in in-line rotor-stator mixers, while Farzad et al. [177] showed that  $d_{32}$  is inversely correlated to the average shear rate in the vessel  $\langle \dot{\gamma} \rangle$ . This is related to increased mixing intensity with increase in  $U_{tip}$  and  $\langle \dot{\gamma} \rangle$ , which increases the local disruptive stress on the droplets. For low viscosity liquids, the only opposing cohesive stress ( $\tau_c$ ) originates from the interfacial tension at the droplet interface.  $\tau_c$  is constant at different rpms, thus the net stress at the droplet interface increases with increase in  $U_{tip}$  and  $\langle \dot{\gamma} \rangle$ , which produces smaller droplets.

The increase in the rate of droplet breakage with rpm is substantiated from the FBRM counts in **Figure 5-10b**, which shows the counts in the lower bins progressively increasing with time. This contrasts with **Figure 5-8b**, where the FBRM counts stabilize after 25 minutes, which indicates a stable particle size distribution has been attained in the crystallizer.

#### 5.3.4 Effect of Solvent to Antisolvent Ratio

**Figure 5-11a** shows that as sasr is increased, the final end-of-batch mean chord length of the particles reduces, which is substantiated in **Table 5-5**. At lower sasr = 0.0125, the small-particle (10-100  $\mu m$ ) FBRM counts increase monotonically throughout the batch (**Figure 5-11b**), whereas for higher sasr m= 0.05, the FBRM counts first increases until 12 min followed by decrease until the end-of-batch.

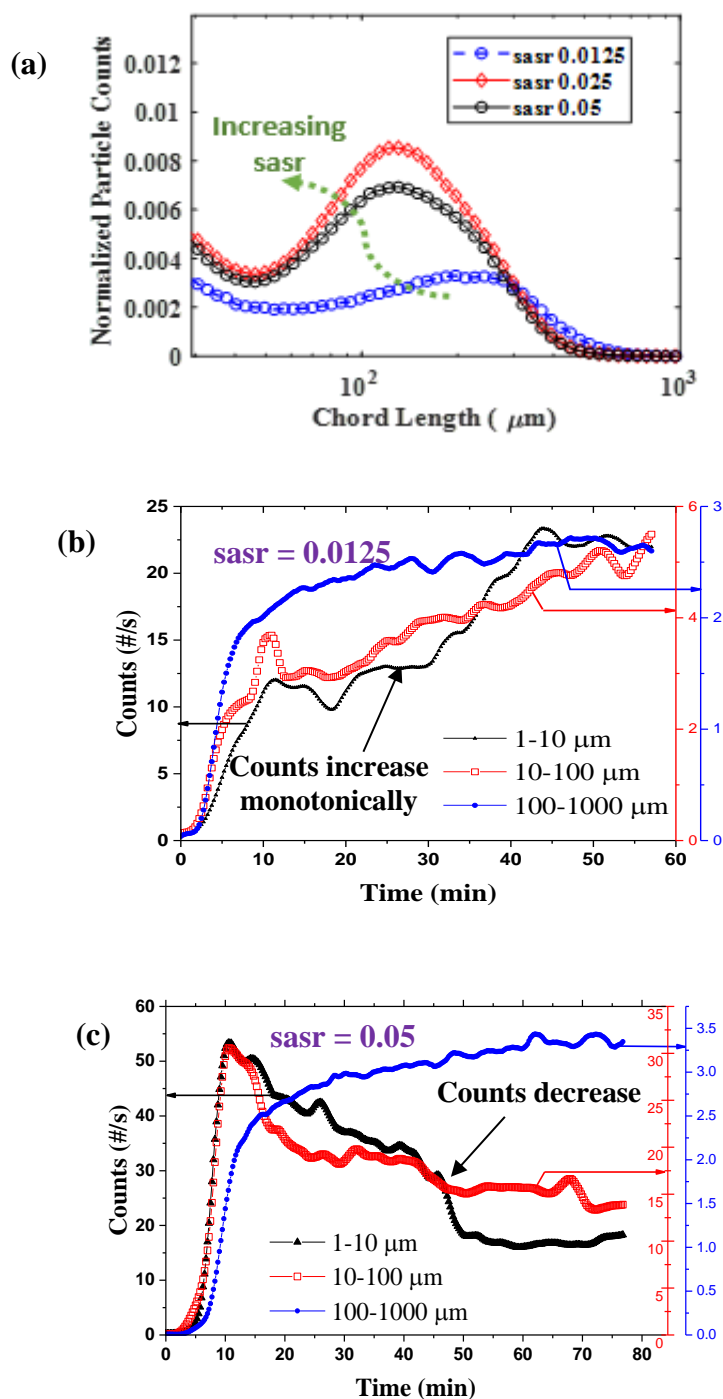


**Figure 5-11.** (a) End-of-batch Chord Length Distribution becomes left skewed with increase in *sasr*; (b) at lower *sasr*, small-particle(10-100  $\mu\text{m}$ ) FBRM counts increase monotonically throughout the batch; (c) at higher *sasr*, FBRM counts first increase but then decrease throughout the batch.

**Table 5-5.** End-of-batch mean chord length decreases with increase in sasr.

sasr	Mean Chord Length ( $\mu\text{m}$ )
0.0125	255
0.025	143
0.05	135

Note that the emulsifier concentration was increased proportionately to the increase in solvent to antisolvent ratio following previous work in literature [148]. Emulsifier attaches to the interface between the droplets and the continuous phase and reduces the interfacial tension. Thus, the emulsifier concentration should have been increased proportional to the increase in surface area of the droplet ( $\Delta S$ ), whereas it was increased proportionately to the increase in droplet volume ( $\Delta V$ ). A hypothetical case of increase in number of droplets is shown in **Figure 5-12a** where the increase in sasr led to an increase in the amount of emulsion droplets. The increase in the number density of emulsion droplets led to an increase in the surface area ( $\Delta S$ ) as well as the volume ( $\Delta V$ ) of the droplets. In equation (65),  $n_1$  and  $n_2$  are the number of droplets before and after increase of sasr and all the droplets are assumed to be monodisperse with radius  $r$ .

$$\begin{aligned}
 \Delta S &= (n_2 - n_1) 4\pi r^2 \\
 \Delta V &= (n_2 - n_1) \frac{4}{3} \pi r^3 \\
 r &\ll 1 \\
 \frac{\Delta S}{\Delta V} &= \frac{3}{r} \gg 1
 \end{aligned}
 \tag{65}$$

However, the increase in droplet surface area is higher than the increase in the droplet volume as shown in equation (65).

Thus at high sasr, the surface area increased more than necessary, whereas the emulsifier amount was not increased proportionately. At high sasr, there is less emulsifier in solution than the nominal case (**Figure 5-12b**). Using equations (49)-(60), the time scales for mass transfer at two representative sasrs are calculated and shown in **Table 5-6**. At low sasr,  $t_{MT} \gg t_G$  and hence the system is mass transfer limited. **Figure 5-13b** illustrates the increasing resistance faced by antisolvent molecules which leads to slower formation of primary crystals within the droplets.

However at a higher sasr (**Figure 5-13a**)  $t_{MT} \approx t_G$ , so there is faster diffusion of antisolvent followed by crystallization of PCs within the droplets.

**Table 5-6.** Timescales of diffusion and primary crystal growth at low and high sasrs.

Variable	Numerical Estimate
$t_{MT}$ (sasr = 0.05)	2.68 s
$t_{MT}$ (sasr = 0.0125)	14.67 s
$t_G$	3.1 s

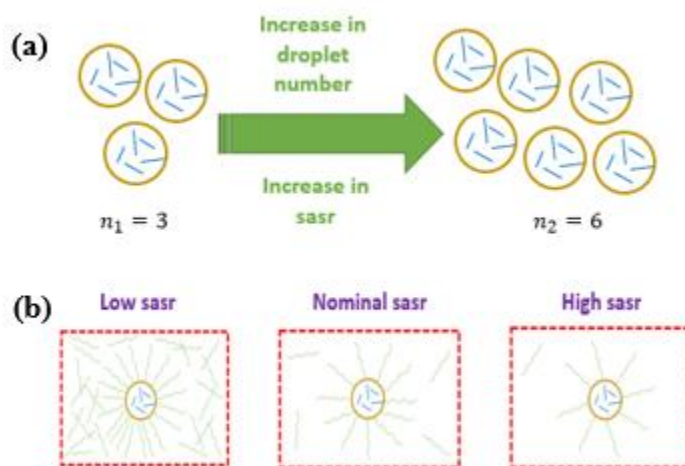


**Figure 5-12.** (a) Increase in sasr leads to an increase in the number of droplets in the crystallizer; (b) at a low sasr, the number number density of emulsifier molecules in solution is higher than nominal, while at high sasr, the number density of emulsifier molecules is lower than nominal.

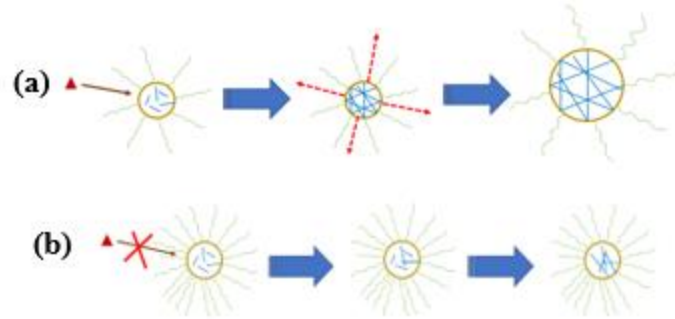


**Figure 5-13.** (a) At higher sasr, the emulsifier concentration is lower than necessary; so the antisolvent diffusion is faster, which causes rapid crystallization and the droplets expand; (b) at lower sasr, the emulsifier concentration is higher than necessary; so the antisolvent diffusion is slower, which causes slower crystallization.

### 5.3.5 Conceptual Model Formulation

The fundamental mechanistic interpretations elucidated in **Sections 5.3.1-5.3.4** opens a new vista of multiscale product and process design. In this paradigm, inferential analytics on real time PAT data is used to design particulate processes starting from the macroscale phenomena to the microscale attributes. Although the PAT guided inferential process understanding (PIPU) developed in this work does not directly give quantitative estimates of primary particles, it can provide valuable information into the development of a mechanistic process model. For brevity, the full mathematical model is not shown here, but will be discussed in detail in a follow-up work. However, for illustration the effect of this inferential mechanistic understanding on the mathematical model development is now elucidated.

A preliminary mechanistic population balance model (PBM) is given in equation (66) which describes the evolution of the droplet size distribution within the crystallizer. The evolution of the crystal population within the individual droplets is taken into consideration via the moments of the population ( $\mu_0, \mu_1, \mu_2, \mu_3$ ).

$$\begin{aligned}
 & \frac{\partial \omega}{\partial t} + \frac{\partial \omega}{\partial \tau} + \frac{\partial}{\partial \bar{C}} (\omega \dot{\bar{C}}) + \frac{\partial}{\partial \bar{C}_{sol}} (\omega \dot{\bar{C}}_{sol}) + \sum_{i=0}^3 \frac{\partial}{\partial \mu_i} (\omega \dot{\mu}_i) + \frac{\partial}{\partial a} (\omega G(a, \mu_0)) \\
 & = \frac{N_0}{\theta} \delta(a - a_0) \delta(\tau) \delta(\bar{C} - \bar{C}_0) \delta(\bar{C}_{sol} - \bar{C}_{sol,0}) + h(\omega, a, \bar{C}, t) \\
 & - \frac{\omega \dot{F}_{sol}}{(V_{sol} + \dot{F}_{sol} t)} (1 - H(t - t_{sol}))
 \end{aligned} \tag{66}$$

Here  $\omega(a, \bar{C}, \bar{C}_{sol}, \mu_i)$  represents the droplet population within the crystallizer where the internal coordinates are the droplet size ( $a$ ), the average API concentration ( $\bar{C}$ ) and solution concentration within the droplets ( $\bar{C}_{sol}$ ) and the moments of the crystal population ( $\mu_i$ ). The function  $h(\omega, a, \bar{C}, t)$  represents the rate of birth and death of droplets due to breakage. The last term represents that the API solution is pumped into the crystallizer only up to a certain time ( $t_{sol}$ ) viz. 10 min in **Figure 5-1c**. An additional term associated with the growth of the droplets, due to stress generated from the primary crystal growth, has also been included in equation (66). The functional dependence  $G(a, \mu_0)$  indicates that the growth rate is dependent on the droplet size as well as the mass of PCs within the droplet.

In equation (66),  $h(\omega, a, \bar{C}, t)$  represents the birth and death of droplets only due to breakage as elucidated in Lam et al. [178] However, as illustrated before, agglomeration of droplets happens at lower emulsifier concentration. Thus, an agglomeration term needs to be introduced for the droplets, in addition to the breakage term, which is illustrated in equation (67).

$$h(\omega, a, \bar{C}, t) = \text{breakage term} + \frac{1}{2} \int_0^a \frac{\beta((a^3 - \lambda^3)^{1/3}, \lambda)}{(a^3 - \lambda^3)^{2/3}} \omega((a^3 - \lambda^3)^{1/3}, t) \omega(\lambda, t) d\lambda - \omega(a, t) \int_0^\infty \beta(a, \lambda) \omega(\lambda, t) d\lambda \quad (67)$$

The rate of agglomeration of two particles is also dependent on the emulsifier concentration in the crystallizer ( $C_e$ ) via equation (68). Here the rate of agglomeration decreases with an increase of emulsifier concentration (**Figure 5-9**), where  $\kappa$  is a scaling constant that needs to be estimated from experimental data.

$$\beta(a, \lambda, C_e) = \beta(a, \lambda, C_{e,0}) \exp\left(-\kappa \frac{C_e}{C_{e,0}}\right) \quad (68)$$

## 5.4 Conclusions

In this work, a systematic study was carried out to gain a fundamental understanding of the mechanistic processes underlying emulsion solvent diffusion. An in-situ PAT tool viz. FBRM was used to gain a mechanistic understanding of the dynamics of antisolvent diffusion and

crystallization within the emulsion droplets. This work proposes a novel framework where dynamical trends in FBRM counts can be used to gain a multiscale understanding of fundamental mechanistic processes happening within the emulsion droplets. The work also promotes a system perturbation approach to process understanding viz. by changing the critical process variables around their nominal values and deconvoluting the underlying process mechanisms from the process dynamics. This approach enabled to identify phenomena, that emerged upon changing the API concentration and emulsifier concentration viz. droplet expansion due to stress from crystals, droplet coalescence, which had not been considered before. A mechanistic process model is proposed and modifications to the process model, due to the enhanced process understanding, are then illustrated. In the next chapter, the full multiscale PBM has been solved for a representative experimental scenario, which will enable rapid process design for new API-excipients formulations in the drug development pipeline.

## 6. MATHEMATICAL MODELING OF EMULSION SOLVENT DIFFUSION FOR SPHERICAL CRYSTALLIZATION: HOW TO DECONVOLUTE PRIMARY CRYSTAL SIZE DISTRIBUTION FROM AGGLOMERATE SIZE DISTRIBUTION?

Reproduced with permission from Kanjakha Pal<sup>+</sup>, Doraiswami Ramkrishna<sup>+</sup>, Zoltan K. Nagy<sup>+</sup>, submitted to *Industrial and Engineering Chemistry Research*, in review.

<sup>+</sup>*Davidson School of Chemical Engineering, Purdue University, West Lafayette.*

### 6.1 Introduction

Pharmaceutical manufacturing (PM) is undergoing an era of rapid change [179]. The cost of pharmaceutical research and development (R&D) has increased significantly [84] over the past decades, however manufacturing innovations have not caught pace to offset this cost increase. Spherical crystallization [145] is a process intensification (PI) strategy, which can lead to significant cost savings. Traditionally, PM first involves drug substance (DS) manufacturing [180] following the sequence of unit operations crystallization [181], filtration [182], drying [183]. This is followed by drug product manufacturing [155] following, for example, the sequence of unit operations milling [184], blending [87], granulation [185] and tableting [186]. The major barrier to integrating DS and DP manufacture was the inability to control the bioavailability [187] and manufacturability [188] simultaneously while crystallizing the active pharmaceutical ingredient (API). Spherical crystallization [116] (SC) produces spherical agglomerates of fine crystals directly within the crystallizer, thereby enabling direct compounding of the drug substance. This also allows to bypass the DP manufacture stages viz. milling, granulation, blending, which substantially reduces the cost of manufacturing.

The US Food and Drug Administration (FDA) has been encouraging pharmaceutical companies to shift from a Quality-by-Testing (QbT) [189] to a Quality by Design (QbD) [190] paradigm. QbD emphasizes enhancing process understanding [159] based on elucidation of the underlying process mechanisms. Mathematical modeling [191] is one of the key enablers of QbD paradigm in PM. Mathematical models enhance process understanding [192] and provide in-silico tools for process optimization [193], which significantly reduces the experimentation cost [194] during drug development. Mathematical models fall into three broad categories – empirical [195], mechanistic [196] and hybrid models [197]. Mechanistic models of particulate processes enable

prediction of the critical quality attributes [159] (CQAs) of the end-of-batch products viz. particle size [198], shape [199] as a function of the critical process parameters [117] (CPPs).

Population balance equations (PBE) [200][30][201] have been widely used to model particulate processes. PBEs can characterize the evolution of the particle size distribution in the crystallizer, one of the most important CQAs of the drug substance (DS). This makes PBEs one of the most effective frameworks to characterize the multiscale evolution of droplet population, along with the crystal population within the droplets. Aamir et al.[202] modeled the dynamic evolution of crystal size distribution of a crystallizer using PBEs. They found that a combined method of moments (MOM) and method of characteristics (MOC) approach was much faster for model-based dynamic optimization of crystallizers. Various numerical methods have also been developed to solve PBEs. Kumar et al.[109] [203] used fixed pivot and moving pivot techniques to solve PBEs incorporating various mechanistic rate processes viz. nucleation, growth and agglomeration. PBEs have also been widely used to model spherical agglomeration unit operation, where particulate agglomeration takes place in suspension [96]. Blandin et al. [9] used PBEs to understand how the timescales of the fundamental mechanistic processes – nucleation, growth and agglomeration affect the product agglomerates. Madec et al. [123] used multi-dimensional agglomeration kernels, which incorporated novel process and product properties viz. bridging liquid concentration, particle size in the model formulation. However, the traditional SA process needs the presence of a binding liquid to agglomerate the crystals. This creates additional problems when a suitable binder-solvent combination is not available.

Emulsion solvent diffusion [204] (ESD) can produce spherical crystals in solution, without the addition of a binder. Kawashima et al. [153] was the first to describe the ESD process where coacervate droplets were gradually converted to pliable beads due to solvent diffusion. Niwa et al. [205] prepared polymer coated microcapsules using a two stage emulsion based process. Khidr et al. [206] prepared sustained release microspheres of meclofenamic acid using ESD. However, although there have been numerous literature reports on experimental work using ESD, mathematical modeling of spherical crystallization using ESD has been relatively rare. The exception was the work by Chang et al. [207] who modeled the pervaporation process of emulsion droplets to produce spherical particles. They compared PBEs to plug flow reactor models and found PBEs to yield better predictions on experimental measurements of PSDs. However, PBEs have been used to model mass transfer in liquid-liquid dispersions, which have many similarities

in the underlying process mechanism with ESD. Some of the earlier works for this purpose [208] considered the inlet dispersion to the reactor to be heterogeneous and used interfacial transport equations to model the mass transfer process. Shah and Ramkrishna [209] were the first to use PBE for modeling mass transfer into the dispersed phase, which took into account the heterogeneity induced in the droplet population due to fundamental rate processes viz. breakage. It was found using PBEs for this purpose significantly improved the model predictability over the previous works, which considered only the rate of interfacial mass transport into the droplets.

In the current work, PBEs have been used to model the multiscale evolution of droplet population and the population of crystals within the droplets during ESD. Method of characteristics [210] have been used to solve the PBEs and the time-course evolution of the size distributions were evaluated. The evolution of the conditional number density of primary crystals within the droplets, given two widely different droplet sizes, was then investigated. The time course of evolution of the API and the solvent concentration within the droplets were also elucidated to investigate the differences in the crystal size distribution for two different droplet sizes.

## 6.2 Theory

### 6.2.1 Process Description

ESD is a particle design methodology to produce spherical crystals directly in the crystallizer. An example process flow diagram of a traditional PM involving a sequence of unit operations is shown in **Figure 6-1a**. The impure API solution coming from upstream processes is first crystallized to remove any impurities. Simultaneously, the crystallization unit operation serves as a particulate design stage to control the product CQAs viz. particle size, shape. This is followed by milling to improve the bioavailability of the dried crystals. These milled crystals are further agglomerated in a granulator along with excipients to improve the downstream manufacturability of the agglomerates. ESD is a one-step method that combines the processes of crystallization, milling, blending and granulation to make spherical co-agglomerates (**Figure 6-1b**) inside the crystallizer, which can be sent directly to the tablet press.

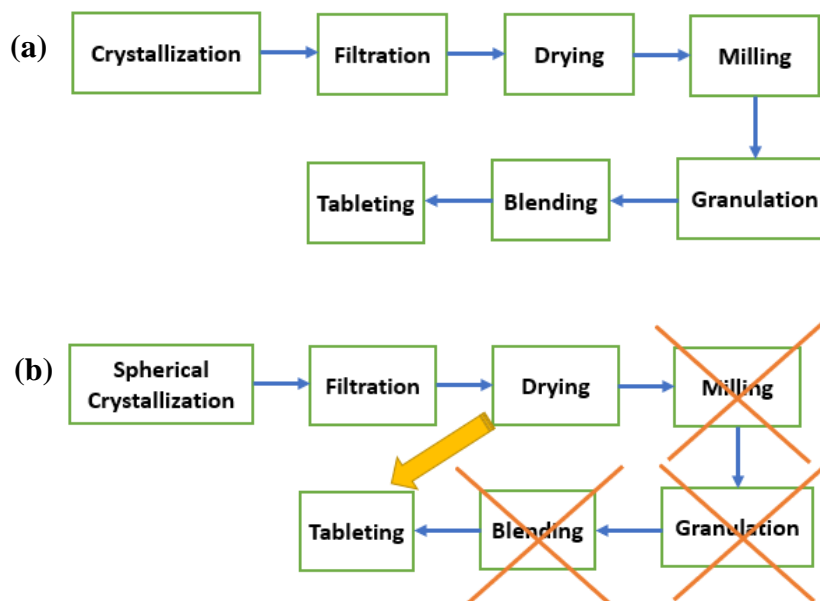


**Figure 6-1.** (a) An example process flow diagram of a traditional PM process for solid oral dosage pharmaceutical manufacturing, where the downstream manufacturing consists of seven unit operations, (b) Proposed process flow diagram of an intensified PM process, where the downstream drug manufacturing consist of only four unit operations. The unit operations milling, granulation and blending have been eliminated and the particle design for producing spherical agglomerates is carried out directly inside the crystallizer.

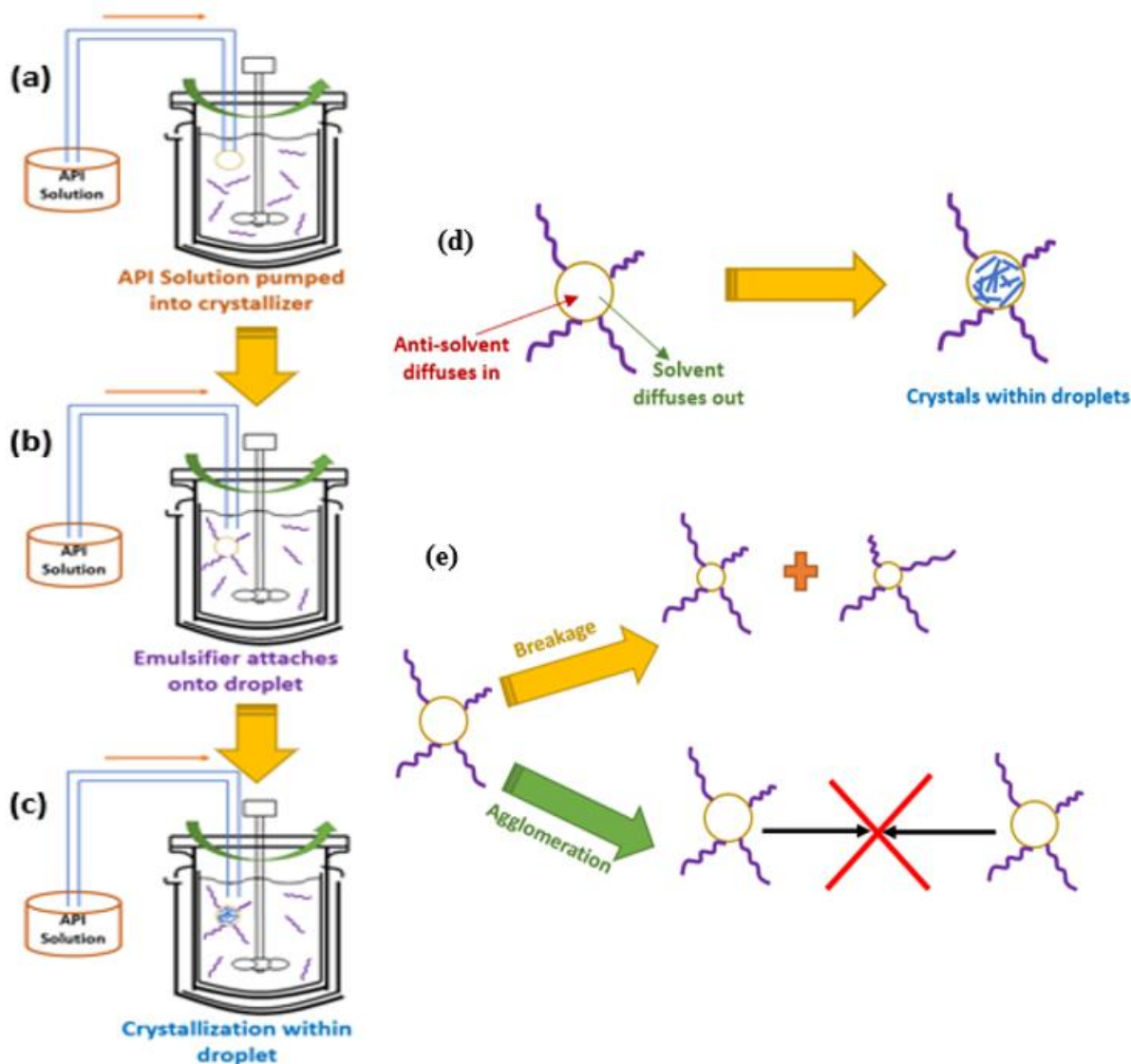


**Figure 6-2.** Process development for SC (a) API solution pumped into crystallizer creates droplet at the nozzle tip (b) Emulsifier attaches to detached droplet interface (c) Crystallization occurs within droplets due to supersaturation generation (d) Due to good miscibility, antisolvent from bulk solution diffuses into droplets while solvent inside droplets diffuses out. Since the API within the droplet is insoluble in the antisolvent, it crystallizes out. (e) Droplet breakage occurs due to collision with the stirrer, however droplet agglomeration is prevented due to emulsifier attached to droplet interface.

**Figure 6-2** shows a process development schema for the SC process. API solution is first pumped into the crystallizer, which contains the emulsifier dissolved in an anti-solvent via a dip-tube. In **Figure 6-2a**, droplets are generated at the nozzle of the dip-tube, with size determined by the diameter of the nozzle tip and the fluid flow conditions in the crystallizer. **Figure 6-2b** shows

the emulsifier in solution attaching to the interface of the detached droplets followed by droplet detachment into the continuous phase (**Figure 6-2c**). Since the solvent within droplets and antisolvent in the bulk phase are miscible, diffusion of solvent from the droplets into the bulk phase starts (**Figure 6-2d**). This is followed by counter-diffusion of the antisolvent into the droplets, which leads to API crystallization within the droplets (**Figure 6-2c-d**). Droplet breakage also occurs inside the reactor due to collision with the stirrer and the walls of the crystallizer (**Figure 6-2e**). However, droplet agglomeration is prevented due to the emulsifier attached to the droplet interface.

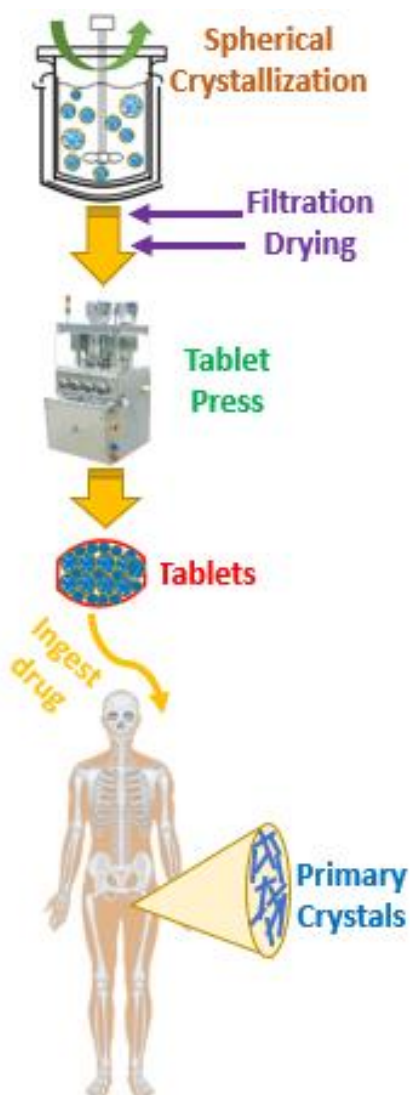


**Figure 6-3.** API tablet produced in the tablet press contains the spherical crystals, which forms the compact tablets due to the compression force exerted by the tablet press. The tablet ingested by the human is broken down in the digestive tract, however the actual bioavailability of the tablets depends on the primary crystal size distribution that forms the agglomerates.

**Figure 6-3** shows the schema of DP formation by SC process, followed by subsequent ingestion into the human body. The spherical crystals from the crystallizer are first filtered and dried and then sent directly to the tablet press, where they are compressed to form tablets. The manufacturability of the tablets in the tablet press is determined by the agglomerate size distribution (ASD). However, the dissolution of the API in the human body is dictated by the size distribution of the primary crystals forming the agglomerates.

Thus, the most important critical quality attributes (CQAs) of the product agglomerates are the agglomerate size distribution (ASD) and the size distribution of the primary crystals (PC) within each agglomerate. However, in-line particulate characterization tools viz. focused beam reflectance measurement (FBRM), particle vision measurement (PVM) and offline characterization tools viz. laser diffraction can only provide information about the ASD. However, real-time measurement of CQAs that control the agglomerate bioavailability remains elusive. This necessitates the use of mechanistic mathematical models, which can provide information about the evolution of the PC size distribution within each agglomerate. The primary focus of this work is to investigate the effect of the droplet size on controlling not just the manufacturability, but also the bioavailability of the product agglomerates.

## 6.2.2 Mathematical Modelling of Spherical Crystallization

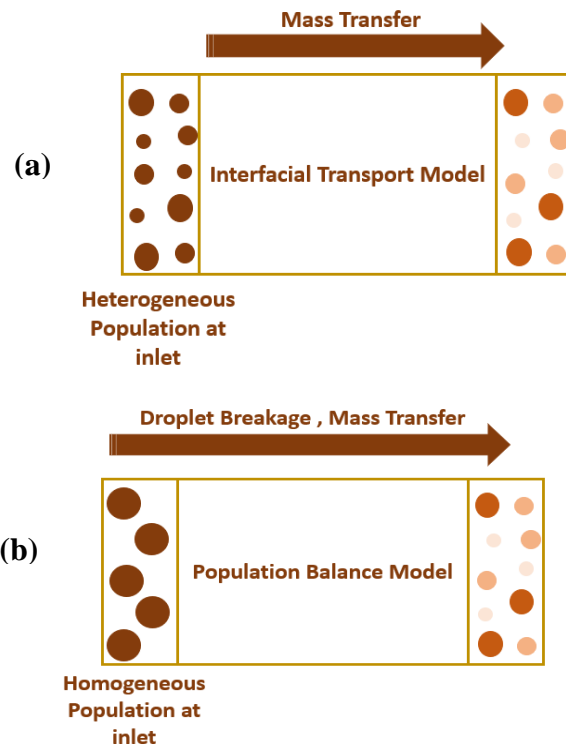


**Figure 6-4.** (a) Interfacial mass transport model, where a heterogeneous droplet population is considered at the reactor inlet (b) Population balance model, where a homogeneous droplet population is considered at the reactor inlet.

**Figure 6-4a-b** show the differences in mass transport between an earlier proposed model viz. Interfacial transport (IT) model (Gal-or et al. [208]) from the PBM (Shah et al.[209] ). For the IT model, a heterogeneous droplet population is considered at the inlet of the reactor. Mass transport of anti-solvent occurs into the droplets, which leads to a progressive depletion of solvent concentration. However, for smaller droplets the rate of transport is higher, which leads to lower solvent concentration at the exit. But for the PBM, all the droplets at the reactor inlet are of the same size. Simultaneous mass transfer of antisolvent and droplet breakage occurs in the crystallizer, which leads to a heterogeneous droplet population at the exit in terms of two internal coordinates viz. droplet size and solvent concentration.

### Assumptions

- (a) The API crystals formed within the droplets are forming compact bonds; however, the agglomeration process of crystals within the droplets is not modeled here.

- (b) The expansion of the droplet interface, due to stress from the growing crystals, is not considered in this model. The size of the final product agglomerates is assumed to be determined by the size of the droplets.
- (c) The emulsifiers attached to the droplet interface are assumed to be removed during the filtration, washing and drying stages and do not end up in the final product agglomerates.

The PBE for the droplet population is given by equation (69). Here  $\omega$  represents the population density of droplets in the crystallizer,  $\tau$  represents the droplet age,  $\bar{C}$  represents the average solute concentration and  $\bar{C}_{sol}$  represents the average solvent concentration within the droplets,  $\mu_i$  represents the  $i$ -th moment of crystal population within the droplets,  $\dot{N}_0$  represents the rate of droplets entering the crystallizer with internal coordinates  $\mathbf{Z}_0 = [a_0 \ 0 \ \bar{C}_0 \ \bar{C}_{sol,0}]$ ;  $h(\omega, a, \bar{C}, t)$  represents the birth and death of droplets due to breakage. The last term comes due to the dilution effect in the crystallizer – for  $t < t_{sol}$  the volume of the solution in the crystallizer keeps changing. The initial solution volume is  $V_{sol}$  (the initial volume of the continuous phase) and the flow rate of API solution into the crystallizer is  $\dot{F}_{sol}$ .

$$\begin{aligned} & \frac{\partial \omega}{\partial t} + \frac{\partial \omega}{\partial \tau} + \frac{\partial}{\partial \bar{C}} (\omega \dot{\bar{C}}) + \frac{\partial}{\partial \bar{C}_{sol}} (\omega \dot{\bar{C}}_{sol}) + \sum_{i=0}^3 \frac{\partial}{\partial \mu_i} (\omega \dot{\mu}_i) \\ & = \dot{N}_0 \delta(a - a_0) \delta(\tau) \delta(\bar{C} - \bar{C}_0) \delta(\bar{C}_{sol} - \bar{C}_{sol,0}) \prod_{i=0}^3 \delta(\mu_i) + h(\omega, a, \bar{C}, t) \\ & \quad - \frac{\omega \dot{F}_{sol}}{(V_{sol} + \dot{F}_{sol} t)} (1 - H(t - t_{sol})) \end{aligned} \quad (69)$$

The population balance equations for the primary crystals within the droplets are given by equations (70)-(73). In equation (73),  $a$  is the droplet size and  $K_{MT}$  is the mass transfer coefficient at the droplet interface.

$$\frac{d\mu_0}{dt} = \dot{B} \quad (70)$$

$$\frac{d\mu_i}{dt} = iG\mu_{i-1} \quad (71)$$

$$\frac{d\bar{C}}{dt} = -3\rho k_v G \mu_2 \quad (72)$$

$$\frac{d\bar{C}_{sol}}{dt} = \frac{k_v \dot{\mu}_3}{1 - k_v \mu_3} \bar{C}_{sol} - 3aK_{MT} \bar{C}_{sol} \quad (73)$$

Equations (2-5) can be solved using an ODE solver provided the initial droplet size distribution (DSD) is known. The challenge comes with solving equation (1), which is an integro-partial differential equation with non-homogeneous terms. In view of this, numerical methods need to be used to solved equations (69)-(73) in a nested manner.

The API supersaturation within the droplet is given by equation (74). The nucleation and growth rates of primary crystals within the droplets are given by equations (75)-(76).

$$S = \frac{\bar{C}V_{sol}}{E} - C_{sat} \quad (74)$$

$$\dot{\mu}_0 = k_{B1} \exp\left(-\frac{C_{sol}}{k_{B2}}\right) S \quad (75)$$

$$G = k_{g0} \exp\left(\frac{T}{k_{g1}}\right) S \quad (76)$$

The right-hand side of equation (1) is redefined as equation (77).

$$\begin{aligned} H(t, \omega, \tau, a, \bar{C}, \bar{C}_{sol}) = & \dot{N}_0 \delta(a - a_0) \delta(\tau) \delta(\bar{C} - \bar{C}_0) \delta(\bar{C}_{sol} - \bar{C}_{sol,0}) \prod_{i=0}^3 \delta(\mu_i) (1 - H(t - t_{sol})) \\ & + h(\omega, a, \bar{C}, t) - \frac{\omega \dot{F}_{sol}}{(V_{sol} + \dot{F}_{sol} t)} (1 - H(t - t_{sol})) \end{aligned} \quad (77)$$

Using equation (77), equation (1) can be now redefined as equation (78).

$$\frac{\partial \omega}{\partial t} + \frac{\partial \omega}{\partial \tau} + \frac{\partial}{\partial \bar{C}} (\omega \dot{\bar{C}}) + \frac{\partial}{\partial \bar{C}_{sol}} (\omega \dot{\bar{C}}_{sol}) + \sum_{i=0}^3 \frac{\partial}{\partial \mu_i} (\omega \dot{\mu}_i) = H(t, \omega, \tau, a, \bar{C}, \bar{C}_{sol}) \quad (78)$$

The internal coordinates of the droplet are represented by a vector  $\mathbf{Z} = [a, \tau, \bar{C}, \bar{C}_{sol}, \mu_0, \mu_1, \mu_2, \mu_3]$  and the number density can now be described by  $\omega = \omega(\mathbf{Z})$ .

The breakage rate of droplets is given by equation (79).

$$h(\omega(\mathbf{Z}), \mathbf{Z}, t) = h^+(\omega(\mathbf{Z}), \mathbf{Z}, t) - h^-(\omega(\mathbf{Z}), \mathbf{Z}, t) \quad (79)$$

where  $h^+(\omega(\mathbf{Z}), \mathbf{Z}, t)$  and  $h^-(\omega(\mathbf{Z}), \mathbf{Z}, t)$  are the rates of birth and death of droplets via breakage given by equations (80)-(81).

$$\begin{aligned} h^+(\omega(\mathbf{Z}), \mathbf{Z}, t) &= h^+(\omega, a, \bar{C}, \bar{C}_{sol}, \mu_i, t) \\ &= 2 \int_0^{a_0} da' \int_0^{\bar{C}_0} d\bar{C}' \int_0^{\bar{C}_{sol,0}} d\bar{C}'_{sol} \int_0^{\mu_{i,0}} d\mu'_i \int_0^\infty d\tau' p(\mathbf{Z}) \Gamma(a', \bar{c}', \bar{c}'_{sol}, \tau', \mu'_i) da' d\bar{c}' d\bar{c}'_{sol} d\mu'_i d\tau' \end{aligned} \quad (80)$$

$$h^-(\omega(\mathbf{Z}), \mathbf{Z}, t) = h^-(\omega, a, \bar{c}, \bar{c}_{sol}, \mu_i, t) = \Gamma(a) \omega(a, \bar{c}, \bar{c}_{sol}, \mu_i, t) \quad (81)$$

Here  $\Gamma(\mathbf{Z})$  represents the rate of breakage of droplets of state  $\mathbf{Z}$  and  $p(\mathbf{Z}, \mathbf{Z}')$  represents the probability of formation of a droplet of state  $\mathbf{Z}$  from a droplet of state  $\mathbf{Z}'$ .

### Further Assumptions

- (a) The rate of breakage of the droplet of state  $\mathbf{Z}$  is assumed to depend only on the droplet size, which is characterized by equation (82).

$$\Gamma(a', \bar{c}', \bar{c}'_{sol}, \tau', \mu'_i) = \Gamma(a') \quad (82)$$

- (b) The droplets break into two equal sized daughter droplets with age 0. The probability of forming daughter droplets is assumed to be independent of the other internal coordinates viz.  $\bar{c}, \bar{c}_{sol}, \mu_i$  given by equation (83). This is a justified assumption since the concentration of the API within the droplets or the population of crystals within the droplets does not affect the droplet collisions, which ultimately is responsible for breakage of the droplets.

$$p(a, \bar{c}, \bar{c}_{sol}, \tau, \mu_i, a', \bar{c}', \bar{c}'_{sol}, \tau', \mu'_i) = 2\delta(\tau)\delta(a - \frac{a'}{2^{1/3}}) \quad (83)$$

Now we simplify some of the term on the LHS of equation (69) viz. equations (84) - (91).

$$\begin{aligned} \frac{\partial}{\partial \bar{C}} (\omega \dot{\bar{C}}) &= \dot{\bar{C}} \frac{\partial \omega}{\partial \bar{C}} + \omega \frac{\partial}{\partial \bar{C}} \left\{ -3\rho k_v k_{g0} \exp\left(\frac{T}{k_{g1}}\right) \left(\frac{\bar{C}V_{sol}}{E} - C_{sat}\right) \mu_2 \right\} \\ &= \dot{\bar{C}} \frac{\partial \omega}{\partial \bar{C}} - 3\rho g k_v \mu_2 k_{g0} \exp\left(\frac{T}{k_{g1}}\right) \frac{V_{sol}}{E} \omega \end{aligned} \quad (84)$$

$$\begin{aligned}
\frac{\partial}{\partial \bar{C}_{sol}}(\omega \dot{\bar{C}}_{sol}) &= \dot{\bar{C}}_{sol} \frac{\partial \omega}{\partial \bar{C}_{sol}} + \omega \frac{\partial \dot{\bar{C}}_{sol}}{\partial \bar{C}_{sol}} \\
&= \dot{\bar{C}}_{sol} \frac{\partial \omega}{\partial \bar{C}_{sol}} + \omega \frac{\partial}{\partial \bar{C}_{sol}} \left( \frac{k_v \dot{\mu}_3}{1 - k_v \mu_3} \bar{C}_{sol} - 3aK_{MT} \bar{C}_{sol} \right) \quad (85)
\end{aligned}$$

$$\begin{aligned}
&= \dot{\bar{C}}_{sol} \frac{\partial \omega}{\partial \bar{C}_{sol}} + \omega \left( \frac{k_v \dot{\mu}_3}{1 - k_v \mu_3} - 3aK_{MT} \right) \\
\frac{\partial}{\partial \mu_0}(\omega \dot{\mu}_0) &= \dot{\mu}_0 \frac{\partial \omega}{\partial \mu_0} + \omega \frac{\partial \dot{\mu}_0}{\partial \mu_0} \quad (86)
\end{aligned}$$

$$\begin{aligned}
\frac{\partial \dot{\mu}_0}{\partial \mu_0} &= \frac{\partial}{\partial \mu_0} \dot{\mu}_0(\bar{C}) \\
&= \frac{\partial}{\partial \bar{C}} \dot{\mu}_0(\bar{C}) \frac{\partial \bar{C}}{\partial \mu_0} \\
&= \frac{\partial}{\partial \bar{C}} \dot{\mu}_0(\bar{C}) \left( - \frac{\frac{d\bar{C}}{dt}}{\frac{d\mu_0}{dt}} \right) \\
&= \frac{\partial}{\partial \bar{C}} \left\{ k_{B1} \exp\left(-\frac{C_{sol}}{k_{B2}}\right) (\bar{C} - C_{sat}) \right\} \left( - \frac{\frac{d\bar{C}}{dt}}{\frac{d\mu_0}{dt}} \right) \\
&= -3 \frac{\rho k_v k_{g0} V_{sol}}{E} \exp\left(\frac{T}{k_{B1}}\right) \quad (87)
\end{aligned}$$

$$\frac{\partial}{\partial \mu_i}(\omega \dot{\mu}_i) = \dot{\mu}_i \frac{\partial \omega}{\partial \mu_i} + \omega \frac{\partial \dot{\mu}_i}{\partial \mu_i} \quad (88)$$

$$\frac{\partial}{\partial \mu_i} \dot{\mu}_i = \frac{\frac{\partial}{\partial L} \dot{\mu}_i}{\frac{\partial}{\partial L} \mu_i} \quad (89)$$

$$\frac{\partial \mu_i}{\partial L} = L'n(L, t) \quad (90)$$

$$\begin{aligned}
\frac{\partial}{\partial L} \dot{\mu}_i &= \frac{\partial}{\partial L} (iG\mu_{i-1}) \\
&= iG \frac{\partial}{\partial L} (\mu_{i-1}) \\
&= iGL^{i-1}n(L,t)
\end{aligned} \tag{91}$$

So, equation (89) now reduces to equation (92).

$$\frac{\partial}{\partial \mu_i} \dot{\mu}_i = \frac{iG}{L} \tag{92}$$

Thus, the LHS of equation (7) can be rewritten as equation (93).

$$\begin{aligned}
&\frac{\partial \omega}{\partial t} + \frac{\partial \omega}{\partial \tau} + \frac{\partial}{\partial \bar{C}} (\omega \dot{\bar{C}}) + \frac{\partial}{\partial \bar{C}_{sol}} (\omega \dot{\bar{C}}_{sol}) + \sum_{i=0}^3 \frac{\partial}{\partial \mu_i} (\omega \dot{\mu}_i) \\
&= \frac{\partial \omega}{\partial t} + \frac{\partial \omega}{\partial \tau} + \dot{\bar{C}} \frac{\partial \omega}{\partial \bar{C}} + \dot{\bar{C}}_{sol} \frac{\partial \omega}{\partial \bar{C}_{sol}} + \sum_{i=0}^3 \dot{\mu}_i \frac{\partial \omega}{\partial \mu_i} \\
&+ \omega \left[ -3\rho g k_v k_g (\bar{C} - \bar{C}_{sat})^{g-1} \mu_2 + \frac{3k_v G \mu_2}{1 - k_v \mu_3} - 3aK_{MT} + \sum_{i=1}^3 \frac{iG}{L} + \frac{6\rho_v k_g G \mu_2}{\ln^3\left(\frac{\bar{C}}{C_{sat}}\right) C_{sat}} \right]
\end{aligned} \tag{93}$$

Thus, using equations (84)-(92), equation (93) can be reduced to equation (94).

$$\begin{aligned}
&\frac{\partial \omega}{\partial t} + \frac{\partial \omega}{\partial \tau} + \dot{\bar{C}} \frac{\partial \omega}{\partial \bar{C}} + \dot{\bar{C}}_{sol} \frac{\partial \omega}{\partial \bar{C}_{sol}} + \sum_{i=0}^3 \dot{\mu}_i \frac{\partial \omega}{\partial \mu_i} \\
&= \delta(\tau) [\dot{N}_0 \delta(a - a_0) \delta(\tau) \delta(\bar{C} - \bar{C}_0) \delta(\bar{C}_{sol} - \bar{C}_{sol,0}) \prod_{i=0}^3 \delta(\mu_i) (1 - H(t - t_{sol})) \\
&+ 2 \int_a^{a_0} \int_0^\infty \Gamma(a') \delta\left(a - \frac{a'}{2^{1/3}}\right) \omega(a', \bar{C}, \bar{C}_{sol}, \tau', \mu_i) da' d\tau'] \\
&- \left[ \Gamma(a) - 3\rho g k_v \mu_2 k_{g0} \exp\left(\frac{T}{k_{g1}}\right) \frac{V_{sol}}{E} + \frac{3k_v G \mu_2}{1 - k_v \mu_3} - 3aK_{MT} + \right. \\
&\left. \sum_{i=1}^3 \frac{iG}{L} - 3 \frac{\rho k_v k_{g0} V_{sol}}{E} \exp\left(\frac{T}{k_{B1}}\right) + \frac{\dot{F}_{sol} (1 - H(t - t_{sol}))}{(V_{sol} + \dot{F}_{sol} t)} \right] \omega
\end{aligned} \tag{94}$$

Equation (94) can now be rewritten as equation (95).

$$\begin{aligned}
& \frac{\partial \omega}{\partial t} + \frac{\partial \omega}{\partial \tau} + \dot{\bar{C}} \frac{\partial \omega}{\partial \bar{C}} + \dot{\bar{C}}_{sol} \frac{\partial \omega}{\partial \bar{C}_{sol}} + \sum_{i=0}^3 \dot{\mu}_i \frac{\partial \omega}{\partial \mu_i} \\
& = - \left[ \Gamma(a) - 3\rho g k_v \mu_2 k_{g0} \exp\left(\frac{T}{k_{g1}}\right) \frac{V_{sol}}{E} + \frac{3k_v G \mu_2}{1 - k_v \mu_3} - 3aK_{MT} + \sum_{i=1}^3 \frac{iG}{L} \right. \\
& \quad \left. - 3 \frac{\rho k_v k_{g0} V_{sol}}{E} \exp\left(\frac{T}{k_{B1}}\right) + \frac{\dot{F}_{sol}(1 - H(t - t_{sol}))}{(V_{sol} + \dot{F}_{sol}t)} \right] \omega
\end{aligned} \tag{95}$$

with the boundary condition given by equation (96).

$$\begin{aligned}
& \omega(a, \bar{C}, \bar{C}_{sol}, \dot{\mu}_i, \tau = 0, t) = \omega(\mathbf{Z}_{\tau,t}, \tau = 0, t) \\
& = \dot{N}_0 \delta(a - a_0) \delta(\tau) \delta(\bar{C} - \bar{C}_0) \delta(\bar{C}_{sol} - \bar{C}_{sol,0}) \prod_{i=0}^3 \delta(\mu_i) (1 - H(t - t_{sol})) \\
& + 2 \int_a^{a_0} \int_0^\infty \Gamma(a') \delta\left(a - \frac{a'}{2^{1/3}}\right) \omega(a', \bar{C}, \bar{C}_{sol}, \tau', \mu_i) da' d\tau'
\end{aligned} \tag{96}$$

The initial condition is given by equation (97)

$$\omega(a, \bar{C}, \bar{C}_{sol}, \dot{\mu}_i, \tau, t = 0) = \omega(\mathbf{Z}_{\tau,t}, \tau, t = 0) = 0 \tag{97}$$

Using method of characteristics (MOC), the characteristic curve is identified by the set of ordinary differential equations (98).

$$\begin{aligned}
& \frac{dt}{ds} = 1 \\
& \frac{d\tau}{ds} = 1 \\
& \frac{d\bar{C}_{sol}}{ds} = \dot{\bar{C}}_{sol} \\
& \frac{d\bar{C}}{ds} = \dot{\bar{C}} \\
& \frac{d\mu_i}{ds} = \dot{\mu}_i, i = 0, \dots, 3
\end{aligned} \tag{98}$$

Equation (95) now can be modified to equation (99).

$$\frac{d\omega}{ds} = - \left[ \begin{array}{c} \Gamma(a) - 3\rho g k_v \mu_2 k_{g0} \exp\left(\frac{T}{k_{g1}}\right) \frac{V_{sol}}{E} + \frac{3k_v G \mu_2}{1 - k_v \mu_3} - 3aK_{MT} + \sum_{i=1}^3 \frac{iG}{L} \\ -3 \frac{\rho k_v k_{g0} V_{sol}}{E} \exp\left(\frac{T}{k_{B1}}\right) + \frac{\dot{F}_{sol} (1 - H(t - t_{sol}))}{(V_{sol} + \dot{F}_{sol} t)} \end{array} \right] \omega \quad (99)$$

The solution of equation (99) along the characteristics now becomes equation (100), while the solution of equation (98) is given by equations (101)-(102).

$$\omega[s] = \omega_0 \exp \left( \int_0^s - \left[ \begin{array}{c} \Gamma(a) - 3\rho g k_v \mu_2 k_{g0} \exp\left(\frac{T}{k_{g1}}\right) \frac{V_{sol}}{E} + \frac{3k_v G \mu_2}{1 - k_v \mu_3} - 3aK_{MT} + \sum_{i=1}^3 \frac{iG}{L} \\ -3 \frac{\rho k_v k_{g0} V_{sol}}{E} \exp\left(\frac{T}{k_{B1}}\right) + \frac{\dot{F}_{sol} (1 - H(t - t_{sol}))}{(V_{sol} + \dot{F}_{sol} t)} \end{array} \right] ds' \right) \quad (100)$$

$$\tau = \tau_0 + s \quad (101)$$

$$t = t_0 + s \quad (102)$$

The initial condition is given by at  $s = 0$  ,  $t = t_0$  ,  $\tau = \tau_0$  ,  $\omega = \omega_0$  where

$$\omega_0 = \omega(a, \bar{C}, \bar{C}_{sol}, \mu_i, \tau_0, t_0) \quad (103)$$

Equation (101) can now be reduced to equations (104)-(105).

$$\tau = \tau_0 + s = \tau_0 + t - t_0 \quad (104)$$

$$t_0 = \tau_0 + t - \tau \quad (105)$$

For  $\tau > t$  , the curve traces back to  $t=0$ , which is the Initial Condition.

For  $\tau < t$  , the curve traces back to  $\tau = 0$  , which is the Boundary Condition.

This is shown schematically in **Figure 6-5**.

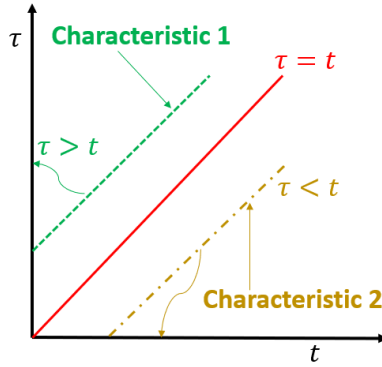


**Figure 6-5.** Characteristic curves for solution of the population balance equations for droplet size distribution. When the droplet age  $\tau < t$  (time), the characteristic curve falls to  $\tau=0$  and the problem reduces to solving the boundary value problem. However, then  $\tau > t$ , the characteristic curve falls to  $t=0$  and the problem reduces to solving the Initial Value Problem.

From equation (105), if  $\tau = \tau'$ , then  $t' = \tau' + t - \tau$ .

Thus, if  $t' = 0$ , then  $\tau' = \tau - t$  and if  $t' = t$ , then  $\tau' = \tau$ .

Equation (100) is now redefined as equation (106) where the integrand is given by  $\beta(\tau', t')$ .

$$\begin{aligned} \omega(\mathbf{Z}_{t,\tau}, t, \tau) &= \begin{cases} \omega(\mathbf{Z}_{t,\tau}, t' = 0, \tau') \exp\left(-\int_{\tau-t}^{\tau} \beta(\tau', t') d\tau'\right), t \leq \tau \\ \omega(\mathbf{Z}_{t,\tau}, t', \tau' = 0) \exp\left(-\int_0^{\tau} \beta(\tau', t') d\tau'\right), \tau \leq t \end{cases} \\ &= \begin{cases} \omega(\mathbf{Z}_{t,\tau}, t' = 0, \tau - t) \exp\left(-\int_{\tau-t}^{\tau} \beta(\tau', \tau' + t - \tau) d\tau'\right), t \leq \tau \\ \omega(\mathbf{Z}_{t,\tau}, t - \tau, \tau' = 0) \exp\left(-\int_0^{\tau} \beta(\tau', \tau' + t - \tau) d\tau'\right), \tau \leq t \end{cases} \end{aligned} \quad (106)$$

The boundary condition (96) now reduces to equation (107).

$$\begin{aligned} \omega(\mathbf{Z}_{t,\tau}, \tau = 0, t) &= \frac{N_0}{\theta} \delta(a - a_0) \delta(\tau) \delta(\bar{C} - \bar{C}_0) \delta(\bar{C}_{sol} - \bar{C}_{sol,0}) \prod_{i=0}^3 \delta(\mu_i) (1 - H(t - t_{sol})) \\ &+ 2 \int_a^{a_0} \int_0^{\infty} \Gamma(a') \delta\left(a - \frac{a'}{2^{1/3}}\right) \omega(a', \bar{C}, \bar{C}_{sol}, \tau', \mu_i) da' d\tau' \\ &= \alpha(t) + 2 \int_a^{a_0} \int_0^{\infty} \Gamma(a') \delta\left(a - \frac{a'}{2^{1/3}}\right) \omega(a', \bar{C}, \bar{C}_{sol}, \tau', \mu_i) da' d\tau' \end{aligned} \quad (107)$$

$\omega(\mathbf{Z}_{t,\tau}, \tau = 0, t)$  is now redefined according to equation (108)-(109).

$$\omega(\mathbf{Z}_{t,\tau}, \tau = 0, t) = h(\mathbf{Z}_{t,\tau}, t) \quad (108)$$

$$\begin{aligned} h(\mathbf{Z}_{t,\tau}, t) &= \alpha(t) + 2 \int_a^{a_0} \int_0^t \Gamma(a') \delta(a - \frac{a'}{2^{1/3}}) \omega(a', \bar{C}, \bar{C}_{sol}, \tau', \mu_i) \omega(\mathbf{Z}_{t,\tau}, t, \tau) da' d\tau' \\ &\quad + 2 \int_a^{a_0} \int_t^\infty \Gamma(a') \delta(a - \frac{a'}{2^{1/3}}) \omega(a', \bar{C}, \bar{C}_{sol}, \tau', \mu_i) \omega(\mathbf{Z}_{t,\tau}, t, \tau) da' d\tau' \\ &= \alpha(t) + \int_a^{a_0} \int_0^t \omega(\mathbf{Z}_{t,\tau}, 0, t - \tau) [2\Gamma(a') \delta(a - \frac{a'}{2^{1/3}}) \exp\left(-\int_0^\tau \beta(\tau', \tau' + t - \tau) d\tau'\right)] da' d\tau' \\ &\quad + \int_a^{a_0} \int_t^\infty \omega(\mathbf{Z}_{t,\tau}, \tau - t, 0) [2\Gamma(a') \delta(a - \frac{a'}{2^{1/3}}) \exp\left(-\int_{\tau-t}^\tau \beta(\tau', \tau' + t - \tau) d\tau'\right)] da' d\tau' \end{aligned} \quad (109)$$

From equation (108), we can now get equation (110).

$$h(\mathbf{Z}_{t,\tau}, t - \tau) = \omega(\mathbf{Z}_{t,\tau}, \tau = 0, t - \tau) \quad (110)$$

The integral kernel in equation (109) is now redefined as equation (111) and an additional integral term is defined according to equation (112).

$$K(t, \tau, a, a') = 2\Gamma(a') \delta(a - \frac{a'}{2^{1/3}}) \exp\left(-\int_0^\tau \beta(\tau', \tau' + t - \tau) d\tau'\right) \quad (111)$$

$$G(t) = 2 \int_a^{a_0} \int_t^\infty \omega(\mathbf{Z}_{t,\tau}, \tau - t, 0) \Gamma(a') \delta(a - \frac{a'}{2^{1/3}}) \exp\left(-\int_{\tau-t}^\tau \beta(\tau', \tau' + t - \tau) d\tau'\right) da' d\tau' \quad (112)$$

Equation (109) now gets redefined to equation (113):

$$h(\mathbf{Z}_{t,\tau}, t) = \alpha(t) + \int_a^{a_0} da' \int_0^t d\tau h(\mathbf{Z}_{t,\tau}, t - \tau) K(t, \tau, a, a') + G(t) \quad (113)$$

Equation (113) is solved by the method of successive approximations[30] viz.

- (1) Initiate  $h^{(0)}(\mathbf{Z}_{t,\tau}, t) = G(t)$
- (2) Iteratively solve equation (114) until convergence between two successive iterations.

$$h^{(n+1)}(\mathbf{Z}_{t,\tau}, t) = \alpha(t) + \int_a^{a_0} da' \int_0^t d\tau h^{(n)}(\mathbf{Z}_{t,\tau}, t - \tau) K(t, \tau, a, a') + G(t) \quad (114)$$

A further simplification is made to the initial condition viz. equation (115) which indicates that there are no droplets initially in the crystallizer.

$$\begin{aligned}\omega(\mathbf{Z}_{\tau,t}, \tau, t=0) &= 0 \\ \Rightarrow G(t) &= 0\end{aligned}\quad (115)$$

Thus the integral equation (113) gets modified to equation (116).

$$\begin{aligned}h(\mathbf{Z}_{t,\tau}, t) &= \alpha(t) + \int_0^{a_0} da' \int_0^t d\tau h(\mathbf{Z}_{t,\tau}, t-\tau) K(t, \tau, a, a') \\ &= \alpha(t) + \int_0^{a_0} da' \int_0^t d\tau h(a', \bar{C}, \bar{C}_{sol}, \mu_i, t-\tau) 2\Gamma(a') \delta\left(a - \frac{a'}{2^{1/3}}\right) \exp\left(-\int_0^\tau \beta(\tau', \tau' + t - \tau, a') d\tau'\right) \\ &= \alpha(t) + 2 \int_0^{a_0} da' \delta\left(2^{1/3} a - a'\right) \left\{ \int_0^t d\tau h(a', \bar{C}, \bar{C}_{sol}, \mu_i, t-\tau) \Gamma(a') \exp\left(-\int_0^\tau \beta(\tau', \tau' + t - \tau, a') d\tau'\right) \right\} \\ &= \alpha(t) + 2 \int_0^\infty da' \delta\left(2^{1/3} a - a'\right) \left\{ \int_0^t d\tau h(a', \bar{C}, \bar{C}_{sol}, \mu_i, t-\tau) \Gamma(a') \exp\left(-\int_0^\tau \beta(\tau', \tau' + t - \tau, a') d\tau'\right) \right\} \\ &= \alpha(t) + 2\Gamma\left(2^{1/3} a\right) \int_0^t d\tau h\left(2^{1/3} a, \bar{C}, \bar{C}_{sol}, \mu_i, t-\tau\right) \exp\left(-\int_0^\tau \beta(\tau', \tau' + t - \tau, 2^{1/3} a) d\tau'\right)\end{aligned}\quad (116)$$

### 6.2.3 Crystal agglomeration within droplets

The PCs within the droplets can also agglomerate as the batch progresses, which increases the mean size of the PCs. The evolution of the number density of the crystal population within the droplets is given by equation (117). Here  $n_{pc}$  is the number density of primary crystals and  $\beta(L, \lambda)$  represents the agglomeration kernel given by the constant kernel viz. equation (118). It is to be noted that no distinction has been made between the un-agglomerated and agglomerated crystal populations within the droplets viz.  $n_{pc}$  characterizes both the agglomerated and un-agglomerated primary crystal populations within a droplet.

$$\frac{\partial n_{pc}(L)}{\partial t} + \frac{\partial(Gn_{pc}(L))}{\partial L} = \dot{B}\delta(L) + \frac{L^2}{2} \int_0^L \frac{\beta\left(\left(L^3 - \lambda^3\right)^{1/3}, \lambda\right)}{\left(L^3 - \lambda^3\right)^{2/3}} n_{pc}\left(\left(L^3 - \lambda^3\right)^{1/3}\right) n_{pc}(\lambda) d\lambda \quad (117)$$

$$- n_{pc}(L) \int_0^\infty \beta(L, \lambda) n_{pc}(\lambda) d\lambda$$

$$\beta(L, \lambda) = \beta_0 \quad (118)$$

Equation (117) can be solved using the method of finite volume [109]. However, since only the moments of the primary crystal population are of concern, equation (118) can be

converted to equation in terms of moments viz. equation (119). The quadrature method of moments [211] approximation is used to approximate the set of moments viz. equation (120).

$$\mu_k(t) = \int_0^{\infty} n_{pc}(L) L^k dL \quad (119)$$

$$\mu_k = \sum_{i=1}^{N_{pc}} w_i L_i^k \quad (120)$$

The equations for the moment of the crystal population within the droplets viz. equations (70)-(72) are now modified to equations (121)-(123).

$$\frac{d\mu_k}{dt} = k \sum_{i=1}^{N_{pc}} w_{pc,i} L_i^{k-1} G + \delta(k) \dot{B} - D_{agg}(k) + B_{agg}(k) \quad (121)$$

$$B_{agg}(k) = \frac{1}{2} \sum_{i=1}^{N_{pc}} w_i \sum_{j=1}^{N_{pc}} w_j (L_i^3 + L_j^3)^{\frac{k}{3}} \beta(L_i, L_j) \quad (122)$$

$$D_{agg}(k) = \sum_{i=1}^{N_{pc}} w_i L_i^k \sum_{j=1}^{N_{pc}} w_j \beta(L_i, L_j) \quad (123)$$

#### 6.2.4 Conditional Density Distributions

*Conditional number density of primary crystals within droplets*

Equation (116) gives the evolution of the droplet number density as a function of time, which is a multi-dimensional distribution. But our real interest lies in being able to predict the conditional CSD given a particular droplet size, at the final batch time viz. equation (124).

$$\omega(\mu_0, \mu_1, \mu_2, \mu_3, t | a) = \frac{\omega(\mu_0, \mu_1, \mu_2, \mu_3, a, t)}{\omega(a, t)} \quad (124)$$

The conditional densities are given by equations (125)-(126).

$$\omega(\mu_0, \mu_1, \mu_2, \mu_3, a, t) = \int_0^{\bar{C}_m} \int_0^{\bar{C}_{sol,in}} \int_0^{\tau_{max}} h(Z_{t,\tau}, \tau, t) d\bar{C} d\bar{C}_{sol} d\tau \quad (125)$$

$$\omega(a, t) = \prod_{i=0}^3 \int_0^{\mu_i} \int_0^{\bar{C}_m} \int_0^{\bar{C}_{sol,in}} \int_0^{\tau_{max}} h(Z_{t,\tau}, \tau, t) d\bar{C} d\bar{C}_{sol} d\mu_i \quad (126)$$

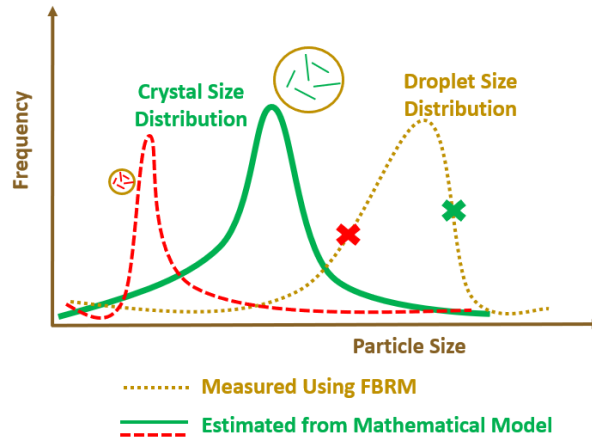


**Figure 6-6.** DSD can be reconstructed from the FBRM measurements, while the CSD within the droplets need to be estimated from a mathematical model. The CSD depends on the droplet size and is very different (green and red curves) for different droplet sizes.

#### Conditional concentration Evolution

The evolution of the API concentration, given a droplet size, is given by equation (127).

$$\omega(\bar{C}, t | a) = \frac{\omega(\bar{C}, a, t)}{\omega(a, t)} \quad (127)$$

The joint pdf in the numerator of equation (127) is given by equation (128) while the denominator is given by equation (126).

$$\omega(\bar{C}, a, t) = \int_0^{\bar{C}_{sol, in}} \int_0^{\tau_{max}} \int_0^{\mu_{0, in}} \int_0^{\mu_{1, in}} \int_0^{\mu_{2, in}} \int_0^{\mu_{3, in}} h(Z_{t, \tau}, \tau, t) d\bar{C}_{sol} d\tau d\mu_0 d\mu_1 d\mu_2 d\mu_3 \quad (128)$$

The evolution of the mean API concentration within the droplet, given a particular droplet size, is then given by equation (129).

$$\bar{C}_{avg}(t | a) = \int_0^{\bar{C}_{max}} \bar{C} \omega(\bar{C}, t | a) d\bar{C} \quad (129)$$

The evolution of the mean antisolvent concentration within the droplet is similarly given by equation (130).

$$\bar{C}_{sol, avg}(t | a) = \int_0^{\bar{C}_{sol, max}} \bar{C}_{sol} \omega(\bar{C}_{sol}, t | a) d\bar{C}_{sol} \quad (130)$$

A summary of the important steps involved for solution of the multiscale PBEs is shown in **Figure 6-7**.

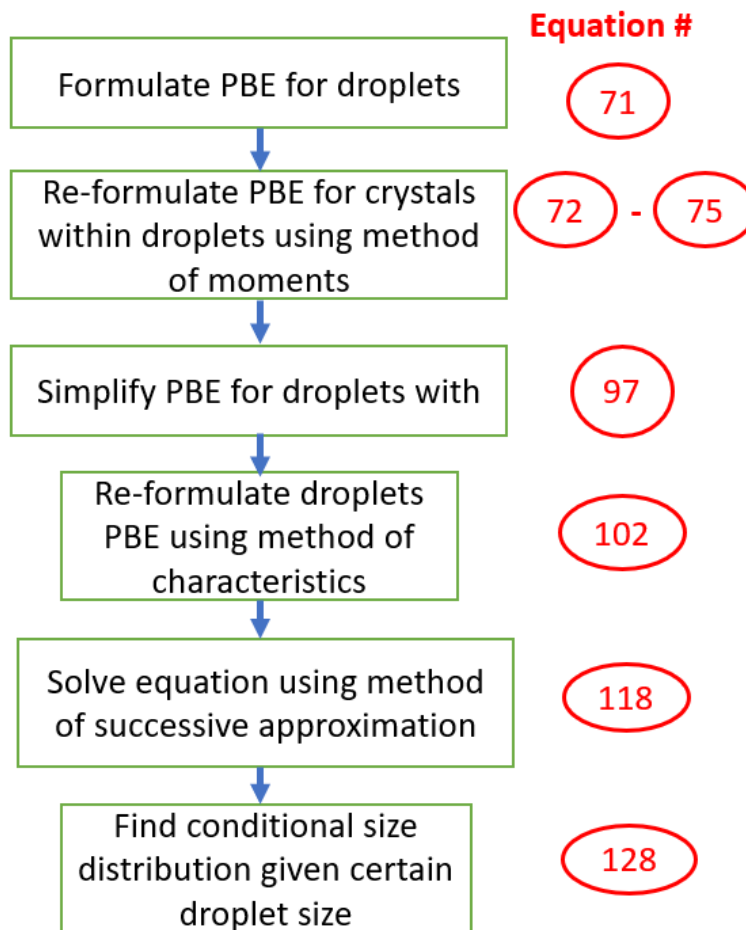


**Figure 6-7.** Summary of important steps for solving multiscale PBEs.

### 6.3 Results and Discussions

The model API was ibuprofen, with ethanol as the solvent and water as the antisolvent. The solubility data and the kinetic parameters associated with nucleation and growth of PCs were taken from Rashid et al.[47][48] and are shown in **Table 6-1**, along with the process parameters.

**Table 6-1.** Kinetic and process parameters associated with spherical crystallization.

Parameter	Numerical value
$k_{B1}$	$4.2 \times 10^9 \text{ \#/ cm}^3 / \text{min}$
$k_{B2}$	0.12
$k_{g0}$	$4.8 \times 10^{-4} \text{ cm / min}$
$k_{gl}$	29
$\dot{F}_{sol}$	5 mL/min
$V_{sol}$	400 mL
$\dot{N}_0$	100 /min
$\bar{C}_0$	0.5 g/mL
$\bar{C}_{sol,0}$	1 g/g
$T$	25 °C
$\rho$	1.03 g/cc
$K_{MT}$	$0.01 \text{ \#/ cm / min}$
$\beta_0$	$0.3 \times 10^{-6}$
$a_0$	330 $\mu\text{m}$
$t_{sol}$	20 min

### 6.3.1 Effect of droplet size (r) on primary crystal number densities at different times

**Figure 6-8a** shows the evolution of the particle size distribution (PSD) within the droplets over the batch for a smaller droplet of radius  $r = 20 \mu\text{m}$ . Before  $t = 12.5 \text{ min}$ , diffusion of antisolvent occurs into the droplets from the bulk phase, along with a simultaneous counter-diffusion of solvent into the bulk phase. This leads to supersaturation generation in the droplets since the API is immiscible in the antisolvent. Primary nucleation takes place around  $t = 12 \text{ min}$  followed by crystal growth from 12-27 min. However, the entire supersaturation is depleted during this time

period, which leads to negligible crystal growth during 27-120 min. This is reflected in the similar size distributions at  $t=27$  min and 120 min. **Figure 6-8b** shows the evolution of the PSD for a larger droplet. Due to the large droplet size, the supersaturation takes much longer to generate, within the droplet which is reflected in the late onset of nucleation at  $t = 29$  min. The rate of nucleation is also much lower, which is reflected in the lower number density of crystals in **Figure 6-8b** ( $\sim 2000$ - $5000$ ) compared to **Figure 6-8a** ( $\sim 10^5$ ). However, the crystal growth rates are now much higher, which is reflected in the gradual right shifting of the number density distribution throughout the batch. The final PSD in **Figure 6-8b** has a much higher mean crystal size ( $\sim 98 \mu\text{m}$ ) compared to **Figure 6-8a** ( $\sim 27 \mu\text{m}$ ), which leads to larger primary crystals for larger droplets.

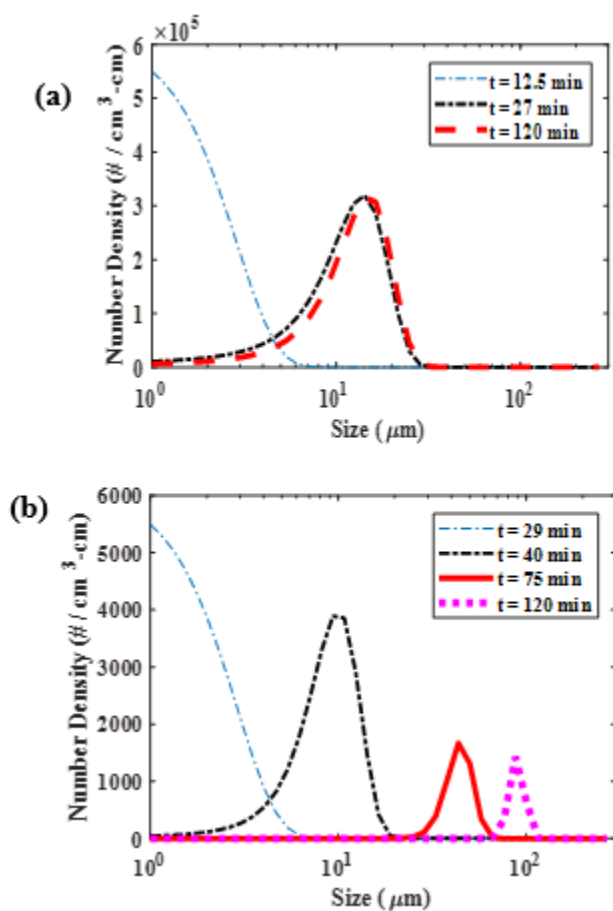


**Figure 6-8.** Particle size distribution for (a) smaller droplet of radius  $20 \mu\text{m}$ ; (b) larger droplet of radius  $240 \mu\text{m}$ . This illustrates that smaller droplets have higher nucleation rates of primary crystals, which produces smaller particles at the end of the batch. For larger droplets, thenucleation rates are lower and the crystallization process is growth dominated, which produces larger primary crystals at the end of the batch.

Conditional concentration evolution as a function of time in the phase diagram

**Figure 6-9** shows the concentration evolution throughout the batch for two droplet radii. For smaller radius of 20  $\mu\text{m}$ , there is rapid concentration drop around 12.5 min due to rapid nucleation.

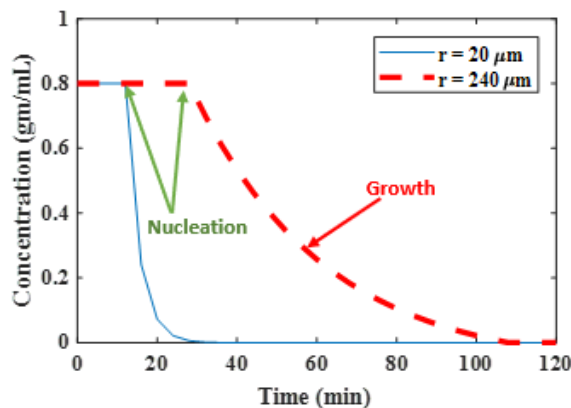


**Figure 6-9.** Concentration evolution during the batch for two different droplet radii. For smaller droplet, the concentration rapidly decreases around 12.5 min due to high rates of primary nucleation.

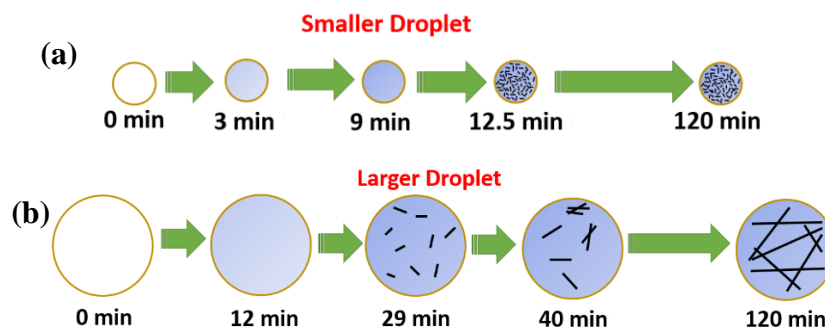


**Figure 6-10.** (a) For smaller droplets, rapid antisolvent diffusion into the droplet during 0-9 min creates high supersaturation which leads to high rate of primary nucleation at 12.5 min. However, the crystal growth rate is much lower which produces smaller Primary Crystals at the end of the process (b) For larger droplet, antisolvent diffusion is much slower which generates supersaturation more slowly. At 29 min, nucleation of primary crystals is triggered followed by crystal growth over the entire batch which produces larger end-of-batch primary crystals.

A process schema shown in **Figure 6-10a** illustrates the mechanistic processes within the droplets. From  $t = 0$ -9 mins, antisolvent gradually diffuses into the droplets, which leads to rapid supersaturation generation and produces a high number density of primary crystals at  $t = 12.5$  min. However, this leads to rapid supersaturation depletion during 9-12.5 min, which leads to very low

growth rates during the remaining period of the batch (12.5 – 120 min). Thus, the number density of crystals at the end of the batch ( $t=120$  min) is very similar to the number density at  $t = 12.5$  min. **Figure 6-9** also shows the concentration evolution for a higher droplet of radius  $120\ \mu\text{m}$ , which shows crystal nucleation at  $t=29$  min followed by gradual drop in API concentration from 29-120 min. This leads to high crystal growth rates during 29-120 min, which is also illustrated in **Figure 6-10b**. The final end-of-batch product crystals are also larger for larger droplet size (**Figure 6-10b**) than smaller droplet size (**Figure 6-10a**).

### 6.3.2 Evolution of the conditional antisolvent concentration within the droplet as a function of time

To facilitate comparison, instead of plotting the time course evolution of the antisolvent concentration ( $X_w$ ) within the droplets (**Figure 6-9**), it is plotted alongside the API concentration in **Figure 6-11**. It can be seen for lower droplet radius, the nucleation happens at a much higher supersaturation (point A), which leads to rapid drop in API concentration from the point A to C in **Figure 6-11**. However, for higher droplet radius, nucleation happens at a lower supersaturation (point B), which leads to lower nucleation rates and slower depletion of supersaturation within the droplet. The operating point crosses into the growth dominated zone which leads to higher crystal growth rates, forming larger crystals at end of the batch (**Figure 6-10b**).

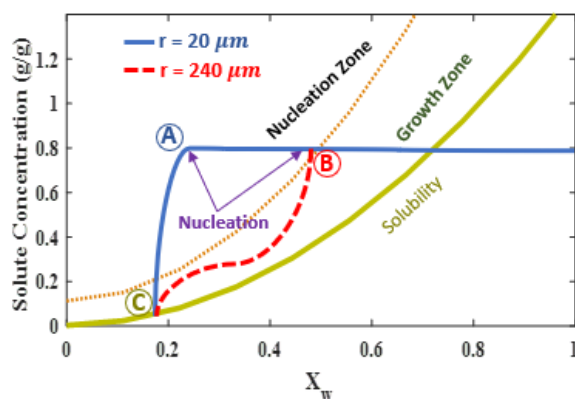


**Figure 6-11.** Operating curve in the phase diagram of API concentration-antisolvent concentration for two different droplet radii. For smaller radius droplet, nucleation happens at a higher supersaturation (point A), which generates smaller primary crystals. For larger droplets, nucleation happens at lower supersaturation (point B), which leads to lower nucleation rates but higher growth rates, which ultimately produces larger primary crystals.

### 6.3.3 Number density evolution with agglomeration

**Figure 6-12** compares the evolution of number density distribution with and without crystal agglomeration within the droplet for  $t = 29, 120$  min for  $\beta_0 = 10^{-6}$ . The comparison in **Figure 6-12** was carried out for a larger droplet size ( $240 \mu m$ ). **Figure 6-12a** shows that when agglomeration is present, there is a bimodal size distribution at 29 min with peaks at  $4 \mu m$  and  $30 \mu m$ . The peak at  $4 \mu m$  is due to the presence of primary crystals and the peak at  $30 \mu m$  is due to the agglomerated crystals. **Figure 6-12b** also shows a bimodal distribution at the end of the process (120 min). However, the number density at the smaller peak ( $69 \mu m$ ) is much smaller than that at the larger peak ( $148 \mu m$ ). This happens because as the batch time increases, more crystals agglomerate, which increases the proportion of agglomerated crystals compared to the primary crystals within the droplets (**Figure 6-12c**).

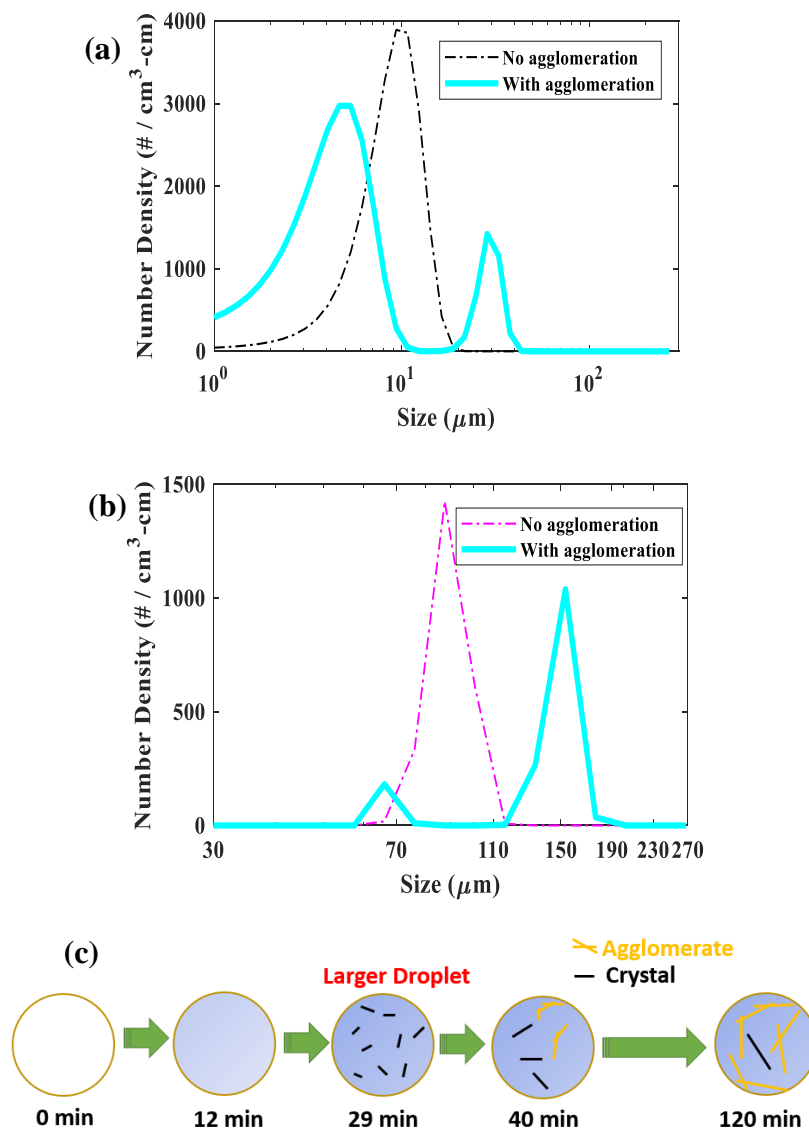


**Figure 6-12.** Number density of primary crystals within droplet of size  $240 \mu\text{m}$  with and without agglomeration for (a)  $t = 29 \text{ min}$ ; and (b)  $t = 120 \text{ min}$ ; (c) Evolution of crystal agglomerates within the droplet.

## 6.4 Conclusions

A multiscale population balance framework was constructed to elucidate the evolution of the populations of droplets and crystals within droplets. The multi-dimensional PBE was solved using method of characteristics, which was then used to investigate the time course of evolution of the number densities of crystals within the droplets. It was found that the fundamental rate processes of crystal nucleation and growth within the droplets were very different depending on the size of



## 7. MODEL-BASED OPTIMIZATION OF COOLING CRYSTALLIZATION OF ACTIVE PHARMACEUTICAL INGREDIENTS UNDERGOING THERMAL DEGRADATION

Reproduced with permission from Kanjakha Pal<sup>+</sup>, Yang Yang<sup>+</sup>, Zoltan K. Nagy<sup>+</sup>, published in *Cryst. Growth Des.* 2019, 19, 6, 3417-3429.

<sup>+</sup>*Davidson School of Chemical Engineering, Purdue University, West Lafayette.*

### 7.1 Introduction

Crystallization is one of the most widely used unit operations in separation processes[1]. If designed properly, crystallization can give products of very high purity[214] with very low capital and operating costs and it is therefore widely used in the fine chemical and pharmaceutical industries, where product purity is of paramount importance. Crystallization depends on the fundamental thermodynamic principle that the solubility of a solute in a solvent is a strong function of critical process parameters such as temperature and anti-solvent to solvent ratio[82]. There are different modes of crystallization, including cooling, anti-solvent[78], evaporative[215] and combined cooling/antisolvent crystallization[216]. The type of crystallization used[217] depends on factors such as the compound's solubility curve, thermal stability, yield and operational requirements. Cooling crystallization is one of the most widely used crystallization processes. Cooling crystallization is based on the fact that for most compounds, the solubility decreases with decreasing temperature. Hence by decreasing the temperature in a controlled manner[218], crystals of desired size distribution can be obtained. Cooling crystallization has many advantages over antisolvent or evaporative crystallization, which either require the use of extra operational volume and extra chemical species to generate the requisite supersaturation in solution or cannot effectively reject impurities during the process. However cooling crystallization also poses concerns because many solutes are thermally unstable and degrade at the initial high process temperature.

Cooling crystallization essentially involves cooling the solution from an initial temperature to a final temperature. The initial and final temperatures depend on the desired yield[219] of the particular product. One of the most important factors in cooling crystallization is the temperature profile followed during the cooling process[220]. Many important properties, such as the final

crystal size distribution (CSD), depend on the cooling profile[221]. It was shown by Doki et al.[181] that the final crystal size distribution obtained after crystallization of potash alum was strongly dependent on the mode of cooling. A controlled cubic cooling profile gave crystals with much higher mean size than natural cooling profiles. The cooling profiles have been traditionally obtained by using an optimizer that optimizes a defined objective function which is representative of the product properties under consideration (maximum average final crystal size, minimum coefficient of variation, etc). Biegler et al.[222] used dynamic optimization to obtain optimal cooling profiles for batch cooling crystallization. They used minimum batch process time and maximum final crystal size as their two objective functions for the optimization. They found that the key final product properties viz. the mean crystal length depends on the optimum cooling profiles obtained for various optimization objectives. Ma et al.[223] investigated the effect of different optimized temperature profiles on the size and shape of the product crystals in a batch stirred tank crystallizer. They simulated a multidimensional population balance model using finite volume method and found that the CSD is very different along the height of the crystallizer and changing the optimal cooling profile also had an effect on the spatio-temporal variation of these properties. Miller et al.[224] studied the sensitivity of optimal cooling profile to changes in model parameters. They formulated the optimal control problem in terms of the parameters of interest and quantified the model uncertainty by using the worst-case uncertainty criterion. Mesbah et al.[225] designed a closed loop optimal control cooling profile for batch cooling crystallization, using a Luenberger type observer to estimate the state of the system. They found that implementing this closed loop optimal control policy led to a great increase in crystal volume fraction at the end of the batch and the method was also robust to variations between batches. Model based and model-free approaches have also been used to control polymorphic purity during cooling crystallization of small molecules[226][227]. There have also been significant advances in modelling the stability of industrial crystallizers[228] including the case that also considers the evolution of crystals shape[229], where the principles of optimal control of crystallizers can be used to better predict stability under dynamic conditions.

Although cooling crystallization is the most widely used crystallization strategy, some compounds do not have steep solubility variation with temperature. For such compounds, the decrease of process temperature needs to be large to obtain the desired yield. Hence for such compounds, the initial starting temperature needs to be high. Many small molecules degrade in

solution at high temperatures[230]. The degradation may be by hydrolysis[231] or by some other mechanism like oxidation, photolysis, etc. The rate of degradation usually increases as the temperature increases. Thus if such APIs are purified by cooling crystallization, it may be possible that the compound starts degrading at higher temperatures. Degradation of the API leads to decreased yield as instead of obtaining the active product it is converted into a degraded product. It is also possible that the degraded product gets incorporated as impurity during crystallization, thereby affecting the product purity. For example, many researchers have reported that impurities, especially those that have similar structures as the solute, can be preferentially adsorbed and incorporated into the crystal lattice of the solute even at low impurity concentration[232]. Thus, impurity rejection must be carried out to the maximum extent possible to minimize the amount of impurity formed as well as the amount of impurity that goes inside the crystal lattice. Various analytical methods such as High Performance Liquid Chromatography (HPLC)[233],[234] and Mass-Spectrometry[235] have been used to find the concentration of degraded product during accelerated stability tests.

For such thermally unstable APIs, other crystallization strategies viz. antisolvent crystallization[214], reactive crystallization[236] may be used. However, the use of such alternate crystallization strategies may be limited due to limited solubility[237] or generation of undesired crystal forms[238]. So cooling crystallization remains the only viable choice in such cases. However the most widely used cubic cooling profile, which maximizes average particle size may be inappropriate as it keeps the solution at high temperature for a long time and may promote degradation. The present work proposes a methodology for finding the optimal cooling profile for the crystallization of APIs viz. aspirin, paracetamol which undergo decomposition at high temperatures. A model-based framework has been first constructed to find the evolution of the desired product properties. Two different optimization criteria have been used in this study: (i) maximization of final crystal size and (ii) minimization of final impurity concentration in the solution. It was also shown experimentally that implementing the calculated optimum cooling profiles provided better control of the final mean crystal size and purity of the final product. However, for the degradation product concentration minimization objective, a qualitative difference in the trends in the evolution of the experimentally observed and the model predicted concentrations was observed. Further, it was seen that a modified kinetic model with an additional

impurity adsorption term incorporated was able to explain the experimental observations much better.

## 7.2 Theory

The Population Balance Equation (PBE) describes the evolution of number density of crystals in the slurry is given by equation (131).

$$\frac{\partial f}{\partial t} + \frac{\partial}{\partial L}(Gf) = B\delta(L - L_0) \quad (131)$$

where  $f$  is the number density of crystals in the solution,  $L$  is the size of the crystals,  $B$  is the rate of nucleation of crystals in solution and  $G$  is the growth rate of the crystals.  $\delta(L)$  is the Dirac Delta function which indicates that nucleation occurs at minimum crystal size.

The rates of primary nucleation and the growth of the crystals are given by equations (132)-(133).

$$B = k_{n1} \exp\left(-\frac{k_{n2}}{RT}\right) \exp\left(-\frac{k_{n3}}{\ln^2(S)}\right) \quad (132)$$

$$G = k_{g1} \exp\left(-\frac{k_{g2}}{RT}\right) (C_{sat}(S-1))^{k_{g3}} \quad (133)$$

$S$  is the relative solution supersaturation given by

$$S(T) = \frac{C_s}{C_{sat}(T)} \quad (134)$$

Here  $C_s$  is the concentration of the solute and  $C_{sat}(T)$  is the saturation concentration at the process temperature.  $k_{n1}$ ,  $k_{n2}$ ,  $k_{n3}$ ,  $k_{g1}$ ,  $k_{g2}$ ,  $k_{g3}$  are nucleation and growth kinetics parameters. The solubility of aspirin as a function of temperature at the specified solvent composition is given by equation (135) where  $T$  is in °C which is calculated from Lindenberg et al. [221] by fixing the solvent composition at constant ethanol weight fraction of  $w_{ethanol} = 0.3$ .

$$C_{sat}(g/mL) = -0.2265 + 0.0371T - 0.0024T^2 + 8.87 \times 10^{-5}T^3 - 1.834 \times 10^{-6}T^4 + 2.07 \times 10^{-8}T^5 - 9.983 \times 10^{-11}T^6 \quad (135)$$

Since solving the fully discretized population balance equation is computationally intensive, it is converted to a set of differential equations in terms of the moments of the

distribution ( $\mu_j$ ). The  $j^{\text{th}}$  moment is given by  $\mu_j = \int_0^{\infty} L^j f(L,t) dL$ . The partial differential equation

(1) is converted into a set of ordinary differential equations (ODEs) in terms of the first 4 moments of the CSD given by:

$$\frac{d\mu_0}{dt} = B \quad (136)$$

$$\frac{d\mu_j}{dt} = jG\mu_{j-1}, \quad j = 1, 2, 3 \quad (137)$$

Equations (136)-(137) are coupled with the mass balance equation for the solute. Assuming that the solute molecules  $S$  degrade according to a simple (pseudo-)first order kinetics into a degradation product  $P$  that represents the impurity in the system ( $S \rightarrow P$ ), the mass balance equation for the solute is given by:

$$\frac{dC_s}{dt} = -3\rho_c k_v G \mu_2 - k_0 e^{-\frac{E}{RT}} C_s \quad (138)$$

$\rho_c$ ,  $k_v$ ,  $E$  are the crystal density, shape factor, and activation energy, respectively. The first term on the right-hand side of equation (138)) represents the loss of solute due to crystal growth and the second term corresponds to the loss of solute due to degradation of the API in solution. Here the degradation by hydrolysis is assumed to follow pseudo-first order kinetics[239]. It is to be noted that the solids density in the suspension considered in the work is less than 5%. This ensures that equation (138) remains valid in the dilute suspension limit.  $k_v$  represents the shape factor of the crystals which is assumed to remain constant throughout the crystallization experiments. However, if this assumption does not hold, multi-dimensional PBEs with different growth rates for different crystal faces need to be used instead of equation (131), which has not been considered here.

To simplify the study further, it is also assumed that only the dissolved solute undergoes degradation whereas the crystals do not. Equations (136)-(138) form a closed set of equations but the equation for the evolution of degradation product is also solved to track the concentration of the degradation product. The mass balance for the degradation product is given by the pseudo-first order degradation kinetics[239] :

$$\frac{dC_p}{dt} = k_0 e^{-\frac{E}{RT}} C_s \quad (139)$$

where  $C_p$  is the concentration of the degradation product (i.e. impurity) in solution.

Multiple objectives have been considered in the study including:

- (i) maximization of the average final product crystal size
- (ii) minimization of the degradation product concentration

It is frequently desired in the pharmaceutical industry to have maximum sized crystals[240] because various downstream unit operations, such as filtration, demand crystals to be as large as possible. But for the case where the API degrades at high temperature, it is also necessary for the concentration of the degradation product in the final batch to be minimum. Impurities reduce the process yield and pose a quality problem if they get incorporated in the crystal lattice.

The maximization of final product crystal size objective (i) is formulated as follows:

$$T_{opt}(k) = \max_{T(k)} \left\{ \bar{L}_{n,final} = \frac{\mu_{1,final}}{\mu_{0,final}} \right\}$$

$$s.t. \left\{ \begin{array}{l} T_{min} \leq T(k) \leq T_{max} \\ R_{min} \leq \frac{dT}{dt} \leq R_{max} \\ C_{s,final} \leq C_{s,fin,max} \\ \forall k = 1, \dots, N \end{array} \right\} \quad (140)$$

Equation (140) indicates maximization of the final mean size of the product crystals ( $\bar{L}_{n,final}$ ) subject to the following constraints:

- (a) The temperatures are bounded between upper and lower bounds
- (b) The rate of decrease of temperature is bounded between upper and lower bounds. This follows from the physical constraint that the rate of cooling has some maximum and minimum values. The minimum rate of cooling is 0 which indicates that the system can only be cooled and not heated, and the maximum rate of cooling is set to 1°C/min by the physical constraints on the cooling apparatus.
- (c) The final product concentration is less than some upper limit. The upper limit is selected based on process yield considerations viz. in this work, it is assumed that at least 90% process yield is attained.

The degradation product concentration minimization objective (ii) is formulated as follows:

$$T_{opt}(k) = \min_{T(k)} C_{p,final}$$

$$s.t. \left\{ \begin{array}{l} T_{min} \leq T(k) \leq T_{max} \\ R_{min} \leq \frac{dT}{dt} \leq R_{max} \\ C_{s,final} \leq C_{s,fin,max} \\ \forall k = 1, \dots, N \end{array} \right. \quad (141)$$

The final concentration of degradation product ( $C_{p,final}$ ) is minimized subject to the same constraints on temperature and rate of cooling and yield.

A multi-objective optimization problem is also solved in-silico where the objective involves a weighted combination of size maximization and degradation product concentration minimization viz. equation (142). The purpose of this multi-objective optimization is to show the smooth transition in the optimal cooling profiles between the two competing objective functions (size maximization and degradation product concentration minimization) as the weight on one of the objectives is changed.

$$T_{opt}(k) = \min_{T(k)} \left\{ w_1 \left( -\frac{\mu_{1,final}}{\mu_{0,final}} \right) + (1 - w_1) C_{p,final} \right\}$$

$$s.t. \left\{ \begin{array}{l} T_{min} \leq T(k) \leq T_{max} \\ R_{min} \leq \frac{dT}{dt} \leq R_{max} \\ C_{s,final} \leq C_{s,fin,max} \\ \forall k = 1, \dots, N \end{array} \right. \quad (142)$$

The optimum cooling profiles are obtained using *fmincon* function of Matlab R2015a and using the *interior-point algorithm*.

It is to be noted that for the model API(Aspirin), there are two degradation products – Salicylic Acid and Acetic Acid[239]. The degradation reaction is given by equation



However, structurally similar impurities have much higher effect on the nucleation and growth rate of crystals than impurities that are not structurally related to the API. So, in this work it is assumed that only Salicylic Acid is adsorbed onto the growing API crystals and the other degradation product (acetic acid) has no effect on the growth rates or purity of the API crystals. The adsorption of impurity within the API crystals has been modeled by considering impurity

adsorption to be a first order process. Equations (2-5) remain the same except that the rate of adsorption of the degradation product into the aspirin crystals is included in the equation for the evolution of concentration of degradation product, which is given by equation (144).

$$\frac{dC_p}{dt} = k_0 e^{-\frac{E}{RT}} C_s - k_a C_p \quad (144)$$

Here  $k_a$  is the kinetic constant for adsorption and the last term on the right-hand side of equation (144) indicates the change in concentration of the degradation product due to adsorption onto the growing API crystals. The intricacies of the adsorption-desorption kinetics of the impurities on the API crystals as elucidated in Borsos et al.[232] have not been included in this model but the entire adsorption phenomena has been lumped onto the first order adsorption kinetics of the degradation product.

## 7.3 Experimental Methods

### 7.3.1 Materials

Aspirin ( $\geq 99\%$ , Alfa Aesar) was used as the model API. Salicylic Acid was the degradation impurity generated in-situ during the crystallization experiment. De-ionized water and Ethanol (200 proof, Fisher Scientific) were used as the solvents. Acetic Acid and Methanol (Optimal LC/MS grade, Fisher Scientific) were used as solvents for isocratic UPLC methods.

### 3.2. Experimental Setup

The experiments were run in a 1 L batch crystallizer. Aspirin was dissolved in a 30% (w/w) ethanol-water mixture, creating a supersaturated solution and then cooled from its saturation temperature (48 °C) to the final temperature (18 °C) following programmed cooling profiles. The solubility surface for aspirin in the solvent mixture is a function of both the temperature and solvent composition as shown in Lindenberg et al[221]. However, in this work the solvent composition is fixed, so the solubility is only a function of temperature which is obtained by fixing the solvent composition at  $w_{\text{ethanol}} = 0.3$  in the solubility polynomial. The initial concentration for the experiments was the saturation concentration at the starting temperature of the experiment viz. 0.044 g/mL which is calculated according to equation (135). An online Ultra Performance Liquid Chromatography (UPLC) system (from Waters<sup>TM</sup> Corporation with ACQUITY UPLC Console and EMPOWER Software) was connected to take samples online and measure concentrations of

Aspirin and Salicylic Acid in situ and in real-time. The online UPLC consists of the Binary Solvent Manager (BSM), Process Sample Manager (PSM), Column Manager (CSM) and a UV detector along with an integrated process sampling and dilution loop. Here the BSM refers to the supervisory control logic within the UPLC which adjusts the flow rates of the solvent and buffer streams for the mobile phase. The outlet of the PSM was recycled back to the reactor to minimize the amount of solution lost due to sampling. Since the initial process temperature (48 °C) is higher than the room temperature, there was potential for clogging in the sampling and the dilution loops. To avoid any clogging, the sampling and dilution loops were wrapped with propriety carbon fiber tubular heaters[241]. Hot air was also blown on the sample valve and the injection valve to avoid further clogging within these valves. Focused Beam Reflectance Measurement (FBRM) G-400 from Mettler-Toledo with IC FBRM 4.3 software was used to track the evolution of counts/s of crystals in the crystallizer in different bins of chord lengths. Although the chord length distribution is different from CSD, it can be used to estimate changes in the CSD qualitatively or quantitatively[195], [242]. Process Vision Microscope (IC PVM 7.0) from Mettler-Toledo was used to obtain in-situ images of particles in the crystallizer. A Pt-100 probe was used to monitor the temperature. The crystallizer was a 1 L vessel (LABTEX) provided with overhead stirring, which was connected to a circulating water bath (Huber) for heating/cooling. These Process Analytical Technology (PAT) tools were connected to the Crystallization Monitoring and Control (CRYMOCO also known as CryPRINS) system via a RS-232 interface. The cooling profile was implemented in CRYMOCO and the set-point temperature from CRYMOCO was sent to a chiller bath (Huber ministat 230) which controlled the reactor temperature through a jacketed heating/cooling arrangement. The details of the setup of the online UPLC have also been explained in a previous publication[163]. All experiments were carried out at 350 rpm. All the isocratic UPLC methods for sample analysis were taken from Yang et al[163].

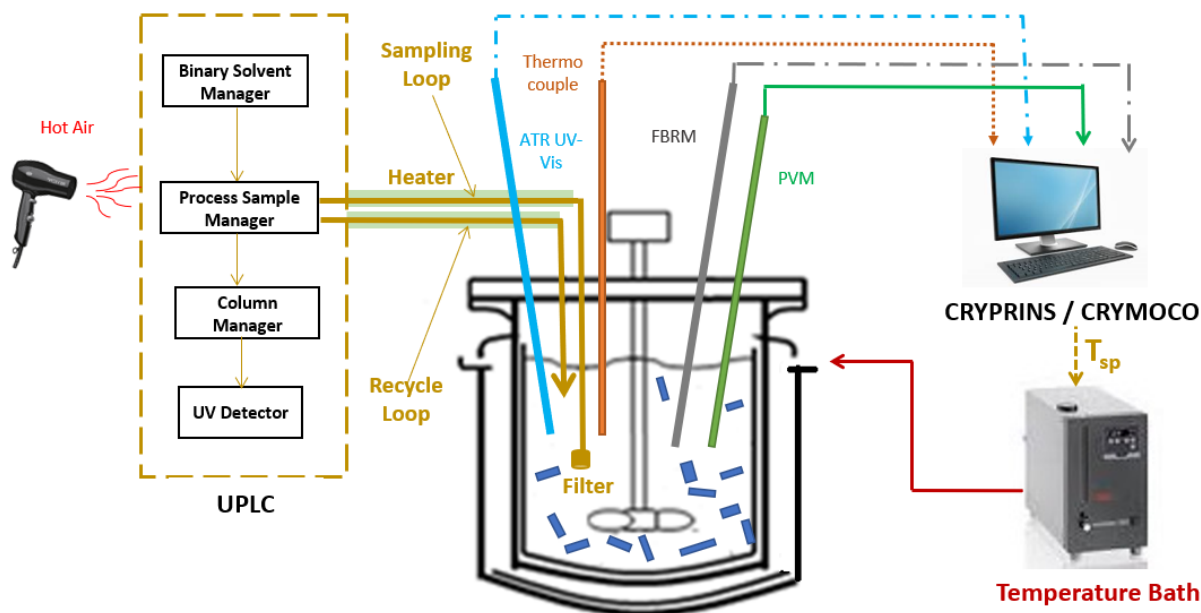


**Figure 7-1.** Schematic of experimental setup showing the jacketed crystallizer and Process Analytical Technology Tools.

#### 7.4 Results and discussions

The growth and nucleation rates as well as the coefficients of the solubility model were taken from Lindenberg et al.[243]. The kinetics of degradation were taken from Alibrandi et al.[239]. The shape factor was assumed to be constant throughout the simulations. The kinetic parameters used in the study have been shown in **Table 7-1**. The maximum value of cooling rate in **Table 7-1** viz.  $R_{\max} = 0^{\circ}\text{C}/\text{min}$  indicates that the solution can only be cooled. The minimum value of cooling rate in **Table 7-1** viz.  $R_{\min} = -1.35^{\circ}\text{C}/\text{min}$  was chosen based on studies on the actual experimental system in the laboratory.

Four scenarios of different objective functions and with/without degradation kinetics were investigated and compared, as shown in Table 2.

**Table 7-1.** Kinetic parameters of nucleation, growth and degradation processes

$k_{J1}$	$6.9 \times 10^{16} \text{ \#/cm}^3/\text{min}$
$k_{J2}$	$7.67 \times 10^4 \text{ J/mol/K}$
$k_{J3}$	0.16
$k_{g1}$	$1.9260 \text{ \mu m/min}$
$k_{g2}$	$2.560 \times 10^4 \text{ J/mol/K}$
$k_{g3}$	1.0
$k_0$	$2.409 \times 10^6 \text{ /min}$
E	$6.66 \times 10^4 \text{ J/mol}$
$R_{\min}$	$-1.35 \text{ }^\circ\text{C/min}$
$R_{\max}$	$0^\circ\text{C/min}$
$C_{s,fin,init}$	0.053 g/mL
$C_{s,fin,max}$	0.0053 g/mL
$k_v$	0.94

## 7.5 Optimization of batch cooling crystallization

### 7.5.1 Optimal Cooling for product crystal size maximization

**Figure 7-2** shows the optimum cooling profiles for the crystallization of aspirin with the two optimization objectives which are obtained by solving the optimization problems (140)-(141). It can be seen from **Figure 7-2** that for the size maximization objective, the optimum cooling profile with degradation kinetics turned on (scenario O2, red curve) is steeper compared to the case with degradation kinetics turned off (scenario O1, blue curve). The kinetics of degradation follows a first order rate law and increases with temperature which follows from equation (139). So, when degradation occurs, the temperature needs to be reduced faster (red curve in **Figure 7-2**) compared to no degradation case (blue curve in **Figure 7-2**) to reduce the rate of degradation. However, the

solution cannot be cooled too rapidly (black curve in **Figure 7-2**) because it would lead to rapid nucleation which will produce very small crystals, thereby defeating the optimization objective of size maximization. Thus, to maintain balance between these two extremes viz. slow cooling which leads to higher API degradation and rapid cooling which leads to rapid nucleation, the optimizer follows the cooling profile in the presence of degradation (red curve in **Figure 7-2**).

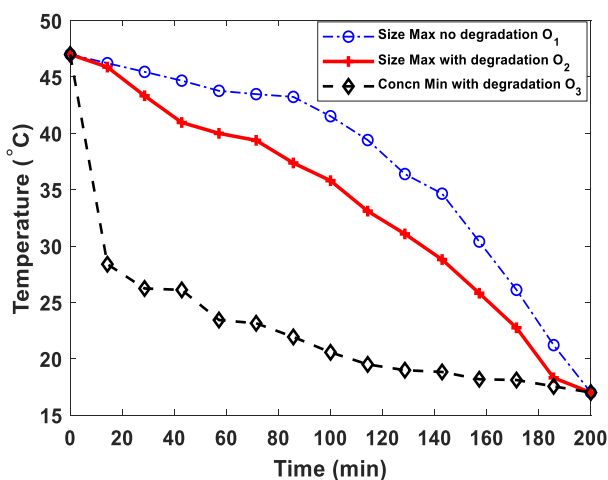


**Figure 7-2.** Simulated optimum cooling profiles for (O1) size maximization without degradation kinetics, (O2) size maximization with degradation kinetics and (O3) degraded product concentration minimization.

### 7.5.2 Optimal Cooling for degraded product concentration minimization

**Figure 7-2** also shows that the cooling profile for the degraded product concentration minimization objective O3 is much steeper compared to the size maximization objective O1 and O2. The rationale for the steep temperature decrease follows from the previous discussion – to decrease the rate of degradation, the optimizer decreases the temperature rapidly (black curve in **Figure 7-2**). The sharp temperature drop quickly generates a high degree of supersaturation which leads to high rates of primary nucleation. However, in this case the optimizer is not worried about the crystal size at all. Comparing the cooling profiles for the two objectives, it can be inferred that choosing the correct optimization objective is of paramount importance since the two profiles (red and black curves in **Figure 7-2**) are very different, even qualitatively.

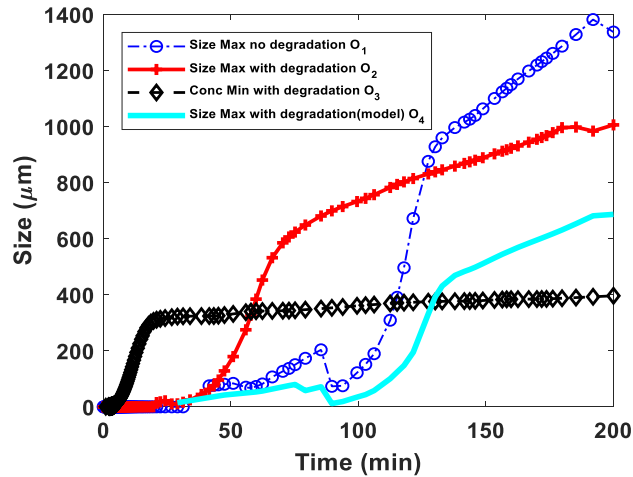


**Figure 7-3.** Evolution of mean crystal size for (O1) size maximization without degradation kinetics, (O2) size maximization with degradation kinetics and (O3) degraded product concentration minimization objective. The final Mean Crystal Size is higher for size maximization objective than degradation product concentration minimization objective.

**Table 7-2.** Different Optimization studies with the optimization problem formulations and underlying mechanistic models.

Case	Optimization Problem	Mechanistic Model	Scenarios
Size Max no degradation	$T_{\text{opt}}(k) = \max_{T(k)} \frac{\mu_{1, \text{final}}}{\mu_{0, \text{final}}}$	$\frac{d\mu_o}{dt} = B$ $\frac{d\mu_j}{dt} = jG\mu_{j-1}, j = 1, 2, 3$ $\frac{dC_s}{dt} = -3\rho_c k_v G\mu_2$ $\frac{dC_p}{dt} = 0$	O1
Size Max with degradation	$T_{\text{opt}}(k) = \max_{T(k)} \frac{\mu_{1, \text{final}}}{\mu_{0, \text{final}}}$	$\frac{d\mu_o}{dt} = B$ $\frac{d\mu_j}{dt} = jG\mu_{j-1}, j = 1, 2, 3$ $\frac{dC_s}{dt} = -3\rho_c k_v G\mu_2 - k_0 e^{-\frac{E}{RT}} C_s$ $\frac{dC_p}{dt} = k_0 e^{-\frac{E}{RT}} C_s$	O2

**Table 7-2** continued

Conc Min with degradation	$T_{\text{opt}}(k) = \min_{T(k)} C_{p, \text{final}}$	$\frac{d\mu_o}{dt} = B$ $\frac{d\mu_j}{dt} = jG\mu_{j-1}, j = 1, 2, 3$ $\frac{dC_s}{dt} = -3\rho_c k_v G\mu_2 - k_0 e^{-\frac{E}{RT}} C_s$ $\frac{dC_p}{dt} = k_0 e^{-\frac{E}{RT}} C_s$	O3
Size Max with degradation (model)	No optimization problem is solved but optimum profile from problem O1 is used directly to simulate the evolution of process variables	$\frac{d\mu_o}{dt} = B$ $\frac{d\mu_j}{dt} = jG\mu_{j-1}, j = 1, 2, 3$ $\frac{dC_s}{dt} = -3\rho_c k_v G\mu_2 - k_0 e^{-\frac{E}{RT}} C_s$ $\frac{dC_p}{dt} = k_0 e^{-\frac{E}{RT}} C_s$	O4

## 7.6 Evolution of process variables

**Figure 7-3** shows the evolution of mean size for the two different optimization objectives (i) and (ii). The details of the underlying optimization problem as well as the dynamical models on which the optimal cooling profiles were implemented are shown in **Table 7-2**. It can be seen from **Figure 7-3** that when degradation is included in the model (red curve in **Figure 7-3**), the mean crystal size starts increasing much faster around 20 mins since the temperature starts decreasing around that time (**Figure 7-2**). From around 30 minutes till 60 minutes, the mean size increases rapidly because of the high growth rates. After 70 minutes, the growth rates become lower and the mean size still increases from 70-200 minutes but at a much slower pace. When no degradation is considered in the size maximization model, the size increases much slowly initially but increases rapidly after 100 minutes (blue curve in **Figure 7-3**). The final mean crystal size when there is no degradation is higher than when there is degradation because degradation depletes API concentration in solution. The reduced API concentration reduces API supersaturation which decreases the crystal growth rate leading to lower final crystal size. For objective (ii), the mean

particle size increases very rapidly due the fast drop in initial temperature which generates high supersaturation and hence leads to high growth rates. But the high growth rates immediately deplete all the supersaturation and the growth rates for the remaining batch period (20-200 mins) is very low which leads to essentially constant mean particle size from 20-200 mins.

Optimization scenario O4 (**Table 7-2**) represents a common industrial crystallization optimization problem where the optimization problem O1 is run without considering API degradation. But, in fact, there is API degradation which ultimately means a dynamical optimization problem was solved with an incorrect mechanistic model. However, when there is degradation, the correct optimal cooling profile with the proper mechanistic model is given in scenario O2 (**Table 7-2**). **Figure 7-3** shows that the size evolution for scenario O4 (cyan curve in **Figure 7-3**) is very different from the size evolution for scenario O2 (red curve in **Figure 7-3**) and the final mean crystal size is lower for scenario O4. This is because for scenario O4, the crystallizer is now held at a higher temperature for a longer time (blue curve in **Figure 7-2**) whereas the temperature should have been dropped more steeply (red curve in **Figure 7-2**, scenario O2). Holding the temperature high for a longer time (scenario O4) results in more degradation which leads to lower API supersaturation in solution. This leads to lower growth rate of API which produces smaller API product crystals.

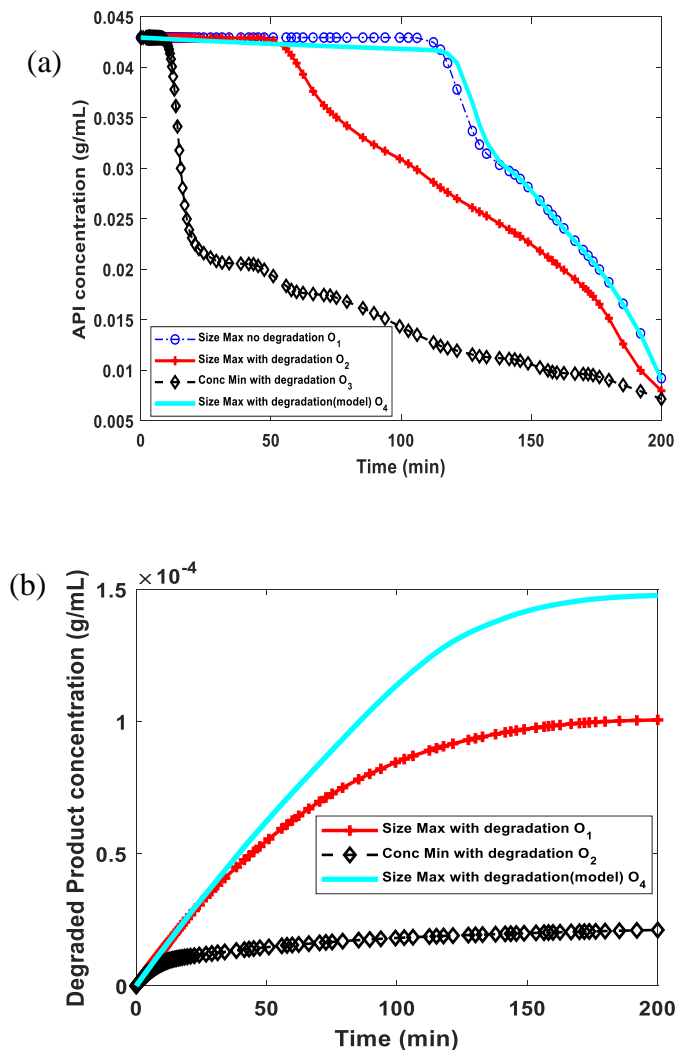


**Figure 7-4.** Evolution of (a) API concentration (b) degradation product concentration. The API concentration reduces much faster with the concentration minimization objective. The final degradation product concentration is much higher with the concentration minimization objective.

**Figure 7-4a** shows the dynamic profiles of change of aspirin concentration for the two different objective functions: (i) size maximization and (ii) degradation product concentration minimization. The API concentration decreases much faster for objective (ii). This happens because of the steep decrease in temperature for objective (ii) (**Figure 7-2**) which leads to high supersaturation generation followed by rapid nucleation and growth which depletes all the supersaturation. It can also be seen that the API concentration decreases much earlier for size maximization with degradation (red curve, **Figure 7-4a**) than without degradation (blue curve, **Figure 7-4b**). This is due to the steeper temperature drop when degradation is included in the

model (red curve in **Figure 7-2**) which essentially leads to faster supersaturation depletion, although not as fast as objective (ii). It is to be noted that the concentration evolution of degradation product for objective (i) with no degradation is not shown since the degradation product concentration is always 0.

**Figure 7-4b** compares the evolution of the concentration of the degradation product for the two different objectives (i) and (ii). As expected, the final degradation product concentration is much lower when the simulation was conducted with the degradation product concentration minimization objective (ii) than the size maximization objective (i). Since the rate of degradation is higher at higher temperatures, for objective (ii), the steep temperature drop at the beginning of the batch (**Figure 7-2**) leads to lower degradation and hence less concentration of degradation product at the end of the batch.

**Figure 7-4** also shows that when the incorrect optimal cooling profile is implemented (scenario O4 in **Table 7-2**), the API concentration decreases much faster (cyan curve , **Figure 7-4a**) than when no degradation is considered (blue curve , **Figure 7-4a** ). This follows from the discussion from **Figure 7-3** – now the temperature is held higher for a longer time (blue curve in **Figure 7-2**) when in fact, it should have been decreased faster (red curve in **Figure 2**). This gives rise to higher rates of API degradation and higher concentration of degradation product in the solution (cyan curve in **Figure 7-4b**). There may be a possibility of the degradation product crystallizing along with the API during cooling crystallization. However, **Table 7-3** shows the solubility of the degradation product (Salicylic Acid) at 25°C in ethanol and water. However, **Figure 7-4** shows that the maximum concentration of the degradation product ( $1.5 \cdot 10^{-4}$  g/mL) is much less than the solubility at 25 °C in either solvents, which voids the possibility of crystallization of the degradation product. This also explains why the incorporation of degradation product in Section 4.6 is modeled only using additional adsorption terms and not co-precipitation.

**Table 7-3.** Solubility of Salicylic Acid in ethanol and water at 25°C

Solvent	Solubility (g/mL)
Ethanol	0.3006
Water	0.0022

#### 4.1. Evolution of nucleation and growth rates

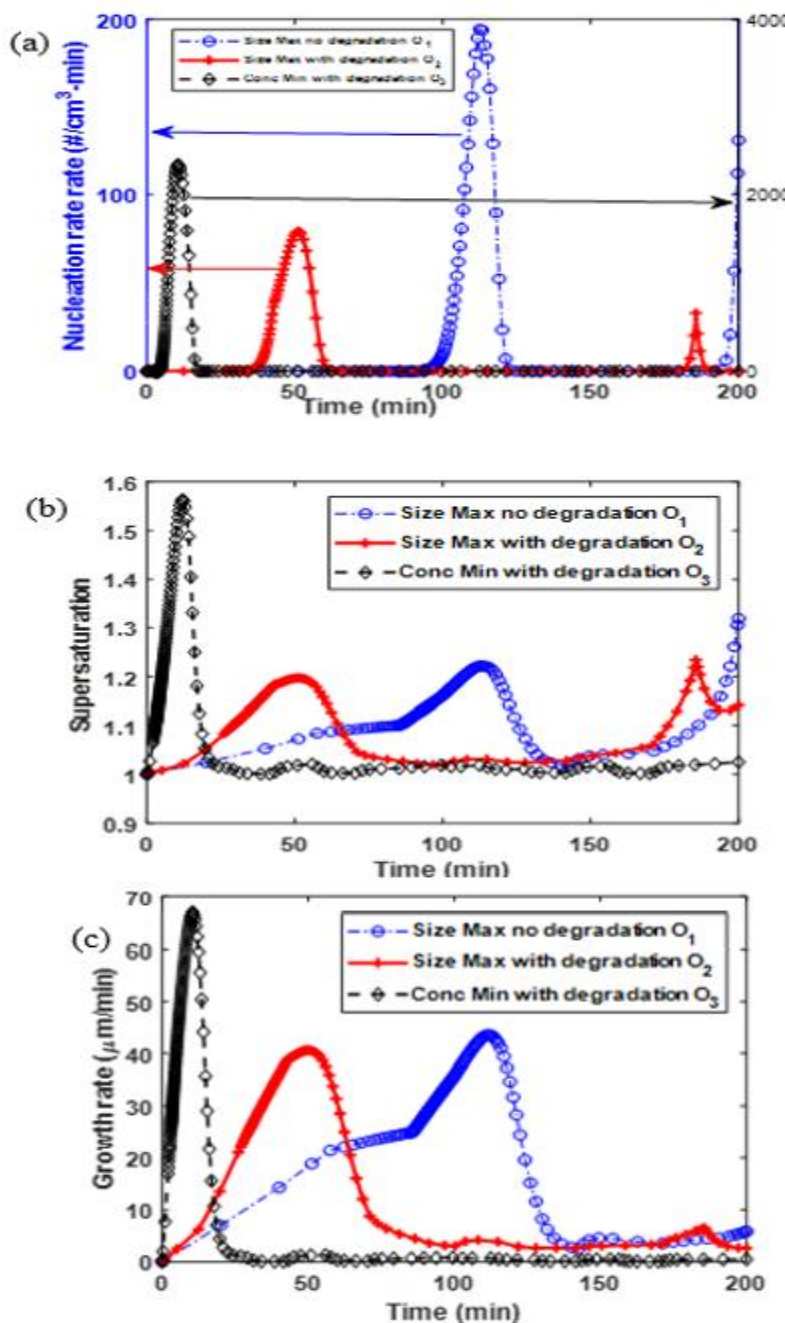


**Figure 7-5.** Nucleation rates for aspirin for (O1) size maximization without degradation kinetics, (O2) size maximization with degradation kinetics and (O3) degraded product concentration minimization. The supersaturation generated is much higher for concentration minimization objective. The growth rates are similar for both the objectives, but the nucleation rate is much higher for concentration minimization objective.

**Figure 7-5a** shows the rate of nucleation for aspirin for the two different optimization objectives. For size maximization objective, when degradation is considered, nucleation occurs much earlier ( $\sim 50$  min) than without degradation ( $\sim 110$  min). The nucleation onset is the earliest for concentration minimization objective and occurs around 10 minutes. The trends in nucleation onset follows the trends in temperature drop in the cooling profile (**Figure 7-2**) – for concentration minimization objective, the temperature drop is very sharp towards the beginning of the batch leading to earlier nucleation. The rate of nucleation is also much higher for concentration minimization objective ( $\sim 2000 \text{ \#/cm}^3 / \text{min}$ ) compared to size maximization objective ( $\sim 100\text{-}200 \text{ \#/cm}^3 / \text{min}$ ) which happens due to the differences in supersaturation generated for the two objectives (**Figure 7-5b**). The nucleation at large times ( $\sim 180\text{-}200$  min) in **Figure 7-5a** happens because the rate of cooling is very fast towards the end of the batch (**Figure 7-2**) leading to small nucleation events at the end of the batch. The Area Under the Curve (AUC) for the second nucleation event is much smaller than the first nucleation event which makes this assumption valid. Such nucleation events can be neglected for all practical purposes since they will not considerably affect the final product CSD.

A subtlety in the size evolution can be noted by comparing **Figure 7-5a** and **Figure 7-3** – the mean crystal size in **Figure 7-3** starts decreasing around 85 minutes whereas the nucleation event in **Figure 7-5a** starts around 90 minutes. This happens due to numerical interpolation between the time axes for the different optimization objectives and is only a numerical artefact.

**Figure 7-5b** shows the temporal evolution of growth rates for the two different objective functions (i) and (ii). The maximum growth rates for both the objectives are very similar. Thus, the differences in final mean particle size (**Figure 7-3**) is primarily due to differences in nucleation rates at the middle of the batch viz. 50 mins for red curve and 100 mins for blue curve in **Figure 5**. Differences in rate of nucleation (**Figure 7-5a**) gives rise to different number density of particles in solution, so with similar growth rates, when the rate of nucleation is higher, the final particle size is lower.

It is to be noted that scenario O4 was only a hypothetical scenario constructed to prove the importance of using the correct mechanistic model for solving the dynamical optimization problem. Hence, the dynamics of nucleation and growth rates for optimization scenario O4 are not elucidated in **Figure 5**.

## 7.7 Multi-objective optimization

The multi-objective optimization equation (142) and simulations were run for different values of  $w_1$ , the weight for size maximization objective. It is to be noted that for  $w_{\text{ethanol}} = 0.3$ , the optimal cooling curves for different values of  $w_1$  were getting too cluttered. Hence the optimal cooling profiles in **Figure 7-6** were obtained for  $w_{\text{ethanol}} = 0.35$  to better illustrate the smooth transition on sequentially changing  $w_1$ . From **Figure 7-6**, it can be seen that as the objective function gets weighted more towards the size maximization objective ( $w_1=1$ ), the temperature profiles become more convex which illustrates the smooth transition on changing the value of  $w_1$ . However, it is to be noted that the multi-objective optimization study was carried out only in-silico whereas for experimental validation, the optimal cooling curves corresponding to **Figure 7-2** were implemented.

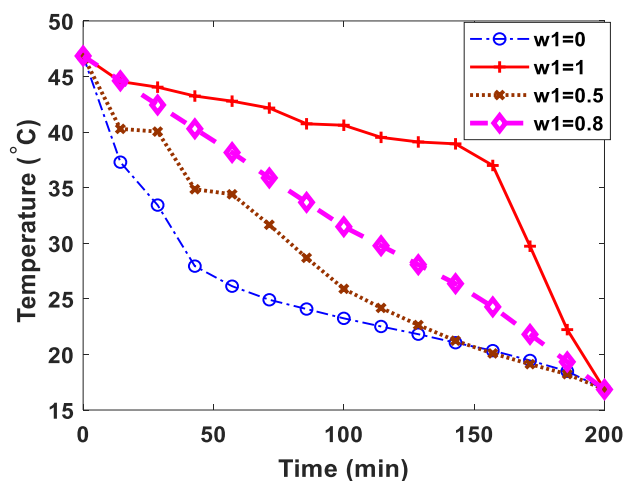


**Figure 7-6.** Temperature profiles obtained from the multi-objective optimization using different weights between size maximization objective and degradation minimization objective. The cooling profile shows a monotonic shift in the shape of the profile as the weight given to the individual objective is changed.

### 7.7.1 Experimental Validation

All the experiments were conducted with aspirin in 30% (w/w) ethanol-water mixture.

#### *Experimental validation for size maximization objective*

The optimal cooling profile for size maximization with degradation (red curve in **Figure 7-2**) was implemented experimentally. **Figure 7-7** shows the concentration evolution of aspirin (API) and

salicylic acid (degradation product) in the crystallizer which was measured using UPLC. It can be seen from **Figure 7-7** that the concentration of aspirin first showed a slight increase but decreased monotonically as time progressed. The slight increase is hypothesized to be due to some solvent evaporation initially at high temperatures. Comparing **Figure 7-4a** and **Figure 7-7**, it can be seen that the evolution of API concentration between the model predictions and the experiments are qualitatively similar. A slight mismatch between the initial API concentrations from model predictions (**Figure 7-4**) and experimental measurements (**Figure 7-7**) is evident which happens due to solvent evaporation at the high initial temperatures in the sampling loop from the UPLC. However, this mismatch in API concentrations is neglected for the purposes of this study since only qualitative trends in API concentrations are sought here.

**Figure 7-8a** shows the evolution of the FBRM counts of the API crystals in the batch. The nucleation event occurring around 70 min is indicated by the sudden increase in the FBRM counts of the particles. There is no increase in counts in bin 1-10 from 75-180 min, whereas the counts in the bins 10-100 and 100-1000 keep on increasing indicating a growth dominated process. The slight nucleation event observed in the simulations (**Figure 7-5a**) is evident towards the end of the batch (~3 h) however this has a very small effect on the final product crystals. **Figure 7-8b** shows the evolution of the Square Weighted Mean Chord Length (SWMCL), which shows a clear trend in growth of crystals. Since aspirin crystals are needle shaped, the evolution of FBRM counts is not representative of the actual evolution of particle size in the crystallizer but in-situ PVM images taken during the experiment (**Figure 7-9**) clearly show large needle shaped crystals present at the end of the experiment.

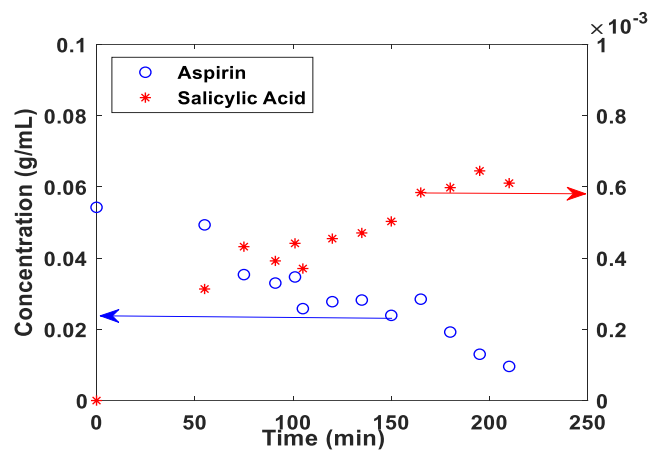


**Figure 7-7.** Experimental Concentration evolution of Aspirin (API) and salicylic acid (degraded product) for size maximization objective. The API concentration decreases due to crystallization and degradation while the degradation product concentration increases with time.

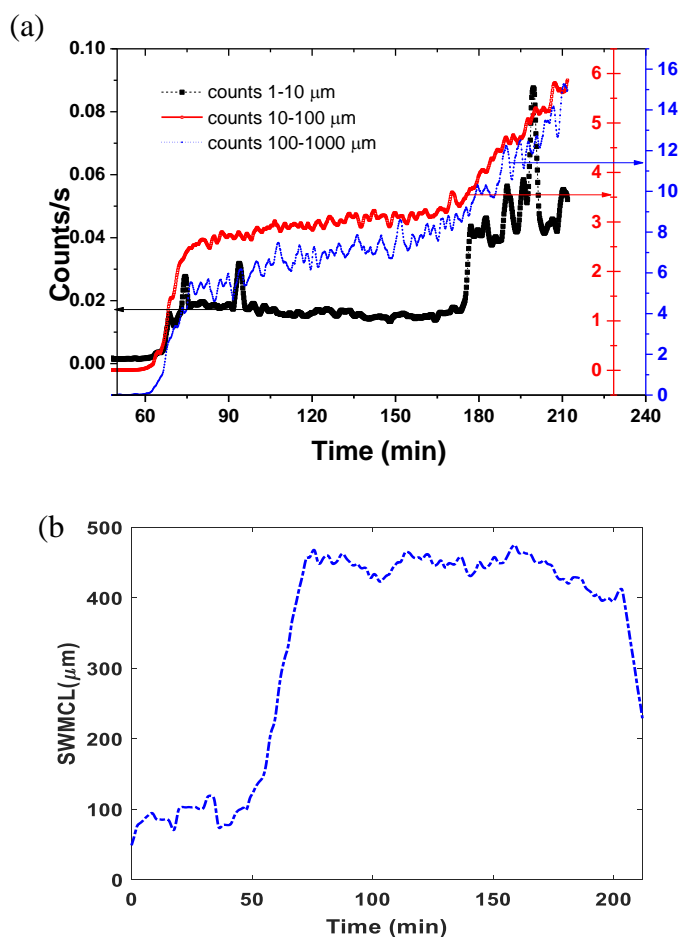


**Figure 7-8.** Experimental evolution of (a) number of chord counts for a certain size range per second (b) SWMCL in FBRM for objective of size maximization.

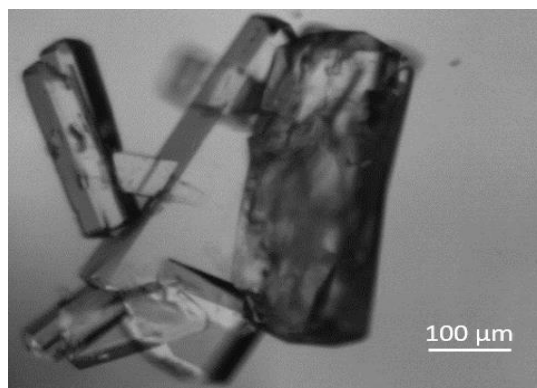


**Figure 7-9.** PVM image of final product crystals when operated with the objective of size maximization.

*Experimental validation for degradation product concentration minimization objective*

For the objective of degraded product concentration minimization, the cooling profile corresponding to the black curve in **Figure 7-2** was implemented. **Figure 7-10** shows the evolution of the concentration of the API (aspirin) and the degradation product (salicylic acid). Comparing **Figure 7-10** and **Figure 7-7**, it can be seen that the final concentration of the degradation product (salicylic acid) for objective (ii) is lower than for objective (i), which validates the results from the simulations (**Figure 7-4b**). It can also be seen from **Figure 7-10** that the initial concentration of the API shows an increase due to solvent evaporation at high temperature followed by monotonic decrease. There are qualitative differences between the shape of the evolution of concentration of salicylic acid between the experiments and the simulation (**Figure 7-10** and **Figure 7-4**). In the experiments, the concentration of the degradation product first increases followed by a slight decrease towards the middle of the batch (**Figure 7-10**), whereas in the simulations, the concentration of the degradation product increases and then stabilizes (**Figure 7-4b**). These differences can be explained by the adsorption of the degradation product onto the API crystals – as the degradation product adsorbs onto the growing crystals, their solution concentration decreases. **Figure 7-11** shows the evolution of the chord length data in FBRM. Comparing **Figure 7-9b** and **Figure 7-11b**, it can be seen that the final SWMCL in **Figure 7-11b** is much lower, which also validates the results of the simulations (**Figure 7-3a**). It is to be noted that the underlying mechanistic models (136) - (137) are moment based models and the actual CSD cannot be accurately reconstructed from the evolution of the moments. Thus, quantitative trends in the actual crystal size distributions between the model simulations and the experiments are not

evaluated here; rather, qualitative trends between the mean particle size from model simulations and SWMCL from FBRM are elucidated. The deviation between the actual final mean crystal size predicted from the simulations (**Figure 7-3a**) and the final SWMCL obtained from the experiments can be attributed to plant-model mismatch, which can be easily corrected by an online parameter re-estimation [244] during an actual process run.

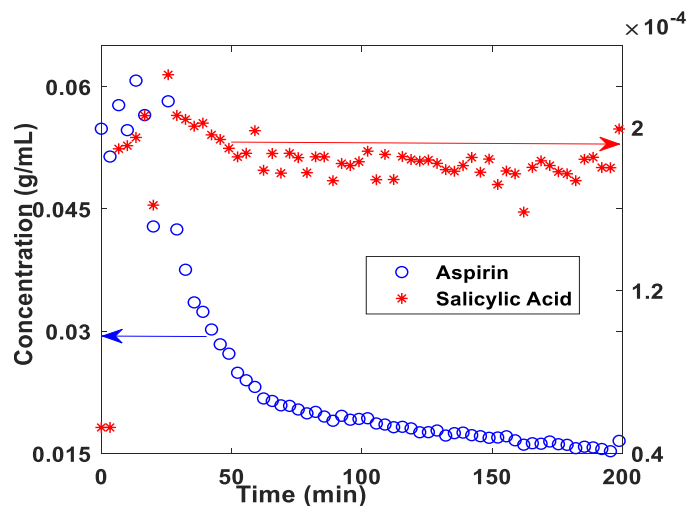


**Figure 7-10.** Concentration evolution of (a) aspirin, and (b) salicylic acid (degradation product) for optimization with objective as minimization of concentration of degraded product.

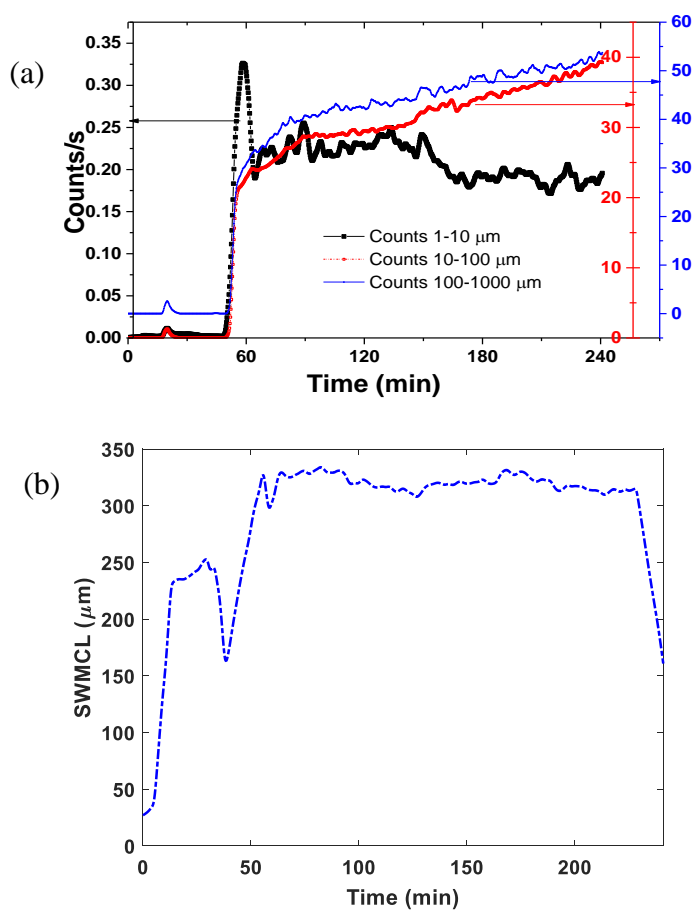


**Figure 7-11.** Evolution of (a) counts/s in FBRM and (b) SWMCL for objective of minimization of concentration of degradation product.

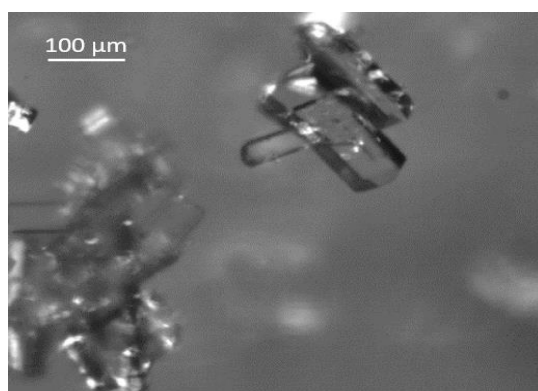


**Figure 7-12.** PVM image of particles for objective of minimization of concentration of degradation product showing smaller crystals compared to size maximization.

*Modeling the crystallization system considering the adsorption of degradation product within the product crystals*

It is also possible that the impurities get adsorbed onto the product crystals as crystallization progresses rather than remaining in solution (**Figure 7-10b**). This would lead to reduced product quality of the final crystals since the degradation product cannot be eliminated by filtration. The resulting evolution of concentrations for the API and the degradation product are shown in **Figure 7-13** for  $k_a = 0.02 \text{ mol m}^{-3}$  and  $k_a = 0.2 \text{ mol m}^{-3}$  in equation (144). These kinetic rate constants for adsorption were chosen to illustrate the effect of a tenfold increase in the adsorption coefficient on dynamics of the impurity concentration profiles.

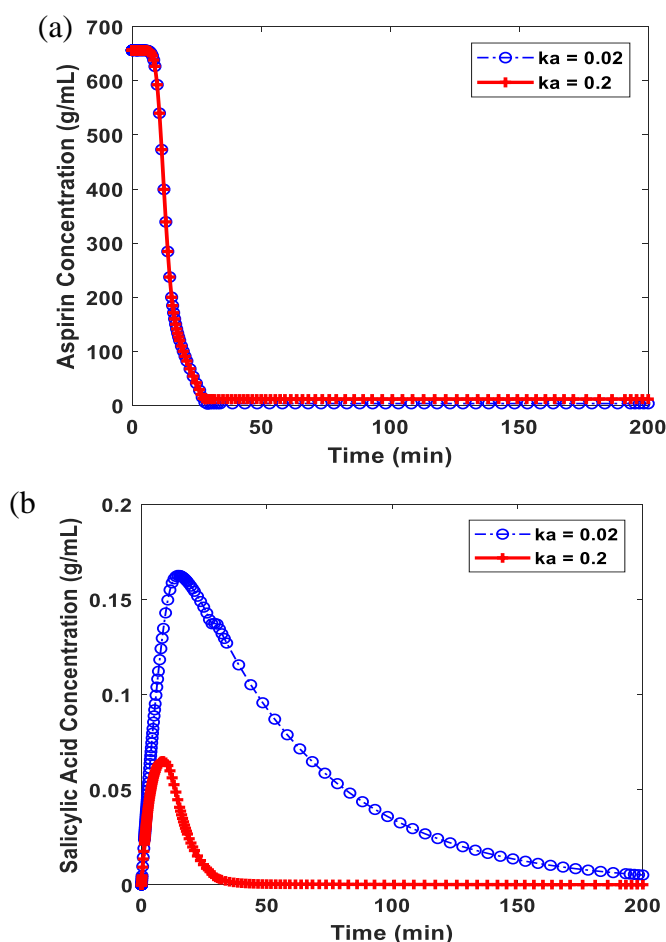


**Figure 7-13.** Concentration evolution of (a) aspirin (API) and (b) salicylic acid (degradation product) for two different adsorption kinetic constants. The API concentration does not change with change in adsorption kinetics because the growth rate of the API is assumed to be independent of the adsorption of impurities. The degradation product concentration changes on changing the adsorption kinetics since faster adsorption onto crystals leads to lower concentration of degradation product in the solution.

It can be seen from **Figure 7-13a** that the evolution of aspirin concentration does not change by changing the rate of adsorption of the degradation product since it is assumed that the impurity adsorption does not affect the growth rate of aspirin. **Figure 7-13b** shows that the concentration of the degradation product increases initially, followed by a decrease due to adsorption of the degradation product onto the API crystals, which leads to depletion of the solution concentration of the degradation product. **Figure 7-13b** shows that the maximum concentration of salicylic acid is much less for  $k_a = 0.2 \text{ mol m}^{-3}$  than for  $k_a = 0.02 \text{ mol m}^{-3}$ . This is due to the difference in adsorption kinetics - for  $k_a = 0.2 \text{ mol m}^{-3}$ , the adsorption is much faster. As soon as the salicylic acid forms in solution, it starts getting adsorbed onto the crystals and the solution concentration decreases rapidly. But for  $k_a = 0.02 \text{ mol m}^{-3}$ , the adsorption of salicylic acid onto the API crystals is much less rapid, so its solution concentration increases initially to 0.16 g/mL before the adsorption kinetics starts dominating.

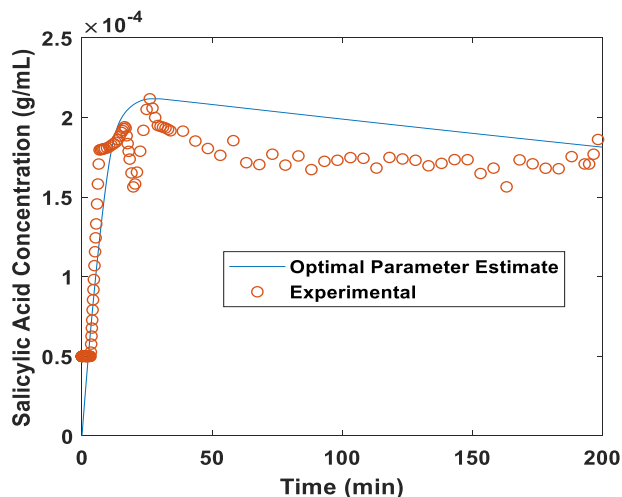


**Figure 7-14.** Concentration of degradation product with optimal parameter estimate. The model simulations run with the optimal estimated parameter shows very good match to the experimental concentrations. The slight model mismatch happens because either (i) the degradation product (SA) first gets adsorbed onto the aspirin crystals but then desorption of the adsorbed also takes place, which was not considered in the kinetic model (ii) adsorption rate constant is actually temperature dependent which was not modeled in this work.

The adsorption constant that best fits the experimental data was estimated by minimizing the deviation between the experimental degradation product concentration and the model estimates.

The optimal estimate of the adsorption kinetic constant is  $k_{a,opt} = \min_{k_a} \sum_{i=0}^N (C_{exp,i} - C_{model,i})^2$ , where  $C_{exp}$  and  $C_{model}$  are the experimental and predicted concentrations of the degradation product. The optimal parameter estimate for the adsorption rate constant was estimated to be  $k_a = 1.13 \times 10^{-3} \text{ mol m}^{-3}$ . **Figure 7-14** shows the evolution of the degradation product concentration for the model simulation with the optimal parameter estimates compared to the experimental data. There is still some plant-model mismatch since the model predicts a steady decrease in degradation product concentration whereas the experiments predicted the concentration was essentially constant after ~75 minutes. This can be further rectified by including a temperature dependent Arrhenius term for the adsorption kinetics; at lower temperature the rate of adsorption is lower, which leads to less adsorption after ~75 minutes when the temperature has dropped significantly. Inclusion of a desorption kinetics of the degradation product from the crystal surface may also explain the experimental data better – as degradation product gets adsorbed onto the crystals, the rate of desorption from the crystal surface also increases and ultimately a stage is reached where the overall adsorption rate is balanced by the rate of desorption, which leads to no change in the concentration of the degradation product in the solution.

It is also to be noted that while surface adsorption of impurity is a possible mechanisms which explains the experimental results, there can be various other methods of impurity incorporation onto crystals viz. substitutional or interstitial incorporation, kinetic incorporation, and impurity inclusion[245]. However, these alternate methods of impurity incorporation and subsequent impurity purge strategies are not elucidated in this work but will be discussed in detail in a future work. Another limitation of the proposed mathematical model is that the growth rate in equation (133) is assumed to be independent of the impurity concentration. However, there have been reports in literature[246] where both the impurities and solvents affect the crystal growth rate. Since the time-course evolution of the model predictions correlated well with the experimental observations in **Figure 7-14**, such effects were not modeled in the crystal growth rate equation ( equation (133)) for this particular API-solvent-impurity combination. However, as a cautionary note, this assumption cannot be extrapolated for all API-solvent combinations and the growth rate in equation (133) needs to be modified on a case-by-case basis. Such mechanistic investigations

of the effect of impurities on the rate of crystal growth and the effect on the optimal cooling profile will be elucidated in a future publication.

The process model considered here can also be applied to the closed-loop control of crystallization process that involves degradation. Model predictive control strategies for batch cooling crystallization [247][161][248][218][249] have been reported in literature, where the process model is used online to calculate the optimal control moves in a receding horizon framework so that the system reaches the desired target setpoint at the end of the batch, in the presence of system uncertainties. Similar closed-loop control framework can also be achieved by incorporating the online UPLC system used in this work and the degradation model to adjust the cooling profile automatically in real-time to minimize degradation.

## 7.8 Conclusions

In this work the crystallization of an API, which undergoes degradation at high temperatures was modelled considering nucleation, growth, degradation and impurity absorption followed by an experimental validation using PAT tools including FBRM, PVM and a novel online UPLC system. This is an industrially relevant problem since APIs often have low solubilities, and hence need to be cooled from a high initial process temperature at which the API may be thermally unstable. For such APIs, an optimal cooling profile that balances the objectives to achieve large final mean particle size versus minimizing the degradation of the API is crucial to the successful performance of the crystallization process. In this study Aspirin in ethanol/water mixture is used as the model system. Two objective functions are chosen for the process: (i) maximization of the average final product crystal size, and (ii) minimization of the degradation product concentration. It was shown that the cooling profiles required for these two objectives are very different and a trade-off exists between obtaining large crystals or minimizing the degradation of the API. If the end objective is to maximize the final particle size, the system needs to be kept at higher temperatures for a longer duration, but this leads to more degradation of API. However, if the end objective is to minimize the API degradation, the system needs to be cooled very fast, but this leads to smaller particles due to high rate of nucleation. It is shown in this work that the experimental results and the model simulation results are qualitatively consistent when the objective is to maximize the final particle size. However, when the objective is to minimize the concentration of the degradation product, the concentration evolution profiles of the degradation product are qualitatively different between the

experiments and the model simulations. This difference is attributed to structural uncertainty of the process model and the process model is modified to include adsorption of the degradation product into the API crystals. The optimal parameter estimate of the adsorption kinetics is obtained by fitting the experimental data. Using the optimal parameters, a better correlation between the model predictions and the experimental data was achieved when the impurity adsorption is included in the model.

## 8. FUTURE DIRECTIONS

It is hoped that the novel tools and technologies developed in this thesis will accelerate the rapid industrial deployment of Spherical Crystallization technology. However, there remains areas, which can benefit from further scientific research endeavors:

1. There needs to be more automated methods to detect the best solvent/antisolvent/binder combinations for development of successful SC technology of new APIs. There have been recent advances in literature on automated solvent selection for crystallization viz. [250]. Extension of such technology and adaptation to SC process will significantly reduce the time for process development.
2. Robust and accurate imaging-based sensors need to be developed to quantify the in-situ PSD and ASD during SA. The major bottleneck in industrial deployment of robust NMPC for SA is the lack of state-of-the-art in-situ measurement tools to characterize the ASD. Current PAT tools viz. FBRM have the limitation that it is hard to decouple the ASD from the PSD from in-situ CLD data. Moreover, retro-calculation of the PSD from the CLD is an ill-posed problem [251], which needs newer and more robust mathematical techniques for particles of arbitrary shapes. However, there are newer imaging-based tools coming out in the market viz. Blazemetrics probe [252], which can provide accurate in-situ estimates of the ASD.
3. With rapid advances in microfluidic crystallization, there needs to be more research on development of novel platform technology which can validate the experimental findings for co-agglomeration. Tracking the crystallization kinetics within droplets, in a lab-scale crystallizer is a challenging task. In-situ PAT tools viz. PVM cannot effectively track individual droplets over enough time duration, since the droplets rapidly disappear from the focal window of the PVM. However, with accurate engineering of channel dimensions in the microfluidic setup, along with multiple sensors positioned smartly along the channel, what happens within each droplet can be tracked.
4. Novel mathematical frameworks need to be developed which can rapidly detect the fundamental mode of impurity adsorption, from PAT data. This can enable online model adaptation, which will accelerate the convergence between mathematical modeling and experiments for industrial crystallization engineering.

## REFERENCES

- [1] Z. K. Nagy and R. D. Braatz, "Advances and New Directions in Crystallization Control," *Annu. Rev. Chem. Biomol. Eng.*, vol. 3, pp. 55–75, 2012.
- [2] Z. K. Nagy, E. Aamir, and C. D. Rielly, "Systematic Design of Supersaturation Controlled Crystallization Processes."
- [3] H. M. May, P. A. Helmke, and M. L. Jackson, "Gibbsite solubility and thermodynamic properties of hydroxy-aluminum ions in aqueous solution at 25°C," *Geochim. Cosmochim. Acta*, vol. 43, no. 6, pp. 861–868, 1979.
- [4] A. C. Oliveira, M. G. Coelho, R. F. Pires, and M. R. Franco, "Solubility of benzoic acid in mixed solvents," *J. Chem. Eng. Data*, vol. 52, no. 1, pp. 298–300, 2007.
- [5] P. A. Leggieri, M. Senra, and L. Soh, "Cloud point and crystallization in fatty acid ethyl ester biodiesel mixtures with and without additives," *Fuel*, vol. 222, no. February, pp. 243–249, 2018.
- [6] C. Bian, H. Chen, X. Song, and J. Yu, "Metastable zone width and the primary nucleation kinetics for cooling crystallization of NaNO<sub>3</sub> from NaCl-NaNO<sub>3</sub>-H<sub>2</sub>O system," *J. Cryst. Growth*, vol. 518, no. April, pp. 5–13, 2019.
- [7] G. M. Maggioni and M. Mazzotti, "Modelling the stochastic behaviour of primary nucleation," *Faraday Discuss.*, vol. 179, pp. 2012–2013, 2015.
- [8] H. Zhang, Y. Chen, J. Wang, and J. Gong, "Investigation on the spherical crystallization process of cefotaxime sodium," *Ind. Eng. Chem. Res.*, vol. 49, no. 3, pp. 1402–1411, 2010.
- [9] A. F. Blandin, D. Mangin, C. Subero-Couroyer, A. Rivoire, J. P. Klein, and J. M. Bossoutrot, "Modelling of agglomeration in suspension: Application to salicylic acid microparticles," *Powder Technol.*, vol. 156, no. 1, pp. 19–33, 2005.
- [10] C. Subero-Couroyer, D. Mangin, A. Rivoire, A. F. Blandin, and J. P. Klein, "Agglomeration in suspension of salicylic acid fine particles: Analysis of the wetting period and effect of the binder injection mode on the final agglomerate size," *Powder Technol.*, vol. 161, no. 2, pp. 98–109, 2006.
- [11] M. Maghsoodi, "Effect of process variables on physicochemical properties of the agglomerates obtained by spherical crystallization technique.," *Pharm. Dev. Technol.*, vol. 16, no. 5, pp. 474–82, 2011.
- [12] J. Kreuter, "Nanoparticles and microparticles for drug and vaccine delivery.," *J. Anat.*, vol. 189 ( Pt 3, no. Ii, pp. 503–505, 1996.
- [13] M. Folic', Folic', C. S. Adjiman, and E. N. Pistikopoulos, "Computer-Aided Solvent Design for Reactions: Maximizing Product Formation," pp. 5190–5202, 2008.
- [14] J. Thati and A. C. Rasmuson, "Particle engineering of benzoic acid by spherical agglomeration," *Eur. J. Pharm. Sci.*, vol. 45, no. 5, pp. 657–667, 2012.
- [15] D. Hebel, M. Ürdingen, D. Hekmat, and D. Weuster-Botz, "Development and scale up of high-yield crystallization processes of lysozyme and lipase using additives," *Cryst. Growth Des.*, vol. 13, no. 6, pp. 2499–2506, 2013.
- [16] B. Chattopadhyay, L. Jacobs, P. Panini, I. Salzmann, R. Resel, and Y. Geerts, "Accessing Phase-Pure and Stable Acetaminophen Polymorphs by Thermal Gradient Crystallization," *Cryst. Growth Des.*, vol. 18, no. 3, pp. 1272–1277, 2018.

- [17] F. Espitalier, B. Biscans, J.-R. Authelin, and C. Laguerie, "Modelling of the Mechanism of Formation of Spherical Grains Obtained by the Quasi-Emulsion Crystallization Process," *Chem. Eng. Res. Des.*, vol. 75, no. 2, pp. 257–267, 1997.
- [18] J. Katta and A. C. Rasmuson, "Spherical crystallization of benzoic acid," *Int. J. Pharm.*, vol. 348, no. 1–2, pp. 61–69, 2008.
- [19] S. Jitkar, R. Thipparaboina, R. B. Chavan, and N. R. Shastri, "Spherical Agglomeration of Platy Crystals: Curious Case of Etodolac," *Cryst. Growth Des.*, vol. 16, no. 7, pp. 4034–4042, 2016.
- [20] J. F. Wu, C. Y. Tai, W. K. Yang, and L. P. Leu, "Temperature Effects on the Crystallization Kinetics of Size-Dependent Systems in a Continuous Mixed-Suspension Mixed-Product Removal Crystallizer," *Ind. Eng. Chem. Res.*, vol. 30, no. 9, pp. 2226–2233, 1991.
- [21] C. Lindenberg, L. Vicum, and M. Mazzotti, "L -Glutamic Acid Precipitation: Agglomeration Effects 2008," *Cryst. Growth Des.*, vol. 8, no. 1, pp. 224–237, 2008.
- [22] Y. Kawashima, F. Cui, H. Takeuchi, T. Niwa, T. Hino, and K. Kiuchi, "Parameters determining the agglomeration behaviour and the micromeritic properties of spherically agglomerated crystals prepared by the spherical crystallization technique with miscible solvent systems," *Int. J. Pharm.*, vol. 119, no. 2, pp. 139–147, 1995.
- [23] J. Thati and A. C. Rasmuson, "On the mechanisms of formation of spherical agglomerates," *Eur. J. Pharm. Sci.*, vol. 42, no. 4, pp. 365–379, 2011.
- [24] M. Yousuf and P. J. Frawley, "Secondary Nucleation from Nuclei Breeding and Its Quantitative Link with Fluid Shear Stress in Mixing: A Potential Approach for Precise Scale-up in Industrial Crystallization," *Org. Process Res. Dev.*, vol. 23, no. 5, pp. 926–934, 2019.
- [25] A. R. Paradkar, A. P. Pawar, J. K. Chordiya, V. B. Patil, and A. R. Ketkar, "Spherical crystallization of celecoxib," *Drug Dev. Ind. Pharm.*, vol. 28, no. 10, pp. 1213–1220, 2002.
- [26] A. Brucato, M. Ciofalo, F. Grisafi, and R. Tocco, "On the simulation of stirred tank reactors via computational fluid dynamics," *Chem. Eng. Sci.*, vol. 55, no. 2, pp. 291–302, 2000.
- [27] J. Baldyga, J. R. Bourne, and B. Zimmermann, "Investigation of mixing in jet reactors using fast, competitive-consecutive reactions," *Chem. Eng. Sci.*, vol. 49, no. 12, pp. 1937–1946, 1994.
- [28] R. Ramachandran *et al.*, "Experimental studies on distributions of granule size, binder content and porosity in batch drum granulation: Inferences on process modelling requirements and process sensitivities," *Powder Technol.*, vol. 188, no. 2, pp. 89–101, 2008.
- [29] A. M. Bouwman *et al.*, "The effect of the amount of binder liquid on the granulation mechanisms and structure of microcrystalline cellulose granules prepared by high shear granulation," *Int. J. Pharm.*, vol. 290, no. 1–2, pp. 129–136, 2005.
- [30] D. Ramkrishna, "Population Balances: Theory and Applications to Particulate Systems in Engineering," *Elsevier*, 2000.
- [31] G. Morris, G. Power, S. Ferguson, M. Barrett, G. Hou, and B. Glennon, "Estimation of Nucleation and Growth Kinetics of Benzoic Acid by Population Balance Modeling of a Continuous Cooling Mixed Suspension, Mixed Product Removal Crystallizer," *Org. Process Res. Dev.*, vol. 19, no. 12, pp. 1891–1902, 2015.

- [32] J. Chakraborty, J. Kumar, M. Singh, A. Mahoney, and D. Ramkrishna, "Inverse Problems in Population Balances. Determination of Aggregation Kernel by Weighted Residuals," *Ind. Eng. Chem. Res.*, vol. 54, no. 42, pp. 10530–10538, 2015.
- [33] A. N. Sathyagal, D. Ramkrishna, and G. Narsimhan, "Solution of inverse problems in population balances-II. Particle break-up," *Comput. Chem. Eng.*, vol. 19, no. 4, pp. 437–451, 1995.
- [34] S. a. Cryer, "Modeling agglomeration processes in fluid-bed granulation," *AIChE J.*, vol. 45, no. 10, pp. 2069–2078, 1999.
- [35] K. Pal and J. Chakraborty, "Stability of Crystallizer-Producing Shape-Engineered Crystals," *Ind. Eng. Chem. Res.*, vol. 54, no. 42, pp. 10510–10519, 2015.
- [36] H. M. Hulburt and S. Katz, "Some problems in particle technology," *Chem. Eng. Sci.*, vol. 19, no. 8, pp. 555–574, 1964.
- [37] A. D. Randolph, "A population balance for countable entities," *Can. J. Chem. Eng.*, vol. 42, no. 6, pp. 280–281, 1964.
- [38] K. M. Dhanasekharan, J. Sanyal, A. Jain, and A. Haidari, "A generalized approach to model oxygen transfer in bioreactors using population balances and computational fluid dynamics," *Chem. Eng. Sci.*, vol. 60, no. 1, pp. 213–218, 2005.
- [39] A. W. Bryson and D. L. Hofman, "A population balance approach to the study of bubble behaviour at gas-evolving electrodes," *J. Appl. Electrochem.*, vol. 19, no. 1, pp. 116–119, 1989.
- [40] W. Fan, X. Hao, Y. Xu, and Y. Li, "Simulation of catalyst on-line replacement for Fischer-Tropsch synthesis in slurry bubble column reactor," *Chem. Technol. Fuels Oils*, vol. 47, no. 2, pp. 116–133, 2011.
- [41] M. Sow, E. Crase, J. L. Rajot, R. M. Sankaran, and D. J. Lacks, "Electrification of particles in dust storms: Field measurements during the monsoon period in Niger," *Atmos. Res.*, vol. 102, no. 3, pp. 343–350, 2011.
- [42] S. A. Hosseini and N. Shah, "Modelling enzymatic hydrolysis of cellulose part I: Population balance modelling of hydrolysis by endoglucanase," *Biomass and Bioenergy*, vol. 35, no. 9, pp. 3841–3848, 2011.
- [43] D. Bonvin, B. Srinivasan, and D. Hunkeler, "Control and optimization of batch processes," *IEEE Control Syst. Mag.*, vol. 26, no. 6, pp. 34–45, 2006.
- [44] A. Fiordalis and C. Georgakis, *Design of Dynamic Experiments versus model-based optimization of batch crystallization processes*, vol. 18, no. PART 1. IFAC, 2011.
- [45] Y. Yuan, Z. Li, and B. Huang, "Robust optimization under correlated uncertainty: Formulations and computational study," *Comput. Chem. Eng.*, vol. 85, pp. 58–71, 2016.
- [46] A. Mesbah, J. Landlust, A. E. M. Huesman, H. J. M. Kramer, P. J. Jansens, and P. M. J. Van den Hof, "A model-based control framework for industrial batch crystallization processes," *Chem. Eng. Res. Des.*, vol. 88, no. 9, pp. 1223–1233, 2010.
- [47] M. Diehl *et al.*, "Real-time optimization and nonlinear model predictive control of processes governed by differential-algebraic equations," *J. Process Control*, vol. 12, no. 4, pp. 577–585, 2002.
- [48] J. S. Logsdon and L. T. Biegler, "Accurate Solution of Differential-Algebraic Optimization Problems," *Ind. Eng. Chem. Res.*, vol. 28, no. 11, pp. 1628–1639, 1989.

- [49] D. Bonvin and B. Srinivasan, "Optimal operation of batch processes via the tracking of active constraints," *Isa Trans.*, vol. 42, no. 1, pp. 123–134, 2003.
- [50] R. T. Rockafellar and R. J. B. Wets, "Stochastic variational inequalities: single-stage to multistage," *Math. Program.*, vol. 165, no. 1, pp. 331–360, 2017.
- [51] V. M. Zavala and L. T. Biegler, "Large-scale parameter estimation in low-density polyethylene tubular reactors," *Ind. Eng. Chem. Res.*, vol. 45, no. 23, pp. 7867–7881, 2006.
- [52] W. Paengjuntuek, P. Kittisupakorn, and A. Arpornwichanop, "Optimization and nonlinear control of a batch crystallization process," *J. Chinese Inst. Chem. Eng.*, vol. 39, no. 3, pp. 249–256, 2008.
- [53] L. T. Biegler, A. M. Cervantes, and A. Wächter, "Advances in simultaneous strategies for dynamic process optimization," *Chem. Eng. Sci.*, vol. 57, no. 4, pp. 575–593, 2002.
- [54] K. Pal, Y. Yang, and Z. K. Nagy, "Model-Based Optimization of Cooling Crystallization of Active Pharmaceutical Ingredients Undergoing Thermal Degradation," *Cryst. Growth Des.*, p. acs.cgd.9b00305, 2019.
- [55] Z. Ugray, L. Lasdon, J. Plummer, F. Glover, J. Kelly, and R. Marti, "Scatter search and local NLP solvers: A multistart framework for global optimization," *INFORMS J. Comput.*, vol. 19, no. 3, pp. 328–340, 2007.
- [56] A. Gorban, N. Kazanzis, Kevrekidis, and Ottinger, *Model Reduction and Coarse-Graining Approaches for Multiscale Phenomena*, 2nd ed. 2006.
- [57] S. Kameswaran and L. Biegler, "Simultaneous dynamic optimization strategies: Recent advances and challenges," *Comput. Chem. Eng.*, vol. 30, no. 10–12, pp. 1560–1575, 2006.
- [58] Z. K. Nagy and R. D. Braatz, "Worst-Case and Distributional Robustness Analysis of Finite-Time Control Trajectories for Nonlinear Distributed Parameter Systems," *IEEE Trans. Control Syst. Technol.*, vol. 11, no. 5, pp. 694–704, 2003.
- [59] A. Mesbah, A. E. M. Huesman, H. J. M. Kramer, and P. M. J. Van Den Hof, "A comparison of nonlinear observers for output feedback model-based control of seeded batch crystallization processes," *J. Process Control*, vol. 21, no. 4, pp. 652–666, 2011.
- [60] S. Subramanian, S. Lucia, and S. Engell, "Handling structural plant-model mismatch via multi-stage nonlinear model predictive control," *2015 Eur. Control Conf. ECC 2015*, pp. 1602–1607, 2015.
- [61] A. Mesbah, S. Streif, R. Findeisen, and R. D. Braatz, "Stochastic nonlinear model predictive control with probabilistic constraints," *2014 Am. Control Conf.*, pp. 2413–2419, 2014.
- [62] B. Feng, M. Fu, H. Ma, Y. Xia, and B. Wang, "Kalman filter with recursive covariance estimation-Sequentially estimating process noise covariance," *IEEE Trans. Ind. Electron.*, vol. 61, no. 11, pp. 6253–6263, 2014.
- [63] S. N. Kavuri and V. Venkatasubramanian, "Combining pattern classification and assumption-based techniques for process fault diagnosis," *Comput. Chem. Eng.*, vol. 16, no. 4, pp. 299–312, 1992.
- [64] M. Emory, J. Larsson, and G. Iaccarino, "Modeling of structural uncertainties in Reynolds-averaged Navier-Stokes closures," *Phys. Fluids*, vol. 25, no. 11, 2013.
- [65] J. A. K. Suykens, J. Vandewalle, and B. De Moor, "Optimal control by least squares support vector machines," *Neural Networks*, vol. 14, no. 1, pp. 23–35, 2001.

- [66] C. F. W. Sanders, M. J. Hounslow, and F. J. Doyle, "Identification of models for control of wet granulation," *Powder Technol.*, vol. 188, no. 3, pp. 255–263, 2009.
- [67] D. E. Rivera, M. Morarl, and S. Skogestad, "Internal Model Control: Pid Controller Design," *Ind. Eng. Chem. Process Des. Dev.*, vol. 25, no. 1, pp. 252–265, 1986.
- [68] M. V. Kothare, V. Balakrishnan, and M. Morari, "Robust constrained model predictive control using linear matrix inequalities," *Automatica*, vol. 32, no. 10, pp. 1361–1379, 1996.
- [69] Z. K. Nagy and R. D. Braatz, "Robust nonlinear model predictive control of batch processes," *AIChE J.*, vol. 49, no. 7, pp. 1776–1786, 2003.
- [70] R. Bellman, "On the boundedness of solutions of nonlinear differential and difference equations," *Trans. Am. Math. Soc.*, vol. 62, no. 3, pp. 357–357, 1947.
- [71] C. R. Cutler and B. . Ramaker, "Dynamic matrix control - a computer control algorithm," in *Joint American Control Conference*, 1979.
- [72] H. M. Huynh, "A Large-Scale Quadratic Programming Solver Based on Block-LU Updates of the KKT System," no. September, 2008.
- [73] V. Dua, T. S. Hené, and E. N. Pistikopoulos, "A hybrid parametric/stochastic programming approach for mixed-integer nonlinear problems under uncertainty," *Recent Adv. Appl. Theor. Math.*, pp. 67–77, 2000.
- [74] L. Mockus, G. Reklaitis, K. Morris, and D. LeBlond, *Risk based approach for batch release*, vol. 43. Elsevier Masson SAS, 2018.
- [75] J. A. D. Rodrigues and R. Maciel Filho, "Optimal feed rates strategies with operating constraints for the penicillin production process," *Chem. Eng. Sci.*, vol. 51, no. 11, pp. 2859–2864, 1996.
- [76] A. J. Barbera and V. D. McConnell, "The impact of environmental regulations on industry productivity: Direct and indirect effects," *J. Environ. Econ. Manage.*, vol. 18, no. 1, pp. 50–65, 1990.
- [77] R. Bindlish and J. B. Rawlings, "Target Linearization and Model Predictive Control of Polymerization Processes," *AIChE J.*, vol. 49, no. 11, pp. 2885–2899, 2003.
- [78] Z. K. Nagy, M. Fujiwara, and R. D. Braatz, "Modelling and control of combined cooling and antisolvent crystallization processes," *J. Process Control*, vol. 18, no. 9, pp. 856–864, 2008.
- [79] D. B. Patience, J. B. Rawlings, and H. A. Mohameed, "Crystallization of para-xylene in scraped-surface crystallizers," *AIChE J.*, vol. 47, no. 11, pp. 2441–2451, 2001.
- [80] A. Patist and D. Bates, "Ultrasonic innovations in the food industry: From the laboratory to commercial production," *Innov. Food Sci. Emerg. Technol.*, vol. 9, no. 2, pp. 147–154, 2008.
- [81] J. Niu, J. Sha, Y. Wang, X. Ma, and D. Yang, "Crystallization and disappearance of defects of the annealed silicon nanowires," *Microelectron. Eng.*, vol. 66, no. 1–4, pp. 65–69, 2003.
- [82] M. Fujiwara, Z. K. Nagy, J. W. Chew, and R. D. Braatz, "First-principles and direct design approaches for the control of pharmaceutical crystallization," *J. Process Control*, vol. 15, no. 5, pp. 493–504, 2005.
- [83] R. Gunawan, D. L. Ma, M. Fujiwara, and R. D. Braatz, "Identification of Kinetic Parameters in Multidimensional Crystallization Processes," *Int. J. Mod. Phys. B*, vol. 16, no. 01n02, pp. 367–374, 2002.

- [84] S. D. Schaber, D. I. Gerogiorgis, R. Ramachandran, J. M. B. Evans, P. I. Barton, and B. L. Trout, "Economic analysis of integrated continuous and batch pharmaceutical manufacturing: A case study," *Ind. Eng. Chem. Res.*, vol. 50, no. 17, pp. 10083–10092, 2011.
- [85] T. Jiang and M. Phelan, "Extractables from filter components in model solvent streams for pharmaceutical filtration processes.," *PDA J. Pharm. Sci. Technol.*, vol. 57, no. 4, pp. 287–299, 2003.
- [86] P. K. Akkisetty, U. Lee, G. V. Reklaitis, and V. Venkatasubramanian, "Population balance model-based hybrid neural network for a pharmaceutical milling process," *J. Pharm. Innov.*, vol. 5, no. 4, pp. 161–168, 2010.
- [87] G. J. Vergote *et al.*, "In-line monitoring of a pharmaceutical blending process using FT-Raman spectroscopy," *Eur. J. Pharm. Sci.*, vol. 21, no. 4, pp. 479–485, 2004.
- [88] M. Landin, P. York, M. J. Cliff, R. C. Rowe, and A. J. Wigmore, "Scale-up of a pharmaceutical granulation in fixed bowl mixer-granulators," *Int. J. Pharm.*, vol. 133, no. 1–2, pp. 127–131, 1996.
- [89] J. I. Jinno *et al.*, "Effect of particle size reduction on dissolution and oral absorption of a poorly water-soluble drug, cilostazol, in beagle dogs," *J. Control. Release*, vol. 111, no. 1–2, pp. 56–64, 2006.
- [90] R. Vehring, "Pharmaceutical particle engineering via spray drying," *Pharm. Res.*, vol. 25, no. 5, pp. 999–1022, 2008.
- [91] P. A. Smith and R. A. Haber, "Effect of Particle Packing on the Filtration and Rheology Behavior of Extended Size Distribution Alumina Suspensions," *J. Am. Ceram. Soc.*, vol. 78, no. 7, pp. 1737–1744, 1995.
- [92] M. Nakach, J. R. Authelin, A. Chamayou, and J. Dodds, "Comparison of various milling technologies for grinding pharmaceutical powders," *Int. J. Miner. Process.*, vol. 74, no. SUPPL., 2004.
- [93] Y. Kawashima, M. Imai, H. Takeuchi, H. Yamamoto, K. Kamiya, and T. Hino, "Improved flowability and compactibility of spherically agglomerated crystals of ascorbic acid for direct tableting designed by spherical crystallization process," *Powder Technol.*, vol. 130, no. 1–3, pp. 283–289, 2003.
- [94] R. Petela, "Investigation of the product size in the agglomeration of coal particles," vol. 70, no. Figure 1, pp. 509–517, 1991.
- [95] R. David, A. M. Paulaime, F. Espitalier, and L. Rouleau, "Modelling of multiple-mechanism agglomeration in a crystallization process," *Powder Technol.*, vol. 130, no. 1–3, pp. 338–344, 2003.
- [96] R. Peña, C. L. Burcham, D. J. Jarmer, D. Ramkrishna, and Z. K. Nagy, "Modeling and optimization of spherical agglomeration in suspension through a coupled population balance model," *Chem. Eng. Sci.*, vol. 167, pp. 66–77, 2017.
- [97] P. M. Reilly, "Statistical methods in model discrimination," *Can. J. Chem. Eng.*, vol. 48, no. 2, pp. 168–173, 1970.
- [98] T. Hsiang and P. Reilly, "A practical method for discriminating among mechanistic models," *Can. J. Chem. Eng.*, vol. 49, no. 6, pp. 865–871, 1971.
- [99] I. Vatcheva, H. De Jong, O. Bernard, and N. J. I. Mars, "Experiment selection for the discrimination of semi-quantitative models of dynamical systems," vol. 170, pp. 472–506, 2006.

- [100] S. Hsu *et al.*, “Bayesian Framework for Building Kinetic Models of Catalytic Systems,” pp. 4768–4790, 2009.
- [101] Y. Cui, J. J. Jaramillo, T. Stelzer, and A. S. Myerson, “Statistical Design of Experiment on Contact Secondary Nucleation as a Means of Creating Seed Crystals for Continuous Tubular Crystallizers,” *Org. Process Res. Dev.*, vol. 19, no. 9, pp. 1101–1108, 2015.
- [102] S. P. Asprey and S. Macchietto, “Statistical tools for optimal dynamic model building,” *Comput. Chem. Eng.*, vol. 24, no. 2–7, pp. 1261–1267, 2000.
- [103] K. G. Gadkar, R. Gunawan, and F. J. Doyle, “Iterative approach to model identification of biological networks,” *BMC Bioinformatics*, vol. 6, p. 155, 2005.
- [104] C. R. Rojas, J. S. Welsh, G. C. Goodwin, and A. Feuer, “Robust optimal experiment design for system identification,” *Automatica*, vol. 43, no. 6, pp. 993–1008, 2007.
- [105] F. Galvanin, M. Barolo, and F. Bezzo, “Online model-based redesign of experiments for parameter estimation in dynamic systems,” *Ind. Eng. Chem. Res.*, vol. 48, no. 9, pp. 4415–4427, 2009.
- [106] S. H. Chung, D. L. Ma, and R. D. Braatz, “Optimal model-based experimental design in batch crystallization,” *Chemom. Intell. Lab. Syst.*, vol. 50, no. 1, pp. 83–90, 2000.
- [107] K. A. Ramisetty, A. B. Pandit, and P. R. Gogate, “Ultrasound-assisted antisolvent crystallization of benzoic acid: Effect of process variables supported by theoretical simulations,” *Ind. Eng. Chem. Res.*, vol. 52, no. 49, pp. 17573–17582, 2013.
- [108] S. Qamar, M. P. Elsner, I. A. Angelov, G. Warnecke, and A. Seidel-Morgenstern, “A comparative study of high resolution schemes for solving population balances in crystallization,” *Comput. Chem. Eng.*, vol. 30, no. 6–7, pp. 1119–1131, 2006.
- [109] S. Kumar and D. Ramkrishna, “On the solution of population balance equations by discretization—I. A fixed pivot technique,” *Chem. Eng. Sci.*, vol. 51, no. 8, pp. 1311–1332, 1996.
- [110] M. Bahrami, E. Nattaghi, S. Movahedirad, S. Ranjbarian, and F. Farhadi, “The agglomeration kinetics of aluminum hydroxide in Bayer process,” *Powder Technol.*, vol. 224, pp. 351–355, 2012.
- [111] R. Zauner and A. G. Jones, “Determination of nucleation, growth, agglomeration and disruption kinetics from experimental precipitation data: The calcium oxalate system,” *Chem. Eng. Sci.*, vol. 55, no. 19, pp. 4219–4232, 2000.
- [112] P. C. Kapur, “Kinetics of granulation by non-random coalescence mechanism,” *Chem. Eng. Sci.*, vol. 27, no. 10, pp. 1863–1869, 1972.
- [113] E. X. Berry, “Cloud Droplet growth by collection,” *J. Atmos Sci.*, vol. 24, pp. 688–701, 1967.
- [114] G. Menon and R. L. Pego, “Approach to self-similarity in Smoluchowski’s coagulation equations,” *Commun. Pure Appl. Math.*, vol. 57, no. 9, pp. 1197–1232, 2004.
- [115] P. D. Thompson, “A Transformation of the Stochastic Equation for Droplet Coalescence,” *Proc. Int. Conf. Cloud Phys.*, pp. 115–126, 1968.
- [116] R. Peña and Z. K. Nagy, “Process Intensification through Continuous Spherical Crystallization Using a Two-Stage Mixed Suspension Mixed Product Removal (MSMPR) System,” *Cryst. Growth Des.*, vol. 15, no. 9, pp. 4225–4236, 2015.
- [117] K. Pitt *et al.*, “Particle design via spherical agglomeration: A critical review of controlling parameters, rate processes and modelling,” *Powder Technol.*, vol. 326, pp. 327–343, 2018.
- [118] S. L. Lee *et al.*, “Modernizing Pharmaceutical Manufacturing: from Batch to Continuous Production,” *J. Pharm. Innov.*, vol. 10, no. 3, pp. 191–199, 2015.

- [119] L. Boskovic, I. E. Agranovski, and R. D. Braddock, "Filtration of nanosized particles with different shape on oil coated fibres," vol. 38, pp. 1220–1229, 2007.
- [120] L. X. Liu, I. Marziano, A. C. Bentham, J. D. Litster, E. T. White, and T. Howes, "Effect of particle properties on the flowability of ibuprofen powders," vol. 362, pp. 109–117, 2008.
- [121] D. F. Rivas, E. Castro-hernández, A. Luis, and V. Perales, "Evaluation method for process intensification alternatives," *Chem. Eng. Process. Process Intensif.*, vol. 123, no. August 2017, pp. 221–232, 2018.
- [122] J. Fotopoulos, C. Georgakis, and H. G. Stenger, "Uncertainty issues in the modeling and optimization of batch reactors with tendency models," *Chem. Eng. Sci.*, vol. 49, no. 24, pp. 5533–5547, 1994.
- [123] L. Madec, L. Falk, and E. Plasari, "Modelling of the agglomeration in suspension process with multidimensional kernels," *Powder Technol.*, vol. 130, no. 1–3, pp. 147–153, 2003.
- [124] D. L. Ma and R. D. Braatz, "Robust identification and control of batch processes," *Comput. Chem. Eng.*, vol. 27, no. 8–9, pp. 1175–1184, 2003.
- [125] D. J. Louwerse and A. K. Smilde, "Multivariate statistical process control of batch processes based on three-way models," vol. 55, 2000.
- [126] Z. K. Nagy and R. D. Braatz, "Robust Nonlinear Model Predictive Control of Batch Processes," *AIChE*, vol. 49, no. 7, pp. 1776–1786, 2003.
- [127] A. Bemporad and M. Morari, "Robust Model Predictive Control : A Survey Optimizer," *Lect. Notes Control Inf. Sci.*, vol. 245, pp. 207–226, 1999.
- [128] K. K. Benke, K. E. Lowell, and A. J. Hamilton, "Parameter uncertainty , sensitivity analysis and prediction error in a water-balance hydrological model," vol. 47, pp. 1134–1149, 2008.
- [129] Z. K. Nagy and R. D. Braatz, "Open-loop and closed-loop robust optimal control of batch processes using distributional and worst-case analysis," *J. Process Control*, vol. 14, no. 4, pp. 411–422, 2004.
- [130] Z. K. Nagy and R. D. Braatz, "Distributional uncertainty analysis using power series and polynomial chaos expansions," *J. Process Control*, pp. 229–240, 2006.
- [131] Z. K. Nagy and R. D. Braatz, *Distributional Uncertainty Analysis of a Batch Crystallization Process Using Power Series and Polynomial Chaos Expansions*, vol. 39, no. 2. IFAC, 2006.
- [132] K. K. K. Kim and R. D. Braatz, "Generalised polynomial chaos expansion approaches to approximate stochastic model predictive control†," *Int. J. Control*, vol. 86, no. 8, pp. 1324–1337, 2013.
- [133] K.-K. K. Kim, D. E. Shen, Z. K. Nagy, and R. D. Braatz, "Wiener's Polynomial Chaos for the Analysis and Control of Nonlinear Dynamical Systems with Probabilistic Uncertainties," *Control Syst. IEEE*, no. October, pp. 58–67, 2013.
- [134] Y. Yang *et al.*, "Application of Ultra-Performance Liquid Chromatography as an Online Process Analytical Technology Tool in Pharmaceutical Crystallization."
- [135] L. L. Simon, Z. K. Nagy, and K. Hungerbuhler, "Comparison of external bulk video imaging with focused beam reflectance measurement and ultra-violet visible spectroscopy for metastable zone identification in food and pharmaceutical crystallization processes," *Chem. Eng. Sci.*, vol. 64, no. 14, pp. 3344–3351, 2009.

- [136] L. L. Simon, K. Abbou Oucherif, Z. K. Nagy, and K. Hungerbuhler, "Bulk video imaging based multivariate image analysis, process control chart and acoustic signal assisted nucleation detection," *Chem. Eng. Sci.*, vol. 65, no. 17, pp. 4983–4995, 2010.
- [137] P. A. Larsen and J. B. Rawlings, "The Potential of Current High-Resolution Imaging-Based Particle Size Distribution Measurements for Crystallization Monitoring," *AIChE J.*, vol. 55, no. 4, pp. 896–905, 2009.
- [138] Z. Gao, D. Zhu, Y. Wu, S. Rohani, J. Gong, and J. Wang, "Motion-based multiple object tracking of ultrasonic-induced nucleation: A case study of L-glutamic acid," *Comput. Syst. Technol. Div. 2017 - Core Program. Area 2017 AIChE Annu. Meet.*, vol. 2017–Octob, pp. 562–565, 2017.
- [139] M. Li, D. Wilkinson, and K. Patchigolla, "Obtaining particle size distribution from chord length measurements," *Part. Part. Syst. Charact.*, vol. 23, no. 2, pp. 170–174, 2006.
- [140] E. L. Haseltine and J. B. Rawlings, "Critical evaluation of extended Kalman filtering and moving-horizon estimation," *Ind. Eng. Chem. Res.*, vol. 44, no. 8, pp. 2451–2460, 2005.
- [141] D. Xiu and G. E. M. Karniadakis, "THE WIENER–ASKEY POLYNOMIAL CHAOS FOR STOCHASTIC DIFFERENTIAL EQUATIONS," *SIAM J. SCI. Comput.*, vol. 24, no. 2, pp. 619–644, 2002.
- [142] R. Preece, S. Member, N. C. Woolley, S. Member, and J. V Milanovi, "The Probabilistic Collocation Method for Power-System Damping and Voltage Collapse Studies in the Presence of Uncertainties," *IEEE Trans. Power Syst.*, vol. 28, no. 3, pp. 2253–2262, 2013.
- [143] B. Carpenter *et al.*, "Stan: A probabilistic programming language," *J. Stat. Softw.*, vol. 76, no. 1, pp. 1–32, 2017.
- [144] J. A. Paulson, E. A. Buehler, and A. Mesbah, "Arbitrary Polynomial Chaos for Uncertainty Propagation of Correlated Random Variables in Dynamic Systems," *IFAC-PapersOnLine*, vol. 50, no. 1, pp. 3548–3553, 2017.
- [145] K. Kachrimanis, I. Nikolakakis, and S. Malamataris, "Spherical crystal agglomeration of ibuprofen by the solvent-change technique in presence of methacrylic polymers," *J. Pharm. Sci.*, vol. 89, no. 2, pp. 250–259, 2000.
- [146] M. S. Yang *et al.*, "Preparation of sustained-release nitrendipine microspheres with Eudragit RS and Aerosil using quasi-emulsion solvent diffusion method," *Int. J. Pharm.*, vol. 259, no. 1–2, pp. 103–113, 2003.
- [147] Y. Kawashima and C. E. Capes, "Further studies of the kinetics of spherical agglomeration in a stirred vessel," *Powder Technol.*, vol. 13, no. 2, pp. 279–288, 1976.
- [148] Y. Kawashima, T. Iwamoto, T. Niwa, H. Takeuchi, and T. Hino, "Role of the solvent-diffusion-rate modifier in a new emulsion solvent diffusion method for preparation of ketoprofen microspheres," *J. Microencapsul.*, vol. 10, no. 3, pp. 329–340, 1993.
- [149] J. Chakraborty and D. Ramkrishna, "Identification of markov matrices of milling models," *Ind. Eng. Chem. Res.*, vol. 48, no. 21, pp. 9763–9771, 2009.
- [150] Y. Yang *et al.*, "Application of feedback control and in situ milling to improve particle size and shape in the crystallization of a slow growing needle-like active pharmaceutical ingredient," *Int. J. Pharm.*, vol. 533, no. 1, pp. 49–61, 2017.
- [151] A. Nokhodchi, M. Maghsoodi, D. Hassan-Zadeh, and M. Barzegar-Jalali, "Preparation of agglomerated crystals for improving flowability and compactibility of poorly flowable and compactible drugs and excipients," *Powder Technol.*, vol. 175, no. 2, pp. 73–81, 2007.

- [152] M. K. Raval, K. R. Sorathiya, N. P. Chauhan, J. M. Patel, R. K. Parikh, and N. R. Sheth, "Influence of polymers/excipients on development of agglomerated crystals of secnidazole by crystallo-co-agglomeration technique to improve processability," *Drug Dev. Ind. Pharm.*, vol. 39, no. 3, pp. 437–46, 2013.
- [153] Y. Kawashima, T. Iwamoto, T. Niwa, H. Takeuchi, and T. Hino, "Uniform and improved bioavailability of newly developed rapid and sustained release suspensions of ibuprofen microspheres," *Int. J. Pharm.*, vol. 89, no. 1, pp. 9–17, 1993.
- [154] M. Maghsoodi and a S. Tajalli Bakhsh, "Evaluation of physico-mechanical properties of drug-excipients agglomerates obtained by crystallization.," *Pharm. Dev. Technol.*, vol. 16, no. 3, pp. 243–9, 2011.
- [155] C. Vervaet *et al.*, "Development of a continuous direct compression platform for low-dose drug products," *Int. J. Pharm.*, vol. 529, no. 1–2, pp. 329–346, 2017.
- [156] A. Pawar, A. Paradkar, S. Kadam, and K. Mahadik, "Agglomeration of Ibuprofen with talc by novel crystallo-co-agglomeration technique.," *AAPS PharmSciTech*, vol. 5, no. 4, p. e55, 2004.
- [157] B. Genikal and A. Rajendra, "Formulation Of Crystallo-Co-Agglomerates Of Naproxen : Study Of Effect Of Polymers On Drug Release," vol. 5, no. 3, pp. 852–864, 2013.
- [158] M. K. Raval, P. D. Vaghela, A. N. Vachhani, and N. R. Sheth, "Role of excipients in the crystallization of Albendazole," *Adv. Powder Technol.*, vol. 26, no. 4, pp. 1102–1115, 2015.
- [159] K. C. Garala, J. M. Patel, A. P. Dhingani, and A. T. Dharamsi, "Quality by design (QbD) approach for developing agglomerates containing racecadotril and loperamide hydrochloride by crystallo-co-agglomeration," *Powder Technol.*, vol. 247, pp. 128–146, 2013.
- [160] C. L. Viswanathan, S. K. Kulkarni, and D. R. Kolwankar, "Spherical agglomeration of mefenamic acid and nabumetone to improve micromeritics and solubility: a technical note.," *AAPS PharmSciTech*, vol. 7, no. 2, p. E48, 2006.
- [161] B. Szilágyi, Á. Borsos, K. Pal, and Z. K. Nagy, "Experimental implementation of a Quality-by-Control ( QbC ) framework using a mechanistic PBM-based nonlinear model predictive control involving chord length distribution measurement for the batch cooling crystallization of L -ascorbic acid," vol. 195, pp. 335–346, 2019.
- [162] H. G. Claycamp, R. Kona, R. Fahmy, and S. W. Hoag, "Quality-by-Design II: Application of Quantitative Risk Analysis to the Formulation of Ciprofloxacin Tablets," *AAPS PharmSciTech*, vol. 17, no. 2, pp. 233–244, 2015.
- [163] Y. Yang *et al.*, "Application of Ultra-Performance Liquid Chromatography as an Online Process Analytical Technology Tool in Pharmaceutical Crystallization," *Cryst. Growth Des.*, p. acs.cgd.6b01302, 2016.
- [164] D. A. Acevedo, J. Ling, K. Chadwick, and Z. K. Nagy, "Application of process analytical technology-based feedback control for the crystallization of pharmaceuticals in porous media," *Cryst. Growth Des.*, vol. 16, no. 8, pp. 4263–4271, 2016.
- [165] D. Sathe, K. Sawant, H. Mondkar, T. Naik, and M. Deshpande, "Monitoring temperature effect on the polymorphic transformation of acitretin using FBRM-lasentec," *Org. Process Res. Dev.*, vol. 14, no. 6, pp. 1373–1378, 2010.

- [166] E. Simone, A. N. Saleemi, and Z. K. Nagy, "In situ monitoring of polymorphic transformations using a composite sensor array of Raman, NIR, and ATR-UV/vis spectroscopy, FBRM, and PVM for an intelligent decision support system," *Org. Process Res. Dev.*, vol. 19, no. 1, pp. 167–177, 2015.
- [167] J. Cornel, C. Lindenberg, and M. Mazzotti, "Quantitative application of in-situ ATR-FTIR and Raman spectroscopy in crystallization processes. Submitted to Industrial &," *Ind. Eng. Chem. Res. Chem. Res.*, vol. 47, pp. 4870–4882, 2008.
- [168] V. Liotta and V. Sabesan, "Monitoring and feedback control of supersaturation using ATR-FTIR to produce an active pharmaceutical ingredient of a desired crystal size," *Org. Process Res. Dev.*, vol. 8, no. 3, pp. 488–494, 2004.
- [169] K. S. Howard, Z. K. Nagy, B. Saha, A. L. Robertson, G. Steele, and D. Martin, "A Process Analytical Technology Based Investigation of the Polymorphic Transformations during the Antisolvent Crystallization of Sodium Benzoate from IPA / Water Mixture," vol. 9, 2009.
- [170] A. O. Abioye, G. T. Chi, E. Simone, and Z. Nagy, "Real-time monitoring of the mechanism of ibuprofen-cationic dextran crystallization using crystallization process informatics system (CryPRINS)," *Int. J. Pharm.*, vol. 509, no. 1–2, pp. 264–278, 2016.
- [171] L. L. Simon *et al.*, "Assessment of recent process analytical technology (PAT) trends: A multi-author review," *Org. Process Res. Dev.*, vol. 19, no. 1, pp. 3–62, 2015.
- [172] J. Worlitschek, T. Hocker, and M. Mazzotti, "Restoration of PSD from chord length distribution data using the method of projections onto convex sets," *Part. Part. Syst. Charact.*, vol. 22, no. 2, pp. 81–98, 2005.
- [173] E. Rossinsky, K. B. Tarmyshov, M. C. Böhm, and F. Müller-Plathe, "Properties of polyvinyl alcohol oligomers: A molecular dynamics study," *Macromol. Theory Simulations*, vol. 18, no. 9, pp. 545–552, 2009.
- [174] J. T. Su and David Needham, "Mass Transfer in the Dissolution of a Multi-Component Liquid Droplet in an Immiscible Liquid Environment," *Langmuir*, vol. 29, no. 44, pp. 203–210, 2013.
- [175] and N. N. M. Jie Wu, Lachlan J. Graham, "Estimation of Agitator Flow Shear Rate," *AIChE J.*, vol. 52, no. 7, pp. 2323–2332, 2006.
- [176] S. Hall, A. W. Pacek, A. J. Kowalski, M. Cooke, and D. Rothman, "The effect of scale and interfacial tension on liquid-liquid dispersion in in-line Silverson rotor-stator mixers," *Chem. Eng. Res. Des.*, vol. 91, no. 11, pp. 2156–2168, 2013.
- [177] R. Farzad, S. Puttinger, S. Pirker, and S. Schneiderbauer, "Investigation of droplet size distribution for liquid-liquid emulsions in Taylor-Couette flows," *J. Dispers. Sci. Technol.*, vol. 39, no. 2, pp. 250–258, 2018.
- [178] A. Lam, A. N. Sathyagal, S. Kumar, and D. Ramkrishna, "Maximum Stable Drop Diameter in Stirred Dispersions," *AIChE J.*, vol. 42, no. 6, pp. 1547–1552, 1996.
- [179] T. Hörmann *et al.*, "Control of three different continuous pharmaceutical manufacturing processes: Use of soft sensors," *Int. J. Pharm.*, vol. 543, no. 1–2, pp. 60–72, 2018.
- [180] S. Byrn *et al.*, "Achieving continuous manufacturing for final dosage formation: Challenges and how to meet them May 20-21, 2014 continuous manufacturing symposium," *J. Pharm. Sci.*, vol. 104, no. 3, pp. 792–802, 2015.

- [181] N. Doki, N. Kubota, A. Sato, and M. Yokota, "Effect of cooling mode on product crystal size in seeded batch crystallization of potassium alum," *Chem. Eng. J.*, vol. 81, no. 1–3, pp. 313–316, 2001.
- [182] S. Y. Wong, J. Chen, L. E. Forte, and A. S. Myerson, "Compact crystallization, filtration, and drying for the production of active pharmaceutical ingredients," *Org. Process Res. Dev.*, vol. 17, no. 4, pp. 684–692, 2013.
- [183] L. Farber, G. I. Tardos, and J. N. Michaels, "Evolution and structure of drying material bridges of pharmaceutical excipients: Studies on a microscope slide," *Chem. Eng. Sci.*, vol. 58, no. 19, pp. 4515–4525, 2003.
- [184] Q. Su, S. Schiano, C. Y. Wu, Z. K. Nagy, and C. D. Rielly, *Dynamic impact milling model with a particle-scale breakage kernel*, vol. 38. Elsevier Masson SAS, 2016.
- [185] S. Iveson, "Limitations of one-dimensional population balance models of wet granulation processes1," *Powder Technol.*, vol. 124, no. 3, pp. 219–229, 2002.
- [186] A. Gupta, J. Austin, S. Davis, M. Harris, and G. Reklaitis, "A novel microwave sensor for real-time online monitoring of roll compacts of pharmaceutical powders online - A comparative case study with NIR," *J. Pharm. Sci.*, vol. 104, no. 5, pp. 1787–1794, 2015.
- [187] A. Adjei and J. Garren, "Pulmonary Delivery of Peptide Drugs: Effect of Particle Size on Bioavailability of Leuprolide Acetate in Healthy Male Volunteers," *Pharm. Res.*, vol. 7, no. 6, pp. 565–569, 1990.
- [188] C. C. Sun, Hao Hou, P. Gao, C. Ma, C. Medina, and Francisco J. Alvarez, "Development of a High Drug Load Tablet Formulation Based on Assessment of Powder Manufacturability: Moving Towards Quality by Design CHANGQUAN," *J. Pharm. Sci.*, vol. 98, no. 1, pp. 239–246, 2009.
- [189] L. X. Yu, "Pharmaceutical quality by design: Product and process development, understanding, and control," *Pharm. Res.*, vol. 25, no. 4, pp. 781–791, 2008.
- [190] Q. Su, Z. K. Nagy, and C. D. Rielly, "Pharmaceutical crystallisation processes from batch to continuous operation using MSMPR stages: Modelling, design, and control," *Chem. Eng. Process. Process Intensif.*, vol. 89, pp. 41–53, 2015.
- [191] C. M. V. M. Sharmista Chatterjee and M. Nasr, *Comprehensive Quality by Design for Pharmaceutical Product Development and Manufacture*. 2017.
- [192] D. Barrasso *et al.*, "A multi-scale, mechanistic model of a wet granulation process using a novel bi-directional PBM-DEM coupling algorithm," *Chem. Eng. Sci.*, vol. 123, pp. 500–513, 2015.
- [193] B. J. Ridder, A. Majumder, and Z. K. Nagy, "Parametric, Optimization-Based Study on the Feasibility of a Multisegment Antisolvent Crystallizer for in Situ Fines Removal and Matching of Target Size Distribution," *Ind. Eng. Chem. Res.*, vol. 55, no. 8, pp. 2371–2380, 2016.
- [194] E. van Derlinden, L. Mertens, and J. F. van Impe, "The impact of experiment design on the parameter estimation of cardinal parameter models in predictive microbiology," *Food Control*, vol. 29, no. 2, pp. 300–308, 2013.
- [195] H. Li, M. A. Grover, Y. Kawajiri, and R. W. Rousseau, "Development of an empirical method relating crystal size distributions and FBRM measurements," *Chem. Eng. Sci.*, vol. 89, pp. 142–151, 2013.
- [196] A. Chaudhury, A. Niziolek, and R. Ramachandran, "Multi-dimensional mechanistic modeling of fluid bed granulation processes: An integrated approach," *Adv. Powder Technol.*, vol. 24, no. 1, pp. 113–131, 2013.

- [197] V. Venkatasubramanian, R. Rengaswamy, K. Yin, and S. N. Kavuri, "A review of process fault detection and diagnosis part I: Quantitative model-based methods," *Comput. Chem. Eng.*, vol. 27, no. 3, pp. 293–311, 2003.
- [198] H. Kan, H. Nakamura, and S. Watano, "Effect of droplet size on particle-particle adhesion of colliding particles through droplet," *Powder Technol.*, vol. 321, pp. 318–325, 2017.
- [199] T. Khanam, M. Nurur Rahman, A. Rajendran, V. Kariwala, and A. K. Asundi, "Accurate size measurement of needle-shaped particles using digital holography," *Chem. Eng. Sci.*, vol. 66, no. 12, pp. 2699–2706, 2011.
- [200] N. K. Nere and D. Ramkrishna, "Solution of population balance equation with pure aggregation in a fully developed turbulent pipe flow," *Chem. Eng. Sci.*, vol. 61, no. 1, pp. 96–103, 2006.
- [201] D. Ramkrishna and M. R. Singh, "Population Balance Modeling: Current Status and Future Prospects," *Annu. Rev. Chem. Biomol. Eng.*, vol. 5, pp. 123–46, 2014.
- [202] E. Aamir, Z. K. Nagy, C. D. Rielly, T. Kleinert, and B. Judat, "Combined quadrature method of moments and method of characteristics approach for efficient solution of population balance models for dynamic modeling and crystal size distribution control of crystallization processes," *Ind. Eng. Chem. Res.*, vol. 48, no. 18, pp. 8575–8584, 2009.
- [203] S. Kumar and D. Ramkrishna, "On the solution of population balance equations by discretization—II. A moving pivot technique," *Chem. Eng. Sci.*, vol. 51, no. 8, pp. 1333–1342, 1996.
- [204] F. Cui *et al.*, "Design of sustained-release nitrendipine microspheres having solid dispersion structure by quasi-emulsion solvent diffusion method," *J. Control. Release*, vol. 91, no. 3, pp. 375–384, 2003.
- [205] K. K. Niwa, T., Takeuchi H., Hino T., Itoh A., Kawashima Y., "Preparation of Agglomerated Crystals for Direct Tableting and Microencapsulation by the Spherical Crystallization Technique with a Continuous System," *Pharmaceutical Res.*, vol. 11, no. 4, pp. 478–484, 1994.
- [206] S. H. Khidr, E. M. Niazy, and Y. M. El-Sayed, "Development and *in-vitro* evaluation of sustained-release meclofenamic acid microspheres," *J. Microencapsul.*, vol. 15, no. 2, pp. 153–162, 1998.
- [207] T. A. H. Emily P. Chang, Richard D. Braatz, "Pervaporation of Emulsion Droplets for the Templated Assembly of Spherical Particles: A Population Balance Model," *AIChE J.*, vol. 59, no. 10, pp. 3975–3985, 2013.
- [208] B. Gal-or and L. Padmanabhan, "Coupled Energy and Multicomponent Mass Transfer in Dispersions and Suspensions with Residence Time and Size Distributions," *AIChE J.*, vol. 14, no. 5, pp. 709–714, 1968.
- [209] B. H. Shah and D. Ramkrishna, "A population balance model for mass transfer in lean liquid—liquid dispersions," *Chem. Eng. Sci.*, vol. 28, no. 2, pp. 389–399, 1973.
- [210] F. Févotte and G. Févotte, "A method of characteristics for solving population balance equations (PBE) describing the adsorption of impurities during crystallization processes," *Chem. Eng. Sci.*, vol. 65, no. 10, pp. 3191–3198, 2010.
- [211] D. L. Marchisio and R. O. Fox, "Solution of population balance equations using the direct quadrature method of moments," *J. Aerosol Sci.*, vol. 36, no. 1, pp. 43–73, 2005.
- [212] A. Rashid, E. T. White, T. Howes, J. D. Litster, and I. Marziano, "Crystallization Kinetics of Ibuprofen from Ethanol and Aqueous Ethanol," *Chem. Eng. Trans.*, vol. 24, no. 2, pp. 631–636, 2011.

- [213] A. Rashid, E. T. White, T. Howes, J. D. Litster, and I. Marziano, "Growth rates of ibuprofen crystals grown from ethanol and aqueous ethanol," *Chem. Eng. Res. Des.*, vol. 90, no. 1, pp. 158–161, 2012.
- [214] Y. Yang and Z. K. Nagy, "Advanced control approaches for combined cooling/antisolvent crystallization in continuous mixed suspension mixed product removal cascade crystallizers," *Chem. Eng. Sci.*, vol. 127, pp. 362–373, 2015.
- [215] K. L. Choong and R. Smith, "Novel strategies for optimization of batch, semi-batch and heating /cooling evaporative crystallization," *Chem. Eng. Sci.*, vol. 59, no. 2, pp. 329–343, 2004.
- [216] Y. Yang and Z. K. Nagy, "Model-based systematic design and analysis approach for unseeded combined cooling and antisolvent crystallization (CCAC) systems," *Cryst. Growth Des.*, vol. 14, no. 2, pp. 687–698, 2014.
- [217] Y. Yang and Z. K. Nagy, "Combined Cooling and Antisolvent Crystallization in Continuous Mixed Suspension, Mixed Product Removal Cascade Crystallizers: Steady-State and Startup Optimization," *Ind. Eng. Chem. Res.*, vol. 54, no. 21, pp. 5673–5682, 2015.
- [218] A. Mesbah, Z. K. Nagy, A. E. M. Huesman, H. J. M. Kramer, and P. M. J. Van Den Hof, "Nonlinear model-based control of a semi-industrial batch crystallizer using a population balance modeling framework," *IEEE Trans. Control Syst. Technol.*, vol. 20, no. 5, pp. 1188–1201, 2012.
- [219] S. Ferguson *et al.*, "Use of continuous MSMRP crystallization with integrated nanofiltration membrane recycle for enhanced yield and purity in API crystallization," *Cryst. Growth Des.*, vol. 14, no. 2, pp. 617–627, 2014.
- [220] C. B. B. Costa and R. MacIel Filho, "Evaluation of optimisation techniques and control variable formulations for a batch cooling crystallization process," *Chem. Eng. Sci.*, vol. 60, no. 19, pp. 5312–5322, 2005.
- [221] C. Lindenberg, M. Krättli, J. Cornel, M. Mazzotti, and J. Brozio, "Design and Optimization of a Combined Cooling/Antisolvent Crystallization Process," *Cryst. Growth Des.*, vol. 9, no. 2, pp. 1124–1136, 2009.
- [222] Y. d Lang, A. M. Cervantes, and L. T. Biegler, "Dynamic Optimization of a Batch Cooling Crystallization Process," *Ind. Eng. Chem. Res.*, vol. 38, no. 4, pp. 1469–1477, 1999.
- [223] D. L. Ma, D. K. Tafti, and R. D. Braatz, "Optimal control and simulation of multidimensional crystallization processes," *Comput. Chem. Eng.*, vol. 26, no. 7–8, pp. 1103–1116, 2002.
- [224] S. M. Miller and J. B. Rawlings, "Model Identification and Control Strategies for Batch Cooling Crystallizers," vol. 40, no. 8, 1994.
- [225] A. Mesbah, A. N. Kalbasenka, and A. E. M. Huesman, *Real-time Dynamic Optimization of Batch Crystallization Processes*, vol. 41, no. 2. IFAC, 2008.
- [226] E. Simone, A. N. Saleemi, N. Tonnon, and Z. K. Nagy, "Active polymorphic feedback control of crystallization processes using a combined raman and ATR-UV/Vis spectroscopy approach," *Cryst. Growth Des.*, vol. 14, no. 4, pp. 1839–1850, 2014.
- [227] E. Simone, B. Szilagyi, and Z. K. Nagy, "Systematic model identification and optimization-based active polymorphic control of crystallization processes," *Chem. Eng. Sci.*, vol. 174, pp. 374–386, 2017.

- [228] B. G. Lakatos, T. J. Sapundzhiev, and J. Garside, "Stability and dynamics of isothermal CMSMPR crystallizers," *Chem. Eng. Sci.*, vol. 62, no. 16, pp. 4348–4364, 2007.
- [229] K. Pal and J. Chakraborty, "Stability of Crystallizer-Producing Shape-Engineered Crystals," *Ind. Eng. Chem. Res.*, 2015.
- [230] M. Blessy, R. D. Patel, P. N. Prajapati, and Y. K. Agrawal, "Development of forced degradation and stability indicating studies of drugs - A review," *J. Pharm. Anal.*, vol. 4, no. 3, pp. 159–165, 2014.
- [231] F. Amrani *et al.*, "Identification of dabigatran etexilate major degradation pathways by liquid chromatography coupled to multi stage high-resolution mass spectrometry," vol. 5, no. 56, pp. 45068–45081, 2015.
- [232] A. Borsos, A. Majumder, and Z. K. Nagy, "Multi-Impurity Adsorption Model for Modeling Crystal Purity and Shape Evolution during Crystallization Processes in Impure Media," *Cryst. Growth Des.*, vol. 16, no. 2, pp. 555–568, 2016.
- [233] C. Krishnaiah, A. R. Reddy, R. Kumar, and K. Mukkanti, "Stability-indicating UPLC method for determination of Valsartan and their degradation products in active pharmaceutical ingredient and pharmaceutical dosage forms," *J. Pharm. Biomed. Anal.*, vol. 53, no. 3, pp. 483–489, 2010.
- [234] N. W. Ali, S. S. Abbas, H. E. S. Zaazaa, M. M. Abdelrahman, and M. Abdelkawy, "Validated stability indicating methods for determination of nitazoxanide in presence of its degradation products," *J. Pharm. Anal.*, vol. 2, no. 2, pp. 105–116, 2012.
- [235] R. P. Shah, A. Sahu, and S. Singh, "Identification and characterization of degradation products of irbesartan using LC-MS/TOF, MSn, on-line H/D exchange and LC-NMR," *J. Pharm. Biomed. Anal.*, vol. 51, no. 5, pp. 1037–1046, 2010.
- [236] K. Choong, "Optimization of semi-batch reactive crystallization processes," *Chem. Eng. Sci.*, vol. 59, no. 7, pp. 1529–1540, 2004.
- [237] Z. K. Nagy, M. Fujiwara, and R. D. Braatz, "Modelling and control of combined cooling and antisolvent crystallization processes," *J. Process Control*, vol. 18, no. 9, pp. 856–864, 2008.
- [238] M. Nishimaru, S. Kudo, and H. Takiyama, "Cocrystal production method reducing deposition risk of undesired single component crystals in anti-solvent cocrystallization," *J. Ind. Eng. Chem.*, vol. 36, pp. 40–43, 2016.
- [239] G. Alibrandi, N. Micai, S. Trusso, and A. Villari, "Hydrolysis of aspirin studied by spectrophotometric and fluorometric variable-temperature kinetics," *J. Pharm. Sci.*, vol. 85, no. 10, pp. 1105–1108, 1996.
- [240] G. Shan, K. Igarashi, H. Noda, and H. Ooshima, "Production of large crystals with a narrow crystal size distribution by a novel WWDJ batch crystallizer," vol. 85, pp. 161–167, 2002.
- [241] Mr. James R. Zimmerman, "Technology Domain : Electrical Engineering PRF Reference Number : 2016-ZIMM-67551 Technology Readiness Level : 7 Carbon Fiber Tubing Heater," 2016-NaN-67551, 2016.
- [242] H. Li, Y. Kawajiri, M. A. Grover, and R. W. Rousseau, "Application of an empirical FBRM model to estimate crystal size distributions in batch crystallization," *Cryst. Growth Des.*, vol. 14, no. 2, pp. 607–616, 2014.

- [243] C. Lindenberg and M. Mazzotti, “Experimental characterization and multi-scale modeling of mixing in static mixers. Part 2. Effect of viscosity and scale-up,” *Chem. Eng. Sci.*, vol. 64, no. 20, pp. 4286–4294, 2009.
- [244] E. L. H. and J. B. Rawlings, “A Critical Evaluation of Extended Kalman Filtering and Moving Horizon Estimation,” *Twmcc*, no. 1, p. 19, 2003.
- [245] F. L. Nordstrom, B. Linehan, R. Teerakapibal, and H. Li, “Solubility-Limited Impurity Purge in Crystallization,” *Cryst. Growth Des.*, vol. 19, pp. 1336–1346, 2019.
- [246] P. A. Meenan, S. R. Anderson, and D. L. Klug, “Handbook of Industrial Crystallization - Chapter 03 - The influence of impurities and solvents on crystallization,” *Handb. Ind. Cryst.*, pp. 67–100, 2002.
- [247] J. Vissers, P. Jansen, and S. Weiland, “Control of supersaturation in batch cooling crystallization by robust state feedback linearization,” *IEEE Int. Conf. Control Autom. ICCA*, pp. 1114–1120, 2011.
- [248] D. Acevedo and Z. K. Nagy, “Systematic classification of unseeded batch crystallization systems for achievable shape and size analysis,” *J. Cryst. Growth*, vol. 394, pp. 97–105, 2014.
- [249] F. Allgower, R. Findeisen, and Z. Nagy, “Nonlinear model predictive control: From theory to application,” *J. Chinese Inst. Chem. Eng.*, vol. 35, no. 3, pp. 299–315, 2004.
- [250] S. Jonuzaj and C. S. Adjiman, “Designing optimal mixtures using generalized disjunctive programming: Hull relaxations,” *Chem. Eng. Sci.*, vol. 159, no. June 2016, pp. 106–130, 2017.
- [251] M. Mangold, “Use of a Kalman filter to reconstruct particle size distributions from FBRM measurements,” *Chem. Eng. Sci.*, vol. 70, pp. 99–108, 2012.
- [252] R. Becker, “Blazemetrics probe.” [Online]. Available: <https://www.blazemetrics.com/>.